IMAGE PROCESSING FOR THE ANALYSIS OF TI-6AL-4V MICROSTRUCTURES

Andrew Campbell

In the fulfilment of the requirement

For the degree of Doctor of Engineering

Advanced Forming Research Centre

Department of Design, Manufacture and Engineering Management

University of Strathclyde

Supervised by

Dr Paul Murray, Professor William Ion

Professor Stephen Marshall, Dr Evgenia Yakushina

DECLARATION AND COPYRIGHT

This thesis is the result of the author's original research. It has been composed by the author and has not been previously submitted for examination which has led to the award of a degree.

Signed: 

Date: 01/05/19

ACKNOWLEDGEMENTS

There a number of people I would like to thank for their support throughout my studies.

First, I must thank my supervisors Paul Murray, Stephen Marshall, Evgenia Yakushina and William Ion. To have 4 supervisors from different backgrounds take the time to all meet with me regularly provided a great learning experience and allowed me to get maximum benefit from this programme. In-fact the idea of doing a doctorate degree had not even occurred to me before Steve pitched it to me, so my career could have already gone down a very different route. Given how much I have enjoyed the last few years and my current career plans I am very glad that he did so. My supervisors have also worked hard to find further opportunities to develop my career since completion of this thesis for which I am also grateful. I must also say a special thanks to Paul in this section. Paul did not officially become first supervisor until the end of this project but was deserving of the role from day one and dedicated the most hands on time to supporting me throughout the project. He also willingly took on the unenviable task of correcting the typo ridden mess of informal language and spelling mistakes I too often wrote 4 years ago. While this may not seem like the most technically relevant example of his support I could have chosen, I believe having the patience to help fix even aspects of my work which was probably not his job, and that he frankly should not have needed to, highlights the dedication to my development he has always shown. Despite working fairly independently at times the guidance all my supervisors provided was very influential in my own development as well as this project, so thank you all.

I must also thank Etienne Decencière of the Centre of Mathematical Morphology in France for hosting me for at the centre for a few weeks during my studies and for the insight he provided during and after my visit. I must also thank Petr Dokladal and Beatriz Marcotegui for similarly providing support and guidance, and Albane Borocco for providing me with some code and an explanation of her own work, which was influential in Chapter 6 of this thesis. I would also like to thank the many students at the centre who went out of their way to make the non-French speaker with the funny Scottish accent feel welcome and included. It made the trip significantly more

enjoyable and will not be forgotten, nor will the idea of “bridging the gap” which I still hope makes it to the UK one day.

I would also like to thank the rest of my EngD cohort and other residents of the Leonardo Suite. The various holidays, trips, social events and general day to day shenanigans would have been worth spending the last 4 years here for alone (well maybe not Bulgaria). In-fact the monetary value of the biscuits I have stolen from Hanna in that time almost certainly makes it worth it (sorry about that).

I also want to thank all of my family for the support they have shown over the years. I am still not convinced you know what I do but you always had faith I could do it, usually more than I did, and that is what matters.

I must also take the unusual step of thanking my undergraduate course co-ordinator David Harle. I am often seen as extremely relaxed, indeed even ironically called “Mad Andy” by a few, however there was a stage in my studies where everything was less straight forward. If David had not been as supportive as he was, I may not be at Strathclyde writing this today. Therefore, I am obliged to note this here even though basically nobody would have any clue what on earth I am talking about.

Finally, I want to thank my girlfriend Freida for supporting me through the end of the EngD in particular the writing of my thesis. I am well aware that my brutal war with Microsoft word in the latter stages cannot have been pleasant to witness (p.s. if anyone ever reads this because they are soon to write their own thesis, use something else and certainly not an online template). However, your presence (and perhaps the cookies made to distract me from my fury) worked perfectly and were essential for keeping my sanity through this process. Much like my family you have this faith in me that is far greater than my own and is always helpful for me, so thank you.

ABSTRACT

The primary aim of the work presented in this thesis is to develop new and improved methods for analysing the microstructure of titanium alloys, specifically Ti-6Al-4V. This is achieved through the introduction of a software tool which incorporates novel image processing techniques to automate the measurement of a wide range of microstructural features in microscopic images of Ti-6Al-4V. It is shown that these measurements are performed in a faster, more repeatable way, with minimal input from expert materials scientists, when compared with existing methods.

The microstructure of a material consists of individual grains of different shapes and sizes. Precise analysis of these provides information about the properties of the material and thus is valuable for quality assurance and development of new materials, models or manufacturing processes. However, performing this analysis usually depends manual analysis techniques, requiring extensive input from expert materials scientists. Attempts at more efficient automated methods have so far had limited success, largely due to the wide variations that can occur in microstructural images.

In this thesis, a robust set of image processing techniques are proposed to automatically identify and measure key features of microstructural images. Due to the unique challenges posed by different microstructure types, two separate techniques are proposed; one aimed at measuring globular grains within microstructures and another aimed at measuring elongated grains, known as platelets. Measurements of globular grains are obtained using a novel segmentation algorithm that partitions the image such that each grain is individually labelled. Once identified in this way, the size and shape of each grain can then be measured, allowing both individual and aggregated measurements to be reported. The algorithm includes a variety of pre- and post-processing steps that dramatically reduce measurement errors, common in other segmentation methods. However, it was found that this method could not be reliably applied to segment and measure platelets. Measurements of these are instead

determined by shape fitting techniques. Similar approaches are already used for analysing this type of elongated object in similar datasets. However, several limitations exist that negatively affect both the accuracy and usefulness of these methods when applied to the dataset in this study. This thesis proposes novel adaptations to such techniques to improve reliability and extend the range of properties that can be measured. The resulting technique can be applied to measure platelet width, orientation, and morphology. A separate algorithm is also proposed that uses this data to identify and measure colonies of platelets. A software tool is designed to allow these tools to be deployed by material's scientists. This tool provides simple, intuitive feedback to the user to allow the proposed algorithms to be properly parameterised without image processing experience, or a good understanding of their operation.

This work is validated through a range of trials conducted on real world datasets of Ti-6Al-4V microstructural images. The dataset uses images from different microscopy technologies as well as different morphological types of microstructure. Results are validated through comparison with measurements performed by expert materials scientists using the most reliable procedures currently available, and demonstrate accurate results can be achieved automatically, significantly faster than before. The techniques proposed in this thesis also have general value in the wider domain of image processing, due to their robustness in challenging datasets. This is demonstrated by a detailed comparison with existing image processing tools, never before testing on microstructural data.

TABLE OF CONTENTS

1 INTRODUCTION

1.1 Motivation of research

At a microscopic level, materials such as metal alloys consist of a series of grains of different shapes, sizes, and arrangements. These grains form a microstructure, the properties of which are key factors in determining the properties of a material [1]. Chemically identical materials, that would otherwise be expected to exhibit the same mechanical properties, can instead have quite different properties when their microstructures differ. Such differences are a common occurrence and are caused by the application of thermal or mechanical work to the material. The final microstructure of any component, therefore, depends on the manufacturing processes applied to create it. This makes the ability to accurately assess the microstructure of a material important when designing new manufacturing processes, building models to predict the properties of manufactured parts or evaluating existing parts to ensure they are fit for purpose. This is particularly important in high value manufacturing applications, such as aerospace, where the high-performance requirements of such components mean achieving the best microstructure to maximise the desired mechanical properties is critical. The cost of such materials also leads to a desire to reduce waste, meaning a better understanding of material behaviour and how to avoid failing parts is beneficial. However, the advanced alloys used in such applications often have complicated microstructures that are difficult to assess.

Several different imaging technologies exist to enable microstructures to be studied. These include relatively cheap and simple Optical Microscopes (OMs) through to more advanced and expensive Scanning Electron Microscopes (SEMs). These technologies can be used to capture images of the arrangement of individual grains that make up the microstructure of a material. However, accurately measuring relevant features of microstructures can be challenging. The greyscale images produced are often noisy and complex microstructures can contain touching grains of similar pixel intensity which makes the boundaries between these grains challenging to delineate. In other cases, grains are extremely thin or have undergone some deformation, further complicating the identification of their boundaries. For these reasons standardised automated software often fails to correctly identify features of the microstructure in all but the simplest cases. A review of the literature highlights several existing attempts to use image processing to aid the microstructure analysis process. However, every existing method reviewed has key issues that prevent them from producing accurate measurements of key features in Ti-6Al-4V microstructures. This means that analysis is often performed using manual methods, which is a laborious process requiring a large amount of input from experienced materials scientists. This makes the analysis process slow and often prone to human error. Furthermore, measurements performed in this way are often difficult to repeat as true boundary locations are unclear in complex microstructures and even experienced materials scientists will identify features differently in the same image.

There is a clear need for new data processing techniques that can provide reliable measurement of complex microstructures. In this thesis, novel image processing methods are proposed to automatically analyse digital images of materials' microstructures, produced by existing technologies, and provide quantitative measurements for each microstructural feature of consequence.

1.2 Scope of work

The aim of the work presented in this thesis is to develop novel algorithms to automate the quantitative analysis of microstructures. A wide range of materials and microstructures exist and it is widely accepted that over-generalised image processing techniques often do not work for complex cases [2]. However, large variations in

microstructural images of even the same material can exist either due to variations in the microstructure itself or differences in sample preparation or imaging technology used. It is important that the methods proposed are not over-trained to a single microstructure type and are robust enough to measure the types of variations that are likely to occur in real world microscopy. However, it is also important that the proposed methods are specific enough that accurate results can be realistically achieved. Selected a suitable dataset, which balances the risk of over-generalisation and over-training, is critical to the success of this project. As a result, this work is constrained in three ways, as set out in the following sections.

1.2.1 Exclusive use of Ti-6Al-4V

This thesis exclusively studies the popular Titanium alloy, Ti-6Al-4V. The primary reason for this is that this material is extremely widely used [3] but, due to its complex microstructure, no good automated analysis solutions did not already exist, therefore, this was an important material to focus on. However, there are several other factors also motivating this decision. Ti-6Al-4V is a two-phase alloy, whose microstructure can exhibit different morphologies depending on how the material is processed, resulting in a wide variety of interesting features to measure. This increases the likelihood that the techniques proposed in this thesis will be applicable to other challenging microstructures, or even datasets from other fields. Focusing on a single material made it possible to study a wide range of microstructural variations, to ensure the proposed algorithms to detect these. No specific limits were placed on the range of thermal or mechanical process applied to the material and Ti-6Al-4V samples from various experiments and manufacturing processes are used in this work. This means that the dataset included globular, fully lamellar and bimodal microstructures. If the focus has instead been to study different materials then the resulting dataset, if of similar size, may have included only globular microstructures, so would actually contain less variety. Given the time requirements and difficulty in obtaining ground truth data for each microstructure, it was important to keep the dataset to manageable size, while maximising morphological variations. Ultimately, it is believed that the features present in Ti-6Al-4V microstructures, and the challenges in automatically

measuring these images are representative of the difficulties in performing microstructural analysis on other complex alloys.

1.2.2 Imaging Technologies

The scope of this thesis is constrained to study only 2D microstructural images produced by existing technologies. Both OMs and SEMs are used to increase the potential impact of this research, particularly in industrial settings where access to advanced SEMs is expensive and potentially limited. This thesis does not consider novel imaging techniques or any methods focusing on 3D imaging or modelling of the material. As microstructures of material are in reality 3D it would remain the responsibility of materials scientists using the techniques proposed in this thesis to apply them to 2D images at an appropriate set of positions and orientations on the material sample to generate relevant measurements, as is the case with many existing approaches. It is, however, noted that image processing techniques designed to operate in 2D can often be extended to operate in 3D, as has been shown in recent research into granular structures in other materials [4]. For the same reason a small amount of literature aimed at 3D image analysis is included in the review in Chapter 4, where the described technique is also relevant to 2D analysis.

1.2.3 Accuracy

A key constraint put on this work, or perhaps more accurately the claims made in this thesis, is to only match the level of measurement accuracy that expert materials scientists can achieve with existing manual analysis techniques. While it is possible that the proposed image processing techniques may also be more accurate, providing sufficient validation support that claim is problematic. The complex nature of the microstructures in this study means the true measurement of most microstructural features is not known with absolute certainty. Instead all that is known is an expert's best estimate. Different materials scientists would provide slightly different measurements of each microstructural feature. As a result, assessing the accuracy of automated techniques is challenging, and any improvement in accuracy a new method provided could not be reliably and precisely measured in the absence of an absolute ground truth. Advanced microscopy techniques, such as EBSD, could help provide a

more definitive ground truth, however, access to this is limited and required this would have limited the dataset available. The work presented in this thesis, therefore, focuses on performing analysis in a faster, more repeatable and less labour-intensive way than existing manual methods, which is of significant value. The techniques described in this thesis are considered to be accurate provided they can produce measurements within an acceptable range of those produced by expert materials scientist, as defined by existing standards.

1.3 Original contribution and thesis structure

The research goal is to improve microstructural analysis by introducing novel digital image processing algorithms to automate the measurement of microstructural properties. Through the review of recent literature, summarised in Chapter 4, it is demonstrated that automated measurements are achieved in other fields and for a few properties of some microstructures. However, it is also found that a complete, robust, automated analysis of complex Ti-6Al-4V microstructures is not yet possible and this requires the development of new techniques. The core contribution of this thesis is the design of novel image processing algorithms that are robust enough to measure microstructural features of Ti-6Al-4V. Two distinct image processing techniques are proposed that are specifically designed to measure two unique types of microstructural feature. These are then incorporated into a software tool to allow these methods to be applied in industry or academia by materials scientists without prior training in image processing. As a result, microstructural analysis can now be performed in a faster, less labour intensive, less prone to human error and more repeatable way. To achieve the core aims of this research, contributions are made to both materials science and image processing. These contributions can be broken down as follows:

For materials science the contributions are,

- A new technique for measuring features related to the morphology of primary alpha grains of microstructures (Chapter 5) such as:
    - Primary alpha grain size
    - Volume fraction of globular alpha
    - Distribution of individual grain size and globularity

- A new technique for measuring features related to the morphology and orientation of platelets in microstructures (Chapter 6) such as:
    - Width of alpha platelets
    - Size of alpha platelet colonies
    - Shape of platelets and grains
    - Distribution of platelet orientations
- A technique for identifying artefacts within microstructures (Chapter 5).
- A new algorithm to identify colonies of platelets (Chapter 6).

For image processing the contributions are,

- A novel extension to the marker-based Watershed Algorithm [5], [6] to enable better segmentation of images containing touching objects (Chapter 5).
- An improved granulometric procedure for simultaneously computing the dimensions and orientation of elongated structures in images (Chapter 6).

The remainder of this thesis is laid out as follows. Chapter 2 describes the methodology used when conducting the research described in this thesis. Chapter 3 introduces key materials science and image processing concepts critical to understanding the remainder of the thesis. Chapter 4 presents a review of recent literature and establishes the requirements that the new image processing techniques must meet in order to improve microstructural analysis of Ti-6Al-4V when compared to existing approaches. The novel contributions of this thesis are then presented in 3 chapters. Chapter 5 and 6 describe the new image processing techniques proposed. Chapter 5 shows segmentation methods for globular grains and Chapter 6 shows measurement techniques for elongated platelets. Chapter 7 describes a new software tool used to apply these methods to microstructural analysis and intuitively tune the parameters. Validation is provided in Chapter 8 to demonstrate the impact of the presented techniques. Finally, Chapter 9 summarises the work presented and describes some future improvements that could be made to extend this work.

2 RESEARCH METHODOLOGY

This chapter describes the research methodology that was applied to meet the core objective of improving the microstructural analysis of Ti-6Al-4V using image processing. It is generally considered that a methodology should account for factors such as; sources of data, research techniques, outputs, validation and the relationship between these factors [7]. The first step in this project was to study the state-of-the-art in microstructural analysis techniques for Ti-6Al-4V and identify any shortcomings. New techniques were then developed to address these shortcomings and make useful improvements. A suitable dataset was selected which is used to both aid development and evaluate the proposed techniques. Finally, results from experimental trials were used to evaluate whether the core aim of improving microstructural analysis had been met. The individual steps in this methodology and the relationship between them are outlined in the flowchart in Figure 2.1, with more detail on this provided in the remaining sub-sections of this chapter. As trials involving software are cheap and easy to set-up, an efficient way to develop the new techniques is to use an iterative process were ideas discovered in the literature are implemented and tested, with the results guiding future literature review or algorithm development. This type of approach was used in the research presented in this thesis and is indicated in the flowchart in Figure 2.1.

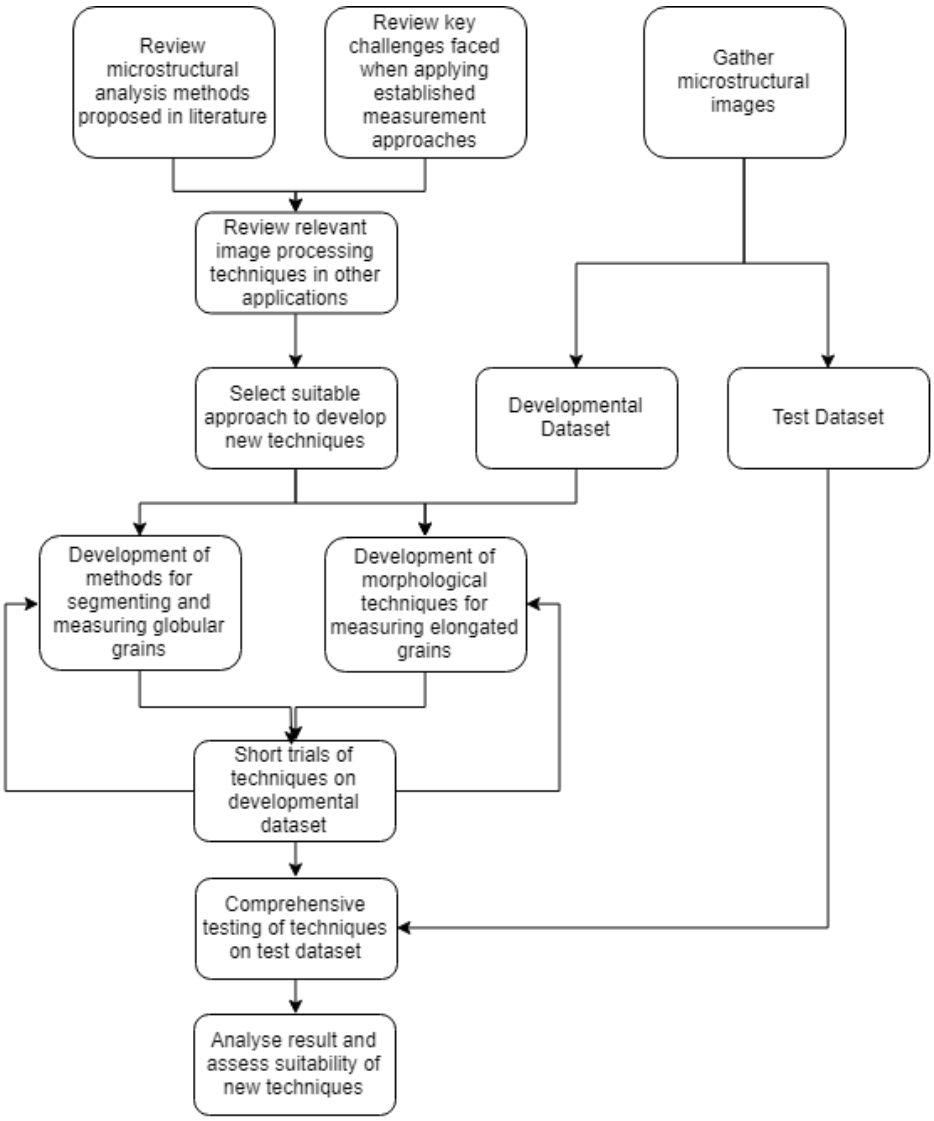

Figure 2.1: Flow chart of research methodology

2.1 Analysis of existing methods

The first step in this project was to review relevant literature, to identify conceptual gaps in current knowledge related to the research aims of this project. This required that the review include both existing manual methods of microstructural analysis and any attempts that have already been made to apply image processing techniques to this problem. The challenges and benefits of each method are assessed in order to identify a baseline performance that the new techniques proposed in this thesis must improve upon.

While this alone is sufficient to justify the contributions to material analysis made in this thesis, an additional review of more fundamental image processing research was also conducted in order to identify the best approach to take when developing the new methods. This was guided by the results of the review of materials science literature and focuses on techniques targeting the type of feature revealed to be both important and challenging to measure. The image processing review included techniques that had not previously been applied to the microstructural analysis of titanium, and mostly not to any other metallic material, but had been successfully applied in other fields featuring similar datasets. Full details on what constitutes a similar dataset are explained in Chapter 4. It became apparent from this review that no existing image processing technique was perfectly suited to provide accurate measurements of all the microstructural features of interest in titanium alloys. Additionally, many potentially suitable methods failed completely in the most challenging cases and would likely not be robust enough to measure the variety of different microstructures investigated. Therefore, as well as identifying the most suitable techniques to incorporate into the new algorithms, important limitations in the knowledge in the field of image processing are also discussed. Addressing these conceptual gaps in the literature is essential to the design of suitable image processing algorithms for microstructural analysis and also leads to contributions in the field of image processing in addition to those in the fields of materials science and microstructural analysis.

2.2 Application of a suitable dataset

The Ti-6Al-4V alloy can exhibit a wide variety of microstructural arrangements depending on the thermal and mechanical history of the material sample investigated. Obtaining a suitable dataset that is varied enough to allow useful techniques to be developed is, therefore, a critical stage in this research. There are several possible approaches to obtain this dataset. Ostensibly, the most rigid and structured approach would be to perform an experiment where samples of material from the same source are subjected to different thermal and mechanical processes to produce a range of different microstructures. As sample preparation and microscopy methods could be tightly controlled, this would likely produce microstructural images that are relatively consistent and predictable with the same level of lighting, scratches and artefacts seen

in each. Such a dataset would allow techniques to be designed that can measure different microstructure types. However, this experiment would be time consuming and expensive and would not inherently add value when compared to existing microstructural data taken from other sources. Additionally, the controlled nature of that type of experiment would produce microstructures that do not reflect the full variation in microstructural images expected in real life situations. Differences in images are often produced by the variety of experimental procedures, material preparation and microscope set-up used in different factories and laboratories. As these factors can be difficult to control, and the effect on the microstructural images produced is difficult to predict. Thus, a more varied and less perfect dataset is preferred to ensure the results presented in this work are representative of what can be achieved in practise. A more pragmatic approach was, therefore, taken where the microstructural images for the titanium dataset were drawn from existing projects conducted at the Advanced Forming Research Centre (AFRC) and by their industrial partners. This allowed a large dataset of images to be obtained that were subject to a variety of different real-world conditions, imaged on different microscopy technologies and measured by different materials scientists. Many of the images used came from a single experimental trial that aimed to study the effects of thermal and mechanical treatment on the shape and size of grains. Therefore, the full range of different microstructure types that would be expected is included within the dataset. The approach taken means that the dataset gathered includes both genuine microstructural variations and image variations produced by differences in how the microstructure images are captured, which are not informative of the underlying microstructure. Both of which are important to include in the dataset in order to validate the robustness of the proposed techniques for real world microscopy.

2.3 Design of new analysis procedures

A new set of techniques are designed that can measure properties of microstructural images as consistently and accurately as possible. This is an iterative process which requires continuous experimentation to observe the effect of different operations on microstructural images. Such an approach is common in the development of software-based methods as there is little cost to this experimentation as it is non-destructive and

requires only a computer and researcher and processor time. The success of this type of methodology depends upon the selection of a suitable development dataset for use during development. A developmental dataset was built by subjectively selecting one or two images from each microstructure type and imaging technology such that the dataset contained as much variations as possible for the smallest number of images. The remaining images were kept for testing and evaluation. As the new algorithms are designed to analyse images from the developmental dataset, it is important that this captures the type and level of variation expected in real-world images. If the developmental dataset does not capture this variety then the resulting techniques will be over-trained to a particular dataset and will likely perform very well on this data only and fail when applied to other data. It is also important that the developmental dataset is not excessively large as this would make the development process slower and more difficult. It is also beneficial to keep as many images as possible for a testing and evaluation dataset. As these are not used in the design of the algorithm, the results obtained on this data are informative of how the new algorithms are likely to perform when used by materials scientists.

It appears likely that all the possible features of titanium alloys are too different to be measured reliably and accurately by a single method. Therefore, the decision is made to propose two distinct techniques; one for the segmentation and measurement of equiaxed features, best suited for globular alpha grains, and another for extracting orientation, size and shape information on a per pixel basis, best suited for elongated grains. A full explanation of the reasoning behind this decision is provided in the literature review in Chapter 4. The techniques proposed are shown in Chapters 5 and 6 with the software implementation described in Chapter 7.

2.4 Validation of new methods

The techniques proposed in this thesis are validated on the set of microstructural images of Ti-6Al-4V, described in Section 2.2. As not all features exist in all microstructures, suitable images to test the measurements of each feature are selected qualitatively from the dataset by the researcher. In each case the largest possible dataset in which each feature could be measured are used.

The validation process requires results to be compared with an alternative measurement considered to be the ground truth. It is set out in the scope of this work, defined in Section 1.2, that the target is to match what expert materials scientists could achieve using manual procedures. Therefore, measurements performed by expert materials scientists using existing manual methods are used as the ground truth in this thesis. Any measurement of a microstructural feature that matches (within a small margin of error) the measurement achieved by a materials scientist indicates that the proposed technique is accurate. The time required to perform each measurement is also monitored to assess if the new techniques could also offer faster measurements. It should also be noted that the automated nature and software implementation of the proposed techniques makes the proposed methods inherently repeatable and less labour intensive than manual alternatives. The contribution of this work is further demonstrated through comparison with existing automated approaches where applicable.

As well as facilitating improved analysis of titanium microstructures, the techniques presented in this thesis also makes contributions to the field of image processing through the techniques described in Chapter 5 and 6. Validation of these contributions requires additional evidence other than measurements of microstructural properties. For the segmentation techniques in Chapter 5, the segmentation accuracy is assessed through comparison with a ground truth segmentation manually drawn by expert materials scientists. For the techniques for analysing thin structures in Chapter 6, measurements performed on a pixel by pixel basis are compared to the ground truth measurements. In both cases the contribution is demonstrated by comparing the results with existing image processing techniques for the same task. As this is used to demonstrate novelty in the image processing field, the experiment includes an evaluation of techniques that have not previously been applied to images of microstructures but have been successfully applied to other similar images.

3 FUNDAMENTALS OF MICROSTRUCTURAL ANALYSIS AND IMAGE PROCESSING

This chapter describes key concepts underpinning this research that are critical to understanding the remaining content of this thesis. As the aim is to provide image processing tools to improve the analysis of titanium microstructures, it is necessary to provide some fundamental information from both the fields of materials science and image processing. The first section of this chapter focuses on materials science and provides an overview of different microstructure types that can exist, the constituent components of these microstructures and the effect that the size and morphology of these features have on a material's properties. This information is used to determine which features of microstructures are the most important to measure. Analysis of some example images are provided to demonstrate the types of challenges that microstructural images present to automated image processing techniques. In the second section of this chapter, definitions are provided of several fundamental image processing concepts that are relevant to the new techniques proposed in this thesis.

3.1 Material and microstructure

The microstructure of a material affects many of its properties. Tensile strength, ductility, yield stress, hardness and surface roughness are all known to be impacted by variations in a material's microstructure [1], [8]. Understanding these variations is important when designing new methods of automated microstructural analysis. As set out in Chapter 1, the scope of this work is restricted to the microstructure of the Ti-6Al-4V alloy. Hence this section will present examples of only this material's

microstructure and describe the variations that can exist within it as well as describing the features it is necessary to measure when analysing this microstructure.

3.1.1 Microstructure types and features

Ti-6Al-4V is a two-phase alloy containing an alpha and beta phase with each phase having a different chemical composition. A full discussion of the details of this composition is beyond the scope of this thesis. What is most important for the type of microstructural analysis methods studied here is that grains of each phase should be measured separately and that these phases typically present as a significantly different intensity in a greyscale microstructural image. Alpha grains can be either equiaxed or elongated [9]. Equiaxed grains are commonly called globular alpha while elongated grains are referred to either as laths or platelets [10].

The shape and size of these grains is determined by the thermal and mechanical processes applied to the material. As the boundaries between these grains are not as strong as their internal structure, this in turn determines material properties. Therefore, the ability to analyse the microstructural evolution of a material is important to understand the effect of different manufacturing processes and the quality of final components. Grains in α+β alloys such as Ti-6Al-4V are nucleated during phase transformation from β phase, which occurs when the material is heated above the β transus temperature. This transformation can be either martensitic or by a diffusion controlled nucleation and growth process, more precise details on the chemistry of which are described in [1]. The martensite transformation involves atoms moving co-operatively by a shear type process and produces a homogeneous microstructure, which contains nearly entirely platelets, the resulting microstructures are often referred to as martensitic microstructures. Nucleation and growth processes can produce different microstructure types based on cooling rates. Sufficiently slow cooling rates will lead to alpha grains nucleating preferentially first along the boundaries of existing beta grains and then into the grain in parallel platelets. This results in a colony structure where either these boundary grains or the existence of these parallel structures indicate the colonies. As the growth of platelets occurs within the beta phase there is often a clear phase change at the boundaries of platelets in this case, which is visible in microscopic images. At faster cooling rates the thickness of platelets decreases, as they

have less time to grow. The size of colonies also decreases as parallel platelets can no longer fill the entire prior beta grain and often nucleate on boundaries of these instead. In some cases, this can result in a basket weave type structure, referred to as a Widmanstatten microstructure, although the likelihood is dependent on the alpha or beta stabilisers in the alloy. The size of globular grains is also determined by the aforementioned processes, however, typically require additional mechanical work to produce them, with the strain applied by this work also contributing to the size and number of these grains.

The microstructure of metal alloys can typically be classed as either globular, bi-modal or lamellar, depending on whether the microstructure consists entirely of one grain type or of a mixture of both. Figure 3.1 presents Scanning Electron Microscope (SEM) images of these microstructure types where the darker regions represent alpha phase. The key features to measure in each microstructure type differs due to the presence of different grain morphologies, as outlined in Section 3.1.2.

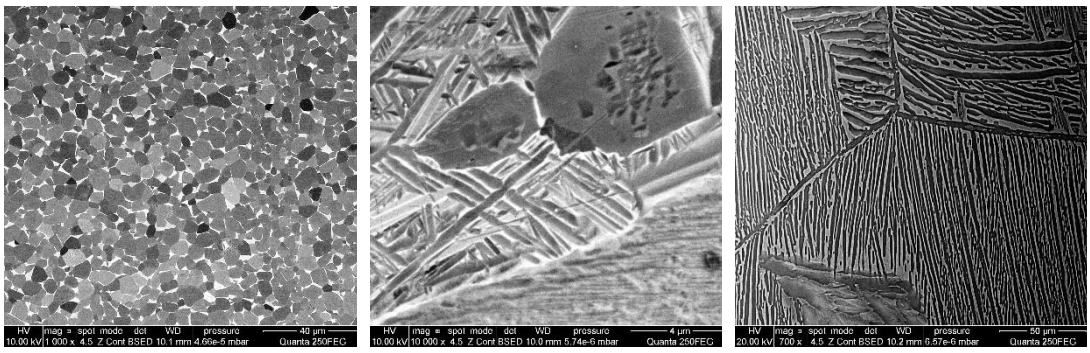

a) b) c)

Figure 3.1: Examples of different microstructure types images by an SEM where a) globular, b) bi-modal and c) lamellar

3.1.2 Microstructural measurements

This section lists and describes the features of Ti-6Al-4V microstructures that are desirable to measure.

3.1.2.1 Volume fraction of alpha phase

The volume fraction of alpha phase, V_α, is considered important to measure regardless of the morphological type of the microstructure [11], [12]. This is defined as the ratio

of the area of the microstructure occupied by alpha phase, A_α, to the entire microstructure area, A_I, as in Equation (3.1).

$$V_\alpha = \frac{A_\alpha}{A_I} \quad \textbf{(3.1)}$$

3.1.2.2 Grain Size

In globular and bi-modal microstructures the size of globular alpha grains are among the most common microstructural features to measure as there is a well-established relationship between grain size and yield strength through the Hall-Petch relationship [13]. Normally this is reported through the mean grain size, G_m, with size being an estimate of the average diameter of the grain, G_s, as in Equation (3.2) where N_g is the number of grains.

$$G_m = \frac{\sum_{i=1}^{N_g} G_i}{N_g} \quad \textbf{(3.2)}$$

3.1.2.3 Volume fraction of globular alpha

In addition to measuring the size of alpha grains, the shape of these grains is also considered significant [11], [12], [14], [15]. The percentage of the microstructure that consists of globular alpha is of particular interest in microstructures containing alpha platelets due to the superior strength of platelet boundaries compared to globular grain boundaries [11]. This is quantified by the globular volume fraction, V_g. This can be defined either as the ratio of globular alpha grains, N_g, to all alpha grains, N_α, as in Equation (3.3), or as ratio of the area of globular alpha grains, A_g, to the total alpha phase area, A_α, as in Equation (3.4).

$$V_g = \frac{N_g}{N_\alpha} \quad \textbf{(3.3)}$$

$$V_g = \frac{A_g}{A_a} \quad \textbf{(3.4)}$$

3.1.2.4 Platelet width

Measurements of platelets pertain to microstructures that have undergone martensite or similar transformations such as bi-modal or lamellar microstructures. The width of alpha platelets, W, is the most widely measured feature of lamellar structures.

Typically it is the mean width of platelets, W_m, that is reported as this has a proven relationship to material properties [10]. This is shown in Equation (3.5) where w denotes platelet width and N_m is the number of measurements performed.

$$W_m = \frac{\sum_{i=1}^{N_m} W_i}{N_m} \tag{3.5}$$

The length of individual platelets is not typically measured as any information given by this is provided by the colony length.

3.1.2.5 Colony size

In certain alloys, such as Ti-6Al-4V, it is common for the alpha platelets to gather in parallel packets known as colonies, as illustrated in Figure 3.2. Colony microstructures can exist where a fully lamellar microstructure consists entirely of platelets organised into colonies. However, colonies can also exist alongside equiaxed alpha grains in bi-modal microstructures. There are several reasons why the size of these colonies is important to measure. Colony size is effectively a measure of slip length [16] and therefore affects both plastic deformation and crack propagation [17]. Smaller colonies have also been found to lead higher tensile strengths [18]. Colony size, *CS*, is reported as the mean size of the colonies in the microstructure, as in Equation (3.6), with the size of each colony being determined by the average diameter of that colony, *dc*.

$$CS = \frac{\sum_{1}^{n} dc_n}{n} \tag{3.6}$$

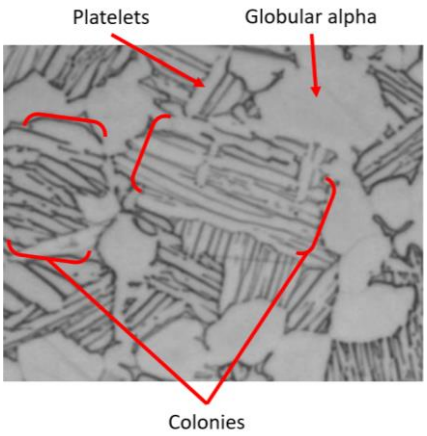

Figure 3.2: Examples of features in a bi-modal image taking using optical microscopy

3.1.2.6 Platelet orientation

In addition to the platelet and colony sizes, the orientation of platelets is sometimes studied to provide information about slip plane and material texture [19]. Typically, this data is presented through histograms of platelet orientation rather than through a concise metric as is the case with the other properties discussed.

3.1.2.7 Summary

A range of features have been identified that are important to measure when analysing images of titanium microstructures. It should be noted that certain features only exist in certain morphological types of microstructures. Platelet width, orientation and colony size are only measured in bi-modal and lamellar microstructures. Globular volume fraction is only relevant in bi-modal microstructures, while alpha grain size is important in both globular and bi-modal structures. A summary of which measurements are of interest in each image is given in Table 3.1, with annotated image indicating the relevant features provided in Figure 3.2.

Table 3.1: Measurements of interest in different microstructure types

Microstructure Type	**Measurement**
Lamellar	• Platelet width • Colony size • Volume fraction of alpha phase • Platelet/colony orientation
Bi-modal	• Grain size • Volume fraction of globular alpha • Volume fraction of alpha phase • Platelet width • Colony size
Globular	• Grain size • Volume fraction of globular alpha • Volume fraction of alpha phase

Features in microstructures are also sometimes referred to as either primary or secondary, depending on whether or not grains were pre-existing or formed during recrystallization as a result of thermal and mechanical process applied to the material. This thesis generally assumes measurements of primary grains, so this distinction is mostly ignored. However, size filtering methods, described in Chapter 5, could allow for separate measurements of secondary grains if required.

3.2 Imaging technologies

This section describes the image technologies used to produce the microstructural images analysed in this thesis and explains the challenges associated with images captured using each technology. As the scope is restricted to 2D microscopy, only optical microscopes and SEMs are discussed here.

3.2.1 Optical Microscopy

Optical microscopes are relatively cheap and readily available. As a result, they are commonly used for microstructural analysis, particularly in industrial factories where the cost of more advanced technologies may be prohibitive. They operate by directing a light source onto the surface of a material sample to be examined and using a powerful microscopic lens to view the microstructure. Magnification levels of up to 2000x can be achieved which is often sufficient to analyse individual alpha grains in a Ti-6Al-4V microstructure. However, the images produced offer a relatively low spatial resolution and depth of field when compared to more advanced microscopes [9]. The relatively low resolution is particularly noticeable when studying thin platelets, as these can give the appearance of overlapping and it becomes unclear where the boundaries between these laths are. The lower depth of field from these microscopes also result in all of the alpha phase being given almost exactly the same intensity value in a grayscale image. This makes boundaries between touching grains of the same phase difficult to identify. These challenges are illustrated in Figure 3.3.

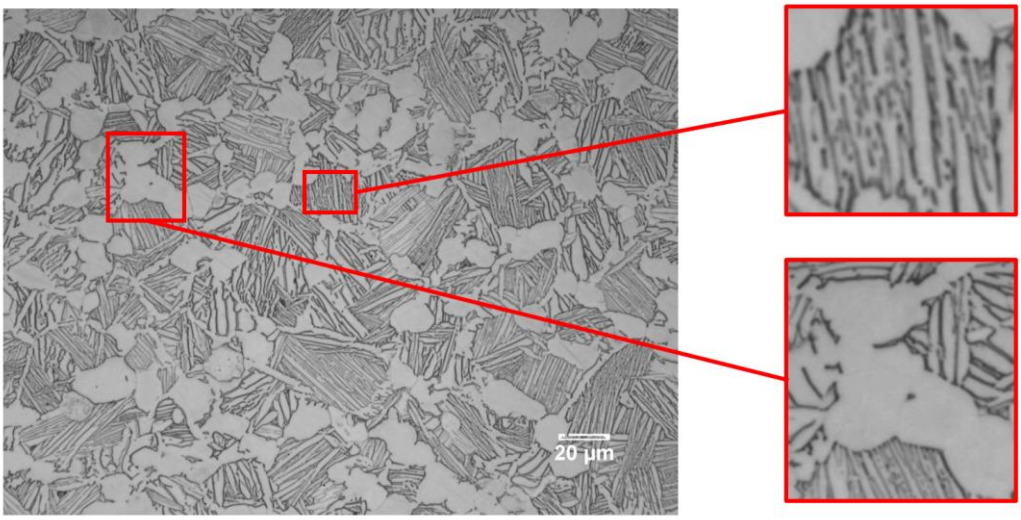

Figure 3.3: Example of limitations of Optical Microscopy, where boundaries between grain are not clearly delineated

3.2.2 Scanning Electron Microscopy

A Scanning Electron Microscope produces images of the microstructure of a material by scanning the surface of the material with a beam of electrons. These electrons are reflected (or back-scattered) onto a screen to produce an image [9]. This type of microscope is more expensive than optical technologies but is still relatively common, particularly in academic studies. It requires the subject of the scan to be electrically conductive but in return can achieve high magnification rates of up to 50,000x and has an exceptional depth of field when compared with optical images. Microstructural images of Ti-6Al-4V, taken using this technology, display clear difference in intensity difference between primary alpha and beta phase. Figure 3.4 shows an example of an image captured using an SEM.

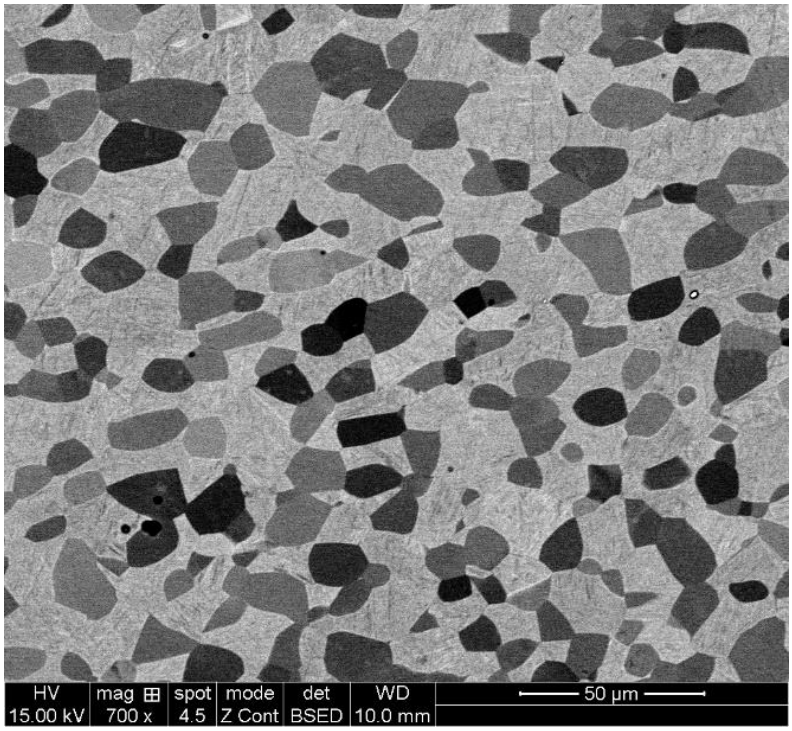

Figure 3.4: Example of SEM image of Ti6Al4V alloy

From Figure 3.4 it can also be observed that individual alpha grains are sometimes indicated by a different grey level than adjacent alpha grains, due to changes in their crystallographic orientation, making grain boundaries easier to delineate in these cases. This is clearly not the case for optical images, shown in Figure 3.3. However, although this additional information is useful for identifying grains, it can be difficult to extract individual grains due to noise. Consider a close up of two, touching grains shown in Figure 3.5 a). The grain on the left is slightly darker, meaning it will have lower intensity values in a greyscale image. However, the grains are both also visibly noisy which results in the histogram in Figure 3.5 b) showing only one mode (ignoring the white background pixels) rather than the two modes expected. The effect of noise is further illustrated by the image of a single grain shown in Figure 3.5 c) and its histogram shown in Figure 3.5 d). It can be observed that pixel values within a single grain appear to follow a Gaussian distribution over a relatively wide range. This noise can mask the location of the additional grain boundaries SEM technologies are expected to reveal. If the additional information provided by an SEM is to be useful, then the analysis techniques must take this into accounting when identifying grains.

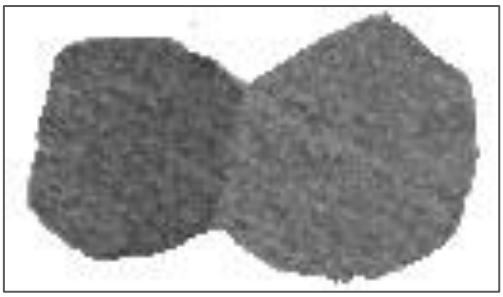

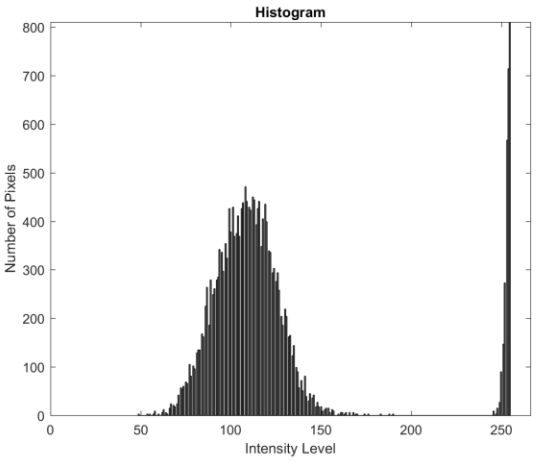

a) b)

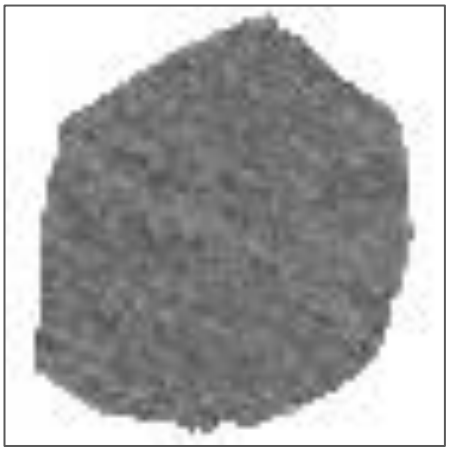

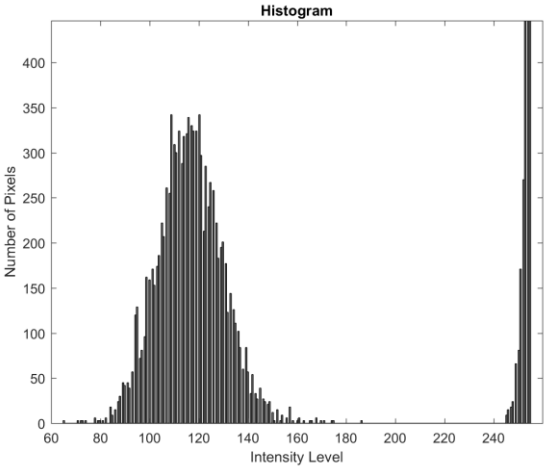

c) d)

Figure 3.5: Close up of 2 adjacent grains where a) shows an image of the grains produced by SEM, b) shows a histogram of intensity values, c) show an individual grain and d) shows a histogram of pixel values within that grain

3.3 Image processing techniques

The following section defines the relevant fundamental image processing background theory and describes techniques that are used to design the novel algorithms proposed in Chapters 5 and 6.

3.3.1 Representations of digital images

In this thesis digital images are represented as a 2D array where each entry in the array is a pixel. The row and column in the array correspond to the y and x position, respectively, of each pixel in the image. The value of each element in the array indicates the intensity of the corresponding pixel. The microstructural images investigated in this study are greyscale and do not contain any colour information, therefore, only greyscale and binary images need to be defined in this section.

In binary images each pixel is either "on" or "off" and is represented by, respectively, a "1" or "0" in the matrix. Visually this appears as either white (on/1) or black (off/0) pixels, as shown in Figure 3.6. The convention is adopted that white pixels represent the image foreground and black pixel represent the background. Formally, a binary image, *f*, can be described as a mapping of the definition domain of *f* into {0,1} where the definition domain is a subset, D_f of $\mathbb{Z}^n$, as in Equation (3.7).

$$f \ : \ D_f \subset \mathbb{Z}^n \rightarrow \{0,1\} \tag{3.7}$$

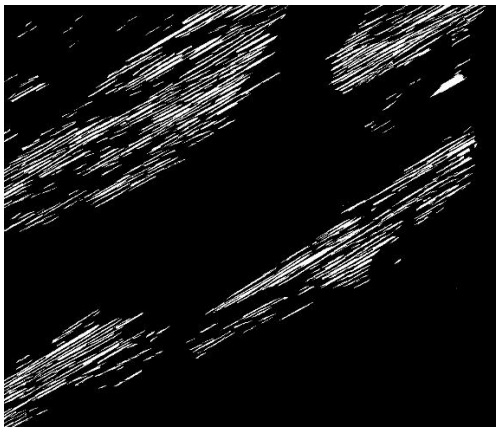

Figure 3.6: Example of a binary image

In greyscale images, pixel values can be within a wider range of non-negative integer values from 0, representing a black pixel, up to *n* representing, a white pixel, where *n* is the number of bits used to store the image. Formally, a greyscale image is defined as the mapping of a definition domain into a bounded set $\{0,1,2,\ldots,2^n\text{-}1\}$ where the

definition domain is a subset, D_f of $\mathbb{Z}^n$, as in Equation (3.8). An example of a greyscale image is given in Figure 3.7.

$$f \ : \ D_f \subset \mathbb{Z}^n \rightarrow \{0,1,2, \ldots . , 2^n - 1\} \quad \textbf{(3.8)}$$

Figure 3.7: Example of a greyscale image

3.3.2 Spatial filtering

Images from real world sources are typically imperfect and contain some form of noise. This noise masks the information that needs to be extracted by altering pixel values, usually, independently from image content. This is true for microstructural images, particularly when captured using sensitive microscopes such as an SEM. Spatial filters can be used to reduce this noise by modifying an image by a sub-image, commonly referred to as a filter, kernel, mask or window, to compute an output image where the value of each pixel is based on the value of its neighbouring pixels in the input image [2]. A common way to perform this is convolution, denoted by *. A kernel is built such that each pixel in that kernel has a value, which is referred to here as a coefficient to avoid confusion with regular image pixels. The convolution of an image

by a kernel is the sum of products of the kernel coefficients and the corresponding image pixels, written generally in Equation (3.9) for each pixel, *x*, where, g is the kernel and D_g is a definition domain where the kernel and image overlap.

$$[f * \mathrm{g}](x) = \sum_{b \in D_g} [f(x-b)\mathrm{g}(b)] \tag{3.9}$$

In this way the output for each pixel can be thought of as a weighted sum of neighbouring image pixels. When filtering an image, the same kernel is applied to each point in the original image to produce a filtered output image. It is, therefore, necessary for the kernel to have an origin, which will be aligned with a pixel in the image when calculating the output value at that pixel. Examples of a 3x3 kernel is given in Figure 3.8, with the equation for the response of this filter provided in Equation (3.10).

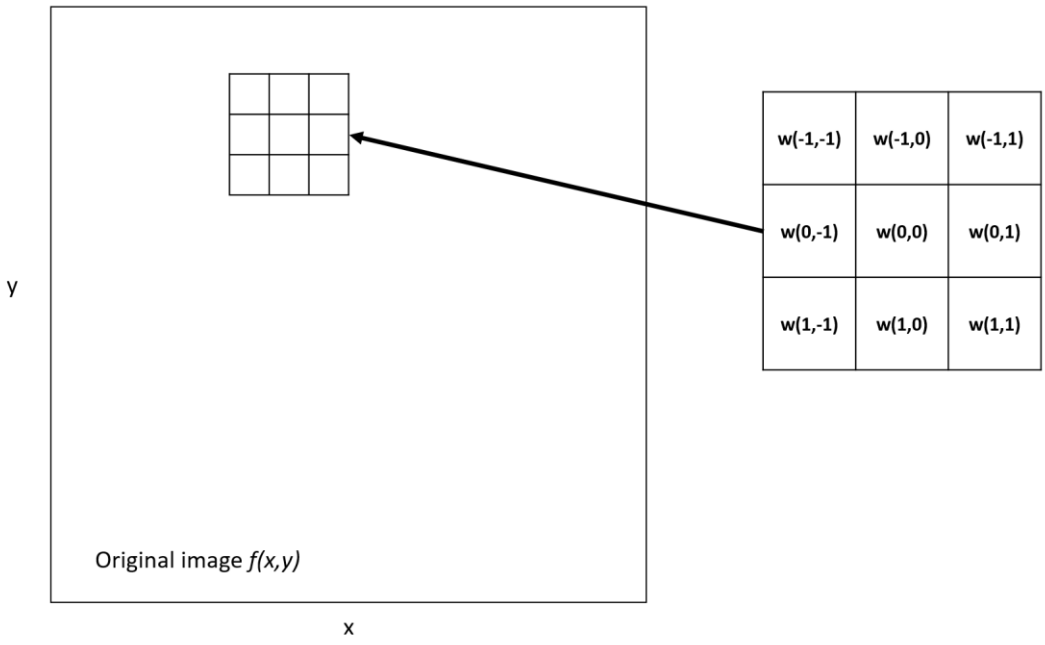

Figure 3.8: Example of kernel applied to filter an image

$$R(x,y) = g(-1,-1)f(x-1,y-1) + g(-1,0)f(x-1,y) + \cdots g(1,1)f(x+1,y+1) \tag{3.10}$$

Kernels are typically rectangular but can be of different sizes. In spatial filtering the size of the kernel is critical to the success of the filter. Therefore, it is necessary to define a more generic equation for the filter response. For an arbitrarily sized rectangular $j \times k$ kernel it is assumed $j=2a+1$ and $k=2b+1$ where a and b are non-negative integer values representing the width and height of the kernel. This means kernel length and height is an odd number and therefore symmetric across the x and y axis through some origin point. Non-symmetrical kernels are not defined in this thesis as these inherently cause distortion and are not useful for de-noising. A general equation for the response of a linear spatial filter is given in Equation (3.11).

$$R(x,y) = \sum_{s=-a}^{a} \sum_{t=-b}^{b} g(s,t) f(x+s, y+t) \quad \textbf{(3.11)}$$

The design of coefficients in the kernel can be used to remove different types of noise. An example of this type of filter is Gaussian filters, which use coefficients values in the kernel designed to remove noise following a Gaussian distribution from the image. This type of filtering is often referred to as Gaussian blur as it has the effect of blurring adjacent pixels together [2]. Non-linear filters such as median filtering do not use convolution, but still use the same approach of applying a kernel to each pixel in an image to compute a new filtered image. This particular filter uses kernels designed to find the median of the pixel values in the original image that overlap with the kernel to remove bright and dark spots, called salt and pepper noise [2]. The most appropriate filter to use will depend on the type of noise present in the image.

3.3.3 Thresholding

Thresholding is the technique of categorising pixels by comparing their value to pre-determined cut-off values. In image processing this is most commonly used to convert greyscale images to binary images by mapping all pixels with a value below a threshold, t, to "0" and all those greater than or equal to t to "1". This is shown in Equation (3.12) where f_{BW} is a binary image, f_G is a greyscale image and x and y are pixel co-ordinates.

$$f_{BW}(x,y) = \begin{cases} 1, & if\ f_G(x,y) \geq t \\ 0, & if\ f_G(x,y) < t \end{cases} \quad \textbf{(3.12)}$$

3.3.4 Distance transform

The distance transform is a simple but useful transform applied to binary data to measure the distance of each point in the image foreground from the background. The distance transform, *DT*, produces an image where each pixel in the foreground has a value equal to the shortest distance, *d*, between that pixel and the nearest non-foreground, i.e. zero valued, pixel, as in Equation (3.13). All non-foreground pixels will remain at "0".

$$[DT(f_{BW})](x) = \min\{d(x,y) | f_{BW}(y) = 0\} \quad (3.13)$$

This transform can provide direct measurements of objects in a binary image, although is useful most effective when used to provide input data to more advanced image processing tools.

3.3.5 Image gradient and edge detection

The gradient of an image describes variations in the intensity level of neighbouring pixels. Two measures of gradient are often considered; the gradient magnitude which measures the difference in intensity values in that neighbourhood, and the gradient orientation which measures the direction in which the greatest difference in intensity variation occurs. An example of the gradient magnitude for a 1D signal is shown in Figure 3.9.

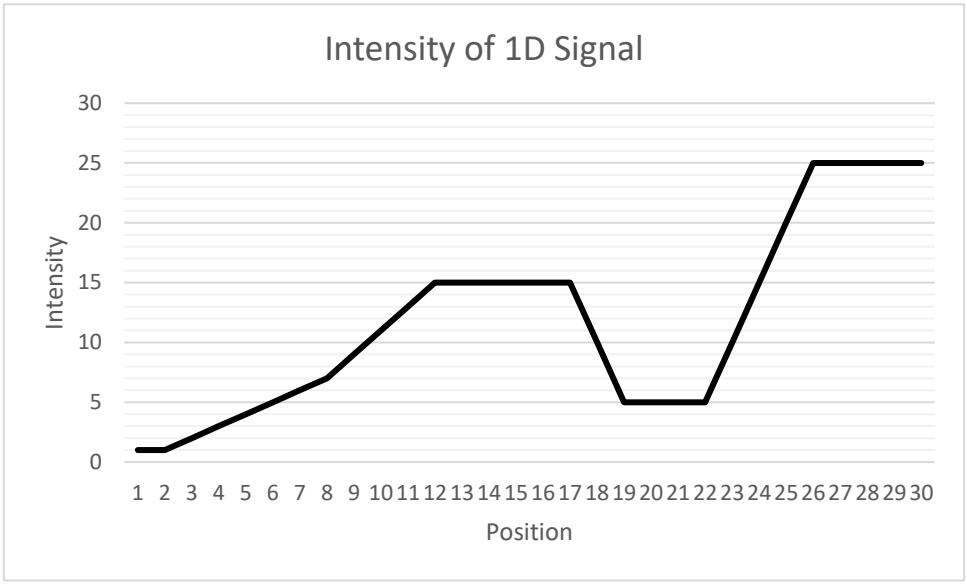

a)

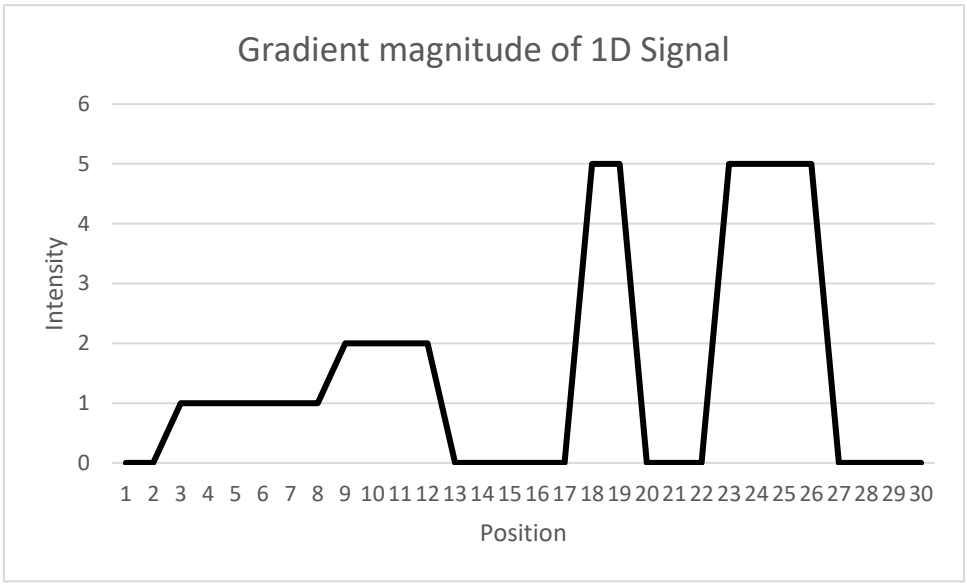

b)

Figure 3.9: Example of gradient magnitude where a) is pixel intensity in 1 dimension and b) is the corresponding gradient magnitude

The process of finding locations of large image gradient is known as edge detection and is useful for finding boundaries between objects of differing intensity. These techniques traditionally use either the first or second derivative to compute gradient [2]. For 2D image data this normally involves filtering the image with pre-defined kernels, specially designed to approximate the derivative of the image. Several

different kernels have been used for this task, with the Sobel [20], and Prewitt [21] operators being among the most commonly used in practise [2]. Each kernel type performs the same task of computing image gradient but achieve slightly different results, a comparison of which is provided in [20]. The Sobel and Prewitt operators are shown in Figure 3.10 Each edge detection method consists of two separate kernels for computing the gradient in two perpendicular directions. The equations necessary to compute the gradient magnitude and orientation at each pixel using these methods is given in Equation (3.14) and Equation (3.15).

-1	0	1
-2	0	+2
-1	0	1

Mask Gx

+1	+2	1
0	0	1
-1	-2	-1

Mask Gy

a)

-1	0	1
-1	0	1
-1	0	1

Mask Gx

-1	-1	-1
0	0	0
1	1	1

Mask Gy

b)

Figure 3.10: Edge detections kernels where a) is the Sobel kernels and b) is the Prewitt kernels

$$G = \sqrt{({G_x}^2 + {G_y}^2)} \quad \textbf{(3.14)}$$

$$\theta = \text{atan}(\frac{G_y}{G_x}) \quad \textbf{(3.15)}$$

Edge detection can be thought of as a thresholding of the gradient magnitude of an image to find only the most significant edges in image data. The threshold value used will. Therefore, determine which potential edges in an image are detected. An example of gradient magnitude, computed using Sobel kernels, and edge detected images with different thresholds applied is given in Figure 3.11.

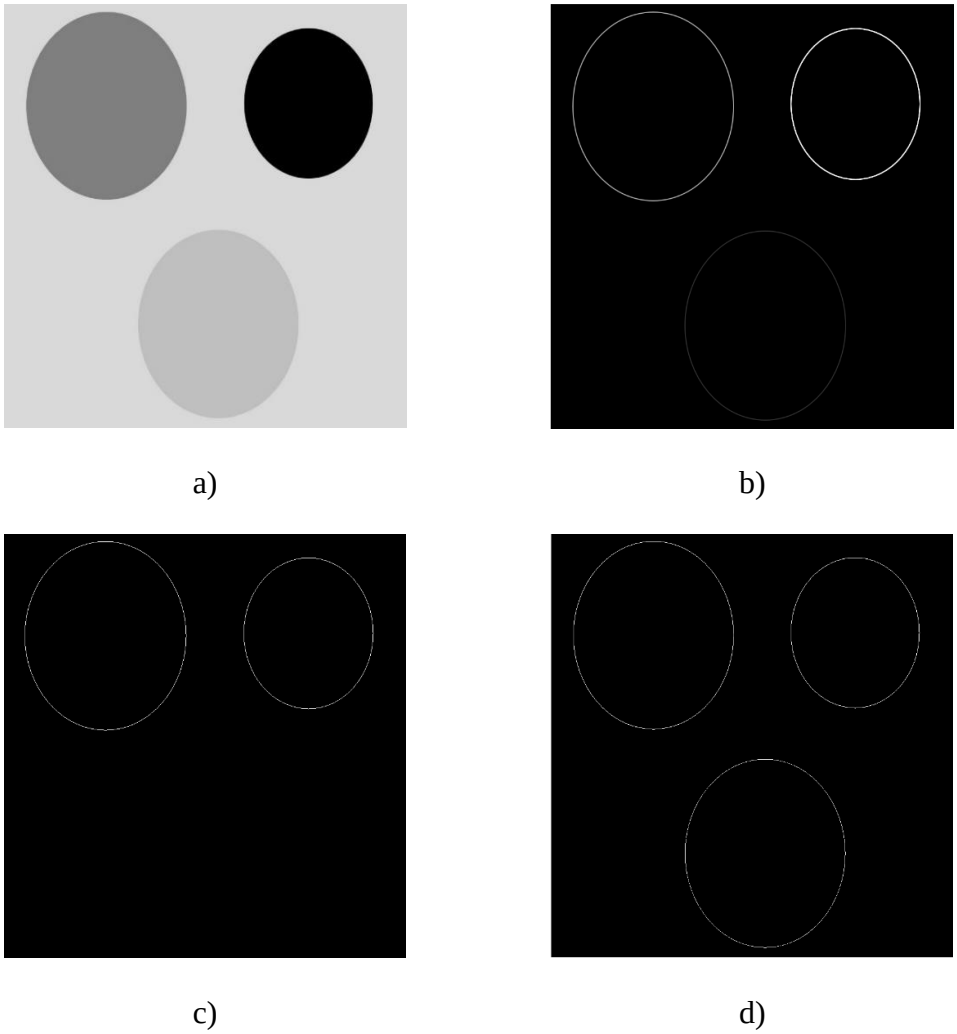

a) b)

c) d)

Figure 3.11: Example of edge detection where a) original image, b) gradient image, c) edge detection with threshold=1 and d) edge detection where threshold=2

3.3.6 Mathematical Morphology

Mathematical morphology is a theory and technique, first introduced by Matheron [22] and Serra [23]. It can be used to analyse spatial structures in images using techniques based on set theory, integral geometry and lattice algebra [24]. A myriad of distinct image analysis techniques exist that are based on Mathematical Morphology. Many of these are built from two fundamental morphological operators called erosion and dilation. These operators function by probing each location in a given image with a pre-defined sub-image known as a Structuring Element (SE). The response from these operators is an image where pixel values are computed as a function of how the SE interacts with features of the investigated image. This section provides the definition of a SE, the two fundamental morphological operations specified, and two further operators, called the opening and closing, which are useful to the work presented in this thesis.

3.3.6.1 Structuring Elements

A SE is a set that is used to probe the image under investigation. A SE can have the same dimensions as an input image so can be either 2D, known as a flat SE, or 3D, known as volumic, non-flat or greyscale SE. The response of a morphological operator using a flat SE depends only on the shape and size of image features while greyscale SE are more sensitive to intensity variations. The aim of this research is to investigate the shape and size of grains so only flat SE are considered in the remainder of the thesis.

A morphological operator will probe the image at every location a SE with an origin at that point. A SE requires a single point be designated as the origin, which is used for positioning the SE at each point in the studied image. The output of the operator will then be stored at the same co-ordinate in the output image. A SE does not need to be symmetrical and the origin can theoretically be any point either inside or outside the surface of the SE. However, for many practical applications a symmetrical SE with an origin at its centre is most useful. Symmetrical SEs are less likely to distort the image and any information extracted using them would relate directly the shape and size of image features.

The shape and size of SEs relative to image features have a significant impact on the output of morphological operators. This relationship is useful for extracting information about the image under study. A good example of this is granulometric techniques [25] where SEs of increasing size are used to obtain size information from an image, discussed later in Chapter 4.

3.3.6.2 Erosion

The erosion, ε, is a fundamental morphological operator named as it often has the effect of shrinking binary sets relative to the SE. If larger SEs were used objects would shrink more or even disappear completely. More precisely, the erosion of a binary image, f_{BW}, by a SE, B, is the locus of points, x, for which B, with origin at x, fits completely within f_{BW} where B is translated through all points in f_{BW}. This is written in Equation (3.16) where B_x is a SE with origin at point x. It can be thought of as the answer to the question, "Does the SE fit the set?" [24].

$$\varepsilon_B(f_{BW}) = \{x | B_x \subseteq f_{BW}\} \quad \textbf{(3.16)}$$

The erosion of a binary set is illustrated in Figure 3.12 where the SE is a 3x3 square.

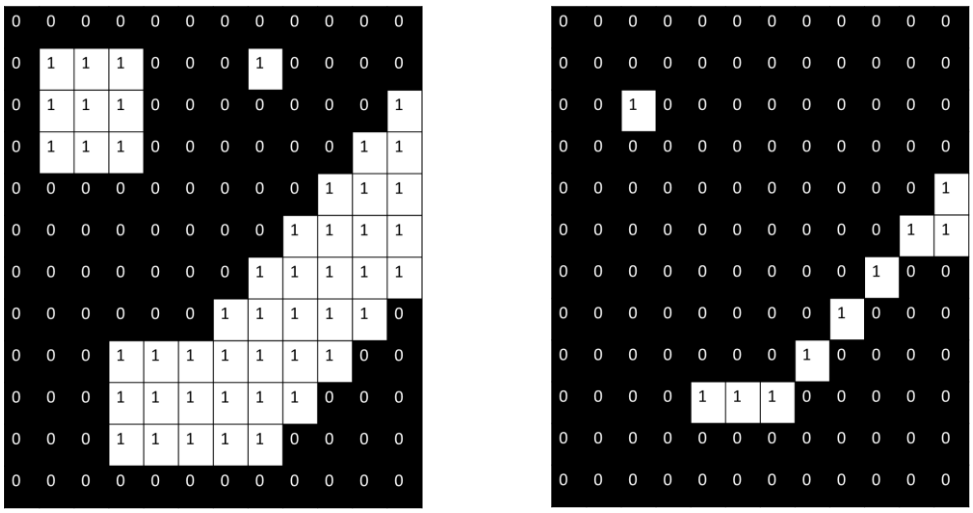

a) b)

Figure 3.12: Example of the erosion of a binary image with pixel values shown where a) original image and b) erosion by 3x3 square SE

The effect of erosion can be observed here as objects in the image are made smaller as when a 3x3 SE overlaps the image with its origin at the outermost pixels of an object,

the SE does not entirely fit the image while SEs with origin at the centre of objects do. The object that was smaller than the SE was removed completely by this operation.

For greyscale images there is no clear binary decision on whether or not the SE fits the image. In this case erosion is instead better defined not as a set of points that fit the SE but the minimum value of all pixels that coincide with that SE at each point, as written in Equation (3.17).

$$[\varepsilon_B(f)](x) = \min_{b \in B}\{f(x+b)\} \tag{3.17}$$

In greyscale images the erosion generally has the effect of reducing bright regions in the image relative to the SE. The effect of this is shown in Figure 3.13 where an 8-bit greyscale image is eroded by a 3x3 square SE. It can be observed that the objects are shrunk or removed as before, however, this time pixels close to object boundaries take on the value of the surrounding region rather than "0".

100	100	100	100	100	100	100	100	100	100	100	100
100	255	255	255	100	100	100	255	100	100	100	100
100	255	255	255	100	100	100	100	100	100	100	255
100	255	255	255	100	100	100	100	100	100	255	255
100	100	100	100	100	100	100	100	100	255	255	255
100	100	100	100	100	100	100	100	255	255	255	255
100	100	100	100	100	100	100	255	255	255	255	255
100	100	100	100	100	100	255	255	255	255	255	100
100	100	100	255	255	255	255	255	255	255	100	100
100	100	100	255	255	255	255	255	255	100	100	100
100	100	100	255	255	255	255	255	100	100	100	100
100	100	100	100	100	100	100	100	100	100	100	100

a)

100	100	100	100	100	100	100	100	100	100	100	100
100	100	100	100	100	100	100	100	100	100	100	100
100	100	255	100	100	100	100	100	100	100	100	100
100	100	100	100	100	100	100	100	100	100	100	100
100	100	100	100	100	100	100	100	100	100	100	255
100	100	100	100	100	100	100	100	100	100	255	255
100	100	100	100	100	100	100	100	100	255	100	100
100	100	100	100	100	100	100	100	255	100	100	100
100	100	100	100	100	100	100	255	100	100	100	100
100	100	100	100	255	255	255	100	100	100	100	100
100	100	100	100	100	100	100	100	100	100	100	100
100	100	100	100	100	100	100	100	100	100	100	100

b)

Figure 3.13: Example of the erosion of a greyscale image with pixel values shown where a) original image and b) erosion by 3x3 square SE

3.3.6.3 Dilation

The dilation, δ, is a fundamental morphological operator named as it often has the effect of increasing the area of a binary set relative to a SE. It is the dual operator of

the erosion defined in Section 3.3.6.2. Formally, the dilation of binary image, f_{BW}, by a SE, *B*, is the locus of points, *x*, where *B*, with origin at *x*, coincides with any point in f_{BW} where *B* is translated through all points in f_{BW}. It can be thought of as the answer to the question, "Does the SE hit the set?" [24]. This is written in Equation (3.18) where $\hat{B}_x$ is a SE with origin at point *x* which is a reflection of *B* through its origin. This reflection has no effect on symmetrical SEs. However, for non-symmetrical SEs the reflection is necessary for erosion and dilation to be combined in meaningful ways, such the opening and closing operators.

$$\delta_B(f_{BW}) = \{x | \hat{B}_x \cap f_{BW} \neq \emptyset\} \quad \textbf{(3.18)}$$

The dilation of a binary set is illustrated in Figure 3.14 where the SE is a 3x3 square. This demonstrates that dilation generally has the effect of increasing the area of foreground objects. This occurs as all pixels originally in the foreground return a "1" as do pixels where the SE, with origin at that, would overlap with any point in the original foreground. If a larger SE was used the background between objects would be made larger still or, if the SE was large enough, the objects would merge and the background would disappear completely.

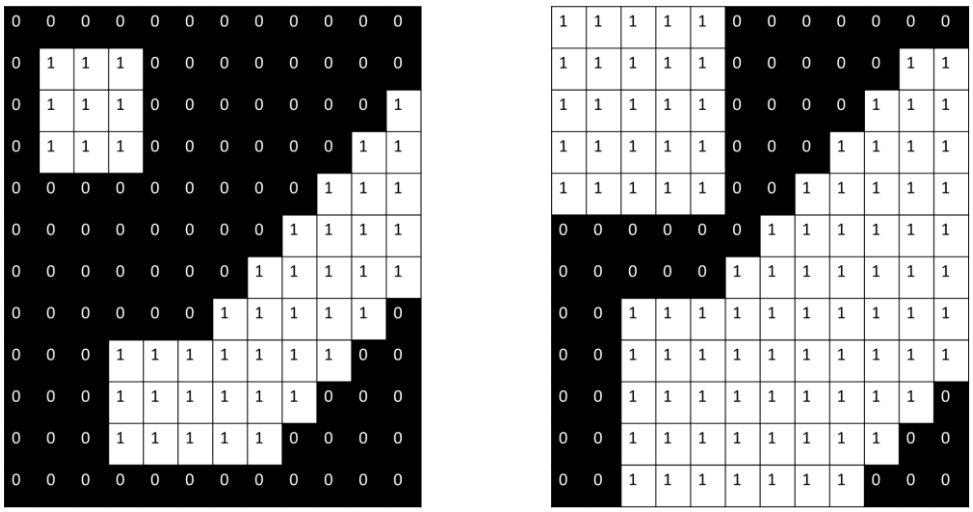

a) b)

Figure 3.14: Example of the dilation of a binary image with pixel values shown where a) original image and b) dilation by 3x3 square SE

For greyscale images there is no clear binary decision on whether or not an SE coincides with the image. For greyscale images dilation is therefore best defined, not as a set of points where the SE hits the image but, as the maximum value of all pixels that coincide with the SE at each point, as written in Equation (3.19).

$$[\delta_B(f)](x) = \max_{b \in B}\{f(x-b)\} \quad \textbf{(3.19)}$$

In greyscale images the dilation generally has the effect of brightening and increasing the area of regions in the image that are brighter than their surrounding area relative to the size and shape of the SE. The effect of this is shown in Figure 3.15 where an 8-bit greyscale image is dilated by a 3x3 square SE. It can be observed that the area of the brighter objects increases, as was the case in binary images, however, the pixels close to object boundaries have the value of the brightest neighbouring pixel rather than "1".

100	100	100	100	100	100	100	100	100	100	100	100
100	255	255	255	100	100	100	100	100	100	100	100
100	255	255	255	100	100	100	100	100	100	100	255
100	255	255	255	100	100	100	100	100	100	255	255
100	100	100	100	100	100	100	100	100	255	255	255
100	100	100	100	100	100	100	100	255	255	255	255
100	100	100	100	100	100	100	255	255	255	255	255
100	100	100	100	100	100	255	255	255	255	255	100
100	100	100	255	255	255	255	255	255	255	100	100
100	100	100	255	255	255	255	255	255	100	100	100
100	100	100	255	255	255	255	255	100	100	100	100
100	100	100	100	100	100	100	100	100	100	100	100

a)

180	180	180	180	180	100	100	100	100	100	100	100
180	180	180	180	180	100	100	100	100	100	180	180
180	180	180	180	180	100	100	100	100	180	180	180
180	180	180	180	180	100	100	100	180	180	180	180
180	180	180	180	180	100	100	180	180	180	180	180
100	100	100	100	100	100	180	180	180	180	180	180
100	100	100	100	100	180	180	180	180	180	180	180
100	100	180	180	180	180	180	180	180	180	180	180
100	100	180	180	180	180	180	180	180	180	180	180
100	100	180	180	180	180	180	180	180	180	180	100
100	100	180	180	180	180	180	180	180	180	100	100
100	100	180	180	180	180	180	180	180	100	100	100

b)

Figure 3.15: Example of the erosion of a greyscale image with pixel values shown where a) original image and b) erosion by 3x3 square SE

3.3.6.4 Opening

The opening, γ, is a combination of the erosion and dilation operators named as it has the effect of removing binary sets that cannot fully contain the SE. An opening can be

implemented by first eroding an image and then dilating the result, as in Equation (3.20).

$$\gamma_B(f) = \delta_B\big(\varepsilon_B(f)\big) \tag{3.20}$$

When performing an opening, the dilation operator attempts to reconstruct data lost during the initial erosion. However, as the dilation is not an inverse operator of the erosion, this is often not done perfectly and some data may still be lost. Critically, objects that are completely removed by the initial erosion cannot then be restored. An example of the erosion of a binary image using a 3x3 square SE is provided in Figure 3.16. The two objects smaller than the SE are completely removed from the image while the other object remains. As the shape of the SE matches the shape of the object the remaining object is perfectly reconstructed. If the shape of the SE does not match the shape of the image object some distortion might occur in the remaining objects.

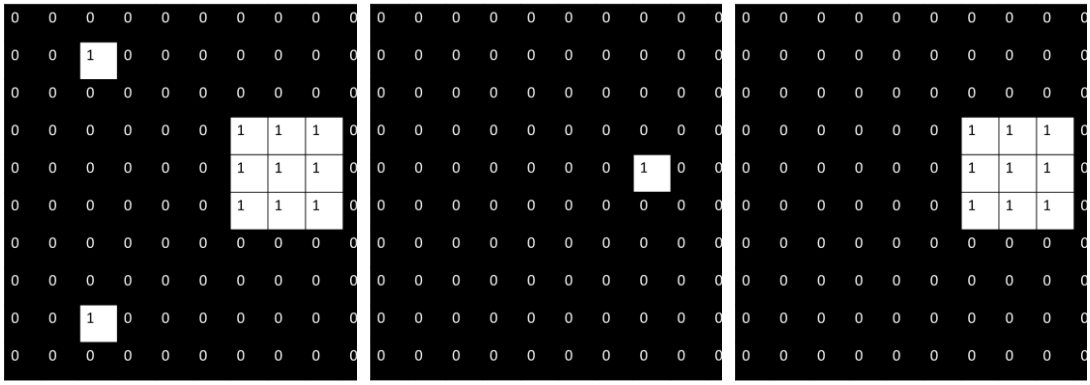

a) b) c)

Figure 3.16: Example of opening a binary image by a 3x3 square SE where a) original image, b) image after erosion and c) image after opening i.e. the dilation of b)

3.3.6.5 Closing

The closing, φ, is the combination of the erosion and dilation operators, named as it often has the effect of filling gaps between objects when the gap is small enough that a SE can be placed such that it coincides with multiple objects. A closing can be performed by first dilating the image and then eroding the result, as in Equation (3.21).

$$\varphi_B(f) = \varepsilon_B\big(\delta_B(f)\big) \tag{3.21}$$

When performing a closing the erosion operator attempts to restore the image to its prior state before the initial dilation, reconstructing the background data in the image. However, as this erosion is not an inverse operator of the dilation, this is not always done perfectly and some data may be lost. Background regions that are completely removed by the initial dilation, i.e. any point where previously separate foreground objects are joined, are often not restored to the previous state by the subsequent erosion. An example of the opening of an image by a 3x3 square SE is provided in Figure 3.17. It can be observed that gaps within objects or between adjacent objects are removed when these gaps are smaller than the SEs. Meanwhile objects that are further apart than the size of the SE remain separate. If the shape of the SE is different than the shape of background regions, then some distortion can occur when performing the closing.

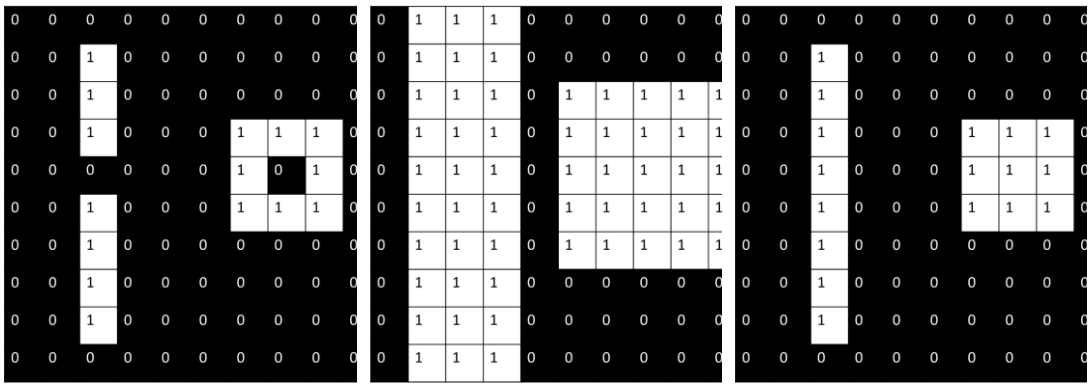

a) b) c)

Figure 3.17: Example of closing on a binary image where a) original image, b) dilated image and c) is the closed image i.e. the erosion of b)

3.3.6.6 Top-Hat Transform

The Top-Hat Transform is a type of morphological filter than can be used for various tasks, including de-noising and resolving lighting inconsistencies. Two complementary operators exist, the White Top-Hat (WTH) and the Black Top-Hat. The WTH is the subtraction of the opening of an image from the original image, as in Equation (3.22). The BTH is the subtraction of the original image by the closing of that image, as in Equation (3.23).

$$WTH(f) = f - \gamma(f) \quad \textbf{(3.22)}$$

$$BTH(f) = \varphi(f) - f \quad \textbf{(3.23)}$$

3.3.6.7 Hit-or-Miss Transform

The Hit-or-Miss Transform (HMT) can identify objects that fit specific size and shape requirements by extracting the pixels from an image matching a given neighbourhood configuration [26]. This is achieved by using two SEs, one which must fit within the foreground, B_{FG}, of the image and another which must miss it, B_{BG}. A formal definition of the HMT of f by B is written in Equation (3.24).

$$HMT_B(f) = \{x|(B_{FG})_x \subseteq f, (B_{BG})_x \subseteq f^c\} \quad \textbf{(3.24)}$$

This can also be written in terms of an intersection of two erosions, as in Equation (3.25).

$$HMT_B(f) = \varepsilon_{B_{FG}}(f) \cap \varepsilon_{B_{BG}}(f^c) \quad \textbf{(3.25)}$$

A simple illustrative example of the HMT to extract circular objects of a specific size is shown in Figure 3.18.

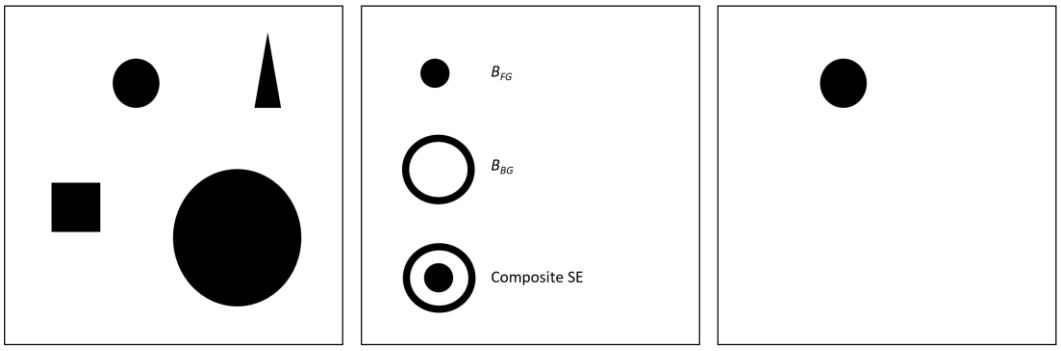

a) b) c)

Figure 3.18: Illustration of HMT where a) original image, b) is the set of SE used and c) is the transformed image with objects extracted

3.3.7 Geodesy, Geodesic Distance and Time

Generally, geodesy is the science of accurately measuring properties of the earth such as the shape and area of its surface. In image processing the concept of geodesy is used to study pixels in an image constrained to remain within some subset of the image

plane [24]. In particular, the idea of geodesic distance is important to image segmentation techniques such as the Watershed Transform, used in Chapter 5 to segment globular alpha grains. Geodesy is defined here primarily in order to facilitate the Watershed definition given later in this chapter.

The geodesic distance is the shortest path between two points on a surface where the path is constrained to exclusively follow that surface. This differs from the Euclidean distance which would be the shortest path between the two points in Euclidean space, as illustrated in Figure 3.19.

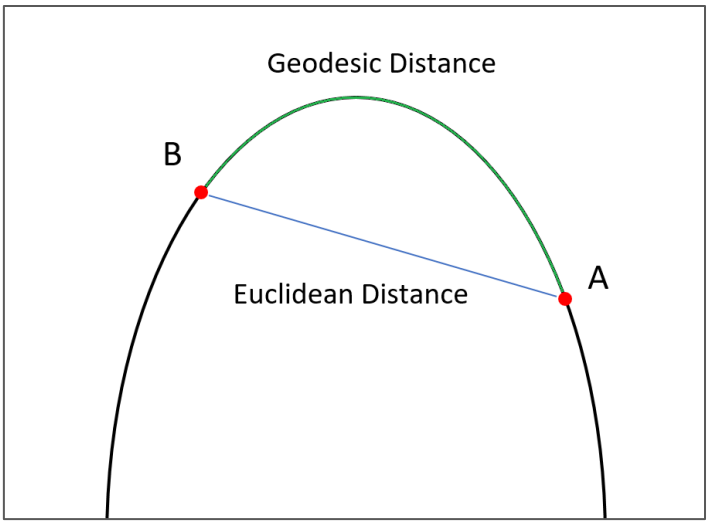

Figure 3.19: Illustration of geodesic and Euclidean distances between two points on a surface

The geodesic distance, $d_a(x,y)$, between point x and y of surface a is the minimum length, L, of all paths, $P=(p_1, p_2,\ldots,p_l)$ that both join x and y and are included in a, as in Equation (3.26).

$$d_a(x,y) = \min\{L(P)|p_1 = x, p_l = y, and\ P \subseteq a\} \quad \textbf{(3.26)}$$

It is possible for multiple paths between two points to have the same minimal length. These paths are called geodesics and the surface, a, is called the geodesic mask. For two points on different geodesic masks, there is no path between them so the geodesic distance in considered infinite. It is often useful to consider the geodesic distance of a point from a set, rather than from another precise point. For such a set, often called a marker set, the geodesic distance, $d_a(x,Y)$, between a point x and marker Y , where both

are subsets of a, is the smallest geodesic distance, $d_a(x,y)$, between point x and any pixel y in Y, as shown in Equation (3.27).

$$d_a(x,Y) = \bigwedge_{y \in Y} d_a(x,y) \tag{3.27}$$

The geodesic distance for each point in a mask, a, between that point and a set, Y, is given by the geodesic distance function, where $d_a(Y)$ is the output of this function, as in Equation (3.28).

$$[d_a(Y)](x) = d_a(x,Y) \tag{3.28}$$

The geodesic distances between a given point and marker sets within a geodesic mask are illustrated in Figure 3.20. These distances are useful later in the definitions of marker-based segmentation techniques as they allow the distance between points and a marker to be calculated taking account of the shape of the mask. More detail on this can be found in Section 3.3.9.

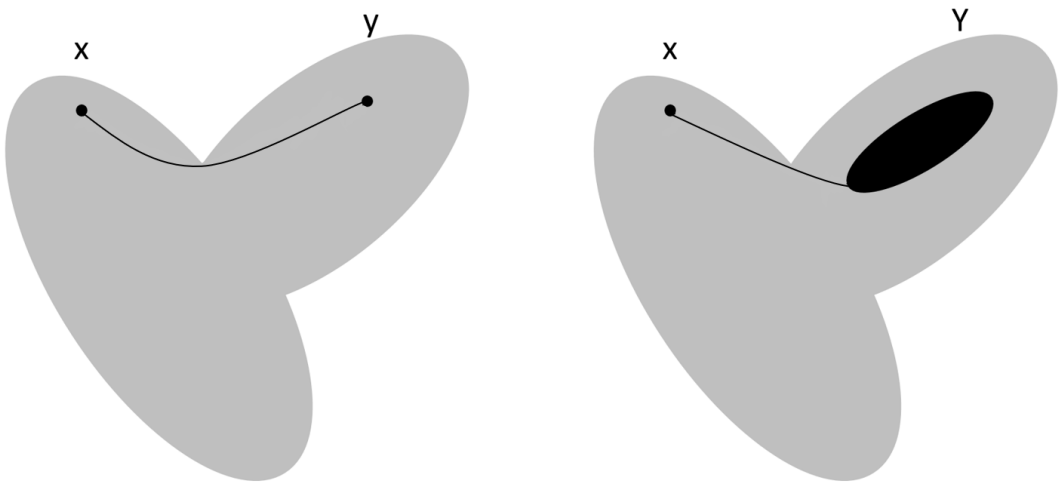

a) b)

Figure 3.20: Illustration of geodesic distances where a) shows the geodesic distance between point x and y and b) shows the geodesic distance between point x and set Y

Geodesic time functions are also defined in this section. As static images do not actually have a time component in their data, the concept of "time" comes from

considering the value of pixels in a greyscale image as a speed for the image. This would imply faster speeds and lower transversal times for low grey levels and vice versa. From this convention the time, $\tau_f(P)$, to cover path, *P*, is the integral of *f* along *p*, as in Equation (3.29).

$$\tau_f(P) = \int_P f(s)ds \tag{3.29}$$

For digital image processing a discrete version of this is required. In this case the time, $\tau_f(P)$, to cover path *P* of length *l* is the sum of the mean values of adjacent pairs of values in *f* along path *p*, as in Equation (3.30).

$$\tau_f(P) = \sum_{i=1}^{l} \frac{f(p_{i-1}) + f(p_i)}{2} = \frac{f(p_0)}{2} + \frac{f(p_l)}{2} + \sum_{i=1}^{l-1} f(p_i) \tag{3.30}$$

The geodesic time, $\tau_a(x,y)$, between two points *x* and *y* on geodesic mask *a* is a measure of the smallest amount of time required to cover any possible path, *P*, along *a* linking *x* and *y*, as in Equation (3.31).

$$\tau_a(x,y) = \min\{\tau_a P | \, P \; links \; x \; to \; y\} \tag{3.31}$$

The geodesic time, $\tau_a(x,Y)$, between a point *x* and a set *Y* on mask *a* is the smallest amount of time to link point *x* with any point in *Y*, as in Equation (3.32).

$$\tau_a(x,Y) = \min_{q \in Y} \tau_a(x,y) \tag{3.32}$$

If *x* belongs to *Y*, then the geodesic time is zero. The key differences between geodesic time and distance is that as it assumes a relationship between the height of a surface and speed, therefore, geodesic time depends on the directionality of a path rather than just its length. This distinction between the time to reach equidistant points is useful in the definition of the Watershed Transform given later in this chapter.

3.3.8 Segmentation by geodesic transforms

The segmentation of a 2D dimensional set can be performed using the geodesic functions defined in this chapter. Although not directly applied to the images in this study the following functions form the basis of the Watershed Transform which plays a key role in the techniques proposed in this thesis. A geodesic mask, *a*, can be segmented by identifying the Influence Zones (IZ) of marker set, *Y*. An Influence

Zone is defined as a set of points at a finite geodesic distance from a marker which are closer to that marker than any other [5], as in Equation (3.33).

$$IZ_a(Y_i) = \{x \in a | \forall j \neq i, d_a(x, Y_i) < d_a(x, Y_j)\} \quad \textbf{(3.33)}$$

This can be calculated to form a complete segmentation of a by the union of the regions of influence for all markers in Y, as in Equation (3.34).

$$IZ_a(Y) = \bigcup_i d_a(Y_i) \quad \textbf{(3.34)}$$

The boundaries between the zones of influence are known as the geodesic skeleton by zones of influence (SKIZ). The skeleton by zone of influence of Y in a, $SKIZ_a(Y)$, is given in Equation (3.35) where / denotes the set difference.

$$SKIZ_a(Y) = X / IZ_a(Y) \quad \textbf{(3.35)}$$

An example of the IZ and SKIZ for a flat surface with two markers is shown in Figure 3.21.

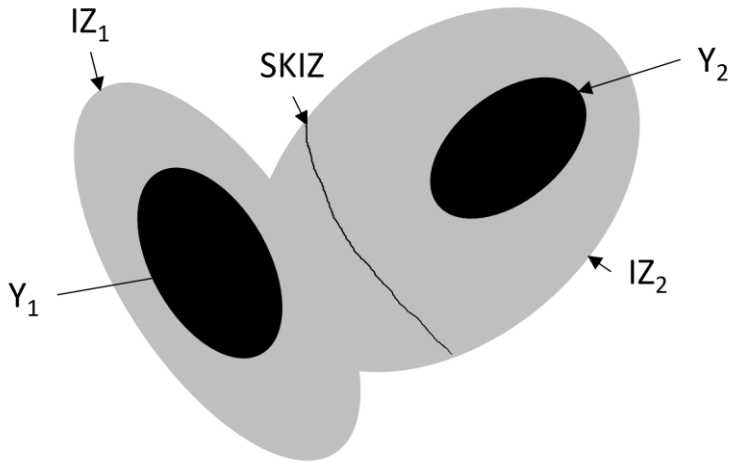

Figure 3.21: Examples of zones of influence of a surface based on 2 markers

3.3.9 The Watershed Transform

The Watershed Transform is a useful image segmentation technique first proposed by Beucher and Lantuéjoul [27]. The concept is based on what happens when rain falls

onto a surface with a varied topography. As the rain falls each droplet of water will run down the hills and valleys of the surface until they reach a local minimum in the height of the surface. The water will then gather to form a basin which will continue to grow until it eventually overlaps with basins from other valleys. The moment before this overlap occurs a ridgeline in the surface appears between the them which is referred to as the watershed. Beucher and Lantuéjoul proposed that this concept could be applied to segment images by using a topographic representation of the image, where the relative differences in the height of the surface corresponds to the probability of adjacent pixels belonging to the same object in an image. The surface would be flooded with floods from different catchment basins are prevented from merging so that ridgelines, often referred to as watershed lines, remain even when the entire surface is flooded. These lines separate each region in the surface. A common implementation is to use the gradient image, defined in Section 3.3.4, as the input to the Watershed Transform. Provided that adjacent pixels of similar intensity are more likely to belong to the same object this provides a suitable topographic representation of the image for segmentation using the Watershed algorithm. In the gradient image, high values are returned at points where a large intensity variation exists, most likely to be object boundaries, and flat, shallow minima are returned in locations where pixel intensity does not change significantly, most likely to be within a single object. An illustration of the Watershed Transform applied to the gradient image is shown in Figure 3.22.

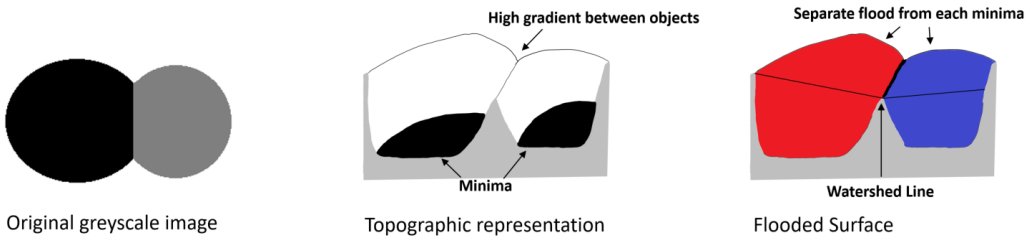

Figure 3.22: Example of a topographic surface and the catchment basins and watershed lines that are formed

Although helpful for understanding the origin of the concept, expressing the watersheds by falling drops of water is not useful in practical applications and cannot

be used to formally define the Watershed Transform. This is because it does not describe how water should flow when there are multiple possible directions of flow or if there is a plateau in the topographic surface. Instead formal definitions of the Watershed Transform fit better with the analogy that the topographic surface has holes punched through each local minimum before the entire surface is slowly submerged in water. Floods from different sources are still prevented from merging to preserve the watershed lines but with this description floods now have a clear origin and direction of flow which makes it possible to define how irregularities in the topographic surface should be handled. The Watershed Transform can be equivalently defined in terms of a simulation of the flooding of a surface or in terms of geodesic transforms [5]. In this section the Watershed definition based on geodesic transforms is used as it is more consistent with other definitions used in this thesis.

To define the Watershed in terms of the geodesic transforms, described in Sections 3.3.6.6 and 3.3.8, the topographic surface representing the image is considered as a geodesic mask, *a*, and the minima from which floods begin as marker sets, *Y*. Catchment basins (*CB*) are considered equivalent to the zones of influence of each marker set. The watershed lines (*W*) are then equivalent to the skeleton by zones of influence (SKIZ). In order for this to correctly mimic the flooding from local minima and perform a correct Watershed Transform a few modifications to the topographic function, representing the image to be segmented, are necessary. First the regional minima, R_{min}, of the topographic function, *f*, representing the input image, should be set to the minimum value possible in this function h_{min}, as in Equation (3.36).

$$f'(x) = \begin{cases} h_{min}, if\ x \in R_{min}(f) \\ f(x), otherwise \end{cases} \quad \textbf{(3.36)}$$

As the standard Watershed algorithm assumes the surface is flooded from all regional minima this ensures all minima are at the same depth, therefore, preventing floods from shallower minima from spilling over into adjacent catchment basins. Next the geodesic time function is applied to the internal gradient of the topographic function, $\tau_{\rho\text{-}(f')}$, with geodesic time measured with respect to the local minima, as in Equation (3.37).

$$f' = \tau_{\rho-(f')}[R_{min}(f)] \quad \textbf{(3.37)}$$

This assigns to each point on the surface a time value based on how long it should take to flood this from its nearest minima. This ensures that there is a clear order for floods to proceed even when there are plateaus in the topographic surface. The use of the geodesic time rather than distance means that lower points on the surface are prioritised, mimicking the flooding ideology on which the Watershed Transform is based. The catchment basins and watershed lines can now be found by computing the influence zones and SKIZ of *f'* with respect to the local minima R_{min}, as described in Equation (3.38) and Equation (3.39).

$$CB_a(Y) = IZ_{\rho-(f')}(R_{min}) \quad \textbf{(3.38)}$$

$$W_a(Y) = SKIZ_{\rho-(f')}(R_{min}) \quad \textbf{(3.39)}$$

The advantage of the Watershed Transform is its effectiveness at segmenting large clusters of objects in an image. As all catchment basins are growing simultaneously depending on the relative height of the topographic surface, this means that knowledge about one object can inform the segmentation of another. For example, if the boundary between objects is unclear then segmentation techniques that attempt to identify each object separately would likely fail as it could miss this boundary entirely. However, provided two local minima exist, the Watershed Transform will always segment the image into 2 regions, placing the boundary at the highest point in the topographic surface between these minima. Therefore, provided local minima in the topographic surface exist for each object, unclear boundaries between them will at worst be misplaced, rather than not being identified. For clustered objects this would often lead to lower segmentation errors than other methods. For example, consider the segmentation of two overlapping objects in a binary image using the Watershed Transform with distance transform as the input function is shown in Figure 3.23. Pixel values at the grain value show the same homogeneity as those within each object, however, as a minimum is found for each object the two objects are still segmented, despite boundary pixels themselves not being directly identifiable.

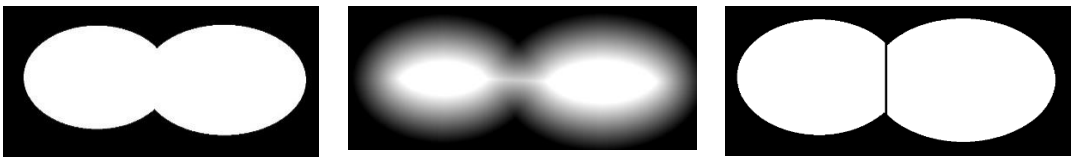

a) b) c)

Figure 3.23 Illustration of segmentation using the Watershed Transform where a) is the original image, b) is the topographic function and c) is the segmented image

3.3.10 Marker-based Watershed Transform

In the standard definition, and examples given previously, the Watershed Transform floods the topographic surface from all local minima to produce a segmentation. However, this often produces segmentation errors particularly in noisy data as a significant number of small local minima can exist in the input image which do not relate to a region of interest in the image. Each of these minima form a catchment basin representing an object in the image, too many local minima would lead to over-segmentation of the image. To resolve this Meyer [28] proposed the use of markers to designate locations from which floods should begin independently from the topographic representation. In the ideal case one marker should be placed within each object in the image. This would ensure the image was divided into the correct number and location of segments. Only errors in boundary location would then be possible and positioning a boundary between multiple markers is the strength of the Watershed Transform. This is demonstrated in Figure 3.24 which shows the separation of two touching grains using the Watershed Transform.

It can be observed that, despite several local minima existing in the image, provided two markers exist as inputs there will also exist two regions in the segmentation. It is also visible that the boundary between these regions occurs at the peak of the topographic function *f*.

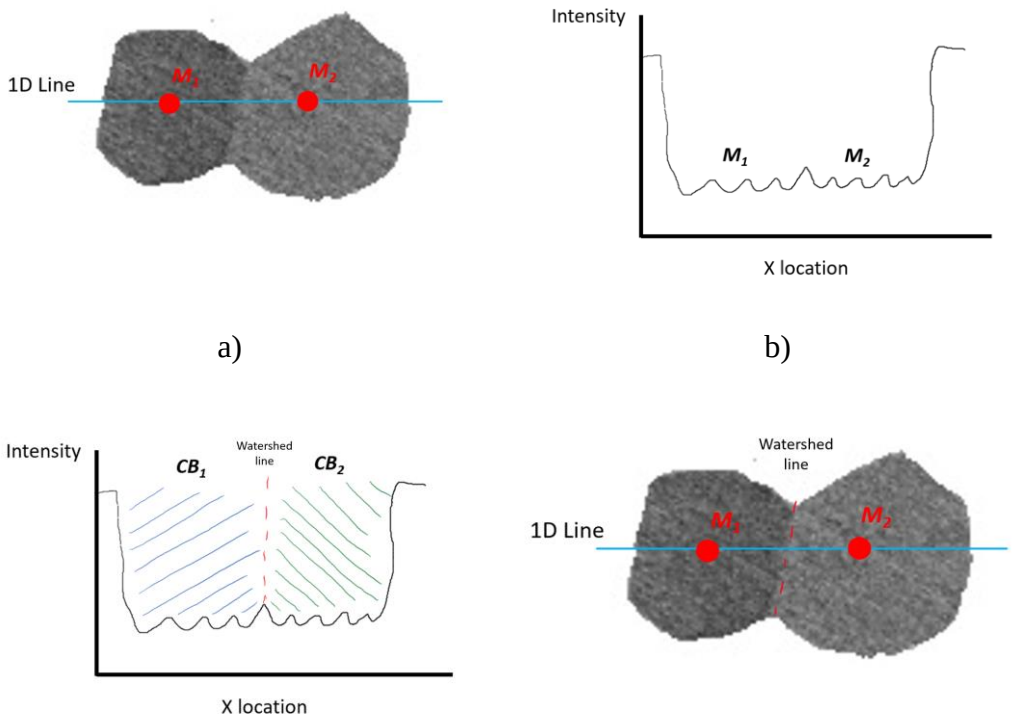

Figure 3.24: Example of a topographic surface and the catchment basins and watershed lines that are formed where a) original image with markers, b) plot of intensity values for the 1D line marked, c) is the result of the watershed transform shown in one dimension d) is the watershed line drawn between the grains in the original image

The marker-based Watershed transform can be defined using geodesic transforms in a similar way as the traditional Watershed, except with the use of R_{min} replaced by a pre-defined marker set, *M*. First only pixels that lie within a marker are set to the lowest possible image value, as in Equation (3.40). For this to work correctly this value must be lower than any other minima in the image.

$$f'(x) = \begin{cases} h_{min}, if\ x \in M(f) \\ f(x), otherwise \end{cases} \quad \textbf{(3.40)}$$

Then the geodesic time, influence zones and SKIZ are calculated by the same method as before but with respect to markers, *M*, as in Equations (3.41), (3.42) and (3.43).

$$f' = \tau_{\rho-(f')}[M(f)] \tag{3.41}$$

$$CB_a(Y) = IZ_{\rho-(f')}(M) \tag{3.42}$$

$$W_a(Y) = SKIZ_{\rho-(f')}(M) \tag{3.43}$$

The benefit of the use of markers is illustrated in Figure 3.25 which shows the segmentation of a microstructure in this study using the Watershed Transform with and without the addition of markers.

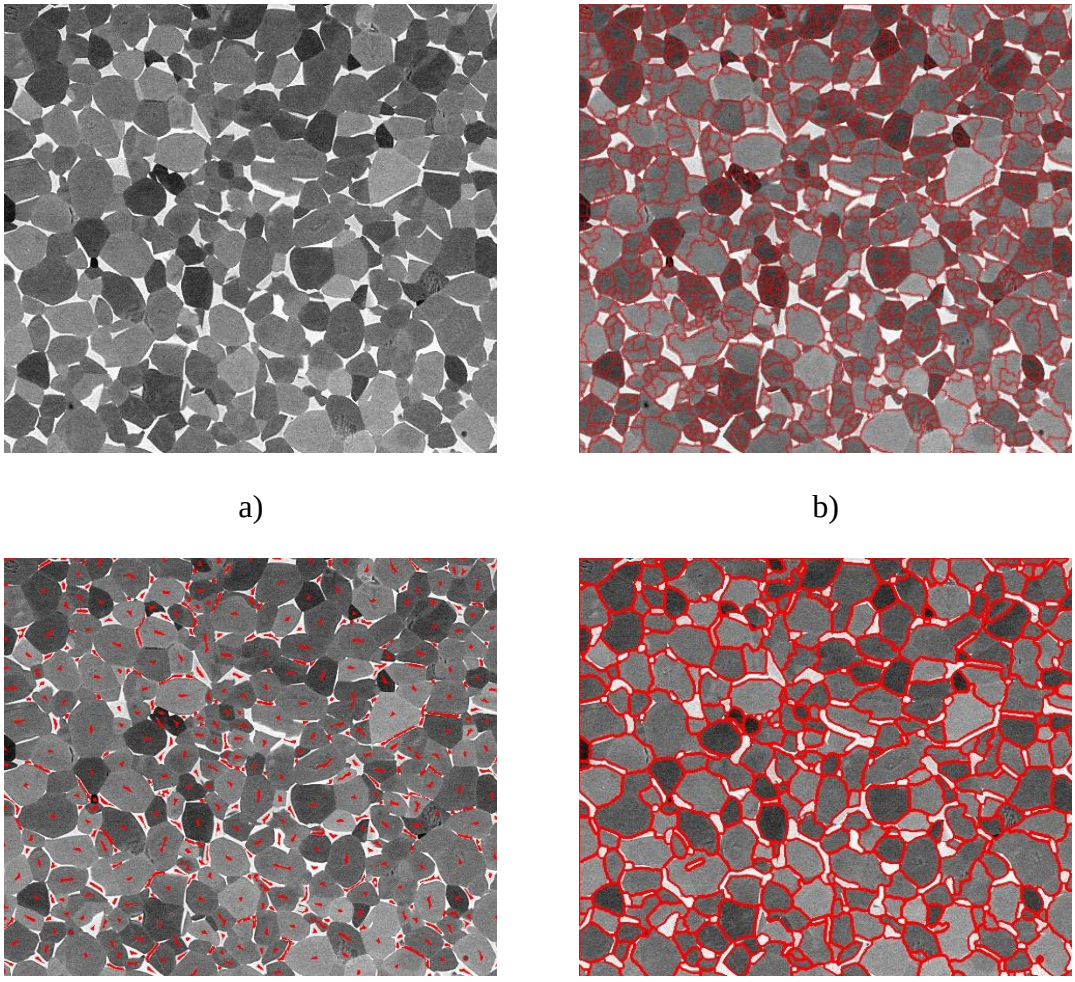

a) b)

c) d)

Figure 3.25 Illustration of segmentation using a Marker Based Watershed Transform where a) original image, b) segmentation using Watershed Transform, c) suitable set of markers and d) segmentation using the a Marker Based Watershed Transform

4 LITERATURE REVIEW

The primary research goal addressed in this thesis is to improve the microstructural analysis of Ti-6Al-4V alloys using automated digital image processing techniques. Ultimately this goal is achieved by the design of a novel image processing algorithms that are well suited to microstructural analysis, which are then validated on a real-world dataset. Achieving this requires an investigation of two key areas. First, existing analysis procedures currently used for measuring titanium microstructures are investigated. This enabled the identification of which features can currently be measured using existing techniques, how they are measured and what weakness exist with the current procedures. This provides an understanding of the state-of-the-art in microstructural analysis techniques and facilitates the identification of conceptual gaps in the knowledge that this thesis can address. Secondly, methods of automating image analysis in other applications are also investigated. The strengths and weaknesses of these procedures are assessed in order to identify which techniques are useful to incorporate into the new microstructural analysis algorithms developed. This review is therefore split into two sections.

The first section focuses on existing techniques that are applied to measure the features of complex microstructures such as Ti-6Al-4V. Both manual, automated and semi-automated techniques are considered in order to identify the challenges with current analysis methods that need to be overcome. This literature represents the baseline performance of microstructural analysis that the techniques proposed in thesis aim to better. This section is therefore critical to illustrating the contribution made by this work.

The second section of this chapter studies image processing techniques applied in other fields that it is believed have not yet been applied to microstructural images like those in this study. The motivation for this is to try and identify the most appropriate, state-of-the-art techniques that can potentially be applied to microstructural analysis. This review will briefly discuss a range of different methods, but the primary focus will be

on techniques that are applied in similar applications and applications producing images with similar looking content and properties. A full explanation of which applications are considered similar is provided in Section 4.2. As well as identifying the best approach for developing image processing tools for microstructural analysis, this section of the review also identifies knowledge gaps in the field of image processing which may negatively impact the applicability of existing methods to microstructural analysis. The novel solutions to these problems, proposed in this thesis, will not only facilitate the design of new and improved microstructural analysis techniques, but also contribute knowledge in the image processing domain.

The specific questions to be addressed in this review are outlined in the relevant section.

4.1 Analysis of microstructures

This section studies existing techniques that are specifically designed for the analysis of the microstructure of materials. It aims to address several key questions:

1. What manual methods are currently available for microstructural analysis?
2. What weaknesses and limitations exist with manual methods which lead to automated solutions being seen as an attractive solution?
3. What attempts are made in the literature to automated material analysis?
4. What weakness and limitations exist with current automated methods?

4.1.1 Existing Manual Methods

For the purpose of this review manual measurement methods are defined as those methods where the measurement of each feature is dependent solely upon expert input from a materials scientist. Such techniques are very commonly used to perform microstructural analysis in both academic and industrial contexts. Different procedures can be applied depending on the type of feature to be measured, however they all require marking the location or boundaries of individual features. As such, the time required to perform these methods depends upon the number of features to be measured and the number and accuracy of marks necessary to measure each feature. As with all manual techniques, human error is always possible, with subjectivity and bias also possible in certain cases. Standardised methods are defined to try and limit

the influence of these factors. This section discusses these methods and estimates how significant the aforementioned problems are in microstructural analysis. Specifically, standards defined by the American Society for Testing and Materials (ASTM) are reviewed. These standards are widely recognised within industry and all academic and industrial research centres involved in this research use either precisely these standards or a bespoke procedure based on them. This section describes both the original standard and the variations that can be used.

4.1.1.1 Linear Intercepts

A set of streamlined methods for manually measuring grain size are defined in the ASTM E112 standard [29] which is useful for measuring grain size. The standard uses linear intercept methods in which the length of line segments that fit within grains are used to measure their size. The standard recommends creating these line segments by overlaying a standardised test pattern of lines on a microstructural image, as shown in Figure 4.1.

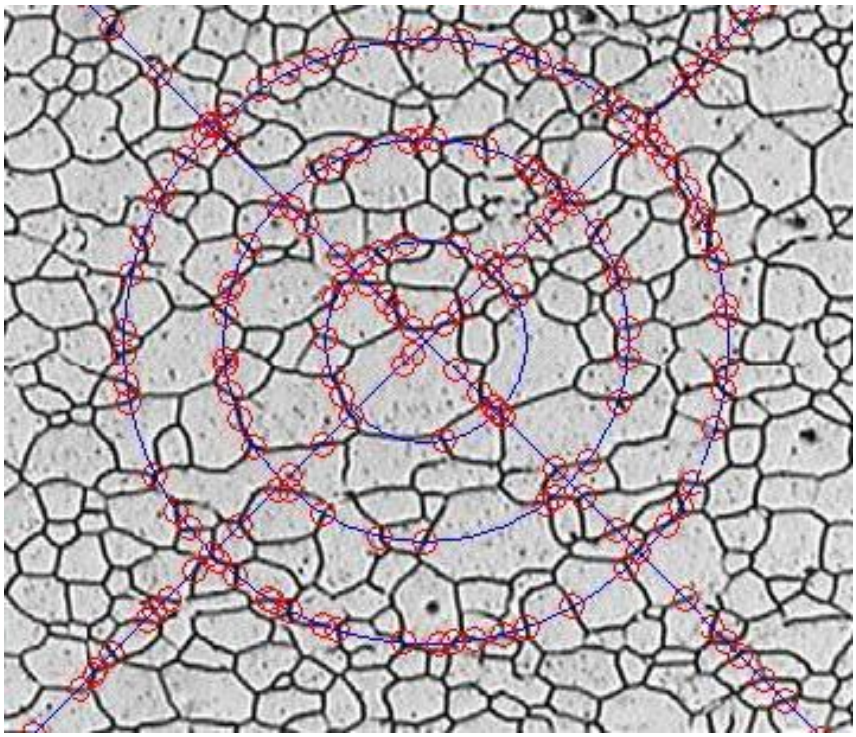

Figure 4.1: Examples of grain size measurement using a standardised test pattern where blue lines indicate the standardised grain and red circles show where the test lines intersect with grain boundaries

An expert materials scientist then manually marks locations where the lines on the test pattern dissects the boundaries of grains, with the distance between each marked location on the same line recorded as a grain measurement. The E1382 standard [30] describes how computer software and a digitising tablet can be used to perform this task efficiently. Test patterns are designed so that the lines dissect grains at random orientations. This means that each individual measurement is not necessarily representative of any specific grain dimension. As a result, it is specified that minimum of 300 measurements are required to achieve a statistically accurate estimate of the mean grain size of the microstructure. It is determined that for relatively equiaxed grains (<3:1 aspect ratio) a suitable estimate of grain size can be achieved using standardised linear or circular test patterns applied to only the longitudinal cross-section of the specimen. For non-equiaxed grains, measurements using such a pattern would need to be repeated on multiple orientations of the specimen (longitudinal, transverse and planar) to estimate the overall grain size. The use of these standardised test patterns mean that the materials scientist is not given any choice over which grains to measure, eliminating the possibility of user bias affecting measurements. However, this also prevents the materials scientist from being able to select specific grains or dimensions to measure. As a result, measurement of shape-based properties, such as the volume fraction of globular alpha, or more precise properties such as platelet width, are not possible using standardised patterns.

To measure properties other than mean grain size, the linear intercept procedures proposed in [29] can be adapted to use manually selected line segments, rather than a pre-determined test pattern. To do this a materials scientist would deliberately place line segments along the dimensions of the grain to be measured. This allows for more precise measurement of individual properties such as platelet width or, provided that the order in which these lines are placed are controlled and stored, individual measurements of grain size and aspect ratio. For example, the size and aspect ratio of individual grains could be assed using line segments placed along the length and width of each grain, terminating on the grain boundary, as illustrated in Figure 4.2.

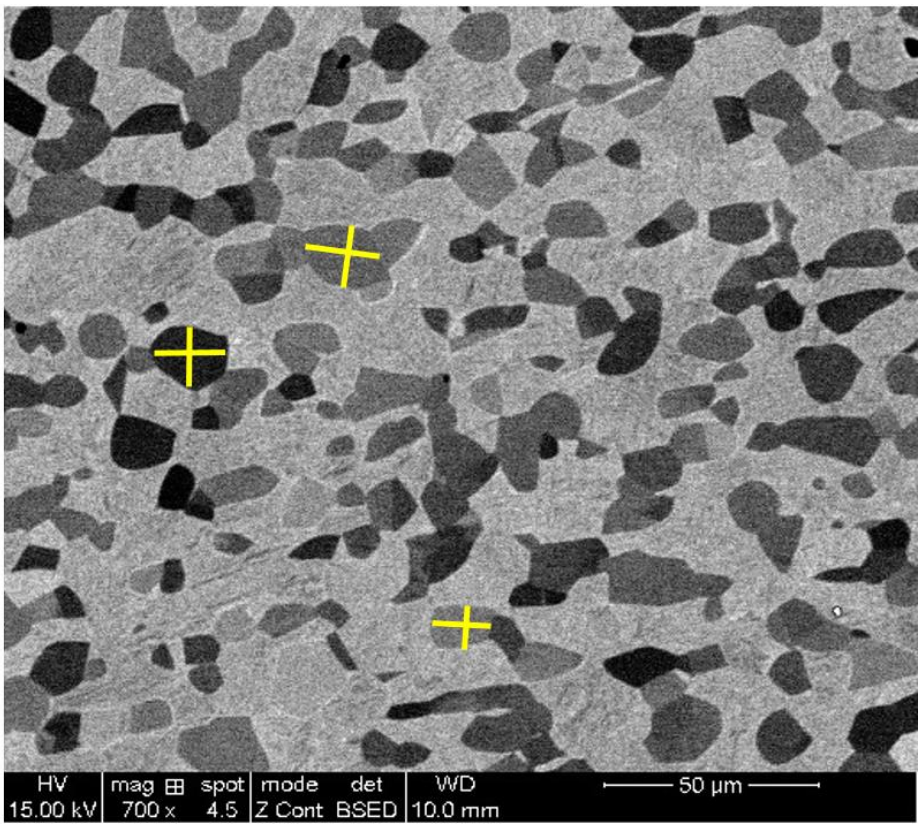

Figure 4.2: Example of linear intercepts using specifically chosen line segments (yellow) drawn across major and minor axis of grains to be measured

In this case the grain size for a single grain is estimated as the mean value of the segments that dissect it. The aspect ratio of the grain is the ratio of the longest to shortest segment that dissects that grain. Manually selecting line segments makes linear intercept procedures more powerful, however, creates a chance of bias effecting results which was not possible when using standardised patterns. In practical scenarios, it is likely that the materials scientist will have some expectation of which samples will have larger grains which could potential lead to an unfair selection of which grains to measure, perhaps even subconsciously. Smaller grains are also more difficult to measure and will often require panning and zooming to correctly place line segments within them. As it is normally only necessary to measure a subset of grains in the image, there is a possibility that, due to the materials scientist being able to select which grains to measure, the smaller and more time-consuming grains are more likely to not be measured. This is more likely to occur when measurements are required quickly. As well as the bias problem, the opportunity to select which dimension to

measure also introduces a chance of human error. In the example in Figure 4.2 the correct “length” and “width” of each grain is difficult to identify, meaning different materials scientists could measure different diameters as the length and width. As manually placed line segments are more likely to represent the true diameter of that grain than a randomly placed segment from standardised pattern, it is not expected that this will be problematic when measuring grain size. However, the difficulty in selecting the length and width could cause more significant variations when measuring aspect ratio, particularly when grains are not perfectly elliptical.

The E112 standard suggests reporting measurements of grain size using the ASTM grain size number, *G*, which is based on the number of grains per square inch at 100x magnification. This thesis instead uses the measurement of the average diameter of a grain in μm as a measurement of grain size, as described in Chapter 3, as this is more common in academic research environments. The E112 standard quantifies the level of subjectivity expected when using linear intercept techniques. It states that measurements of the same microstructure by different users can vary by up to +/- 0.5G, which equates to approximately 16% in μm. This is not particularly precise and has implications for the development of new techniques relying on small incremental improvements. For example, with such high variations in measurement, an improvement in a technique that refined grain size to be 5% smaller would be challenging to detect. Therefore, measurements could misdirect research by failing to identify techniques that had a genuine impact on microstructural evolution. It is important to consider that the subjectivity in grain boundary locations in microstructures is not consistent, so the variations reported by this standard may be lower depending on microstructural complexity. The standard does not estimate measurement time but it was determined empirically that these methods take approximately 15 minutes to produce the 300 grain measurements required for statistically valid results [6]. Due to the 16% variation in repeatability it may be necessary in certain studies or processes to have multiple materials scientists repeat measurements in a round-robin format to validate results. This could lead to very long measurement times when evaluating large datasets. Measuring very fine details such as thin alpha platelets can potentially be even more time consuming due to the need to pan and zoom to mark intersections or place line segments.

4.1.1.2 Point Counting

The ASTM E562 standard [31] describes techniques to measure volume fraction of constituents or phases of a microstructure based on point counting. A set of points are distributed throughout an image and the expert then specifies which points lie within each phase. As with the E112 standard a pre-determined set of test patterns are recommended to remove bias. Specifically, the circular and square grids shown in Figure 4.3 are suggested, although any grid layouts are acceptable provided the points are equally spaced. The percentage of points marked within a single phase gives the volume fraction of that phase. To give statistically reliable results it is often necessary to repeat this technique across multiple images of the same sample and average the result to ensure the grid does not align with the grains of a single phase by chance.

a) b)

Figure 4.3: Examples of possible grid configurations for point count tests where a) shows a circular test grid and b) a square test grid respectively

Repeatability is again a concern with this method and the E562 standard estimated repeatability at around +/-10%. The standard includes an estimate of the time required to perform analysis using this technique at 15-30 minutes depending on the user's experience. Crucially, it should also be considered that this standard is basically a sampling technique and assumes prior knowledge of the phase of each point on the test grid. This means this method can only work when the materials scientist can look at a microstructure and easily and reliably identify which constituent or phase it belongs to. For measuring the volume fraction of a phase in a two-phase alloy such as Ti-6Al-4V this would work well as there is a clear intensity difference in the image making the phases easily distinguishable. However, measurements of globular volume

fraction can be more difficult as it requires the user to estimate the aspect ratio of a grain, which is not always a trivial task and may require further measurements.

4.1.1.3 Other standards

While the E112 and E562 standards are sufficient to measure the size and volume fraction of grains a few other standards exist to measure specific statistical properties of the microstructure. For example, the E930 standard [32] describes methods to measure the grain size of only largest grain in the image. Measurement of this property is necessary in certain cases as the largest grain often corresponds to the initiation and propagation of cracks in the material. The standard specifically states that this method will only work for outlier grains far from the average grain size with a sparse population. The E1181 standard [33] describes methods for characterising grain size in microstructures where grain size does not follow a single log-normal distribution. In these cases, an average size of all grains may insufficiently describe the microstructure and lead to incorrect assumptions about material behaviour. The method estimates the area fraction occupied by different grain sizes and suggest the use of the aforementioned E112 and E930 standards to then measure each area. The procedure also requires the use of the aforementioned E562 standard to estimate the area fraction of each grain size. As such the same time and reliability concerns exist as with these standards.

The E1382 standard [30] describes methods to measure grain size using semi-automatic analysis procedures. The standard describes the use of a digitising tablet to efficiently implement the linear intercept procedures defined in the E112 standard. Additionally, it also provides a procedure to take grain area measurements by tracing the boundary of each grain to be measured. Although a this can extract detailed data, the E1382 standard does not recommend using this method in most practical situations due to its slow and tedious nature, particularly when it must be repeated for a large number of grains to obtain statistically significant results.

4.1.1.4 Summary of manual methods

The manual techniques described here can be used to measure a wide range of microstructural features. Of the key features identified in Chapter 3, only platelet orientation cannot be measured by these existing standards. However, these methods

suffer from high measurement time and poor repeatability. It should also be considered that the E112 and E562 standards have no overlap between them. This means that if grain size and volume fraction were to be measured, then the total time would be the cumulative time of performing both independent measurement procedures. A summary of the manual procedure for each microstructural feature in this study is provided in Table 4.1 along with an estimate of measurement time.

Table 4.1: Manual measurement procedures for each microstructural feature

Microstructural Property	**Standard**	**Type**	**Measurement Time for Experienced User (approx.)**
Grain Size (mean)	E112	Standard grid mark alpha grain boundaries.	8 minutes
Grain Size (distribution)	E112	Manual line segments within alpha grain terminating on grain boundary.	15 minutes per 300 measurements
Volume fraction of alpha phase	E562	Standard grid repeated for multiple views.	15 minutes
Volume fraction of globular alpha	E562/E112	If aspect ratio is clear use E562 and standard grid on multiple views. If accurate measurement of aspect ratio is needed use E112.	15 minutes
Alpha platelet width	E112	Manual line segments parallel to platelet orientation and terminating on platelet boundary.	15 minutes per 300 measurements
Alpha platelet orientation	NA	No standardised manual procedure exists.	NA
Colony size	E112	Manual or standardised lines. Mark/terminate line where at the perimeter of the colony.	15 minutes per 300 measurements

4.1.2 Existing Automated Methods

In recent years, digital image processing techniques have been proposed to improve the microstructural analysis of metal alloys. A key benefit of digital image processing is that it allows for automated measurements, which inherently makes the task less labour intensive and removes opportunities for human error. The following section describes automated methods that are applied either to the Ti-6Al-4V alloy itself or to a metal alloy with a similar complex microstructure. This review is not constrained to fully automated procedures and will also described a range of methods that combine image processing tools with input from expert materials scientists to perform analysis. This review is, however, constrained to only studying microstructures of Ti-6Al-4V alloys or similar where it is clear in the literature how this could be applied to the data in this study. The remainder of the section is divided into sub-sections depending on the microstructural property being measured. Properties for which no automated solution is proposed have no unique sub-section in this review and are instead only discussed in the summary of findings in Section 4.1.2.5.

4.1.2.1 Volume Fraction of Alpha Phase

A simple, but relatively successful, application of image processing in microstructural analysis is the use of thresholding techniques to measure the volume fraction of a phase of material in a two-phase microstructure. This technique is used by a number of different authors [11], [12], [34]–[36] to specifically measure the volume fraction of alpha phase in the Ti-6Al-4V alloy. Thresholding techniques allow pixels in the image to be categorised in phases based on the intensity value of each pixel. As discussed in Chapter 3, one phase of material is often much darker in microscopic images than the other, meaning the intensity value is informative of to which phase each pixel belongs. The accuracy of phase separation depends on image contrast and the selection of an appropriate threshold. For the best accuracy the threshold should be set to a value that exists in between the ranges of intensity values exhibited by each phase. When the contrast is high, a large number of threshold values is likely to yield the same outcome. For low contrast images, a more precise threshold value is necessary. Different solutions to this problem are presented in existing literature. Tiley *et al.* [12] initially suggest a semi-automated thresholding procedure where an expert materials scientist would manually select an appropriate threshold for each image based on a histogram

of pixel intensity values. However, the authors note that variations in intensity within the alpha phase can cause additional peaks to appear in the histogram which can make the threshold select difficult. To solve this problem, they propose using Gaussian filtering to remove these additional peaks and produce a much smoother histogram. As a result, the histogram is easy to interpret, so a suitable threshold can be identified. This filtering also improves phase separation in the image as the standard deviation in pixel intensity within in phase is reduced. Alternatively, Zhang *et al.* [37] propose using automated threshold selection methods. Specifically, Otsu's method [38] is used which separates pixels into two classes such that the inter-class variance is maximised and the intra-class variance is minimised. Each of the methods described are used on Ti-6Al-4V microstructures. However, these approaches generally assume the selection of a global threshold, where every pixel in the image is classified by comparison with a single threshold value. However, challenges associated with microscopic imaging technologies, such as differences in lighting conditions throughout the image, or damage to the surface of a sample, could cause a meaningless difference in brightness between regions of the same images. In such cases the intensity levels present in each phase of material would differ depending on the location in the image. As a result, a single threshold value may not accurately separate the alpha and beta phase [37]. Several authors [36], [37] demonstrate that a solution to this can be provided by using adaptive thresholding techniques. These techniques operate by dividing the image into regions and computing a different threshold for each region independently from other areas of the image. As a result, phases are separated well in all images of the image despite differences in brightness. Figure 4.4 demonstrates the difference between global and adaptive thresholding for titanium micrograph of a Widmanstatten microstructure. When a global threshold is used, shown in Figure 4.4 b), detail is lost in the darkest area of the image. When an adaptive threshold is used far more detail is seen in this area, as shown in Figure 4.4 c).

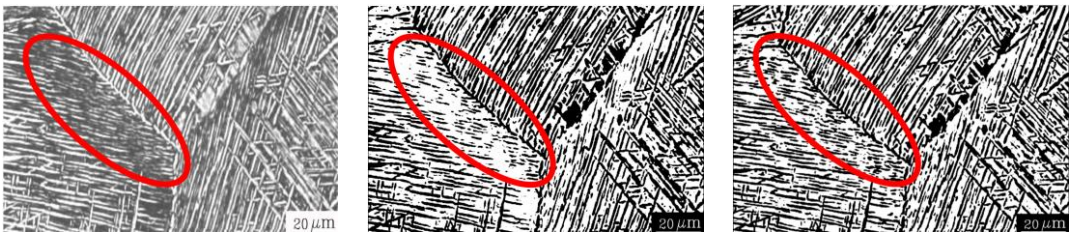

a) b) c)

Figure 4.4: Comparison of global and adaptive Otsu thresholding where a) original image, b) global threshold and c) adaptive threshold [37] **and the red circle indicates a significantly different area**

4.1.2.2 Platelet Measurements

The only automated methods that have been identified for measuring the width of alpha platelets in titanium microstructures are proposed by Collins [11] and Tiley [12]. Both authors present fundamentally the same technique, however, Tiley describes its application to measure fully lamellar microstructures and Collins describes an extended version that can be used on bi-modal microstructures. These authors propose a range of automated and semi-automated procedures for microstructural analysis that are implemented in the commercial Adobe Photoshop extension Fovea Pro, which are discussed throughout this chapter. To measure platelet width, a pre-defined grid of straight, parallel lines is multiplied element-wise by a binary microstructural image, produced by thresholding, where the alpha phase is represented by "1"'s. The result is a set of line segments that fit exclusively within the alpha phase. The length of these line segments provides a measure of the dimensions of platelets. However, no orientation information is available to choose a suitable direction for the grid, therefore, measurements of the length of each individual line segment do not necessarily correspond to the width of a platelet. Instead this operation is repeated with the grid of lines rotated through 180° at 10° increments and statistical theories are applied to extrapolate the true width of platelets based on the lengths of all the line segments produced. In lamellar structures this technique can be applied directly to the binary version of the microstructure, produced using the techniques in Section 4.1.2.1. In bi-modal microstructures it is necessary to first separate the equiaxed and lamellar alpha particles. In the proposed methods [11], [12], significant manual input is required

for this task, as no automated method to separate globular and lamellar grain shapes is provided.

When estimating platelet width based on the length of line segments, the authors note that none of these measurements necessarily reflect the true 3D thickness of the platelet. In manual standards this problem is overcome by measuring the width of platelets using microstructural images captured from different orientations of sample. Collins and Tiley propose an alternative solution based on a mathematical proof provided by Gunderson [39] in his research analysing stereological images of membranes. In that work a membrane is defined as a 3-dimensional object that is finite in one dimension and effectively infinite in the other two. For such a structure it is determined that a probability distribution of the length of random line segments that intersected the membrane would be complex and asymptotic. However, the inverse of the linear intersect lengths would produce a simple triangular distribution where the maximum value was the inverse of the narrowest width of the object, considered by the authors as the *true* width of the membrane. Tiley and Collins [11], [12] propose that the distribution of lines intersecting an alpha platelet should follow a similar pattern as it is very thin in one dimension and far larger in the other two. Due to the triangular distribution the mean inverse of linear intersect lengths is 2/3 of the maximum value, this means that the *true* width can be measured by the formula in Equation (4.1).

$$true\ thickness = \frac{1}{1.5 * mean(\frac{1}{\lambda})} \tag{4.1}$$

The benefit of this approach is that it would allow the true 3D thickness to be calculated even if it was not visible in any of the images themselves. However, when measuring a structure of multiple platelets of different thickness, the mean width may be more informative. The proposed method would only approximate the mean width when platelets in the microstructure are of consistent width. Additionally, the accuracy of this method depends on the underlying assumption that a platelet can be treated as finite in 1 dimension and infinite in the, which is not always the case in titanium microstructures with shorter platelets. Specifically, Collins estimates this technique would become inaccurate when the aspect ratio between the smallest and second

smallest dimensions was less than 20/1 [11]. The reason for this is that for laths with longer aspect ratios the majority of linear segments will be of length approximately equal to the width of the lath while in thicker platelets a significant number of segments will instead be approximate the length of the platelet.

4.1.2.3 Equiaxed Alpha Grain Measurement

The measurement of equiaxed alpha grains is a particularly challenging. Many proposed procedures require this information but are unable to automate this task and instead rely on manual intervention. Collins [11] proposed to measure equiaxed alpha grains in titanium alloys using the same procedure used for platelet width. A grid of parallel lines is multiplied by a binary microstructural image, with the grids rotated through 180° at the same 10° increments. The mean length of these gives the mean diameter of grains, which is reported as the grain size. This method is effectively an automation of methods the linear intercept procedure used in ASTM E112 [29]. However, the measurement of alpha grains is not fully automated as it requires that grain boundaries are already identified in the microstructural image. As the authors found no method capable of this task the image must be manually pre-processed with expert materials scientists required to trace complete boundaries between adjacent alpha grains. As described in industrial standards [30] tracing these boundaries can be slow and tedious compared to other manual procedures, as a result this is not a scalable solution.

While the literature did not present good solutions to this problem a commercial software package called MIPAR showed some promising results. The development of this software is described in academic literature by Sosa *et al.* [36]. This software has a built-in algorithm builder allowing different algorithms to be designed within its interface, either by the end user or by the original software developers. While the effectiveness of this programming environment is not of interest to the work in this thesis, the software has several pre-designed algorithms, freely available online, which are designed for materials science purposes. Of most interest among these is an algorithm called “Grain Segmentation” that is designed to automate the measurement of globular grains in metals. While it is not advertised for Ti-6Al-4V it is described as being intended for general metal segmentation, making it of interest to consider in this

review. Grains are measured by first performing a complete segmentation of the microstructure. To do this an adaptive thresholding technique is applied to locate dark or light lines in the image, as chosen by the user, with the assumption made that these lines represent grain boundaries. The Watershed Transform, described in Chapter 3, is then used to segment alpha grains based on these detected boundaries by using the distance transform of the post-threshold image as the input. Validation of this method is not provided but experiments conducted for this study show that this works well for some simple microstructures, however, is highly inaccurate for more complex images, such as those in the Ti-6Al-4V dataset [6]. This illustrated by an experimental comparison in Chapter 8. The accuracy of this method depends upon a large percentage of the total grain boundaries being detected by the adaptive thresholding method, however, for many microstructures the grain boundaries do not present as a distinct light or dark line. Instead it is common for grain boundaries to be indicated other properties, which this method would not detect.

Another segmentation based analysis technique for titanium alloys is proposed by Zhe *et al.* [35]. This method disregards any intensity information and attempts to separate grains by studying the shape of alpha phase regions after thresholding. The location of concave regions in the alpha phase are identified and marked. These marked locations are then paired with adjacent marked locations and new grain boundaries are drawn which connect these points. This method is specifically designed for separating touching lamellar and globular grains, although it is shown to also separate individual platelets in some situations. The results presented, however, suggest touching globular grains are not well segmented by this technique. Furthermore, the boundaries of individual grains and platelets in the images presented are clearer and easier to identify than in most of the microstructures studied in this thesis so there is more information for Zhe's technique to exploit.

Image segmentation techniques are also employed to measure gamma precipitates in nickel-based superalloys [40], [41]. In this microstructure the precipitates appear as a different intensity, as is the case with the alpha phase in titanium alloys. Region growing techniques are proposed to segment each precipitate by growing a region representing each precipitate from a seed point within it. In the simplest case, the adjacent pixel with the closest intensity to the region is added to that region provided

that the intensity of that pixel is close to the mean intensity of that region. A stopping parameter, indicating the maximum intensity change of pixel to be added to the region, must be defined to stop region growth. However, using intensity information alone in noisy images can be problematic so the authors introduce additional rules to control region growing more accurately and provide a more accurate segmentation. A weighting function is defined which weights pixels based on the density of pixels in the surrounding area that are already labelled as part of the region. The region is only allowed to grow to pixels that already has a significant number of pixels belonging to that region in its neighbouring area. This discourages non-spherical growth and prevents protrusions from the precipitate as the region would only grow into long thin shapes if the intensity was very similar. This is a feature that would be particularly useful in bi-modal type microstructures, where an unclear boundary between adjacent globular and elongated grains could cause errors. Additionally, the authors propose an automated method for computing a stopping parameter, controlling when the growth of each region should end. This is done by repeatedly applying the same method while incrementally increasing the stopping parameter. For each case a penalty function is defined as the difference in mean intensity between pixels within a region and pixels just outside its boundary. The stopping parameter that maximises this penalty function provides the optimum segmentation result. Although good results are achieved in this work, a crucial difference exists between the microstructures used and those studied in this thesis. This is that most of the precipitates considered in [40], [41] are not touching as grains in the microstructures in this study often are. Although the shape of objects is considered during region growing this is used only to prevent protrusions and not to identify boundaries between adjacent grains. The proposed method is therefore best suiting for identifying isolated grains from the background, which, although challenging for precipitates in nickel alloys, is already achievable for images in the dataset used in this thesis. The failure to deal correctly with touching grains is particularly important for Ti-6Al-4V microstructures and is also a common issue in the image segmentation techniques described in 4.2.3.

While the authors cited in this review recognise the need for a reliable segmentation technique for isolating individual alpha grains in Ti-6Al-4V alloys, no method was found in the literature that fully achieved this with acceptable accuracy.

4.1.2.4 Colony Measurements

A fully automated method for measuring colonies was not found in this review. In the methods proposed by Tiley [12], image processing tools are used to aid colony measurement but significant manual input is still required. Random grids of lines are drawn on the image with the length of line that intercepts the colonies used to give an estimate of its size. Unlike their work measuring lath width, where thresholding was used to find each intercept automatically, these intercepts had to be marked manually when measuring colonies. This is because a colony boundary has the same intensity and general appearance as a boundary between the laths within the same colony, as illustrated in Figure 4.5. The authors note that several microstructural images of different surfaces of the sample must be studied when using this technique and that no information relating to the shape of these colonies are obtained.

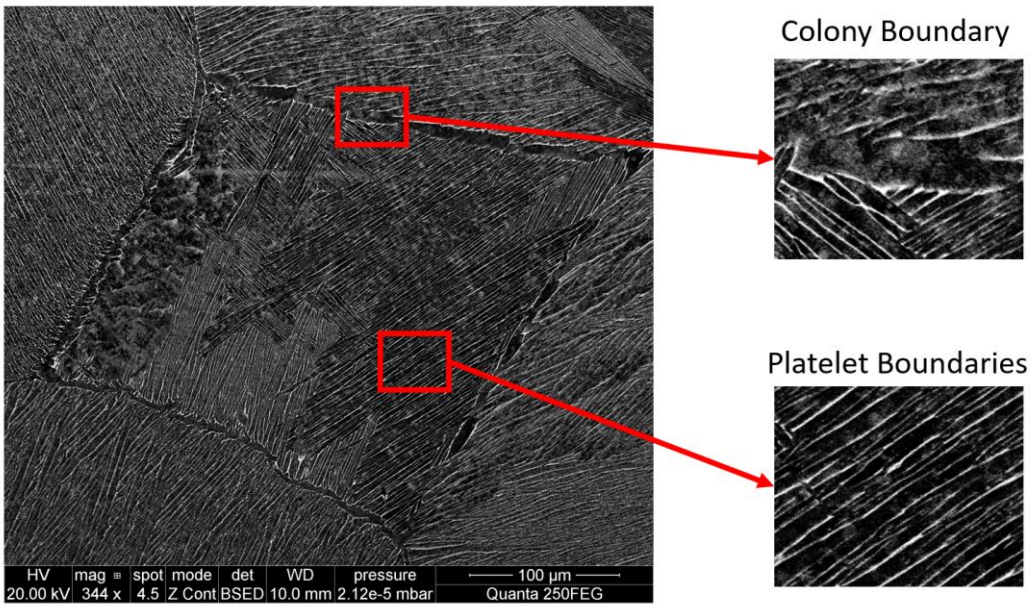

Figure 4.5 Example of colony and grain boundaries in a lamellar microstructure taken with a SEM

4.1.2.5 Other notable techniques

While the approach taken in this thesis is to automate the measurement of individual features, it is it should still be noted that image processing has also been applied to classify microstructures more generally. DeCost *et al.* [42] propose a method to classify microstructures into predefined classes. This is achieved by extracting features

from each class using the popular SIFT algorithm [43] and using this to build a fingerprint for each image. Fingerprints from images of each class are then used to train a machine learning model known as a support vector machine to automatically recognise microstructure class based on this fingerprint. This work was relatively successful (83% accurate), however, the classes of microstructure are very different and no information regarding the spatial correlation of features is included in the fingerprint. This means that while some classification of microstructural data is achieved in an automated way, this method will not obtain the kind of detailed measurements this thesis seeks to automate.

4.1.2.6 Summary of microstructural analysis using image processing

This literature review shows that microstructural analysis can be enhanced through the use of image processing techniques. However, several limitations exist with current methods and, as a result, not all microstructures and features can be measured reliably. Phase separation is currently the most successfully automated measurement, with several authors reporting that this can be achieved through thresholding [11], [12], [34]–[36]. This allows good measurements of the volume fraction of alpha phase to be computed very efficiently. There has also been some success in the automation of platelet width measurements [11], [12]. A method, which is fully automated in the case of lamellar microstructures [12], is proposed that measures the lengths of platelets at a range of orientations and uses this to extrapolate the thickness. However, this method is only reliable for laths of high aspect ratios and consistent thickness. This also measures lath thickness through an estimate of the thinnest point in the lath rather than the mean thickness, which is preferred. This method is, therefore, only reliable when all laths in the image are of a consistent thickness, hence, a more robust technique would be of benefit. Specifically, it is possible that more reliable measurements could be performed by linear segments if they are directed across the narrowest visible dimension of the lath rather than a random orientation, as is already possible in manual standards [29]. However, automatically placing such segments requires orientation measurements which are among the least well researched for titanium microstructures. Both measurements of the orientation of platelets and the size of colonies currently have no proposed methods to automate their analysis in Ti-6Al-4V microstructures. While this is understandable for orientation measurements that given orientation of

platelets is not known to be as critical to material properties as other factors, it is still valuable and can be used to inform measurements of other properties, such as colonies.

Other features that remain challenging to measure are the alpha grain size and the volume fraction of globular alpha. For the complex titanium microstructures investigated in this study no suitable procedures for identifying individual globular alpha particles were identified in the literature. Several authors, who proposed automated techniques for other features, identify this as a problem but state that manual input was still required for measurements of alpha grain size or globular volume fraction [11], [34]. A segmentation algorithm made publicly through the MIPAR software environment offers the most recent attempt at segmenting globular grains in microstructural data [36]. However, the microstructures this is applied to in the demonstration material have far clearer boundaries than is expected in those of titanium alloys, therefore, this approach is not effective for the dataset in this study. This is demonstrated in Chapter 8.

4.2 Image Processing

In this section a review of recent digital image processing literature is conducted. The aim is to identify techniques that may be useful for measuring the features of microstructural images but have not yet been tested in this field.

The main questions addressed in this section are,

1. What type of image processing techniques are potentially useful for microstructural analysis?
2. Are there any limitations with existing image processing techniques that must be addressed to allow these techniques to be used to measure microstructures?

As it is impractical to review all image analysis literature, the review begins by summarising different fundamental approaches to image and identifying those which most merit further investigation. A review of these techniques is then conducted with a focus on recent and important contributions and applications to similar datasets. This first requires a definition of what constitutes a similar dataset. This is relatively challenging as similar datasets do not always come from similar applications. As the techniques described in this thesis are aimed at the microstructural analysis of titanium

alloys, it may be expected that any techniques targeting microscopy images of different materials would share the most similar properties. However, this is often not the case and similar materials can present very different microstructural data. Instead a decision on the similarity of datasets used in other research is made subjectively by comparing the types of images discussed to the images of Ti-6Al-4V microstructures used in this thesis. The titanium dataset used is relatively varied and includes images with both clusters of globular and elongated grains. Images of globular microstructures are characterised by often noisy images of touching roughly equiaxed objects. Images of lamellar microstructures are characterised by elongated structures of various dimensions that are often extremely thin. A similar dataset is considered as any dataset which exhibits either of these set of properties. Fortunately, just as the microstructural analysis of other materials can present quite different datasets, completely unrelated applications can present quite similar ones. Techniques published for analysing these images therefore provide useful information for the design of microstructural analysis methods in this work. Good examples of this are cell nuclei in medical images [44], which resemble globular grains, and systems of fibres [45], which resemble platelets.

4.2.1 Different approaches to digital image analysis

There exist many different techniques for measuring the properties of image data. In some cases, meaningful measurement of the image as a whole can be achieved by statistical analysis of pixel values [46], while in others it is necessary to identify and measure specific image features [47]. This thesis is concerned with the measurement of morphological features, which makes the latter methods of primary importance. In general, approaches to measure individual features can be divided into two categories'; those that attempt to directly measure objects in an image, and those that first segment the image into features of interest prior to performing measurement.

Direct measurements of image features, without a prior segmentation, are often achieved using techniques that probe each point in an image with a pre-defined sub image. Examples of techniques that are applied to measure image features in this way in similar applications are mathematical morphology [48], granulometry [49], the hit-or-miss transform [26], and certain filtering methods [50]. Each of these techniques can be applied directly to an image and produce a numerical output measuring some

property of objects in the image, although some of the techniques mentioned can also segment the image based on this information. Procedures already proposed for microstructural analysis by Tiley [12] and Collins [11] are conceptually similar to the direct measurement techniques discussed here as measurements are produced by comparing the microstructural image with a set of pre-defined images containing grids of lines. Direct measurements often provide results on a per pixel or per sample basis so only statistical data describing the image as a whole is available, rather than measurements pertaining to each individual feature. Specific measurements of each feature normally require that the image is segmented into relevant regions of interest. Image segmentation produces a partitioned image where each pixel is labelled according to which region it belongs, allowing each object to be uniquely measured. A range of techniques exist for this task including, the Watershed Transform [27], Active Contour Models [51], clustering [52], deep learning [53] and semantic segmentation [54] .

The remainder of this section is split into 2 further sections; one discussing methods to directly extract measurements from the image, and the other discussing techniques based on image segmentation. A list of all the publications discussed in this review, the family of technique to which they belong and the field in which they were deployed is provided in Table 4.2.

Table 4.2: List and description of image processing publications included

Refence	Approach	Technique Family	Application Field
49	Direct measurement	Mathematical morphology	General
57			
58			
60			
5			
56			Materials science
63			
59			Remote sensing
45		Bespoke transforms	Medical imaging
65			
27	Segmentation	Watershed	General
72, 75, 76			
77			
78			
98			
5			Coffee beans
73			Remote sensing
74			Nuclear materials
97, 98			Medical imaging
100			
101,102			
44			
103			
80, 81, 82		Active Contour	General
51			
103			Medical imaging
105			
106			
88		Machine learning	General
93, 94			
95			
89			Materials science
90			
91			
92 (review of 300 articles)		Others	Medical imaging
83		Split-and-merge	General
84			
87			
85			Materials science

4.2.2 Direct measurement of feature properties

A variety of successful techniques have been proposed for directly measuring the size, shape and orientation of image features without segmenting and labelling individual features beforehand.

A simple method for measuring the thickness of objects using the distance transform is described by Russ for the analysis microscopic images [55]. A binary image is first required with objects of interest in white. The transform returns, for each white pixel, the value of the distance between that pixel and the nearest black pixel. As the output of the distance transform depends on pixel location as well as image size, pixels close to the boundary would return values not representative of object width so must be discounted from measurements. To resolve this, only output values on the ridge lines of the distance transform, known also as the morphological skeleton, are used. As the distance transform inherently measures radius and not width, the value from the distance transform must be doubled for all measurements greater than 1. A measurement of exactly 1 indicates a line that is a single pixel thick, in which case the response of the distance transform is already be equivalent to the width. Russ describes this method for elongated objects with a high aspect ratio and smooth boundaries, in which case the ridgelines of distance transform remain mostly in the centre of the object. For objects that are not perfectly straight, or have lower aspect ratios, a greater proportion of the ridgelines are not at the objects' centres and, therefore, measurements would not correspond to width. More advanced techniques are necessary for titanium microstructures as grains often do not have a smooth shape.

Adhikari *et al*. [56] also use the skeleton when taking width measurements, in this case for measuring cracks in concrete for bridge inspection. However, in this case measurement, do not come from the distance transform but by dividing the length of the skeleton by the total area of the crack, determined by thresholding. This means that the positioning of the skeleton is less important, but the number of additional branches, no representing the length of a feature, are more important. The effect this has on measurement accuracy is explored in Chapter 8. Adhikari's work splits the skeleton into separate branches to facilitate individual measurements of each crack. If applicable to titanium microstructures this would allow better statistical information about platelets. However, this can only be applied if the measurement methodology is

accurate and there is not an erroneously large number of branches in the skeleton. It is again demonstrated in Section 8.3.3.2 that this method is not accurate for the microstructural images in this study.

a) b)

Figure 4.6: Examples of SE measurement where a) shows disk shape SE for radius measurement and b) linear SE for measuring orientation. In both cases black shapes are the original object, yellow are SE that fit comfortably thus don't describe the feature limits, green are SE the extrema that fits so describes feature properties well and red are SE that do not fit

An alternative method to measure object size is granulometry [49], [57]. This is a technique, first proposed by Serra [58], based on mathematical morphology, that is used to extract size information by probing an image with SEs of iteratively increasing size and recording the response. When the image is opened by a SE that is smaller than an object in an image, that object will still appear in the output. When the SE is larger than the object in the image that object will no longer appear in the output. It is, therefore, known that for each pixel belongs to an object of approximately the same size as that SE that removed it, provided the image objects and SEs are of similar shape. This concept is illustrated in Figure 4.6. During a granulometry, the remaining area after each opening is recorded and a size distribution can be calculated as the first derivative of this data. This method has been deployed recently by Statella *et al.* [59] to measure dust devil tracks on the surface of mars. These tracks are caused by weather patterns on the planet are measured from grayscale images where the tracks present as thin elongated objects that often overlap and are not straight. In this way these have some similarity to the alpha platelets in the current study, despite the difference in the underlying application. A granulometry is performed using disk shaped structuring elements, which ensures that the "size" recorded in the resulting distribution corresponds to the shortest dimension of the object at each pixel, i.e. the width of the object. In addition to obtaining a statistical description of object width, this technique is then used by Statella *et al.* to filter out objects of a separate size to study separately. Spikes in the size distribution indicate a significant number of grains of a particular size, which are likely the best sizes to filter. Morphological openings and closings can

then be used on the original image data to remove object not matching this size. This can provide some segmentation of the image but only by separating grains of different sizes. In titanium microstructures, grains of similar size often overlap and often even clustering into large groups that can appear circular but in fact consist of multiple grains. This technique was found experimentally to not isolate each individual grain which negatively effects filtering attempts and the accuracy of size measurements. For measuring the width of platelets, however, this approach appears very useful and is explored more in Section 8.3.3.2. The use of a disk-shaped structuring element means that measurements of other features, such as orientation is not possible using Statella's implementation.

For measuring the orientation of objects, a number of methods exist that can be directly applied to the data. A common approach is to find the gradient magnitude in two perpendicular directions and use this information to compute the orientation. Edge detection filters, such as Sobel and Prewitt, can be used to compute gradient orientation in this way [2]. However, this is typically computed over a small window. As a result, only local information from neighbouring pixels is used and orientation measurements become meaningless towards the centre of wider objects. Rivest *et al.* [60] proposed methods to compute gradient orientation using mathematical morphology. Based on techniques initially proposed by Beucher [5] to compute the gradient magnitude of the image using mathematical morphology, Rivest's method computes this gradient twice using perpendicularly orientated linear SEs. As these SEs can be set to any size, larger areas could be studied than with the aforementioned edge detection filters. This increases the accuracy of orientation measurements further from object boundaries. It would appear possible that such methods would be applicable to elongated platelets in titanium microstructures. The only concern is whether or not the sampling the gradient in just two directions is sufficient, particularly when platelets are very thin. Altendorf [45] *et al.* use a similar concept to measure the orientation of fibres, relatively similar in appearance to alpha platelets from our dataset. A key difference here is that SEs at a greater number of different orientations are used, which theoretically makes this method more robust. Another difference is that, rather than use the image gradient, the directional distance transform is used to measure the distance between pixels in an object and the object boundary in multiple directions from which information about

the orientation and radius are calculated. The primary focus of Altendorf's work is on 3D images, although, it is included in this review as the potential application to 2D is also discussed. The ability to measure orientation and radius simultaneously is valuable for lamellar and bi-modal microstructures. This approach appears to have potential use for the analysis of thin elongated structures as measurements of both orientation and width can be achieved. However, potentially useful information regarding the shape of features is not explored, presumably as it is not relevant to the target application. The fibre images also have a consistently high aspect ratio, with these fibres showing very little deformation, which is expected to make this application less challenges than platelets in Ti-6Al-4V microstructures. The aforementioned methods do not provide a description of how the orientation information gained to group similarly organised objects together.

When measuring the orientation of thin structures such as alpha platelets, an alternative to calculating the orientation based on a few perpendicular measurements is to use a wider range of orientated operators to measure the gradient in different directions and select the orientation of the smallest gradient as the object orientation. Measurements by this approach are inherently quantised by the discrete number of orientations tested. An example of this is steerable filters [61], which are filters designed so that they can be orientated in different directions. An energy function, called the "oriented energy", is defined based on the output of these filters. The angle which maximises this energy function at each pixel is the orientation of image gradient. Soille *et al.* [48] use mathematical morphology to compute local gradient in a similar way using arbitrarily oriented linear SEs. A practical example of the use of this method to detect road orientation in satellite images has previously been presented [62]. This shows this method can effectively identify the orientation of elongated structures, though in a quite different application.

Very recently, Borocco *et al.* [63] proposed similar techniques for an application more similar to that of this thesis, measurement of the organisation of graphene plans. Linear SEs, of a fixed length, at a pre-defined range of orientations are used with the orientation of SE that best fits within an object in the image selected as the orientation measurement for those pixels. A key feature of Borocco's work is to map these orientation measurements to a binary orientation space. This orientation space was first

proposed by Chen and Hsu [64] and adds an orientation support to the traditional x and y axis of an image so that objects exist on different planes depending on their orientation. For graphene planes this allows similarly orientated plans to be grouped together into “stacks”. This approach has several benefits, a crucial one being an inherent resilience to noise. In many cases, noise in an image will cause the orientation measured at certain pixels to be effectively random. In a regular 2D space these noise corrupted measurements exist adjacent to true measurements making the correct measurement more difficult to identify and parallel objects more difficult to group together. In the orientation space, this noise spreads out across several planes, while true orientation values would cluster together in the same or adjacent planes. This makes true measurements easier to identify and reduces the influence of noise when grouping elongated objects. The clustering of parallel, similarly located objects in a 3D space is also useful for grouping objects more generally, regardless of noise level. If orientation measurements were studied in a 2D space, and clusters existed at various orientations, then a histogram of orientations would be fairly flat, making it difficult to identify a colony [6]. Studying orientation and space in 3D makes this far easier. This offers what is believed to be the best approach that could be applicable to identifying colonies of alpha platelets. The graphene plans share some of the properties of titanium microstructures as they contain noise and very thin objects. However, the width of objects is consistent in Borocco’s data, as this is a known physical property of graphene plans, which is not the case for platelets in titanium microstructures. Additionally, the accuracy of measurements using the method in [63] requires the selection of a suitable parameter, the length of SE to use. In Borocco’s work selecting a suitable length of SE is a moderately trivial task, as a wide range of SE lengths would fit the objects at only one orientation. However, for the more variable size of object in the titanium dataset this is not the case. This technique would inevitably cause errors when the aspect ratio of image objects varied, and the optimal SE length would be challenging to select. Novel solutions to these problems would therefore be necessary to successfully apply similar methods to the dataset studied in this thesis. This is discussed more in Chapter 6 and demonstrated in Chapter 8.

Robb *et al.* [65] also use the orientation space to measure the orientation of objects in images. Instead of using mathematical morphology the orientation space was instead

built using orientated Gaussian filtering techniques [66]. The anisotropic Gaussian filters can be applied directly to greyscale images and are less affected by noise. Rather than the binary approach taken by Borocco, each entry in the orientation space is based on the response of the filter at that location and orientation. However, this extra data is still insufficient to extract size and shape information. Furthermore, the size of the filter must be chosen based on the object radius, so the same problems with aspect ratio and varying sizes exist as in Borocco's work.

4.2.3 Segmentation

Automated image analysis requires techniques that can identify each region of interest in the image. Image segmentation is the process of partitioning an image into multiple regions, at least one of which is normally of interest to measure, by labelling each pixel in the image according to the image feature it belongs to. Image segmentation can be used to subdivide the image the image differently depending on the type of features that are required to be measured. For example, in Ti-6Al-4V microstructures, measuring the volume fraction of alpha phase requires segmentation of the image into two regions, one representing each phase. If grain size measurements are required, it is instead necessary to segment the image into as many regions as there are grains, plus the background (beta phase). In one case the image is segmented into objects of a different class and the other the image is segmented into instances of that class. Performing each of these types of segmentation is a fundamentally different task and requires different algorithms and techniques. In this review the primary focus is on the segmentation of different instances of each class, i.e. the individual grains and platelets. Existing literature already presents a variety of methods to segment different phases, defects or similar constituents of material in complex microstructures [67], [68] and in the case of Ti-6Al-4V microstructures some simpler methods have already been used successfully [11], [12], [34]. In contrast, the segmentation of individual grains is less well research and with existing segmentation attempts often depending on complete separation between each grain [69]. Automated reliable, accurate segmentation of touching grains has not been achieved for titanium microstructures. This is of great value as once a segmentation is available it is relatively easy to produce a variety of measurements of each labelled object in that segmentation. For example,

the area can be computed as the number of pixels with the corresponding label, while the number of objects is the number of unique labels in the segmented image. Other features such as object shape and the length of each dimension require slightly more complex calculations but these can also be computed using well established standardised methods [70]. For the features of interest in in Ti-6Al-4V microstructures, using a segmentation approach means that the precise act of taking measurements is trivial and that all the difficulty lies in producing an accurate initial segmentation. Image segmentation is widely regarded as one of the most challenging tasks in image analysis [2], [24]. The key issue is that the properties that indicate a feature of interest are different depending on the application and sometimes even the specific dataset. For this reason, generic segmentation approaches tend to not work well for complex datasets and image processing algorithms tailored to accurately segment challenging dataset will not necessarily work well for others. Therefore, to segment complex images, such as the microstructures in this study, it is normally necessary for bespoke techniques to be designed to achieve accurate results [24]. This has led to the development of a wide variety of different segmentation algorithms based on the same fundamental theories. Consider, for example, Figure 4.7 which shows images from different sources. In each case there are some features of interest that we can isolate from the rest of the scene, however, the properties that distinguish them in each case are quite different. Hence, it would not be realistic to expect a single algorithm to achieve meaningful results in all of these cases.

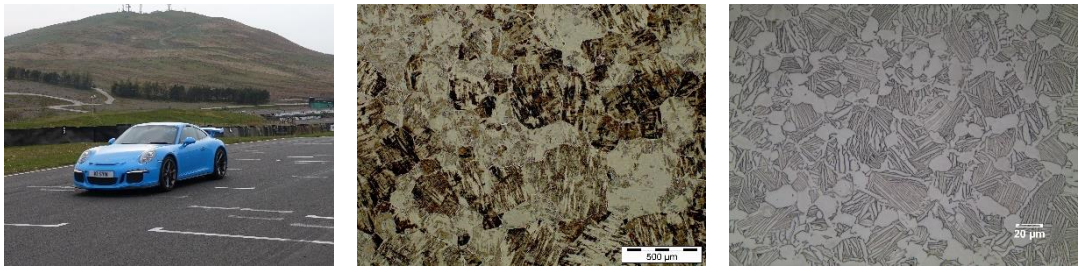

a) b) c)

Figure 4.7: Example of differences in segmentation challenges where a) is natural image from a conventional camera, b) is a microscopic image not from the current study and c) is a Ti-6Al-4V microstructural image

Due to the volume of research on image segmentation it is important to focus on research areas most likely to be applicable to titanium microstructures. While conducting this review it was found that many image segmentation methods presented in the fields of medicine and geology are applied to datasets sharing similar properties and far fewer are applied to the analysis of the microstructures. This view is supported by a very recent review by Dimiduk *et al.* [71] that found recent signal and image processing technologies were applied more regularly to fields such as medicine but less frequently to materials science. In the current review, medical images of cells are found to give some of the most similar images to the microstructural dataset as cells are often elliptical and clustered such that multiple cells can touch at a common boundary. This means that the images present similar segmentation challenges as microstructural data. Several segmentation techniques are proposed in the area of medical image processing that can identify subtle boundaries between touching objects. This is a key challenge in producing globular grain measurements which, as described in Section 4.1, remains unsolved in the materials science literature. Geological images of rocks also present similar challenges for segmentation; however, the images often have a visible 3-dimensional property, while in many cases the images of titanium microstructures studied in this thesis ostensibly appear flat, despite in reality being 3D. Other medical images, such as MRI scans used to identify tumours, have also been the subject of the successful application of digital image segmentation techniques. However, these are not reviewed here as the techniques employed for such problems are fundamentally different. This is because the key challenge is normally locating the precise boundary location for a single object in the presence of noise, rather than locating obscure boundaries between a large number of clustered objects.

4.2.3.1 Watershed Transform

An extremely popular method for segmenting images is the Watershed Transform, defined by Beucher and Lantuéjoul in their seminal work [27]. This transform takes a topographic function representing an image and returns a set of catchment basins, representing each object, and watershed lines, representing the boundaries between them. This is achieved by flooding the topographic function from all local minima and marking boundaries where these floods meet, and the area contained by these floods as a catchment basin. More detail on this was provided in Chapter 3. This transform is

extremely well suited to segmenting clusters of touching objects as it considers the entire topographic function, i.e. the complete image, to produce the segmentation rather than studying each region in turn, as is seen in some other approaches. This means that the properties of both regions help guide the Watershed Transform towards the location of the boundary between them. The additional information this provides is extremely useful when the presence of multiple touching objects is apparent but the boundary between them is unclear. The weakness of this algorithm is that it is prone to over-segmentation, where the image is segmented into more regions than exist in reality. This is because creating an accurate topographic function, where each local minimum represents each unique object in the image, is a difficult task. Normally the gradient function is used, however an excess of local minima can exist due to noise, which often causes the over-segmentation problem. As a result, this transform is still a subject of recent research, with innovation typically coming from methods aimed at reducing over-segmentation.

A common approach to reducing the over-segmentation problems encountered in the Watershed Transform is to modify the input to the Watershed by a pre-defined set of markers, indicating the location of each object, illustrated in Figure 4.8.

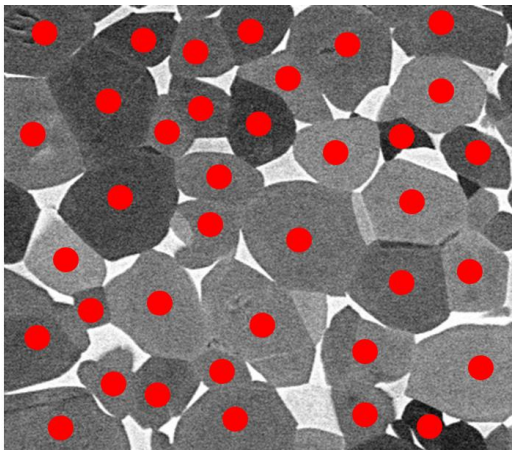

Figure 4.8: Example of a suitable set of markers

A marker is a set of pixels sharing a common label which are, in the ideal case, completely contained within each single object in the image. First proposed by Beucher and Meyer [72], the idea is that rather than flooding the topographic function from all local minima to instead flood exclusively from each marker. Provided that a

single, unique marker is provided for each object then the over-segmentation problem can be eliminated as there may only exist one single region in the resulting segmentation for each object in the original data. The only potential error that would remain is the misplacing of the boundary between these objects, which is less of a concern than over-segmentation as accurately placing boundaries between objects is an inherent strength of the Watershed Transform. However, this solution has some shortcomings, mainly that finding an automated method of computing these markers is often difficult. In-fact it can be argued that marker-based segmentation methods simply take the difficult normally associated with the segmentation of images and move this difficulty to the marker computation stage. Much of the research into image segmentation discussed in this section will therefore cover the computation of these markers.

Beucher and Meyer [5] apply a Watershed Transform using markers to segment images of coffee beans. These beans are normally elliptic in shape, although some variation can occur, and are clustered together in a similar way to grains in globular titanium microstructures. Only small intensity changes can be observed between grains, though the difference between foreground and background is clearer than in titanium microstructural images. To create a suitable set of markers, thresholding is used to create a binary representation of the image and the distance transform is then applied to the result. Assuming objects in the image are approximately globular in shape, local maxima will exist at the centre of objects. This technique appears to be useful for slightly overlapping objects, as a concavity in the foreground region would produce a local minimum at the boundary between the objects, leading to a maximum in each object. As the watershed transform floods from local minima, the result is inverted so each object is marked by a local minimum. However, noise or uneven boundary shapes in the binary image could cause excess local maxima to exist in the distance transform that do not uniquely correspond to a single object. This would also not separate clusters of objects when that cluster appears elliptical after binarization.

Li *et al.* [73] presents an alternative Watershed Transform based segmentation algorithm for the segmentation of remote sensing images. Markers are computed by thresholding the gradient image. The threshold is computed locally using a novel algorithm in which the image is filtered, and a threshold is set so as to leave a certain

percentage of pixels in the binary image. This requires a threshold parameter to be chosen experimentally. Markers are then modified by two post processing steps. First markers below a certain size threshold are removed before edge information is then used to split markers. This was achieved by setting all detected edge locations in the original image to "0" in the marker image. The issue with applying size constraints or similar criteria to modify the set of markers is that the markers are only required to fit within an object. Therefore, correct markers do not necessarily always match a specific set of properties. For example, smaller markers do not always correspond to smaller objects. This suggests that that putting constraints on the final segmented regions to a certain shape and size will be more reliable than trying to constrain markers in the same way, i.e. this type of application domain knowledge should be incorporated as a post-processing step to the initial segmentation rather than a pre-processing step. The addition of edge information to the intensity information, however, does appear likely to help extract the maximum amount of data possible from image with which to build markers. However, the way this is done appears problematic for the work in this thesis. Splitting markers by edge information only works if a complete boundary can be located, which is often not the case for images in the titanium dataset.

Several techniques for computing markers using mathematical morphology are proposed. Willingham [74] recently proposed techniques for segmenting objects in uranium images using a marker-controlled Watershed Transform. The markers are produced by thresholding the image and then eroding the image by a SE of a particular size. However, the use of a fixed sized of SE meant that this could only mark objects where the overlap between adjacent objects is minimal and object size is relatively consistent. This problem had previously been encountered and resolved, for a different image data, by Martinez *et al.* [75] who marked binary images by eroding them by incrementally larger SEs of similar shape to the objects in the image. Given only a small amount of overlap between adjacent objects the erosion would eventually separate the objects leaving a small region at approximately the centre of each object. However, when the extent of this overlap was larger in certain cases, or when object shape varied, a simple erosion by a single shape and size may not work, as there may exist no single SE for which the erosion by this SE would split all objects, without also filtering some out completely. Martinez proposed instead detecting false markers by

using morphological openings at multiple orientations to filter out elongated shapes, and therefore did not match the globular shape expect in the data. A directional erosion, perpendicular to the orientation at which the false elongated marker was detected, was then used to split the regions. However, there are a significant number of potential complications with this procedure that were not considered. These include determining the appropriate direction and size to test for false boundaries and then correctly selecting the SE to be used for the erosion intended to split markers without removing them. Specific selection of these parameters would have a large effect on segmentation accuracy. This technique is also unlikely to work if clusters of more than two touching grains exist. Therefore, it is highly unlikely such methods could be applied the dataset considered in this thesis.

The ultimate opening provides an alternative morphological approach for computing sets of markers to be used for segmentation [76]–[78]. Based on the concept of numerical residues first introduced by Beucher [79], the ultimate opening is performed by repeated morphological openings by SEs of increasing size. After each opening, the residue, the difference between the newly eroded and previously eroded image, is recorded. Once the entire image is eroded, such that all data in the image is removed, the maximum residue at each location in the image and size of opening to produce that residue is computed and stored. Research by Outal *et al.* [76] shows that the ultimate opening can be used to create markers for the Watershed Transform that can accurately segment images of fragmented rocks. The markers are produced by taking the matrix of opening sizes and eroding it by a SE proportional to those opening sizes. The purpose of this is to make opened areas fit within individual objects and not overlap the boundaries. The images used are greyscale, and the fragments of rocks are extremely clustered and vary in size, all of which is similar to microstructural images. However, while grains in microstructures are ostensibly flat (of consistent intensity), apart from Gaussian noise variations, there is a visible 3D property to the rock images with closer rock faces brighter due to reflecting more light. Experimental efforts at marking grains within Ti-6Al-4V microstructural images using this approach only provided acceptable results in simple microstructures, as described in Chapter 8.

Marcotegui *et al.* [78] discussed the use of the ultimate opening on biomedical images of cells, which have greater similarity to microstructural images. Results are presented

which suggest that this technique is very effective when cells are noisy and hard to distinguish from the surrounding background, however, issues with overlapping cells are noted. This is potentially problematic when dealing with microstructural data. In the same article, Marcotegui extends the ultimate opening to include shape information through a technique called the Ultimate Attribute Opening (UAO). The UAO considers a greyscale image as a 3D set of stacked binary images such that if the intensity of a given pixel is 100 then that pixel is "1" in the first 100 stacked binary images and "0" afterwards. An attribute opening is then used to remove the objects from each binary image based on some attribute. In this case a shape constraint is defined for this task. The maximum residue is, therefore, produced by a region that meets this shape criterion rather than matches the size of a SE. This allows the UAO to identify more complex objects such as the façade of buildings and also shows improved results for images of cells. However, doing so required the analysis of 1200 cells to define the properties of cells accurately enough for a precise shape constraint for the UAO to be obtained. Microstructural images often contain around 50-70 grains per image, meaning a large amount of data is potentially needed to train this technique. For the cell images presented, circularity is used seen as the principal attribute, with the consistency of cell size allowing identification to be constrained to a range of 95 pixels in each dimension. Grains in microstructures are less consistent which would make such a criterion difficult to define and would likely require additional training for different microstructures.

4.2.3.2 Active Contour Models

An alternative segmentation approach is the use of Active Contour Models, which can be used to segment objects of various morphologies, from noisy image data, in various applications[80]–[82]. Conceptually, these models segment regions by defining an initial boundary at some image location and deforming it until it matches the boundary of the target object. This deformation is controlled through energy functions and stopping criteria. A key feature of these techniques is that both intensity and shape information can be combined in the energy functions. Kass *et al.* [51], introduced an effective method of deforming such a contour called snakes. In a snake the initial contour is given an energy function consisting of energy from two sources, an external energy and internal energy. The contour is deformed by considering each of these

energies as separate forces which will cause the contour to deform until these forces become balanced. The internal force is typically based on the curvature of the contour while the external force is based on features such as the gradient of the image. The stopping function should be constructed so that a significantly large gradient at the boundary of the object will stop the internal force from the contour. The contour would typically be able to deform slightly in the gaps between known boundary locations, but ideally the internal force should halt this deformation when it would cause an unexpected object shape. The intrinsic benefit of such method is the flexibility of different criteria that can be built into the energy function, allowing a bespoke method to be designed for different segmentation challenges. As with the Watershed Transform, issues can occur due to noise and often it is important to start the initial boundary as close to the true boundary as possible. This is similar to the process of marking objects previously discuss with the exception that 1 marker per object is not sufficient to guarantee accurate segmentation and instead the distance between the marker and the boundary also matters. Another downside to this approach is that each contour is deformed independently so information from adjacent objects is generally not used, while The Watershed Transform can exploit this information effectively.

4.2.3.3 Split-and-Merge

Some authors attempt to segment images using a split-and-merge methodology [83]–[85]. The idea is to over-segment an image such that features of interest in an image may be split into multiple regions, but each region would contain more information than a single pixel. These regions are then merged based on pre-defined rules to form larger segments that, if performed correctly, correspond to the features of interest. In order for a spit-and-merge approach to be successful, the set of regions formed by the initial over-segmentation must between them capture all boundaries required for the final segmentation. This is similar to methods based on representing an image as a set of Superpixels [86]. Superpixels are regions formed by a segmentation of an image such that these regions are homogeneous, made of a single connection partition, adhere to object boundaries and are regular [87]. The difference for a split-and-merge approach is that the regularity is not important, however, the homogeneity and adherence to object boundaries is crucial. Any grain boundary that is not a region boundary cannot possibly be in the set of segmentation boundaries after merging.

Machairas *et al.* [87] show that good superpixels can be created using the Watershed Transform, so it is likely such segmentation algorithms will form a good starting point for a split-and-merge approach. This is confirmed by Krupka *et al.* [85] who uses this approach in the segmentation of grains of sedimentary rock in SEM images. An over-segmented result is produced by the Watershed Algorithm with the boundary between each segmented region evaluated by the average of the gradient magnitude along that boundary in the direction perpendicular to that of the boundary. However, the extreme level of over-segmentation means that multiple different results are possible depending on from which region the merging process started from. This means it is then necessary to evaluate each possible merged region to find those that most likely fit the properties of a grain. This latter idea is very useful, as it allows the integration of expert knowledge into the system. However, evaluating so many possible merges is problematic. Krupka's images contain only 1 grain, which, while complex and difficult to segment from the rest of the image, would give far fewer regions than the titanium images in this study. It would, therefore, be valuable to obtain a far more accurate initial segmentation before user a merging function incorporating expert knowledge.

4.2.3.4 Machine learning

The use of machine learning approaches has become prominent in a wide variety of engineering applications [71] and its popularity and usefulness makes it essential to consider in this review. While more traditional approaches require a skilled engineer to develop a hand-crafted set of rules for performing a task, machine learning techniques instead use software algorithms develop the analysis method. This has historically been achieved through the use of artificial neural networks (abbreviated to either ANNs or NNs) which attempt to mimic the structure of the human brain. Inputs are passed through a network of nodes, connected by branches that perform a function on the data. The nodes then pass data through other hidden layers of nodes with each node receiving a value that is a weighted input from the previous layer. Traditionally, there would be 1-3 hidden layers in this system between the input and output. Annotated data is used to train the network by comparing the output with the expected output and adjusting the weights associated with each branch in the network accordingly. This is repeated for a large dataset ideally until the correct output is reached for new data without further adjustment. In recent years, the use of a subset

of machine learning technique known as deep learning has become particularly prominent in image processing challenges including feature recognition and segmentation [88]. Deep learning has many more hidden layers than previous NNs and, therefore, can understand the content of data, such as images, at a higher level of abstraction. This makes deep learning particularly useful for semantic segmentation, where an image is segmented into regions of different classes. In the field of materials science this type of class-based segmentation would mean separating phases of material but not necessarily separating individual grains.

Machine learning approaches are applied to materials science by Alberquerque *et al.* [89] to segment and measure the volume fraction of pearlite and graphite in microstructural images of cast irons. This is similar to the phase separation task in the microstructures in this study and only measurements of volume fraction are reported. The datasets are relatively simple with a clear intensity difference distinguishing pearlite and graphite in most cases. This suggests that separation of alpha and beta phase is possible but not necessarily globular grains from platelets. A more recent study by DeCost *et al.* [90] uses a dataset of more complex ultrahigh carbon steel microstructures. For these microstructures intensity alone would not distinguish between the different phases, and some understanding of the meaning of textural differences between regions is necessary. Deep learning techniques are developed and were found to be effective at separating cementide particles from a speroidized matrix, which again is similar to the phase separation task. However, the use of textural information suggests that this time globular grains and platelets may be separable. The technique was also shown to allow for measurements of more properties, such as particle size. However, this was only possible as each particle did not have an adjoining boundary with other particles in the image. Therefore, DeCost's method would not appear able to separate and measure the individual grains and platelets in Ti-6Al-4V microstructures. While the separation of phases of material was complex in DeCost's dataset, it has already been shown in Section 4.1 that simpler methods can achieve this in titanium microstructures and that and the key challenge lies in the segmentation of touching grains, which DeCost does not address. Another recent method by Konovalenko *et al.* [91] used a machine learning approach to analyse the rupture surface on images of titanium alloys. The network is trained to classify each pixel as

either an edge or a dimple, the dimple being the feature to be measured. However, as with other machine learning methods the success of this is dependent on the fact that edges pixels and non-edge pixels have some homogeneous property that allow them to be assigned to a different class. This does not appear to be the case for the majority of edge pixels in the titanium datasets when there is a large number of globular grains. As described in Section 3.2, pixels at the boundary between alpha grains often have similar intensity and variance as those within the grains.

Other than the methods cited, however, there is little evidence of machine or deep learning being using for image analysis in materials science. A recent review by Dimiduk addresses exactly this topic [71]. They found that while approaches such as deep learning have been widely adopted, to great benefit, in other fields, materials science has relatively little published research in this area. Medical imaging is again better researched in this regard. Litjens *et al.* [92] present a review of 300 articles applying deep learning in this area, with most being from 2016 onwards. Image segmentation was the most popular application in the study with over 80 of the articles dedicated to this task, with pathology and microscopy images being the most popular. These are cases which often produce images that are similar to those found in the Ti-6Al-4V microstructures so suggests there are opportunities to apply such methods. However, with so little research in applying deep learning to materials science, and none to a Ti-6Al-4V microstructural dataset, it would be difficult to reach the standards set by the years of competitive research on large datasets seen in other fields. Dimiduk *et al.* [71] hypothesises that this absence of data is a major reason for the lack of application of deep learning in materials science. They described the microstructural data available as being wide in scope and having little depth. This is because microstructural images have great variation, even when of the same material, yet few datasets are publicly available. This is particularly problematic as a key challenge that must be overcome when deploying machine learning approaches is the need to appropriately train the network to the required dataset. This process can be time consuming as, to be able to accurately segment images, it requires manual annotation of a large number of images. Suitable datasets do not yet exist for Ti-6Al-4V. Existing research reports different numbers of training images being required for sufficient training, depending on the applications and network used. For example, Ronneberger

et al. [93] use only 30 images for training a network for segmenting image of cells and still achieve reasonable results. Meanwhile, Brosch *et al.* [94] use 250 out of 377 available images to train the segmentation network proposed in their work to segment images multiple sclerosis lesions. They also note that training with too small a dataset risks overfitting the network to a particular dataset. As microstructural data is extremely varied, it is likely that a larger dataset would be required for robust results than in other applications.

The number of images required for training can be reduced by refining an already trained network, rather training a completely naïve network from scratch, using techniques known as transfer learning [95]. This was used very recently by Haberl *et al.* [53] to reduce the amount of training data required to 1/5 of the amount of data required when training their network from scratch. In many fields, deep learning researchers can use established datasets that are published as challenges for researchers and a high volume of research has been conducted on the specific types of images [53], [93], [94]. This means there are many competing networks which can be used for transfer learning. This is not the case in materials science and the applicability of knowledge transferred from networks trained to data in other fields is highly uncertain.

Ultimately, the decision was made to not pursue machine learning or deep learning approaches for the work in thesis. While a clear knowledge gap exists, and great potential benefit is demonstrated in other fields, the limited research and availability of data makes applying these techniques to materials science very challenging and the chances of success uncertain. The primary goal of this thesis is to contribute a new microstructural analysis technique, that improves upon current methods. Advancing deep learning methods in materials science to this level may take both more than one project and more data than is currently available. In particular, a key goal in this project was to develop a method that was robust enough to analyse different and varied datasets and it was not feasible to gather a large set of every possible microstructure available. Therefore, other, more immediately promising approaches are instead pursued that are less likely to require re-training when applied to new data. Additionally, machine learning approaches by their nature obscure the analysis process from the user in a black box process. This would potentially make it more difficult for such methods to be adopted in the manufacturing industry as it would not be possible

to demonstrate to the source of measurements to clients, meaning they are less likely to trust these results. I believe that it is preferable, where possible, to have a clearly defined technique for performing analysis as the inner of workings of which can be peer-reviewed and investigated prior to deployment. Therefore, as the aims of this project could be met with such a conventional, clearly defined technique this approach was instead taken at the expensive of other options such as deep learning. However, as this new technology advances it is possible that deep learning methods may be able to achieve a greater level of accuracy and insight even than human operators, therefore, it is not the suggestion of this thesis that such methods be permanently ignored in this field. Instead the decision made is that, given the current state-of-the-art in automated microstructural analysis, the proposed new algorithms were a more pragmatic next step, with machine learning perhaps revisited once there is a wider range of research and datasets available for development.

4.2.3.5 Similar work from medical imaging

Among the most similar images found in other applications are those in the field of medical imaging. As image processing is applied more frequently to this area than to microstructural analysis, the following section is dedicated to reviewing this area for potentially applicable techniques. In particular images containing clustered cell nuclei show a strong similarity. These images typically show clear differences between foreground and background in the image, although foreground data is often corrupted by noise. The main similarity is that extreme amounts of clustering often exists between adjacent nuclei. This is particularly common in histopathology images, as shown in Figure 4.9.

Clustering between adjacent features of interest is known to make segmentation difficult and this challenge also exists when segmenting the microstructural images in this study. The nuclei are typically globular in shape so are likely to be most applicable to measurements of grain size.

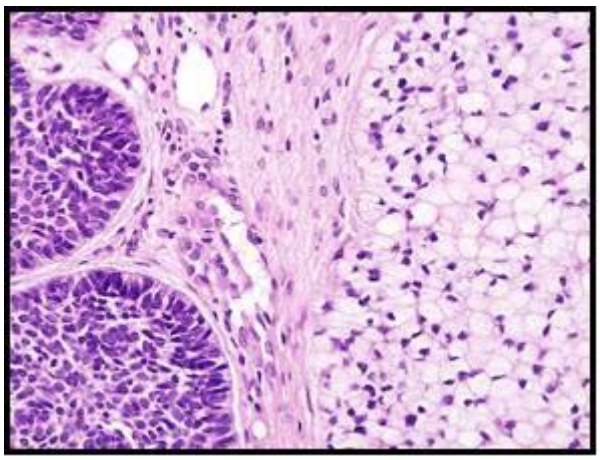

Figure 4.9: Histopathology image with similar challenges to microstructural data such as clustering of objects [96]

Cheng *et al.* [97] present a marking function to enable images of clustered nuclei in medical images to be segmented using the Watershed Transform. As with previous work by Beucher and Meyer [5], the markers are produced by thresholding the image and then applying the distance transform. Ordinarily it is expected that noise will lead to an excess of local maxima in this transform. Cheng *et al.* proposes a solution to resolve this issue by using the h-minima transform [2]. This transform supresses all local minima below a given height threshold. The assumption is that local minima in the distance transform, produced by minor boundary deformation or noise, is likely to be far shallower than minima at the true centre of objects. If an appropriate threshold is selected, the h-minima transform will supress irrelevant minima caused by noise so that only the most significant minima in the distance transform remain. If the aforementioned assumption is correct, the remaining minima are more likely to correspond to the centre of objects, and not to noise. Achieving accurate results via this method requires the selection of a suitable threshold of minima to supress. The feasibility of computing such a threshold depends on the difference in magnitude between minima representing markers and minima representing arbitrary noise or deformation. In this case this threshold was computed by running applying the h-minima transform with incrementally increasing thresholds until markers begin to merge. The largest threshold value for which markers do not merge is used for the entire image. This appears to perform well on the cell nuclei data it was tested on,

though the use of a global threshold means the accuracy of this approach depends on cells being of a similar size.

Jung *et al.* [98] also proposed a Watershed Transform, with markers based on h-minima, for the segmentation of nuclei in cervical and breast cell images. A segmentation distortion evaluation function is proposed to find an optimal h-minima threshold. This function fits a set of ellipses to the foreground regions to be segmented and grades segmentation results based on how closely segmentation results fit this model. This function will therefore only give a good assessment of segmentation accuracy when objects are elliptical, and a significant amount of the grain boundary is known prior to segmentation. To produce the final result, segmentation is performed multiple times with markers computed by different thresholds of h-minima transform. Each result is then evaluated using the distortion evaluation function with the h-minima value producing the highest output from this function taken as the optimal threshold. While the reported results are successful, repeated segmentation is time consuming. A contour parameterization method was also proposed to improve the accuracy of each detected nuclei boundary. The Watershed Transform will normally create a straight boundary between touching objects. However, in reality the nuclei typically do not have this boundary, and this only appears so as nuclei in fact overlap, which is difficult to see in a 2D image. The contour parameterisation uses known boundaries to fit an ellipse to give a more accurate representation of the true boundaries of the nuclei. While touching grains in microstructural images are also sometimes overlapping in this way the shape is less consistent, so it not known when grains are overlapping or merely touching, or if more accurate grain boundaries can be estimated using this approach. Due to the relatively small impact on grain size measurements this is likely to have, it is also unlikely that this is necessary in order to match the measurements produced by current manual methods. Therefore, this thesis will work on the assumption than on a 2D image grains should be measured as they appear from that perspective and not make assumptions about the 3D shape, as outlined in Chapter 1.

An alternative adaptive h-minima suppression technique to automatically select the threshold is presented by Yuan *et al.* [99]. Although not for medical images it is included in this section due to the similarity of the underlying technique. Unlike Jung's

work [98] a different threshold is computed for each local region, rather than for the entire image. This is useful in images where large size differences exist between objects, as local minima that are irrelevant in a large grain may be significant to smaller grains. This type of localised approach would be advantageous in microstructural images where it is necessary to segment grains of significantly different size. However, as this method is presented for the segmentation of natural images, that do not resemble those in the titanium dataset or the biomedical images in this section of the report, it is unknown how applicable such a method would be. In particular, it seems unlikely to work when large and small grains are adjacent, which occurs in microstructural data. A hybrid gradient scheme is also proposed to improve the Watershed Transform by improving the relevance of the topographic function to the image content. While the idea of modifying the basic gradient function to provide a more relevant topographic function to input into Watershed Transform is interesting, this article achieves this using colour information, which is not available in any useful form in the microstructural dataset studied in this thesis. Different techniques would be required to obtain suitable information if the topographic function was to be modified in the case of microstructural analysis.

Zhang *et al.* [100] propose algorithms for segmenting X-ray images using the Watershed Transform and region merging. Markers were produced by thresholding the gradient image, with low gradients indicating areas likely to be within a single region. Equations are provided for selecting a suitable threshold value automatically. As large variations in pixel intensity can occur due to noise, an excess of markers is created, causing over-segmentation. This is resolved by using region merging to identify over-segmented regions and re-join regions where the mean grey value within adjacent regions are similar. While more sophisticated marker computation techniques are seen in other segmentation algorithms, the idea of merging grains based on mean intensity is interesting to titanium image segmentation. Noise often obscures the boundary between adjacent grains, however, it is not uncommon for these same grains to present with different mean intensities. This approach could, therefore, be useful to solve over-segmentation errors provided the initial segmentation found regions large enough for the mean intensity to be a good statistical representation of the intensity of its parent grain. As adjacent grains can have similar intensities it is likely that the

merging criteria will need to be more specific than in Zhang's work and use additional information other than intensity when deciding which regions should merge.

More recently, Konyuncu *et al.* [101] also proposed methods based on the Watershed Transform for images of clustered nuclei. However, while previous authors achieve this by using image gradient as the topographic function and the maxima of the distance map as the markers, Konyuncu's method reverses this paradigm. The key difference this makes is that each grain is marked where bright spots in the image occur and boundaries are placed on the location of maximum concavity between objects, not where the intensity change is greatest. The more popular approach is to use the concavities to identify different grains and intensity changes to place boundaries between them. Due to noise, h-minima suppression again had to be applied to the gradient map when computing markers. However, the authors found that, due to brightness differences between nuclei, some objects were only marked by specific h-minima thresholds and not others. Crucially there was no ideal value where all nuclei where marked. This was the case even over a local area, as bright nuclei could exist next to dark ones in the dataset. Therefore, the previously discussed h-minima suppression methods are not as effective when markers come from the gradient map. To solve this problem multiple marker sets are produced by incrementally increasing the h-minima threshold. For each new marker set, only markers that do not intersect the location of any existing markers are added to the combined marker set. This allows new markers to be added without allowing existing markers to expand and merge together, potentially creating under-segmentation issues.

The prevalence of h-minima suppression in this field is quite obvious and it seems to be highly effective at preventing over-segmentation. However, this does so only by supressing the extracted information, when using the distance transform or gradient function to find these markers, and thus reducing excess of markers often produced. The properties of microstructural images mean that neither function may be able to detect all the grains in the image, so such suppression on its own would not be enough to gain sufficient markers. It is, therefore, also necessary to also study other methods to extracting information.

Al-Kofahi *et al.* [44] studies the use of Laplacian of Gaussian (LoG) filters for marking extremely clustered cell nuclei. Laplacian filters are derivative filters used to find areas of rapid change. A LoG combines this with a Gaussian filter so this change is detected on a smoother, less noise corrupted, the image. Although both these operations are formalised into a single filter in the following literature it should be noted that the response of the filter is a measure of the gradient magnitude of Gaussian filtered image. Therefore, the minima in this output can be used as a marker as previously described. The area over which the Gaussian filter is applied relative to the resolution of the image has a significant effect on the output of the LoG. This is known as the scale. In the work of Lindeberg *et al.* [102] this scale is computed via an automated method. Al-Kofahi instead attempts a multi-scale approach, by using different sizes of Gaussian filters and combining the markers produced for a range of differently filtered images. However, it is found that even mutli-scale approaches do not give adequate markers in the case of such clustered nuclei in noisy images. To resolve this a Euclidean distance map of a binary representation of the image is used to constrain the LoG filtered results so that minima from two adjacent grains cannot merge into a single marker while there exists a maximum in the distance map between them. This means that edge and Gaussian maps are combined, i.e. shape and intensity information, are combined when computing markers. The strong results achieved indicated the benefit of combining different sources of information at the marker computation stage.

Cosatto *et al.* [103] use the Hough Transform to aid the identification of cells in histopathology images. This transform takes an image with imperfect shapes, such as an edge detected image where there are gaps in object boundaries and attempts to identify the shapes. It does so by converting the image to a feature space and assigning values to each pixel allowing it to "vote" on whether or not the feature being searched for exists or not. To identify cells, an edge map of the image is first generated before a Hough Transform is then used where the output for each pixel is the accumulation of directly opposed intensities in the edge map at multiple angles. The transformed image would have peaks at the centres of regions enclosed by boundaries identifiable on an edge map. Active contour methods, specifically Snakes, are then applied, starting at these peaks and stopping at low energy outlines which represent nuclei boundaries. Uppada *et al.* [104] also uses the Hough Transform in the analysis of histopathology

images. However, rather than using active contour methods the Watershed Transform is then applied with the Hough Transform being used to generate markers, in a similar way as described in [103]. Both methods require suitable pre-processing to produce an edge detected image to which the transform can applied. It is logical that the more edge information that exists the more likely it is for such approaches to be successful. As the response of the Hough Transform is dependent on the expected shape of the object, it also follows that more consistently shaped objects will achieve better results. It is believed that the variation in the visibility of contours and shape of objects is one of the biggest differences between microstructural data and histopathology images. Therefore, such methods have a lower probability of success for the dataset in this thesis.

Qi *et al.* [105] use active contour methods for segmenting histopathology images. Instead of the Hough Transform, a novel marking scheme is proposed to mark nuclei using a mean-shift-based single-pass voting system. For each pixel a 2D triangular cone shaped voting area is defined using the direction of negative gradient at that pixel and a predetermined radius, determined by the expected diameter of image objects. A shifted Gaussian kernel is used such that its mean is the centre of the voting area and the kernel is orientated along the voting direction. The value returned by the voting system for each pixel is the convolution of the gradient and Gaussian kernel for each pixel in the image. The proposed technique is demonstrated to be good at dealing with overlapping grains in histopathology images where the main challenge when computing markers is not the level of clustering but that the overlapping region is darker due to translucent nature of the cells. However, as grains in microstructural images are not translucent and are potentially more clustered than some of the examples shown in Qi's work, other approaches are more likely to be successful.

Veta *et al.* [106] also proposed a novel marking scheme for the segmentation of histopathology images, using the fast radial symmetry transform. This transform operates along direction of positive gradient looking for locations of radial symmetry. To do this the gradient orientation is first computed for every pixel studied. For a circular neighbourhood from a given pixel, the positively affected pixels and negatively affect pixels in that neighbourhood, defined as the pixels pointing towards or away from the pixel of interest, are assigned corresponding values. The sum of these

values will be high in areas where the gradient points towards the affected pixel. This will identify bright radially symmetric regions, which can then be marked. Clearly the gradient within an object does not inherently point to its centre in most images, for this reason a Gaussian kernel is included in the algorithm which blurs the boundary of the object inwards to create this effect. The size of Gaussian kernel and circular neighbourhood studied are usually kept to the same value and are critical to the success of marker computation. The gradient magnitude can also be included in the calculation, but it was found that it is most beneficial to just use orientation values unless studying images where only objects of a certain contrast are of interest.

4.3 Summary of knowledge Gaps

This review has identified limitations in existing methods of microstructural analysis where new methods could provide impactful improvements.

For many microstructural features, including the critical property of alpha grain size, no acceptable automated measurement procedure was found in this review. This means that manual methods are often used, which are inherently labour intensive and open to human error and subjectivity. In addition, evidence is provided indicating these methods are slow to implement and achieve relatively poor repeatability [29], [31]. A fully automated image processing technique, capable of measuring microstructural features to a similar level of accuracy as an expert materials scientist can achieve using manual methods, would solve the problem of repeatability and human error. There is also a good chance such methods would also be faster, with some of the existing applications presented achieving accurate measurements in seconds on relatively similar datasets. Microstructural features for which automated methods already exist often have problems with the robustness [11], [63], which are described in Section 4.1, and would not work for every microstructure in the dataset used in this study. Only the volume fraction of alpha phase is sufficiently, reliably measured in existing literature.

There is great scope to add to this knowledge through the development of new image processing techniques. In the latter section of this review, many image analysis methods are presented that have successfully automated measurements of objects in similar data. Most of the methods presented in this section have no documented trial of their use on microstructural images so it is largely unknown how effective such

procedures could be. However, each method reviewed had some difference between the dataset used in its validation and the microstructural data of this study. Therefore, it seems likely that the direct application of these techniques will not yield ideal results, particularly given the variations that can exist in microstructural data. Experimental trials on several existing procedures [5], [44], [76], presented in Chapter 8, support this hypothesis. Instead the methods reviewed were used primarily to guide the development of the novel algorithms proposed in this thesis.

Several of the image processing techniques described in this review demonstrate good results in datasets similar to the titanium image datasets used in this study. Although no single technique appears to be capable of measuring all features expected in microstructural images, measurements similar to those of some of the properties to be measured are obtained through separate methods. However, the difference in the data these techniques are applied to mean these methods are unlikely to give accurate and reliable results in the titanium dataset in their current form. Techniques based on image segmentation can measure a wide range of properties and can provide statistical data both per image object and per unit area. A segmentation approach is, therefore, preferable, however, appears to not be practical in all cases. Most of segmentation methods, used for segmenting individual features in images, found in this review have been applied to segment objects that are globular in shape. In Ti-6Al-4V alloys it is common for elongated grains to align in parallel clusters, which often makes their segmentation more challenging as any overlap between similarly orientated elongated objects, of the same intensity, results in only a small amount of boundary deformation where the two objects meet. In images with very thin features, segmentation is often even more challenging as the resolution is not high enough to obtain precise information about the shape of object boundaries. Good delineation of these boundaries is a key factor in many segmentation algorithms, therefore, attempts to segment each platelet is more likely to lead to errors than for globular grains. Illustrations of these challenges are shown in Figure 4.10.

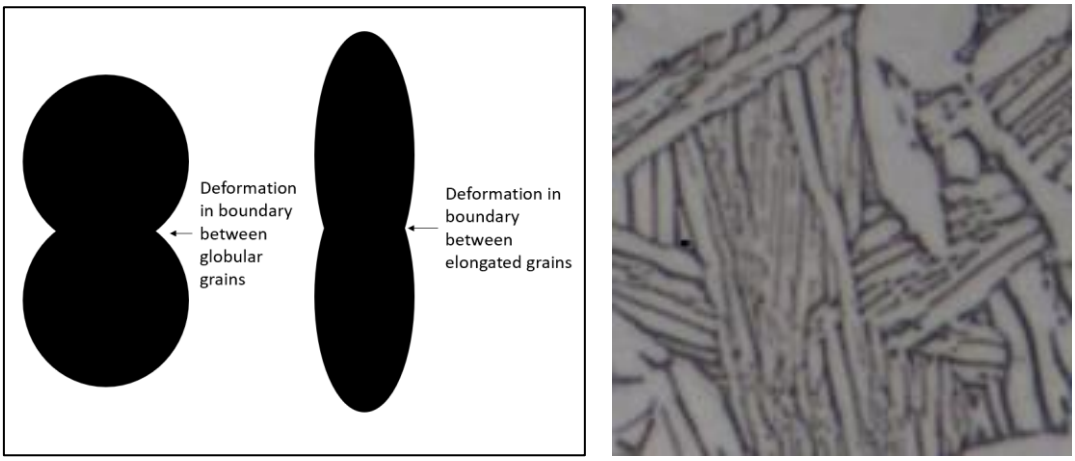

a) b)

Figure 4.10: Examples of properties of images of elongated structures that result in challenging segmentation where a) overlap between globular and elongated grains and corresponding boundary deformation differences and b) very fine platelets where resolution is challenging

Image segmentation would, therefore, seem well suited to the analysis of globular alpha grains but less so for elongated platelets. Techniques for measuring the image directly, without segmentation, have shown success in numerous cases where elongated structures are to be measured. Therefore, it is likely that separate techniques based on these methods are more likely to successfully measure alpha platelets. However, in existing algorithms, it is common for these methods to only measure a certain property of an image feature being investigated, such as size, shape and orientation, rather than measuring all features. Additionally, the techniques presented are known to fail in certain cases and may not be robust enough for the most complex images. Segmentation methods generally fail when objects of similar intensity are touching in noisy images and direct measurements often fail when the shape and size of objects are not at least somewhat predictable. Overall, while many promising approaches have been identified, novel algorithms are required to address limitations of existing methods in order to obtain accurate measurements of titanium data.

In this thesis two separate methods are proposed, one to measure globular grains through segmentation, in Chapter 5, and one to measure elongated platelet properties, in Chapter 6. The methods will primarily aim to address shortcomings in the

microstructural analysis process described in the former section of this review. In doing so, these chapters also introduce and present new image processing techniques to improve upon the state-of-the-art methods identified in the image processing literature.

5 SEGMENTATION OF GLOBULAR ALPHA GRAINS

In this chapter, a new segmentation method is proposed to identify individual globular alpha grains and facilitate accurate, automated measured of grain size and volume fraction. Reliable automated methods to compute these properties of Ti-6Al-4V microstructures was not found in existing literature. We call this algorithm the Clustered Grain Segmentation Algorithm (CGSA) as, unlike methods found in existing literature, it is specifically designed to be effective at segmenting clusters of touching grains, based on a-priori knowledge of common properties of microstructural data. The technique is based upon the widely used Watershed Transform, as this is known to be particularly effective at segmenting touching objects. However, existing methods to apply this transform are likely to result in significant segmentation errors, due to a failure to sufficiently address over-segmentation problems in an appropriate manner for the titanium dataset. Over-segmentation is common in the Watershed Transform, and the complexities of titanium microstructural images increase the extent of this issue. The CGSA addresses this by using novel pre- and post- processing techniques to improve the segmentation accuracy of the Marker Based Watershed Transform (MBWT), a flowchart of the steps in this algorithm is provided in Figure 5.2. This includes a new marker computation technique that we call Clustered Grain Marking (CGM) that is well suited for identifying individual grains within clusters of adjoining grains. The proposed technique builds these markers based on features common to grains in all microstructural data encountered in this study, not just a particular type of image, and plays a key role in reducing over-segmentation in a robust and reliable way. Suitable filtering techniques for de-noising different microstructural data are also described. Additionally, the Hit-or-Miss Transform is introduced as an optional pre-processing step to identify and remove artefacts caused by improper material preparation prior to imaging. A new merging procedure is also presented which

incorporates prior knowledge of the microstructural dataset to reduce over-segmentation errors, as well as a new splitting function to reduce errors caused by under-segmentation. Validation of the accuracy of the new algorithm, both for microstructural measurements and segmentation accuracy, is provided in Chapter 8.

This chapter begins by first assessing the microstructural images used in this study and sets out the key challenges encountered when segmenting these images using the Watershed Transform. A general description of the new segmentation algorithm is then proposed with the remainder of the chapter describing each pre- and post- processing step that is used to improve segmentation accuracy.

Most of the work in chapter is published in an article in the Journal of Materials and Design [6].

5.1 The segmentation challenges associated with Ti-6Al-4V microstructures

Microstructural images have a series of inherent properties that make analysis difficult for both automated and manual techniques. The technique in this chapter segments the image prior to taking measurements, therefore, the accuracy of these measurements is dependent on the ability of the proposed methods to identify the boundaries between microstructural features. In two-phase microstructures, the different phases of material often present as light or dark regions making the boundaries between phases easy to delineate, as can be seen in Figure 5.1. However, the boundaries between grains of the same phase are typically more difficult to distinguish. This difficulty varies based on the microscopy technology used to capture an image of the microstructure. A Scanning Electron Microscope (SEM) can measure the topography and chemical characteristics of a sample so it can produce high contrast images. In these images, adjacent grains often differ in intensity even when they are of the same phase. Optical Microscopes (OMs) are based only on the physical appearance of grains so provide lower contrast images. As a result, adjacent grains of a single phase are usually the same intensity throughout. In some cases, a boundary between adjacent grains of the same phase can still be seen in optical images although this occurs less frequently than in images produced using a SEM. Figure 5.1 shows clusters of equiaxed alpha grains of Ti-6Al-4V from images produced using a SEM and OM respectively.

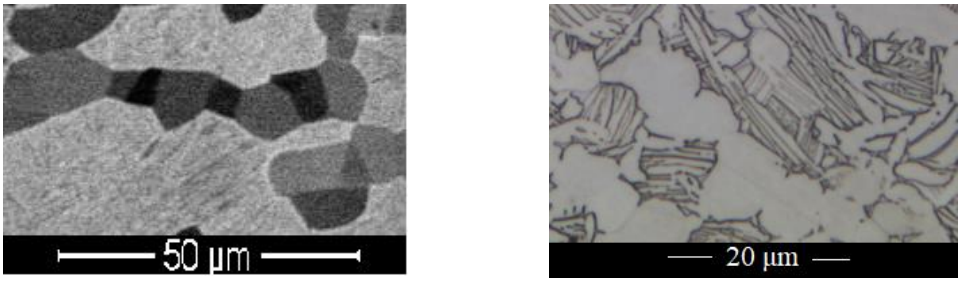

a) b)

Figure 5.1: Images from SEM and OM technologies illustrating grain boundary delineation and noise where a) is a cluster of alpha grains in an SEM images and b) is a similar cluster in an Optical image

Studying the gradient of an image will clearly reveal the location of at least some grain boundaries, in both images. From Figure 5.1 it is clear that in an SEM image, a greater number of boundaries between touching alpha grains may be found in this way, however, the trade-off for this additional intensity information is noise. As described in the analysis of SEM technology in Chapter 3, variations in the intensity of pixels within a single grain can vary greatly. Great care must therefore be taken to distinguish variations due to noise and variations due to grain boundaries. In a Watershed Transform using the gradient as the segmentation function, this noise could produce local minima in the function which will cause over-segmentation errors unless appropriate markers are used prevent this. For the same reason, techniques based on edge detection methods may also detect a high number of "edges" within grains where no grain boundary exists.

In addition to the visible contrast changes between grains, the shape of the grain can also be used to locate boundaries. Grains are usually elliptical and normally do not feature any large concave regions. Therefore, if concavities are seen in a single phase of the material then this would indicate the presence of an overlap between two adjacent grains. These would normally by equally visible in both SEM and OM images as each phase has a clearly different intensity in either technology, result in clear boundaries between each phase. However, much like the intensity variations previously described, these concavities are also not always present so cannot be relied upon exclusively as an indicator of grain boundaries. The images in Figure 5.1

illustrates this point well. In Figure 5.1 b) the cluster of grains clearly has subtle concavities in several areas, however, in Figure 5.1 a) there is a line of touching grains where no concavity is visible.

A final property to consider is that grains of the same type often fall within a similar size range. If the mean size of globular alpha is 5μm it is very unlikely a grain of 0.5μm or 50μm would exist. Objects of 0.5μm may exist in the image but these are likely to be meaningless artefacts or secondary alpha grains, which for this thesis we do not measure. This predictability in size has both benefits and disadvantages. The benefit is that when measuring specific grain types, the worse segmentation errors could be removed by only considering those within a specified deviation of the mean. However, the downside is that size based approaches such as granulometry are less likely to be able to segment these grains.

Further difficulties can be introduced by defects in the image. Studying the microstructure of a material requires several preparation steps such as polishing the sample to remove residue and flatten the surface, and then etching it, to make grain boundaries more visible. Sample preparation is a non-trivial task and can cause scratches or other artefacts to appear in the image. While these features can be limited by good sample preparation methods, it is of benefit for the proposed method to be as robust to these variations as possible.

It is clear from the analysis of microstructural images that there are several key challenges for the segmentation procedure to overcome. A significant amount of noise is present, particularly in SEM images, which is known to cause over-segmentation in the Watershed Transform. While filtering the image to reduce noise is useful, the extent of this is limited by the desire to preserve subtle intensity changes between grains, which will often be the only indicator of grain boundaries. Therefore, extracting a suitable set of markers with which to seed the Watershed Transform is essential to ensure good segmentation accuracy. As the ideal set of markers is a single marker within every grain in the image, the marker computation method must have the ability to decide approximately where each grain exists within the image. The analysis of the images presented makes it clear that no single image feature can reliably be used for this task, therefore, a combination of intensity and shape information is required to

find suitable markers. The difficulty of this task makes segmentation errors still likely, however, the relative predictability of grain size and shape will allow many of these errors to be resolved by post-processing steps that study the shape and size of segmented regions.

5.2 Clustered Grain Segmentation Algorithm (CGSA)

A new segmentation algorithm, termed the CGSA, is proposed which aims to improve the segmentation accuracy of the Watershed Transform when applied to complex microstructural images by using several pre- and post- processing steps. This facilitates accurate and reliable automated measurement of grain size and globular volume fraction. A key factor in the design of this algorithm is the need to achieve a high level of robustness. Microstructural images vary extensively based on the thermo-mechanical history of the material, as well as the imaging methods and technology used to capture these images. Therefore, it is important that the algorithm designed is not excessively dependant on any single factor to locate grains or their boundaries and instead makes use of as much information in the data as possible. The proposed combination of pre- and post-processing steps allow the algorithm presented here to achieve this. The CGSA can detect subtle boundaries between touching grains, even in noisy images or those from less detailed optical microscopes. Two optional functions are included; a pre-processing function aimed at detecting artefacts corrupting the image data and a post-processing step aimed at fixing under-segmentation errors. These were designed and included as they resolve specific issues encountered during the segmentation of some data, however, are left options as their performance was concluded to not be advantageous in the majority of cases. The experimental reasoning behind this decision is explained in Chapter 8. A flow chart of the main steps in the segmentation algorithm, and how they relate to each other, is shown in Figure 5.2.

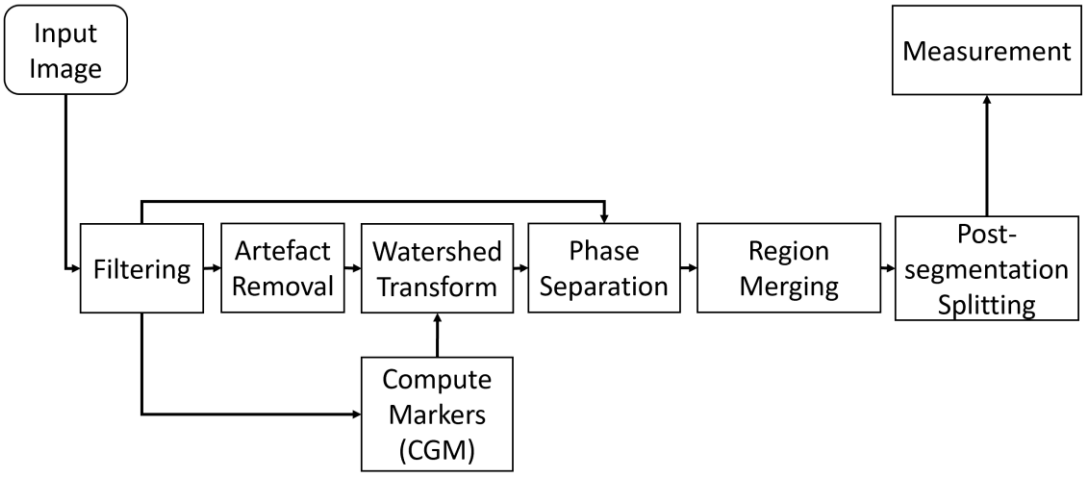

Figure 5.2: Flow chart of stages in CGSA

The algorithm requires a greyscale microstructural image as an input. Filtering procedures should be the first pre-processing step applied as the resulting reduction in noise is beneficial to subsequent steps functions. Phase separation procedures must be performed immediately after the Watershed Transform so that further splitting and merging of regions should only be applied to the alpha grains. This step should be ignored for single-phase microstructures. Merging procedures are used prior to the additional splitting function so that the splitting function operates based on the most accurate segmentation information possible. Finally, standardised measurement techniques are applied to measure the grains in the segmented image.

5.3 Pre-Processing

This section describes a range of pre- processing procedures aimed at preventing the Watershed Transform from producing segmentation errors. These methods particularly target over-segmentation, which is a known weakness of this transform. The use of filtering techniques is described, and evidence is provided as to why Gaussian filtering is considered the most appropriate for microstructural images. This includes both its effectiveness at general noise reduction and also on specific issues such as scratches. An additional artefact detection procedure is also described to limit the impact that image defects have on the segmentation result. Finally, a novel marker computation approach is proposed that is applicable to microstructural images and helps prevent over-segmentation.

5.3.1 Invert SEM Images

The techniques described in this thesis assume the convention that features of interest in an image are brighter than the rest of the image content. Optical images inherently show alpha phase as light and beta as dark so meets this criterion. However, SEM images show alpha phase as relatively dark regions. It is, therefore, necessary to invert images captured with an SEM to match this format. This is achieved by subtracting the intensity of each pixel from the maximum intensity allowed by the bit depth of the image. This is shown in Equation (5.1) where f_{SEM} is the microstructural image produced by a SEM, f is the image after inversion that will use used by the algorithm and b is the bit depth.

$$f(x,y) = 2^b - f_{SEM}(x,y) \tag{5.1}$$

5.3.2 Filtering Microstructural Data

As described in Section 3.2 the microstructural images often contain a significant amount of noise, particularly if a Scanning Electron Microscope (SEM) is used. This noise creates local minima in the gradient of image, which the proposed algorithm uses as an input for the Watershed Transform. The use of markers alone is not sufficient to completely resolve the errors this would cause as it only prevents over-segmentation errors, by marking the locations of grains. Even with markers, noise could still cause errors by fooling the Watershed Transform into positioning boundaries in the wrong location, if noise resulted in larger variations in intensity within grains than at the boundaries between them. High levels of noise could also cause errors when computing the markers using the new CGM method proposed in Section 5.3.3, as this method also considers image gradient. It is, therefore, highly beneficial to filter the input image to reduce noise prior to performing any other step in the proposed segmentation algorithm. However, this must be performed carefully and in a robust way as true grain boundaries are often indicated by subtle intensity changes and it is undesirable to lose this information.

The fundamentals of filters are described in Chapter 3. For the purposes of this section it is recalled that filters operate by assigning each pixel a value based on the value of pixels in the surrounding area, with this area determined by the size of the kernel used

for filtering. For a single grain in a titanium image it can be shown that the intensity values of pixels follow a Gaussian distribution, as in Figure 5.3.

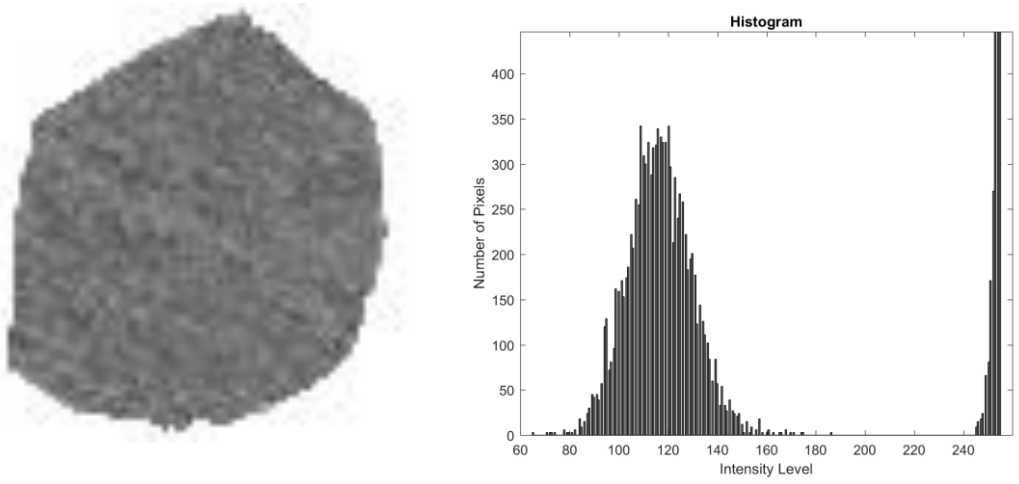

a) b)

Figure 5.3: Illustration of noise in an SEM image where a) individual grain and b) histogram of orientation values

This suggests that Gaussian filtering methods [24] would be the most effective at removing this noise. This is supported by other research into image analysis of Ti-6Al-4V microstructures, which also uses this filtering method [34].

The influence of Gaussian filtering on the identification of grain boundaries can be observed through the filtered image and corresponding gradients shown in Figure 5.4. The effects of different kernel sizes (3x3, 5x5, 9x9) of Gaussian filter are shown by applying them to an image showing 3 tightly packed grains. The grains are of similar yet slightly different intensity, have a few thin beta phase sections between them and have small artefacts on the upper leftmost grain.

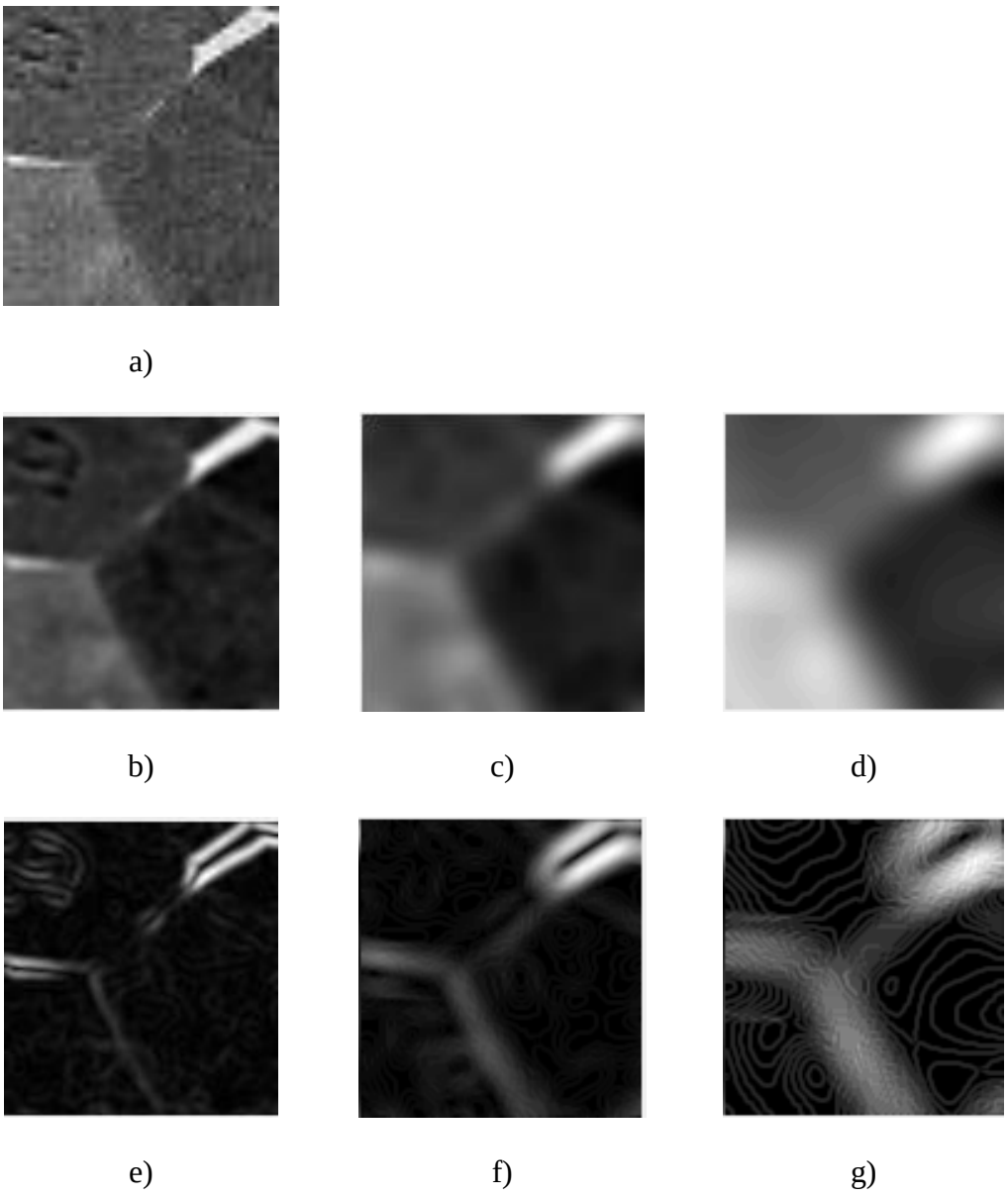

Figure 5.4: Examples of filtering of microstructural images where a) shows the original image, b),c) and d) show a filtered image and e), f) and g) show the corresponding gradient image when filtering using a Gaussian filter of size 3x3, 5x5, and 9x9 respectively

As expected, the results show Gaussian filtering to be effective at reducing noise while preserving grain boundaries, however, the blurring effect caused by this filter is also visible. As filter size gets larger the boundaries become easier to distinguish in the gradient image. An artefact, still visible in the upper left-hand corner of the 3x3 filtered image, is removed by the two larger filter sizes. However, the thin layer of beta phase

seen in the left-hand side of the 3x3 filtered image is no longer visible in the 5x5 filtered image. While the larger beta phase layer on the right-hand side does not disappear, it is clearly larger when the 9x9 filter is used. The ideal size of this filter should therefore be adjusted depending on the dataset to ensure the best results, as the data lost through distortion must be balanced against noise removal. For microscopy applications, SEM images contain more noise than optical ones so require a larger filter. For segmentation of globular grains, obscuring such thin regions due to the blurring effect would not have a significant impact on results. However, this would be unacceptable when measuring thin alpha platelets. For the Ti6Al4V microstructures in the titanium dataset, the best results were achieved using a 5x5 filter for SEM images and a 3x3 filter for optical images or images containing platelets.

As well as reducing level of Gaussian noise in microstructural images, filtering can also reduce the effect of scratches on the material surface. These scratches appear on the image as thin lines of a different intensity than the surrounding grain. Provided these scratches are thin relative to the size of kernel used by the filter then the blurring effect is actually useful as it will remove scratches from the image. An example of this benefit is illustrated in Figure 5.5. This figure shows a microstructural image with a large number of scratches and its corresponding segmentation, with the same technique, before and after the application of a Gaussian filter. While the image appears blurry after filtering, intensity changes between larger spatial features, such as grains, remain visible, while intensity changes at smaller spatial features, such as scratches, are removed. This results in fewer over-segmentation errors. The image shown in this figure is not of Ti-6Al-4V, but of the Inconel 718 alloy. While a full investigation of this alloy was outside the scope of this project, small trials where run and this result is included here as this best illustrates the effect of the filtering process, as a higher density of scratches were present than on any titanium sample in the dataset. Its inclusion also provides a small insight into the general applicability of the methods developed in this thesis.

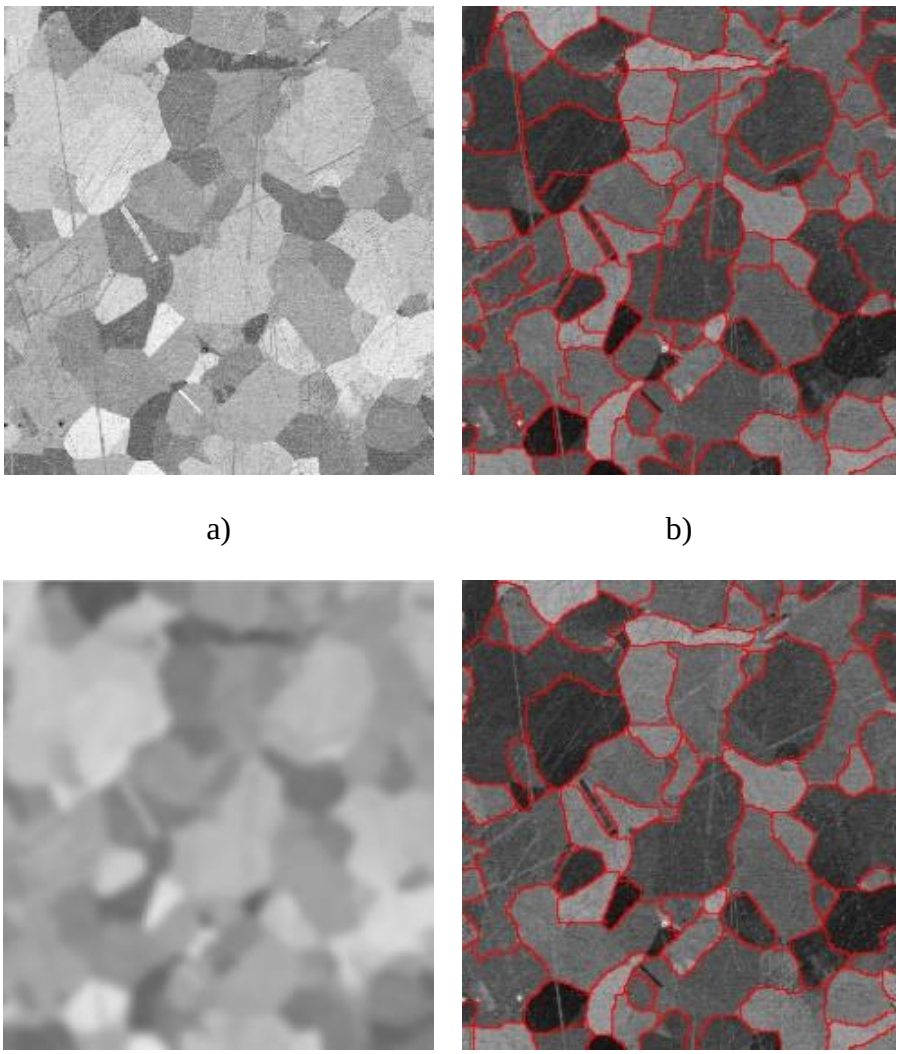

a) b)

c) d)

Figure 5.5: Influence of Gaussian filtering on scratches on images of a Inconel 718 alloy where a) unfiltered image, b) segmentation of unfiltered image, c) filtered image and d) segmentation of filtered image

5.3.3 Clustered Grain Marking (CGM)

Automatically computing a reliable set of markers for the MBWT is a difficult task. In some cases, semi-automatic procedures can get around this problem by allowing the user to manually select seed points to use as markers. However, in microstructural images containing hundreds of grains this is not a practical solution and an automated method to compute these markers is required. In the simplest case the minima of the

image can be used as markers. However, the images in this study contain significant amounts of noise, meaning it is expected that an excess of irrelevant local minima will exist within each object in the image. This means it is important to use markers computed independently from local minima in the image. The need for this set of markers is further illustrated in Figure 5.6 which compares the segmentation produced when flooding from all local minima of the gradient image with floods originating from a pre-defined set of markers, computed from existing methods [77].

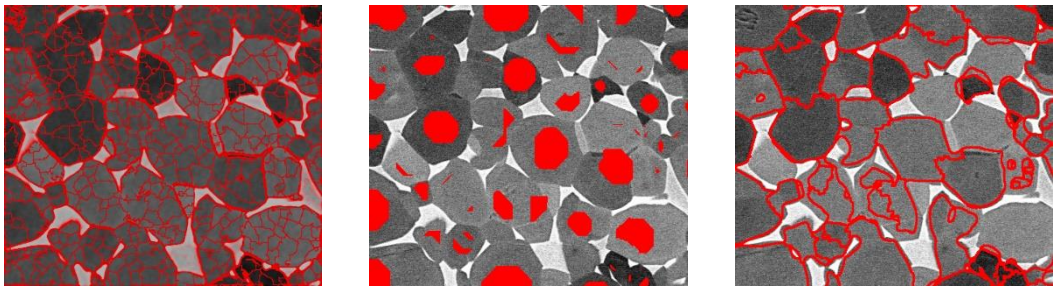

a) b) c)

Figure 5.6: Examples of Watershed Segmentation with and without markers where a) is the Watershed Segmentation based on flooding from all minima, b) is a pre-defined set of markers(from UO [77]) and c) is the Watershed Segmentation result using these markers

It can be observed that severe over-segmentation occurs when the Watershed Transform floods from all local minima while flooding from selected markers reduces this significantly. However, computing such markers are difficult and the use of an insufficiently accurate set of markers, as shown in Figure 5.6, will reduce over-segmentation but still provide unacceptable results. The development of new methods to compute a more accurate and reliable set of markers for grains in Ti-6Al-4V microstructural image data is, therefore, very important. This is achieved through the development of the CGM technique.

CGM is a flexible marker computation approach that combines intensity and shape information to provide a robust set of markers. The motivation is to be able to accurately mark grains in different microstructure types, produced using different imaging technologies, despite fluctuations in the level of detailed shape and intensity information available in different microstructures. This prevents issues found in over-

trained segmentation techniques target features of particular microstructures types, as demonstrated in Chapter 8.

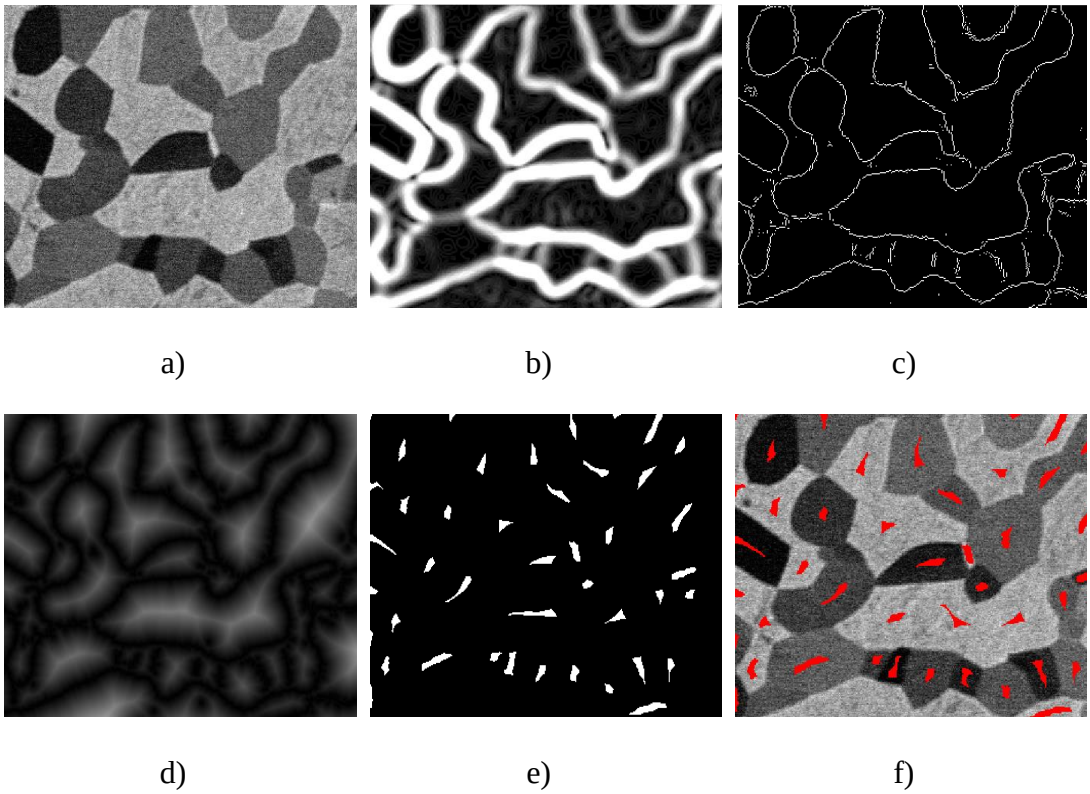

Figure 5.7: Computation of markers where a) original image, b) image gradient, c) sparse edge detection, d) distance transform, e) local maxima with h-maxima suppression and f) overlay showing the final set of markers

Figure 5.7 illustrates the effects of each step in the proposed, novel marker computation process. The markers are computed by first using edge detection techniques to locate significant variations in intensity, that are believed likely to indicate the boundary between grains, as in Figure 5.7 c). This is achieved by using known edge detection techniques, specifically the Sobel filter described in Chapter 3. The gradient image, shown in Figure 5.7 b), is computed by applying Sobel filters to the Gaussian filtered image and a pre-defined threshold, t_s, is then applied to the result to create a binary image marking edges in image data. Shape information is then incorporated into the markers by applying the distance transform to the inverse of the edge detected result. This returns an image where the value at each pixel corresponds to the distance between that point and the nearest detected edge, as in Figure 5.7 d). This creates a topographic map of the image where local maxima correspond to regions

that are central between detected edges. It is believed that local maxima in the distance function, therefore, correspond approximately to the centres of grains, providing suitable markers. However, as noise occurs within grains, some local maxima that are likely to be caused by falsely detected edges. However, these maxima are likely to be smaller than those created by only true grain boundaries. Therefore, h-maxima suppression techniques can be used to supress the smallest maxima a limit the number of excess markers. The remaining local maxima are most likely representations of the location grain so these are extracted and used as a set of markers, as in Figure 5.7 f). The algorithm given below, in terms of the combination of functions used.

Algorithm 1: CGM

Input: I: greyscale image, t_s: edge detection sensitivity

Output: M: markers

1. *E*=edgeDetection(*I*, *ts*)
2. *DT*=distanceTransform(*E*)
3. *Rmax*=findRegionalMaxima(*DT*)
4. *M*=h-maximaSupression(*M*)

Some of the techniques used in this method have been previously applied to compute markers but have not been combined in this way. The use of h-minima suppression has been popularised in research on medical image segmentation as a method of reducing excess markers, as described in Section 4.2.3.5. The CGM techniques proposed uses the inverse of this transform, h-maxima, due to the functions used to compute the markers, but the principal is the same. The use of the distance transform was previously applied by Beucher [5] to mark coffee beans, and more recently by Sosa *et al.* [36] who also aimed to mark grains in microstructures. However, both methods applied the distance transform to a thresholded binary image. As a result, these methods fail to accurately capture boundaries between grains of the same phase. The proposed combination of methods included in the new marker computation algorithm allows a robust set of markers to be built using the beneficial properties of each. Edge detection

provides intensity information while the distance transform provides shape information. The combination of the two means that the shape of even subtle boundaries can be considered while searching for markers, including alpha/alpha grain boundaries that existing methods often fail to consider. The effectiveness of this approach is well demonstrated by the example in Figure 5.7. The linear cluster of grains in the lower section of the image form a relatively smooth region of alpha phase. The boundary between alpha and beta phases here do not show any significant concavity. However, the edge detection, in Figure 5.7 c), finds the intensity change between each grain, indicating where segmentation should occur. Similarly, for the cluster of grains in the upper right-hand corner, no edge is marked between the grains, as shown in Figure 5.7 c). However, the distance transform in Figure 5.7 d) does place distinct local maxima in each due to the concavities in the boundary. The result is that all of the aforementioned grains are marked correctly in the final marker set in Figure 5.7 f) despite the boundaries not sharing a common distinguishing factor.

There are two parameters which govern the effectiveness of marker computation using the proposed method; the sensitivity of the initial edge detection and the level of h-maxima suppression. It was found that a suitable level of h-maxima suppression can be set and used for all microstructures, as this was used only to remove the smallest maxima cause by noise with the larger errors prevented by the range of other pre- and post- processing steps in this algorithm. The sensitivity of edge detection, t_s, determines how large a variation in intensity should be used to indicate the presence of a boundary. There is no global ideal sensitivity value as the intensity change indicating a boundary varies depending on the content, contrast and noise level of the image, as well as any filtering methods applied. As edge detection is the first step in computing markers using this method, the sensitivity of edge detection is critical as it directly affects the level of over- and under- segmentation. The need to empirically set such a crucial parameter has led to the proposed CGM technique being ruled out in research for segmenting images in other applications [107]. However, in microstructural analysis this can be quite useful as it provides an intuitive parameter that controls the level of segmentation. This means that an expert materials scientist, without any image processing experience, could calibrate the segmentation and results measurements to their current expectations and standard. Chapter 7 proposes a new

software tool that allows this to be achieved easily by observing a visualisation of the effect the parameter has on the final segmentation. This allows the marker computation scheme to be adapted to suit a wide range of datasets. Validation of this is undertaken in Chapter 8 for a broad range of titanium microstructures. It is also believed that this technique could be applied to mark objects in images from other applications. While it is outside the scope of this thesis to fully investigate this a brief example of CGM applied to other datasets is provided in Figure 5.8.

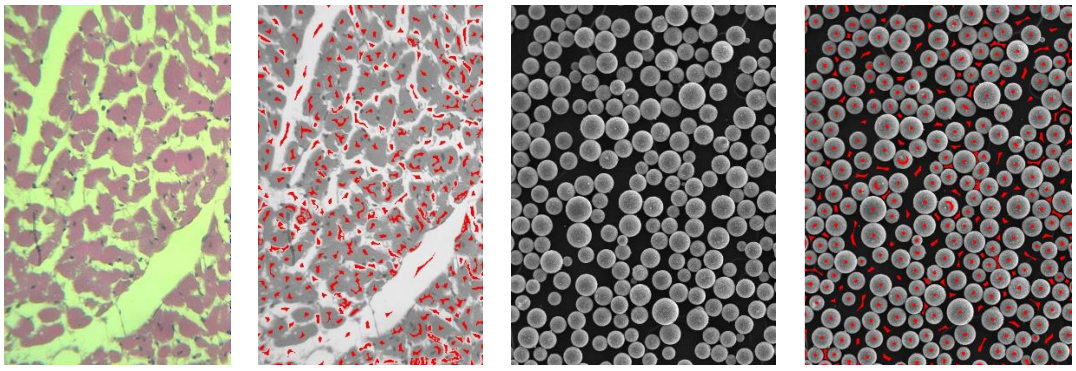

a) b) c) d)

Figure 5.8: Examples of CGM on datasets from other fields where a) image of muscle fibre in human tissue, b) is markers for each fibre, c) image of spherical particles and d) is markers of each particle [36]

For microstructural analysis, it is also important to note that, although this sensitivity parameter affects the segmentation, the use of the distance transform and h-minima means that markers still have to adhere to certain size and shape requirements. When combined with the post-processing methods in Section 5.3, the resulting segmentation algorithm has enough rules in place that changes in edge detection sensitivity will normally allow only relatively small changes to made to the segmentation, rather than this being adjusted to achieve any arbitrary result.

5.3.4 Artefact Detection

This section describes methods to deal with a problem that occurs rarely in the microstructural data, where slightly larger, round artefacts corrupted some of the images in this study. An example of this is shown in Figure 5.9 a).

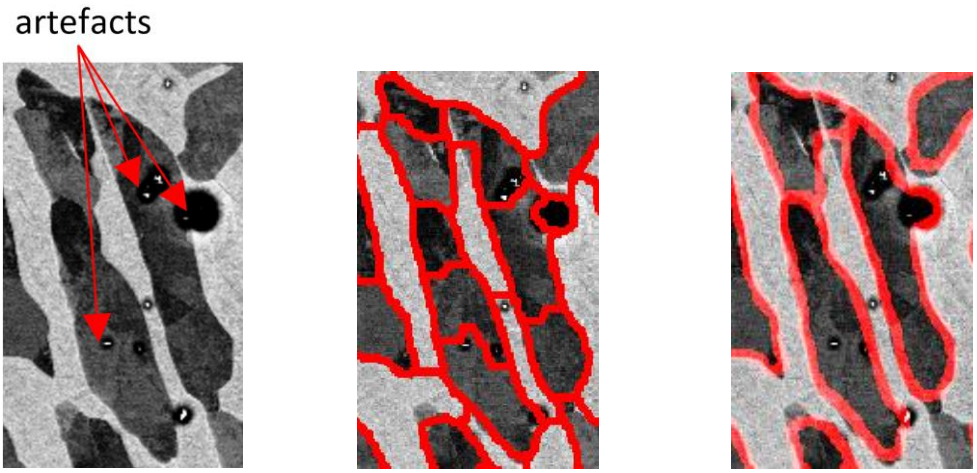

a) b) c)

Figure 5.9: Example of artefacts in an SEM image and their effect on segmentation where a) original image with artefacts indicated, b) segmentation result with artefact corruption and c) segmentation with artefacts removed

These artefacts are dark and circular and often, but do not always contain a white dot at their centre. The intensity change at their boundary will typically be marked by the edge detection functions used in the marker computation algorithm, so a marker may be given to artefacts. This will also affect the gradient image used as the topographic surface of the Watershed Transform, meaning boundaries between objects are more likely to be placed where artefacts exist, even if a marker did not exist at the artefact. As the artefacts relate only to errors when producing microstructural images, and are not informative of the underlying microstructure, it is desirable to ignore their presence when performing analysis. Therefore, the two issues described above must be addressed. Fortunately, these artefacts are very dark, small and round relative to alpha grains in the same image. These properties make it possible to detect these artefacts and then limit their effect on segmentation.

To do this an artefact detection and removal algorithm is proposed based on the hit-or-miss transform [26]. First the top-hat operator is applied to remove bright spots from the centre of artefacts so that artefacts take the form of entirely black circles. This was done as bright spots only appear in some artefacts so cannot be used reliably for identification. The image is then inverted to keep with the convention that the objects to be identified are brighter than the background of the image. The Hit-or-Miss

transform is then used to identify small dark circles. As artefacts of different sizes exist, a range of different sizes of pairs of SE are used, with the artefacts detected by all pairs added to form a complete set of detected artefacts. The result of applying this to a microstructural image containing artefacts is shown in Figure 5.10.

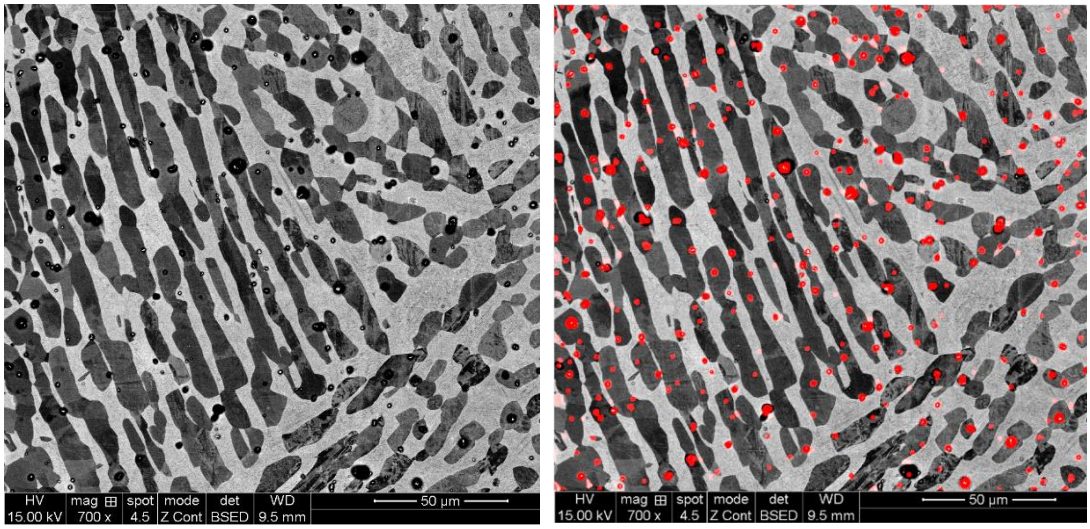

a) b)

Figure 5.10: Example of artefact detection using the hit-or-miss transform where a) original image and b) shows artefacts in red

It is clear from this result that artefacts can be detected successfully using this existing transform. However, removing these artefacts is a more difficult task. To remove artefacts from consideration during the segmentation processes, two operations are performed. First any marker that lies within an artefact is removed from the set of markers previously computed to prevent over-segmentation errors. To do this the edge detection result used for marker computation is modified such that any pixel in a location where an artefact exists does not return a positive value in the edge detection Second, the gradient image used for the Watershed Transform is also set to “0” for all locations that lie within an artefact. This prevents boundaries between two correctly marked grains from being placed at the location of an artefact rather than an intensity change. The effect of segmentation using this artefact resistant marker method is shown in Figure 5.9 c). While this example suggests positive results, it is also possible to introduce under-segmentation errors using this approach. If the artefact occurs at a boundary between grains, the intensity information it obscures cannot be recovered.

While the artefact is present segmentation lines will still exist at the boundary, but without it no segmentation will occurs. The likelihood of grains occurring on grain boundaries will determine the success of this technique. This effect can be limited by constraining detected artefacts not include pixels on the boundary between alpha and beta phase, but this cannot be done for alpha/alpha boundaries. Therefore, this stage is considered optional and report here as an additional function rather than a core part of the segmentation technique.

5.4 Watershed Transform

After pre-processing there exists a filtered version of the original image and set of markers that can be used to produce a segmentation using the Watershed Transform. The transform is now applied by taking the gradient of the filtered image as the topographic function, with this gradient then modified to include global minima only at locations where markers exist, as per the method of Meyer [28]. The result is a complete segmentation of the image with boundaries placed between marker grains at the location of the highest gradient between them. This is illustrated in Figure 5.11, which also shows a ground truth segmentation, created by a materials scientist, for comparison.

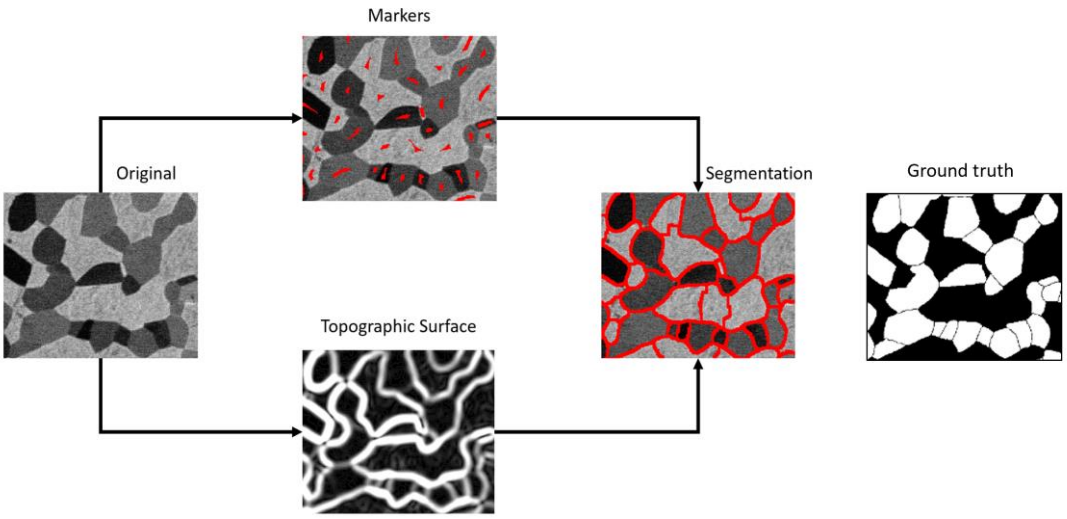

Figure 5.11: Illustration of the inputs and outputs of the Watershed Transform

5.5 Post- Processing

This section describes the post processing steps used in the CGSA. The Watershed Transform produces a complete segmentation of the entire image. As alpha and beta phases are measured separately methods of distinguishing between the two phases are required. As image segmentation is challenging, additional procedures are proposed to correct any segmentation errors based on prior knowledge of the images under study and their content. Region merging procedures have been applied in previous segmentation approaches, as described in Section 4.2.3.3, to incorporate this prior knowledge. An implementation of this is described here using bespoke merging criteria that is suitable for reducing segmentation errors in a wide variety of microstructures. A region splitting approach is then presented to correct any under-segmentation errors based on the shape of the segmented grain boundaries.

5.5.1 Phase Separation

The Watershed Transform produces a complete segmentation of the image, including all phases of material. Before measurements of alpha grains can be performed, alpha and beta phase regions must be distinguished so that no beta phase regions are erroneously included in alpha grain measurements. Thresholding the original image provides an estimate of phase separation on a per pixel basis, as each phase normally is of significantly different intensity. Otsu's method [108] can be used to automatically select a suitable threshold for a given image. This works well in images that are consistently illuminated, however, it can cause phases to be misidentified in areas where illumination varies. In such cases, adaptive versions of Otsu's method can instead be used to accommodate this [109]. Adaptive thresholding applies a different threshold to each local region of the image. This prevents errors identifying phases in regions of the image that are lighter or darker than average in the image. However, dark artefacts in one region of an image are more likely to cause issues in adaptive thresholding techniques so these should only be used when necessary. For the purposes of microstructural analysis, it is often best to use global thresholding techniques for SEM images, where intensity variations are greater, and adaptive methods for OM images, where lighting inconsistencies are more common, as illustrated in Figure 5.12.

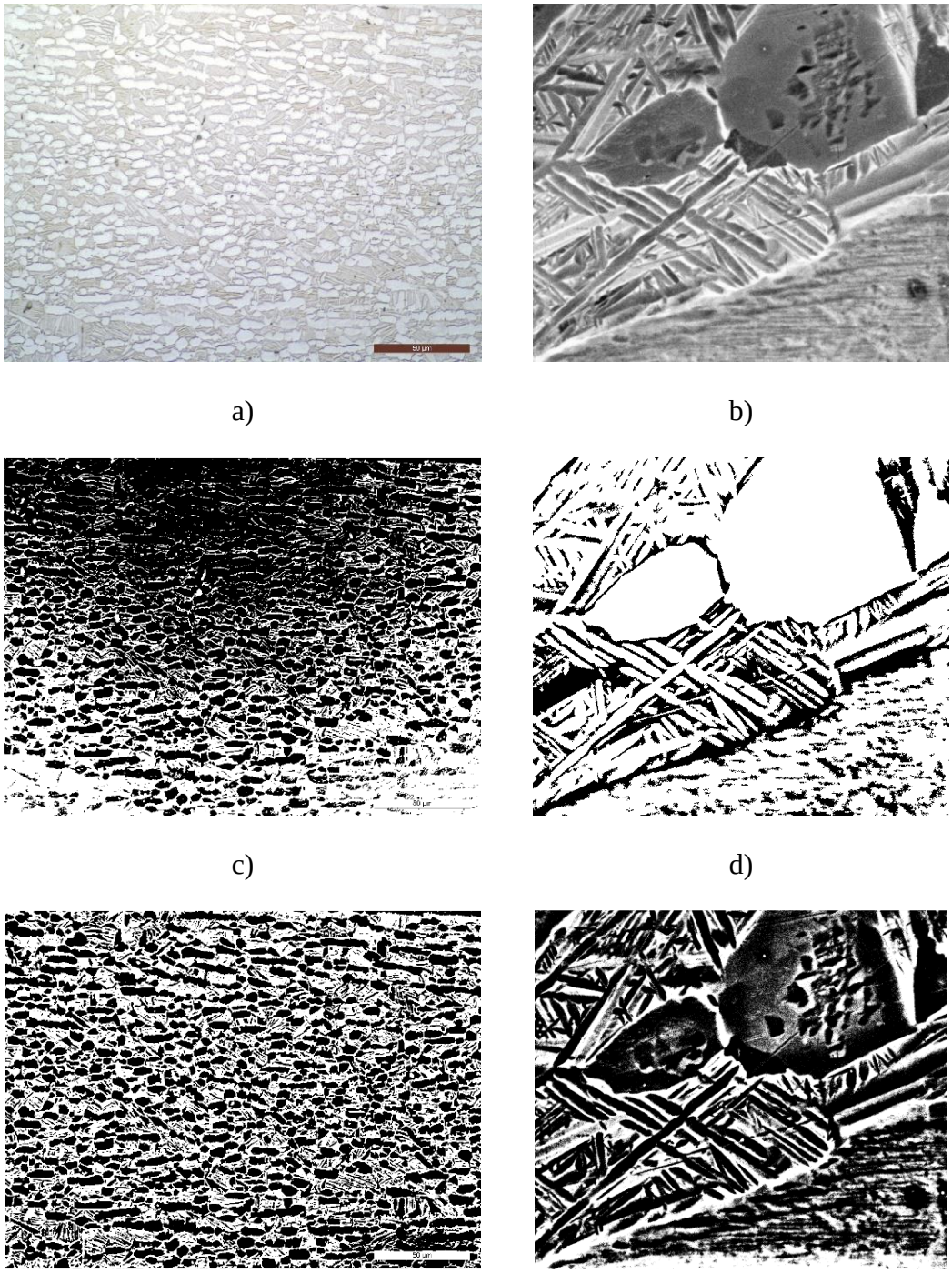

Figure 5.12: Phase separation in SEM and OM images where a) OM image, b) SEM image, c) and d) show the global thresholding of each image and e) and f) show the adaptive thresholding of each image

Due to noise in the images, a single grain may contain some pixels marked as alpha and some that are marked as beta, as can be observed in Figure 5.12 f). A threshold, t_α, is set to determine if a segmented region belongs to the alpha or beta phase based on the percentage of pixels in the segmented region belonging to that phase. If set too low, then beta phase regions may be misidentified as alpha grains. If set too high, then some grains would be ignored from measurements. There may not exist any ideal t_α where all alpha grains are identified, and all beta phase regions are discounted. For the analysis of titanium microstructures, it is generally best to set this threshold high for grain size measurements as measuring fewer grains is preferable to measuring grains incorrectly, as existing standards only require a subset of grains to be measured [29]. Indeed, in existing standards it is already normal to measure only a randomly sampled subset of grains in each microstructure.

In bi-modal microstructures, course alpha platelets exist alongside approximately globular alpha grains. The technique proposed in this chapter is not capable of reliably measuring these platelets due to the over-segmentation issues shown in Figure 5.13, therefore, these should not be measured.

a) b)

Figure 5.13: Example of segmentation of fine platelets using the proposed segmentation algorithm where a) is original image containing platelets and b) is a segmentation which includes platelets

A method for identifying phase differences based on grain shape is presented in Chapter 6 and provides the most accurate method of performing this task. Grain shape information is obtained using during the platelet analysis techniques in Chapter 6

which would allow fine platelets to be removed from further analysis. However, this is a more computationally expensive procedure than the segmentation algorithm described in the current chapter so it is not efficient to use this approach, unless also measuring platelets. A more efficient procedure is to perform a morphological opening [24] on the segmented image by a disk shaped SE of radius larger than the estimated maximum width of platelets, w_p. This will not extract meaningful platelet measurements but will filter out these platelets sufficiently accurately so that measurements exclusively of approximately globular alpha can be produced. While this is likely to cause some distortion to grain boundaries it will typically have minimal effect on segmentation results. The parameter w_p can be set automatically according to the minimum grain size expected in the image.

5.5.2 Region merging

A post-processing procedure is proposed to reduce over-segmentation errors by merging adjacent regions, whose properties suggest they belong to the same feature. Similar approaches have been applied successfully in other image segmentation techniques [83]–[85].

The proposed technique makes use of a region adjacency graph [110] to control the merging of regions. This is a graph, $G = (V, E)$, where each vertex, V, is a region of the image and edges, $E \subset V_i \times V_j$, connect vertices only when the regions share a common boundary, as illustrated in Figure 5.14 a) with vertices in blue and edges in green.

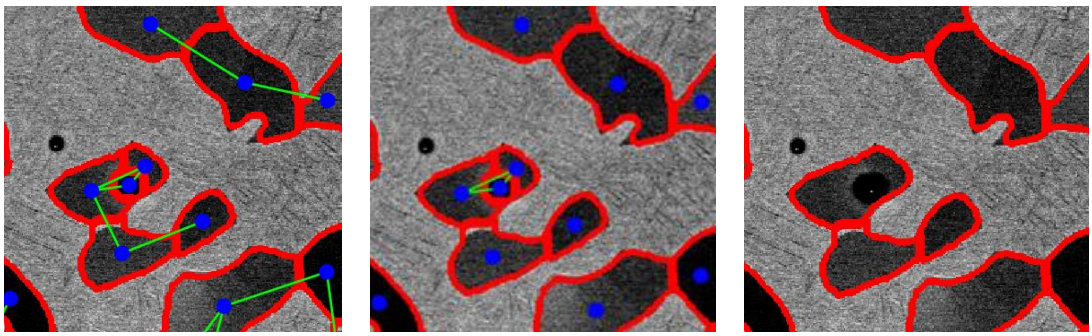

a) b) c)

Figure 5.14: Merging over-segmented regions using a region adjacency graph where a) is the region adjacency graph overlay on a segmented image, b) is the edges between regions belonging to the same grain and c) is the new segmentation

For each edge, a weight, w_{ij}, is typically computed based on the similarity of the regions (vertices) it connects. When the weight of this edge exceeds a predetermined threshold, edges are removed from the graph such that only edges between similar regions remain, as shown in Figure 5.14 b). Any internal boundaries between regions connected by an edge are then removed and the encapsulated region is categorised as a single grain. The updated segmentation is shown in Figure 5.14 c).

Determining suitable edge weights and merging thresholds is critical to the success of the proposed region merging method. The more accurately the properties of objects can be predicted in advance, the more precisely these parameters can be set and the more effective this technique is. In microstructural analysis, it is often difficult to predict grain properties and, therefore, selection of these weights and thresholds is difficult. As a result, 3 separate weights and thresholds are defined to enable a robust examination of which regions should be merged.

Edge weights are based on; the length of boundaries, B, the mean intensity of pixels in the region, I, and region size, S. The first weight, $w1_{ij} = \frac{B_c}{\min(B_i, B_j)}$, is, for two adjacent grains, with boundary lengths B_i and B_j, the percentage of the boundary of the smaller of the two grains that is a common boundary, B_c, with the adjacent grain. The second weight, $w2_{ij} = I_i - I_j$,is the difference in intensity between each grain. The

third weight, $w3_{ij} = \min(S_i, S_j)$, is the size of the smaller of the two regions. The mean diameter of the regions is used as the size measurement in this case, however, other metrics could also potentially be used. Three distinct thresholds, T_B, T_I, T_S, are then used to judge each of these weights and the merge test, M, is positive when regions should merge. This approach differs from the existing literature where the accepted convention is to split-or-merge such graphs based on a single edge weight that is calculated based on all specific properties. However, while that approach has good generality, combining the three weights proposed here into a single weight does not make sense for grain segmentation. The reason for this is that it would allow strong similarity in one aspect to negate dissimilarity in another, i.e. having a very similar intensity would lower the edge weight and allow the merging of grains with longer shared boundaries. This is not believed to be desirable for alpha grain segmentation with the preference being for a well-defined set of rules that can be easily tailored based on knowledge of the microstructure. This can be achieved far easier with separate weights and thresholds than with a combined weight. T_B should be set as the maximum amount of boundary that is expected to be shared between grains, T_I set as the maximum intensity difference expected between regions of the same grain and T_S set as the smallest possible grain size expected in the microstructure. Regions are set to merge either when one region is very small, indicating it is probably caused by an artefact, or when regions share both a large common boundary and a similar intensity. This is shown in Equation (5.2).

$$M = \begin{cases} 1 \; if \; w1_{ij} > T_B, & w2_{ij} > T_I \; or \; w3_{ij} < T_S \\ 0 & otherwise \end{cases} \quad \textbf{(5.2)}$$

Defining an optimal set of thresholds for the merging procedures is difficult as it depends on knowledge of the images under study. In order for the methods to be applicable to a wide range of microstructures, this must be used sparingly by correcting only the most obvious errors. In cases where more specific properties of microstructural features are known in advance, a more extensive merging criterion could be used to obtain more accurate results.

5.5.3 Region Splitting

In addition to the over-segmentation errors addressed so far in this chapter it is also possible that under-segmentation errors can occur, due to the incorrect merging of regions or misidentification of markers. To alleviate this, an additional splitting of the segmented regions, based on their shape, is proposed. This method takes the segmentation result, after any region merging, as an input function and splits regions where significant concavities exist in the boundaries of an object. This same property was previously used to aid the computation of the markers to use in the Watershed Transform. However, at that stage there was less information available as only the shape of boundaries that could be located using edge detection could be assessed, which typically does not represent the complete boundary. By repeating a similar operation as a post-processing step, a more complete estimate of the boundaries, provided by the new segmentation algorithm, could be used to locate extra boundaries that are missed by Watershed Transform. The distance transform is used to study the shape and size of segmented regions. Regions in the centre of segmented regions will, therefore, have high values while regions towards the edge of the region will have lower values. As the distance transform returns a "0" for the existing boundaries in the segmentation, each region has its own separate topography. For regions with smooth boundaries of approximately elliptical shape then only 1 peak will exist. However, if there are any concavities in the boundary then multiple peaks will exist with valleys between these peaks representing a region where a boundary should be, as illustrated in Figure 5.15 c).

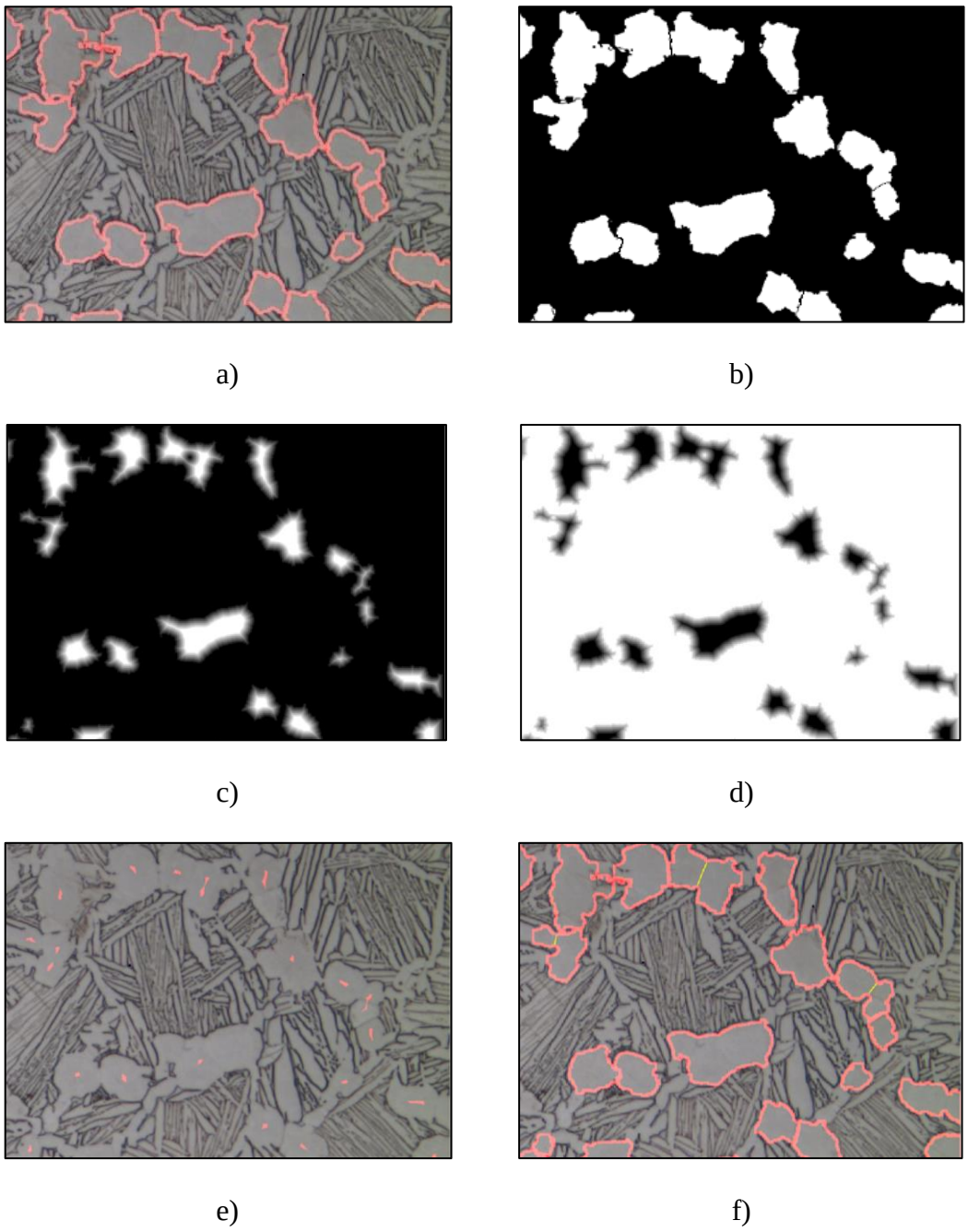

Figure 5.15: Use of distance transform to split already segmented regions where a) original segmentation, b) binary segmentation αseg, c) distance transform of αseg, d) inverse of distance transform, e) markers from h-maxima and f) new segmentation

A fast and efficient way to split these regions is to perform a second Watershed Transform, this time using the distance transform of the first segmented result as the topographic function, rather than the original gradient image. The concept of applying

successive Watershed Transforms has previously been explored through the idea of hierarchical Watershed Transforms [111]. However, the traditional approach to this uses successive Watershed Transforms to reduce over-segmentation, while the technique proposed here aims to further segment the image based on new information extracted by our algorithm. Suitable markers, for the second Watershed Transform used in the splitting function, are computed by applying h-maxima suppression of the distance transform, applied to the segmented results, to identify only the most significant maxima to be used as markers, as in Figure 5.15. As the technique uses the h-minima of the distance transform clearly there will always exist an h-minima threshold where the segmentation result is not changed. Theoretically this means if this parameter is fine-tuned it could be guaranteed that this method at least does not make segmentation worse. However, this would not be a practical application as the segmentation algorithm would be less automated. Instead a single parameter is set empirically which is used for all microstructures. The topographic surface to be segmented is further modified by setting the height of the surface to the maximum height of the image in all locations where a boundary exists in the initial segmentation. This preserves all of the initially detected boundaries so that the additional function can only split existing grains. The result of applying this to an incorrectly segmented region is shown in Figure 5.15.

Generally, aggregated measurements are more accurate when over-segmentation and under-segmentation are balanced. As segmentation algorithms based on the Watershed Transform tend to over-segment a post-processing procedure that increases image segmentation may not improve results, even if it fixes genuine errors, is the type of error may become imbalanced. Therefore, this stage of the algorithm is considered optional and can be applied to the image as required by a user. This is explored in more detail in Section 8.2.5.1.

5.6 Measurement

After phase separation, each grain is represented by a single group of pixels where each pixel is adjacent to at least one other pixel in the group. This configuration is called a connected component (CC) and several techniques have been defined to measure their properties [112]. Measurements of the length, L, and width, W, for each grain are taken

by computing an ellipse that has the same normalised second central moments as the region. This ensures that the length and width measurements are taken perpendicular to each other to give the best estimate of grain size. These values are used to compute the mean grain size, G_m, and globular volume fraction, V_g, using Equations (5.3) and (5.4) where N_g is the number of grains measured.

$$G_m = \sum_{1}^{N_g} \frac{L_{N_g} + W_{N_g}}{2} \tag{5.3}$$

$$V_G = \frac{\sum_{1}^{N_g} \begin{cases} 1 & if \ \frac{L_{N_g}}{W_{N_g}} > 2 \\ 0 & otherwise \end{cases}}{N_g} \tag{5.4}$$

5.7 Conclusions

In this chapter a novel segmentation algorithm has been proposed and presented. The algorithm is designed specifically to be able to segment globular alpha grains in titanium microstructures, something that cannot currently be achieved successfully using existing approaches that have been presented in the academic literature. More generally, the proposed method provides a robust approach for segmenting images where the objects of interest are touching, clustered, not necessarily distinguishable by intensity or shape alone and where images are corrupted by various forms of noise. By combining several pre- and post- processing steps, the Marker Based Watershed Transform is used to achieve superior segmentation results than would normally be expected from this transform. This is demonstrated empirically in Chapter 8 where the results of applying the proposed algorithm to a variety of microstructural data, which present significant segmentation challenges, are shown.

In terms of contributions, the segmentation algorithm described in this chapter provides a novel marker computation technique, that is crucial to preventing over-segmentation issues. Additionally, the appropriate use of techniques such as a

specialised region merging procedure and the hit-or-miss transform [26] to improve segmentation in microstructural images is described.

The proposed algorithm includes several parameters that can be altered. While the need to set parameters in segmentation algorithms can sometimes make their use more challenging, the number of different stages and rules in the proposed approach means that in most cases limited changes to these parameters need to be made. Chapter 7 presents the implementation of the proposed algorithm within a software package. It is demonstrated that through this software, the parameters, rather than making this algorithm difficult to apply, in fact allow easy, intuitive control of segmentation results. In Chapter 8 a complete validation of the method presented in this chapter is provided. This includes comparisons with existing, state-of-the-art microstructural analysis tools and image processing methods which have been presented in the literature.

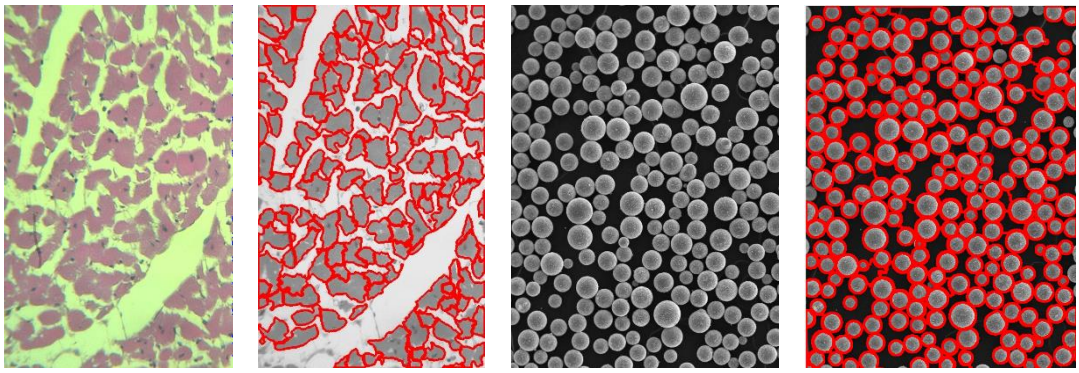

a) b) c) d)

Figure 5.16: Examples of the CGSA on datasets from other fields where a) image of muscle fibre in human tissue, b) segmentation of each fibre, c) image of spherical particles and d) segmentation of each particle [36]

It is also believed that robustness of this algorithm will provide good generalisation to the segmentation of images from different applications outside of the titanium microstructural analysis considered here. Very recent work has cited the published version of the new algorithm [107], [113]–[116] on work on different datasets. While none of these authors applied the CGSA directly, several authors use some of steps of this algorithm as part of their own bespoke analysis procedures [113]–[115].

Comprehensive trials of the CSGA on different datasets from other applications is interesting but is outside the scope of this thesis. Instead a brief demonstration of this algorithm applied to a few images from different fields is provided in Figure 5.16.

6 MORPHOLOGICAL ANALYSIS OF ALPHA PLATELETS

This chapter describes techniques for analysing thin elongated structures within images, specifically platelets in titanium microstructures. The purpose of this is to provide a method to analyse microstructures that contain thin platelets that cannot be properly measured using segmentation techniques, such as those proposed in Chapter 5 of this thesis.

The fundamental approach is not to try and segment individual platelets but to extract information about the size and shape of image features directly. This is achieved by fitting a set of artificial, linear structures to the image and analysing how well each one fits within platelets. In the review of recent literature in Chapter 4, several promising procedures were identified that attempted to measure the width and orientation of structures in this way. However, none of these techniques provided a complete solution for microstructural analysis, as the proposed methods are not robust enough to deal with the wide variations in the size and aspect ratio of alpha platelets. One common reason for this weakness is that some methods measure width without considering orientation [11] and others measures orientation without considering width [63]. The technique described in this chapter resolves such issues by measuring width and orientation simultaneously using the same technique, so that information about one property can guide measurements of the other. This simultaneous approach also allows shape information to be extracted from the same data. To achieve this the proposed method creates a set of SEs of various combinations of length and orientation which are used to probe the image via a morphological opening. The value of each opening describes how well each SE fits each structure in the image. All of the information

generated by this technique is stored by mapping the outputs from all SE's onto a new 3D orientation space called the Feature Length Orientation Space (FLOS). While recent applications of the orientation space to materials analysis assign binary values in this space [63], the method in this chapter instead maps the largest fitting SE to each element in the array. As a result, variations in the orientation and location domain of this space allow a range information about the size, morphology and orientation of image features to be extracted. Finally, a separate algorithm is proposed to locate and measure platelet colonies using this new data. A flowchart showing the interconnected steps in the platelet analysis algorithm is provided in Figure 6.1.

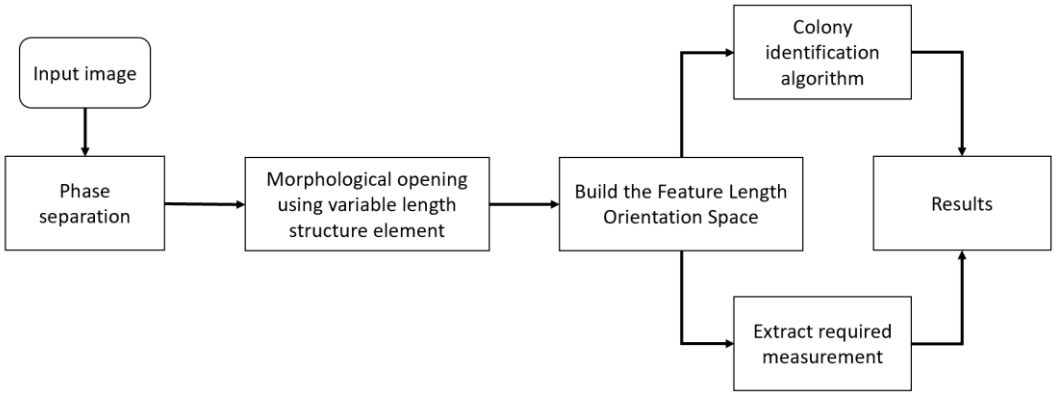

Figure 6.1: Flowchart of morphological platelet analysis techniques

In this thesis, all orientation measurements are reported in degrees counter clockwise from the positive horizontal axis.

6.1 Shape fitting using mathematical morphology

Fundamentally the techniques described in this chapter extract information by testing an image against a predefined set of objects and finding at which size, and orientation of object that best match those in the image. A variety of techniques [60], [63] which attempt to extract information using this approach have been described in Chapter 3. These techniques exploit tools from mathematical morphology, which offer an effective way to measure how well these test objects fit within features of an image. From this point on the test objects are referred to as SEs, for consistency with existing literature and to avoid confusion with the objects in the image which are measured. Mathematical morphology is a family of techniques that includes a range of methods

for analysing spatial structures in images. Useful to this chapter are morphological techniques based on set theory which take a predefined region, known as a SE, *B*, and probe each point in an image to find locations where *B* fits or hits the foreground of the image. The SE must have a designated origin pixel but otherwise can be any arbitrary shape and size. The output of morphological operators is determined by the image content and the shape and size of *B*. Therefore, a set of SEs of different sizes and morphologies can be used to determine the size and morphology of image content by applying morphological operators. In this chapter, two operators called opening, γ, and closing, φ, are used. A complete definition of these operations is provided in Chapter 3. What is important to recall here is the effect each operation has on the value of pixels in the output image relative to those in the input image.

Both the opening and closing operations will return a complete image. Each pixel in the output image will have a value corresponding to either the maximum or minimum value in the neighbouring area defined by a SE with its origin at the pixel. For example, given a binary image, then an opening would give a value of "1" for any a pixel location where the SE could overlap that point and still fit entirely in the image foreground. This means that by performing multiple openings with different structuring elements it is possible to determine which bests fits the foreground at each pixel in the image. The application of this to measure the orientation and dimensions of elongated structures such as alpha platelets is described in Section 6.2 and 6.3 of this thesis. As the closing is the dual operator of the opening, this would act in a similar way except SEs are fitted to the background, such the a "0" would only appear in the output image for a pixel location where the SE could overlap that pixel and still fit in the background. In the microstructural analysis application studied in this thesis, there is no interest in reporting such measurement of the background region, i.e. the beta phase. However, this closing is useful for assessing the distance and organisation of adjacent alpha platelets. An application of this to identify and measure colonies of these platelets is given in Section 6.5.

6.2 Orientation measurements from fixed-length rotational structuring elements

Techniques are proposed in existing literature [48], [62], [63] to measure the orientation of thin elongated objects in images using rotational, linear SEs. It is also demonstrated that this information can then be used to identify groups of parallel structures [63]. This approach has great potential for use in a microstructural analysis procedure to measure the orientation of alpha platelets and size of colonies in titanium microstructures. The most relevant implementation of this method is work by Borocco *et al.* [63] on measuring graphene plans. In this technique, the orientation of an object is measured by finding the orientation of a linear SE that fits within that object. A set of SE, B_θ, are defined where θ is the orientation of any given SE in the set and each SE is 1 pixel wide and is of length, L. To ensure B_θ fits the objects at only the correct orientation, L is fixed at a length greater than the expected width of all objects in the data but less than the expected smallest length of objects to be analysed. An illustration of this approach is shown in Figure 6.2.

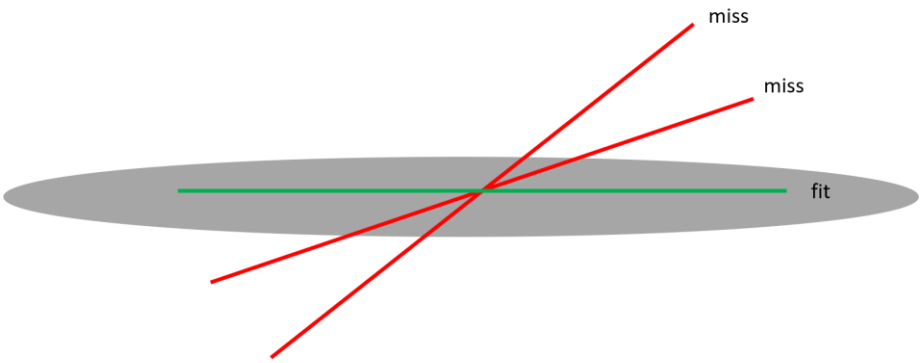

Figure 6.2: Example of measurement using rotational SE where a grey elongated object in an image is measured by 3 SE's of a fixed length. The green line indicates an SE at an orientation that fits and the red line indicates SEs at orientations that do not fit. In this case the orientation of the green line is taken to be the orientation of the original object.

The range of orientations, θ, of SEs should be between 0-180°, to account for all possible orientations. The step size between each orientation, S_θ, defines the maximum

accuracy of measurement. If S_θ=10°, then $\theta \in [10,20 \ldots 180]$, with 0° ignored as this is equivalent to 180°. As a result, all measurements will inherently have a quantisation error of up to +/-5° in this example. Theoretically, any step size can be used, so the potential accuracy could be improved by reducing S_θ. However, reducing the step size increases the number of SEs to be evaluated, which in turn increases computation time. Longer SEs can also enable more accurate results, provided they will still fit image data. For example, if when L=3, it is impossible to differentiate between 40° and 50° in a 2D Cartesian space. This occurs as there is only enough resolution to fit the line in 4 locations (0°, 45°, 90° and 135°), therefore, a 40° and 50° line would both be best measured by the 45° SE. To determine which orientation of a SE fits each object in a given image, a morphological opening, γ, of the image, f, by each SE, B_θ, is computed. Orientation measurements are recorded in a transform of the image, E, where each pixel, x, is set as the orientation of B_θ which returns the highest opening value at that pixel, as shown in Equation (6.1). If multiple orientations give the same opening value only the first orientation is used.

$$\mathrm{E}(x) = \arg sup_\theta \, \gamma_{B_\theta} \mathrm{f}(x) \tag{6.1}$$

E can be visualised using a colourmap where each colour corresponds to the pixel value as shown in Figure 6.3.

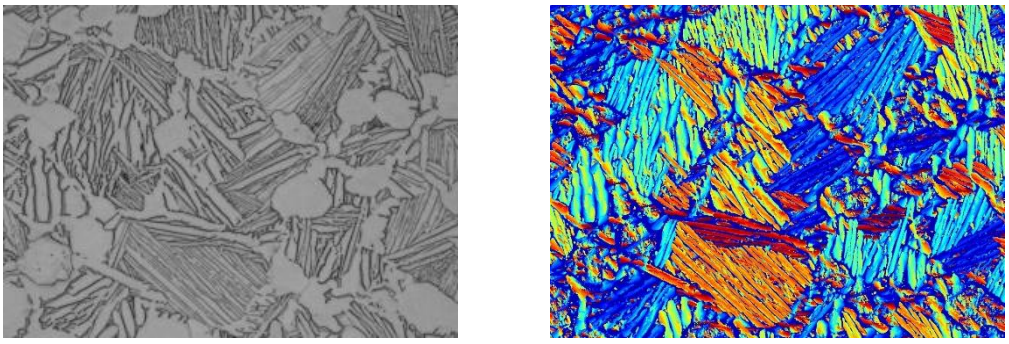

a) b)

Figure 6.3: Illustration of orientation measurement from rotational SE where each colour indicates a unique orientation

This approach is shown to be effective at measuring the orientation values of thin elongated structures without the need to segment individual platelets. As

measurements are based on the opening, each pixel that coincides with the SE that best fits the object will normally be assigned the same orientation value in *E*. This means that orientation measurements within each object are relatively consistent, which is crucial for many material science applications, such as grouping platelets to measure colonies. However, the method is not robust enough for titanium microstructures. No shape information is obtained by this methods which means for bi-modal microstructures, shown in Figure 6.3, meaningless measurements are often returned for pixels within the globular grains. Its reliability is also largely dependent upon the relationship between *L* and the dimensions of each object to be analysed in a given image. In other work implementing this method, such as the measurement of graphene plans presented by Borocco *et al.* [63] this is not an issue as the width of objects is very consistent, however, the same is not always true for titanium alloys. This is illustrated in Figure 6.4 which shows measurement accuracy for different *L* values for synthetic binary images containing elongated objects.

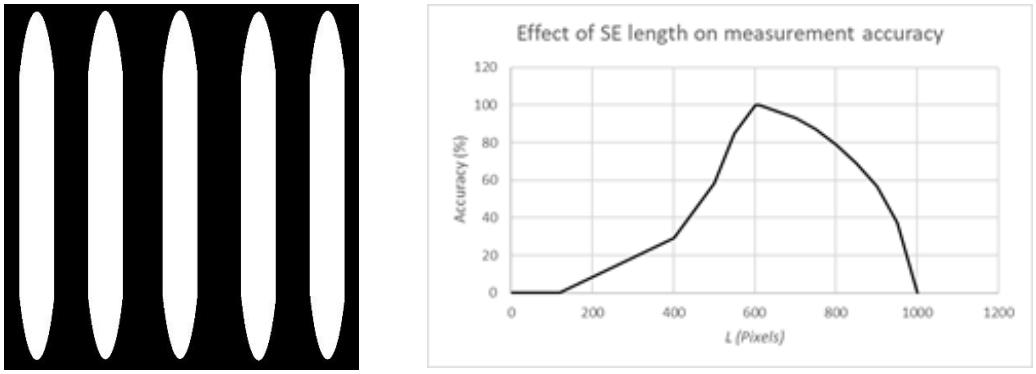

a) b)

Figure 6.4: Example of application of existing method where a) is an image (1000x1000) of elongated objects of the same dimensions and b) is a graph of measurement accuracy for various lengths of SE

Accuracy is defined in this example as the percentage of pixels in the image for which the measured orientation is equal to the orientation at which these objects were drawn (90°). Extremely low accuracy is obtained when *L* is fixed very long or short relative to the length and width of the objects, as B_θ either fits at every orientation or none. An optimum *L* value exists, which in this case is where B_θ fits all objects in the image at

only the true orientation. Selection of this parameter might not always be trivial and presents an opportunity for error.

Additionally, the optimum value of *L* is dependent on the dimensions of objects to be measured in the image. This means that when objects of different sizes exist in a single image, the optimum value of *L* to measure each object differs. This is illustrated in Figure 6.5 which shows two objects of different length and illustrates how no single value of *L* would provide robust measurements of both objects.

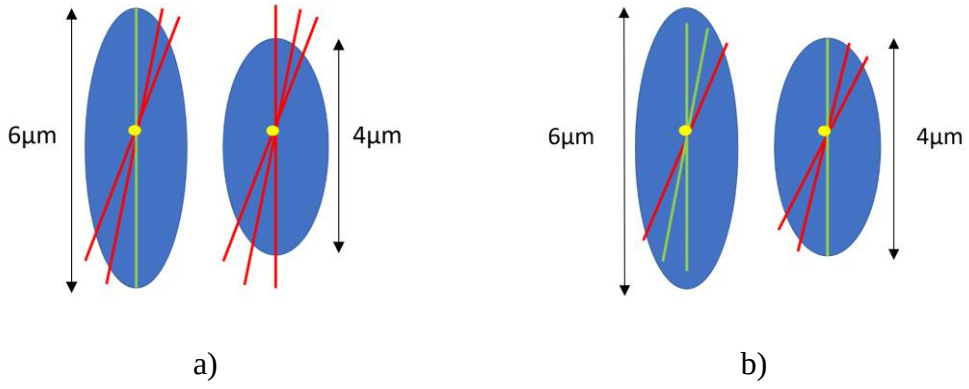

Figure 6.5: Illustration of the problems with fixed SE length where a) shows a length that fits one object at only 1 orientation but does not fit the other and b) shows a length that fits one object at only 1 orientation but the other at many

To further demonstrate this problem, measurement accuracy is again compared when using SEs for different values *L*; this time for an image containing elongated objects of different dimensions, as shown in Figure 6.6.

An optimum length of SE still exists; however, this value no longer achieves ideal results as no single value of *L* will produce an SE which perfectly fits every object in the image. The optimum value of *L* is therefore the length of SE which correctly measures the largest area of the image. In the example shown, the maximum accuracy is still only around 60% even for the best *L*. This is a more extreme case than is typically found in the microstructures in this study but represents good illustration of the type of error that could theoretically occur. An analysis of the extent of the errors found on real world data using this technique is given in Chapter 8.

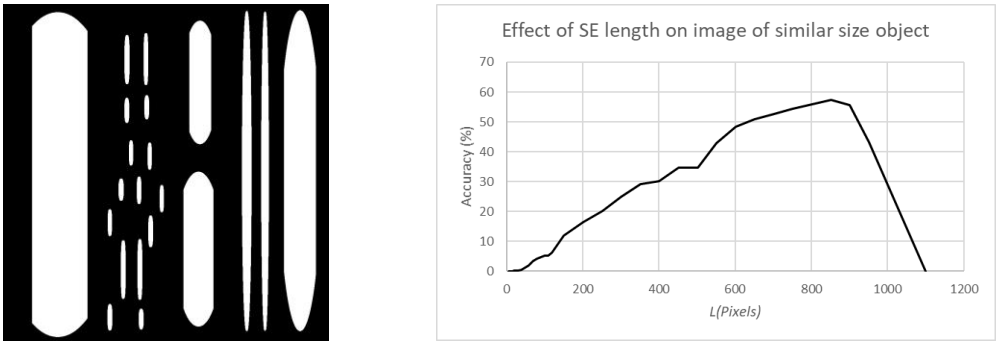

a) b)

Figure 6.6: Example of application of existing method where a) is an image (1000x1000) of elongated objects of different dimensions and b) is a graph of measurement accuracy for various lengths of SE

In datasets of graphene plans used by Borocco [47], where objects are of a consistent width, the method described in this section would work well and a suitable L is relatively easy to determine. However, this is not the case in images from other datasets, including some of the titanium microstructures investigated in this research. The method described in [47] also overlooks some useful data and, with some modifications, has the potential to extract much more. Measurements are taken of how well a single SE fits at each orientation for each pixel in the image. However, only the most probably orientation is recorded, discarding information on how well the SE fits at the other evaluated orientation. This information could potentially be used to describe the shape of objects, however, is not presented in the literature. As the output from the opening also depends on the size of objects there is also potential for size information to be obtained using this type of technique, although this information is limited when using SEs of the same length. The following section provides a new, extended version of the approach outlined in [47] which addresses these areas.

6.3 Orientation measurements from variable length structuring elements

In this section an extension to method described in [47] is proposed. The aim is to improve the robustness of the technique to achieve more reliable orientation measurements. The data produced will also allow further measurements of the size and shape of objects to be achieved, which is described in the subsequent sections. The

current section describes only the use of variable length SEs and assesses the potential impact on orientation measurements.

To prevent the types of error previously described, the use of variable length SEs is proposed, rather than the fixed length SE used in previous techniques. It is shown that the extended method improves the robustness of the approach when the dimensions of objects in the dataset are inconsistent. Limitations and measurement errors in the method presented in Section 6.2 are largely due to the difficulty in selecting a suitable length of SE. As a solution to this problem, this work instead proposes using a set of SEs which vary not only in terms of orientation but also vary in length, thus avoiding the need to find the ideal L. That is, a set of single pixel wide linear SEs, $B_{\theta L}$, are defined where L and θ denote the length and orientation of the SEs in the set. Both length, L, and orientation, θ, are assigned multiple values within a suitable range. θ values can be set according to the same rational as described in [47] and summarised in Section 6.2 of this thesis. L values should be odd numbers with a minimum value of at least 3, so that all members of $B_{\theta L}$ are symmetrical lines centred around a unique origin. A maximum length of SE, L_{max}, should ideally be set to be at a similar length to the longest object in the image. In practise, setting this parameter could be performed using a representative set of training data before the parameter, L_{max} is fixed for deployment. Since SEs that are too long to fit any objects do not affect measurements, setting this higher than necessary does not affect accuracy. However, it will have an impact on execution time as a result of redundant computation. As with the range of orientations, the step size between successive SE length parameters, S_L, can be set to any value. However, a large step size can lead to quantisation errors if this parameter is set too high. It is determined empirically that the most accurate results are achieved when S_L=2 so $L \in [3,5 \ldots L_{max}]$. As in Section 6.2, the morphological opening is used to measure how well $B_{\theta L}$ fits objects in the image.

To measure orientation, the assumption is made that the longest SE that fits inside an object should only do so at a single orientation and that this orientation is parallel to the object itself. This is true for elliptical shapes such as the grains and platelets measured in this thesis but may not be for other applications where objects are of a fundamentally different shape. This eliminates the requirement to select an ideal L as this is instead automatically computed by the software algorithm. Additionally, the proposed

technique also enables the orientation of different objects to be measured by different lengths of SE within the same image. For a binary microstructural image, this means the orientation of each platelet is the orientation of the longest SE that returns an opening value of 1 when coincident with any pixel, *x*, in a given image. This can be defined as follows:

$$G(x) = \arg sup_{\theta L}\, L\, \gamma_{B_\theta} f(x) \qquad \textbf{(6.2)}$$

This approach ensures that every measurement is performed using the most suitable length of SE which addresses the limitations of the method described in [63] and illustrated in Figure 6.5 and Figure 6.6. The novel extension to [63] that is proposed in this thesis is, therefore, more robust to changes in object size meaning it can be used to analyse objects of a range of sizes and orientations.

The improvement in terms of robustness that is offered by the proposed novel extension to the method presented in [47] can be demonstrated by measuring the synthetic binary images from Figure 6.2 and Figure 6.4 using the proposed variable length SEs. The difference in measurement accuracy between the original and new technique, when $S_L=2$, $S_\theta=10°$ and $L_{max}=1000$, is shown in Table 1. The proposed method does not affect the accuracy when objects are of similar dimensions but is drastically better when variations occur. The improved method produces almost perfect results for the more challenging images, with only a minor error caused by some irregularities in object shape.

Table 6.1: Comparison of measurement accuracy between original and new technique when applied to the synthetic image shown in Figure 6.4 and Figure 6.6.

Image	Measurement Accuracy	
	Original	New
Figure 6.3	100%	100%
Figure 6.5	57%	98%

Computational complexity is, however, greater than the previous version of this technique, as a larger number of morphological operations are performed. Morphological procedures can be performed quite fast using modern hardware and

algorithms so the significance of this complexity in terms of execution time would depend on hardware and datasets. The implications for microstructural analysis are evaluated in Chapter 8. Ultimately, it will depend on the application and the complexity of the image data to be processed to ascertain whether or not this extra computation is required for orientation measurements. Depending on the application, it may the case that faster, less exhaustive but less accurate methods can still produce suitable results. In titanium microstructures the shape of grains and platelets changes due to thermal and mechanical processes, of which a large variety already exist, with more being developed all the time. Therefore, difference in the width and aspect ratio of grains are possible and have been observed in some of the data used in this project. This makes the robustness of the variable length SE approach necessary to ensure accurate results, particularly given that even this method is still beneficial when compared to manual approaches, as demonstrated in Chapter 8.

Another key advantage of the approach proposed in this thesis is that it is also possible to accurately measure far more than just object orientation. The method returns an opening value for each pixel for every orientation and length combination. As the data inherently has 4-dimensions (x-position, y-position, orientation and length) it is difficult to analyse in its raw form. Instead this work proposes projecting the data onto a 3-dimensional orientation space we call the FLOS. Variations in the response for each pixel can then be studied to identify the size, morphology and orientation of image features. An efficient method to analyse this data using the FLOS is presented in Section 6.4.

6.4 The Feature Length Orientation Space (FLOS)

The concept of an orientation space, first introduced by Chen and Hsu [64], is a 3 dimensional representation of an image where an orientation axis is added to the traditional x,y positional axis. Values in this space are normally the result of applying some rotationally dependant filter. Previous research has shown that the opening of rotational SEs can provide a useful orientation space. In those methods, a simple binary orientation space is created for grouping parallel objects by placing a binary marker at the correct orientation index [63]. This section proposes a more detailed orientation space where each entry in the 3D array is equal to the length of the best fitting SE at

that location in the original image. This is illustrated in Figure 6.7 which shows how an elongated and globular object are represented in orientation space where dark colours represent higher values.

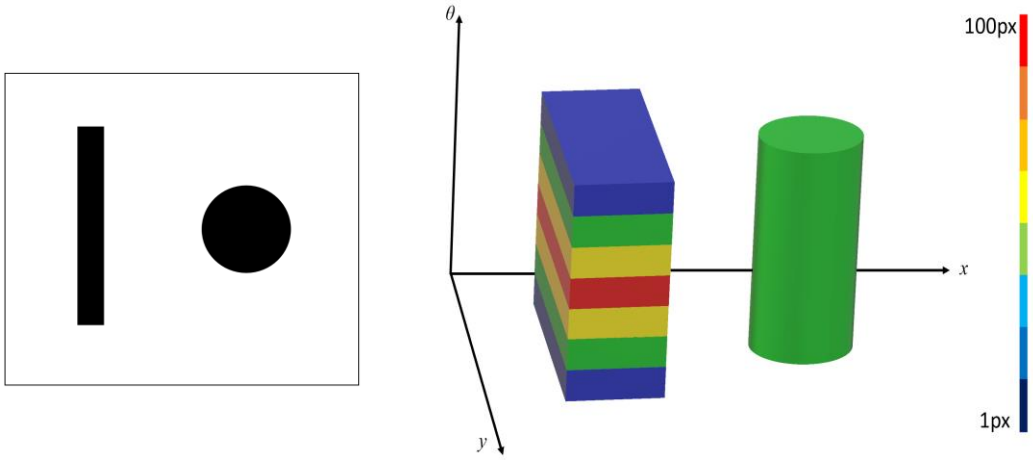

a) b)

Figure 6.7: Example of how objects map to the FLOS where a) original image and b) the corresponding orientation space where colour indicates the value at each location in this space (equivalent to the diameter of the object at that orientation)

For a binary image, the creation of the proposed orientation space, *R*, can be defined formally as the maximum length of SE to return a "1" for each pixel and orientation combination, as in Equation (6.3).

$$R(x, y, \theta) = max_L\, L, (x, y) \in \gamma_{B_{\theta L}} I(x, y) \tag{6.3}$$

For a greyscale image, the opening value returned when a SE fits depends on the grey values of the object and surrounding pixels. This difference between the binary and greyscale implementation is illustrated in Figure 6.8, which shows that for a binary image the output is a clear "1" or "0" while in a greyscale image the output changes between 2 seemingly arbitrary values.

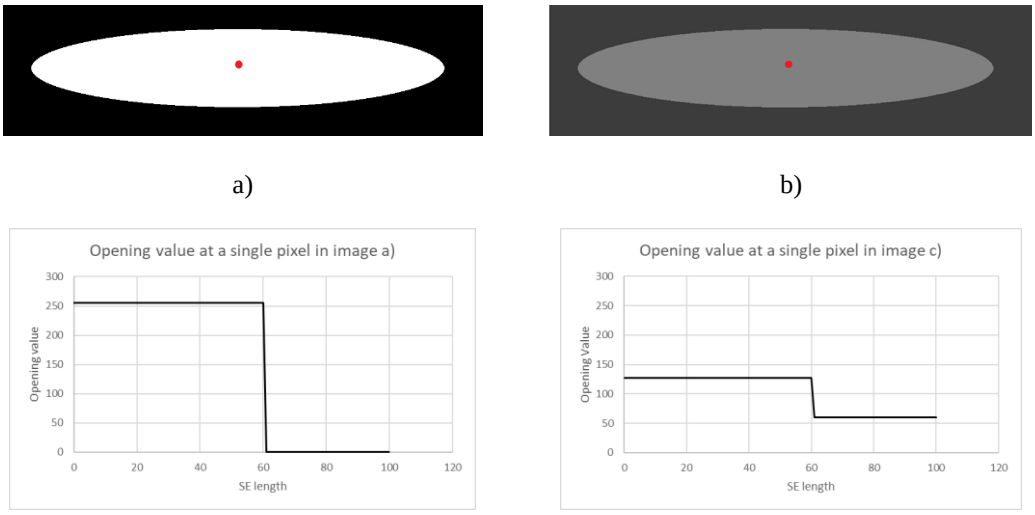

Figure 6.8: Opening value for linear SE at θ=180° for various lengths for a) a binary and b) a greyscale image

Therefore, in order to create the same orientation space, the length used should not be the longest to return a "1" but the longest that is above a pre-defined threshold. In practise the same effect can often be achieved far simpler by instead thresholding the original image and creating R_θ as described in Equation (6.3). An alternative orientation space can, however, also be created by summing the morphological opening value at each pixel and orientation for all lengths, as in Equation (6.4).

$$\mathrm{R}(x, y, \theta) = \sum_{l \in L} \gamma_{B_{\theta L}} I(x, y) \tag{6.4}$$

This works for either binary or greyscale images and does not require any threshold parameter be set. However, the values are not informative of object size meaning that only orientation and shape could be assessed. As thresholding microstructural data to obtain binary images is normally successful, the remainder of this work will use only the orientation space defined in Equation (6.3).

6.5 Measurements from the FLOS

The FLOS contains descriptive information of the dimensions of objects at each location and in a range of orientations. This allows a significant amount of information to be extracted from this space, without the need to segment the image into the individual objects being measured. Consider Figure 6.9 which shows the variation in values in the orientation domain for a pixel that lies inside an elongated object at an orientation of 90°. The maximum, minimum and shape of this curve describe the object that the pixel under study belongs to. The method to extract this information is given in the remainder of this section.

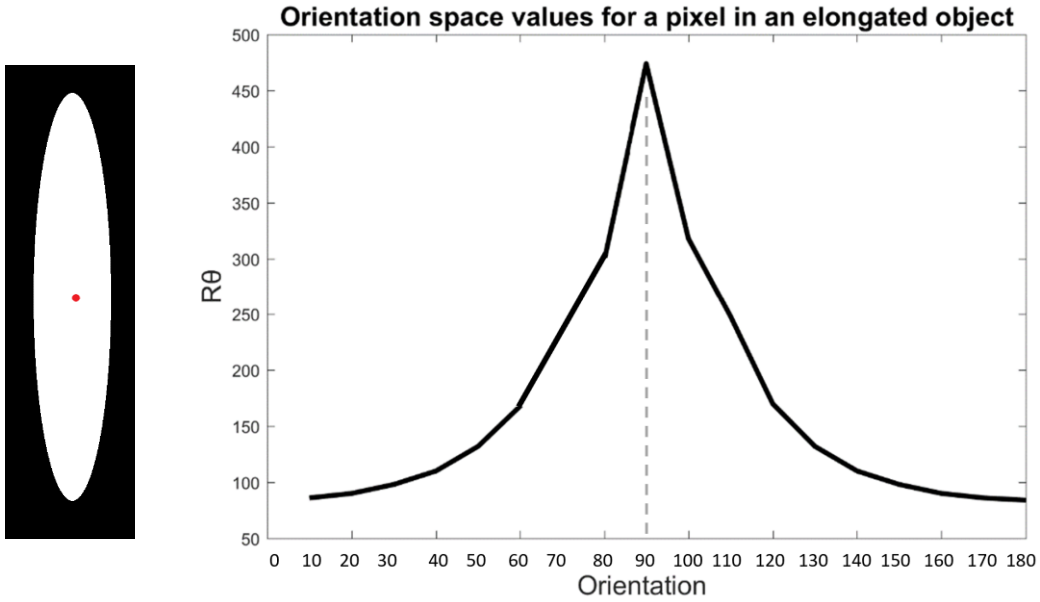

a) **b)**

Figure 6.9: Values in the orientation space for a single pixel that lies within an elongated object where a) image object with x,y value marked, b) *R* for each orientation domain position at that location

6.5.1 Object orientation

The orientation of image objects, f_θ, is equal to the orientation of the longest SE that fits the object. This can be identified in the orientation space by calculating the location of the maximum value in the orientation domain for each pixel, as in Equation (6.5).

$$f_\theta(x, y) = argmax_\theta R(x, y, \theta) \tag{6.5}$$

6.5.2 Object dimensions

The length of an object, f_L, is equivalent to the length of the longest SE to fit within that object at any orientation. This is indicated by the maximum value in R_θ, as in Equation (6.6). The width of an object, f_W, is equivalent to the length of the longest SE to fit the object at the orientation where this length is shortest. This is indicated by the minimum value in R_θ, as in Equation (6.7).

$$f_L(x, y) = max_\theta R(x, y, \theta) \tag{6.6}$$

$$f_W(x, y) = min_\theta R(x, y, \theta) \tag{6.7}$$

6.5.3 Object Shape

Variations in the orientation space are illustrative of the shape of objects. For an elongated feature, such as in Figure 6.9, there is a very clear peak value in the orientation domain. By comparison, an equiaxed feature returns more consistent values for each SE, as illustrated in Figure 6.10.

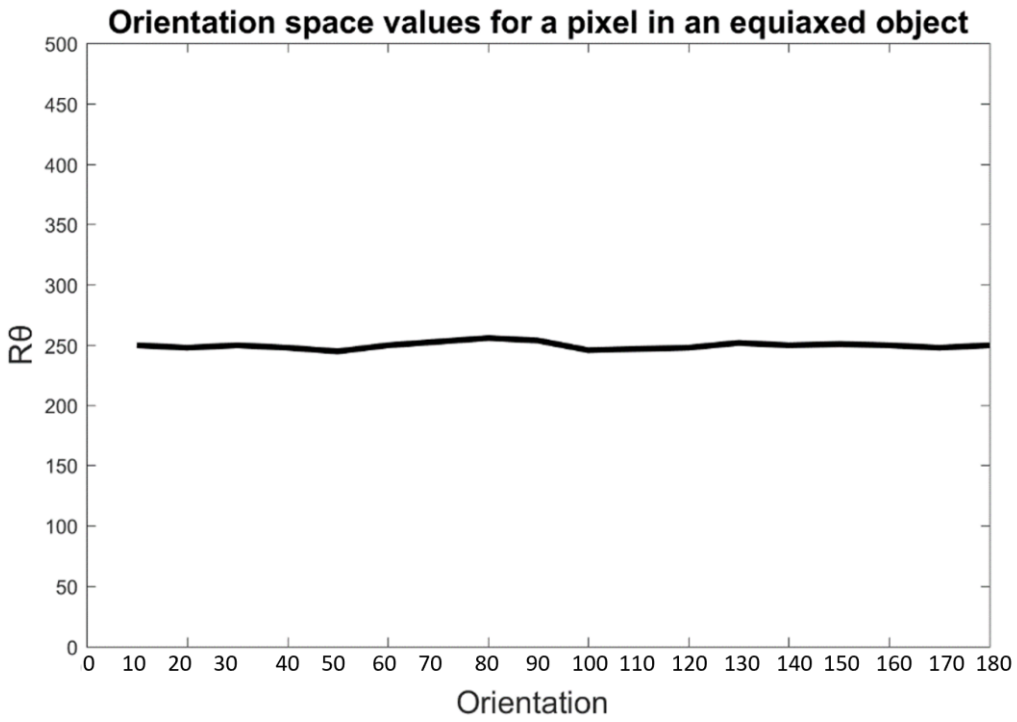

Figure 6.10: Values in the orientation space for a single pixel that lies within a globular object

This information can be used to measure the elongation of image features. The variance in the orientation domain, as in Equation (6.8), provides a measure of the roundness of image features, *Rd*. As the variance for larger objects will be larger for bigger objects of the same shape this metric is normalised by dividing the result by the maximum value of R_θ, for each pixel. The ratio between maximum and minimum values, as in Equation (6.9) approximates the aspect ratio of objects, *AR*, provided they are elliptical. Note that as this definition considers only the maximum and minimum values this is more prone to noise or distortion than the *Rd* shape descriptor. For pixels where the maximum of *R* is 0 then then these equations should be disregarded and the output should also be 0. This should only apply to the image background.

$$Rd(x,y) = {\sigma^2}_\theta\big(R(x,y,\theta)\big) \Big/ sup_\theta\, R(x,y,\theta) \tag{6.8}$$

$$AR(x,y) = \sup R_\theta(x,y,\theta) \Big/ \inf R_\theta(x,y,\theta) \tag{6.9}$$

6.6 Analysis of microstructural images using the orientation space

It is described in Section 6.5 how the orientation space can be used to extract feature measurements on a per pixel basis. The proposed technique is intended to measure features relating to elongated alpha platelets. As such, the features of interest are,

- Platelet width
- Platelet orientation
- Volume fraction of globular alpha
- Size of platelet colonies

The remainder of this section illustrates how these measurements can be aggregated into overall measurements of each microstructural feature, in line with the standards expected in microstructural analysis. This includes a novel algorithm for isolating colonies of alpha platelets based on the recorded data. Only qualitative data suggesting the effectiveness of these techniques are given in this section. Full quantitative validation is provided in Chapter 8.

6.6.1 Thresholding

The proposed analysis techniques measure platelets by finding the orientation and length at which a SE fits within the alpha phase. Thresholding techniques are used to create binary representations of an image based on the intensity of pixels, a property that is significantly different between the two phases in Ti-6Al-4V microstructural images. This can, therefore, be used to create a binary microstructural image where only alpha phase pixels have the value "1". Unlike larger alpha grains, where intensity variations within each phase provide valuable information regarding grain boundaries, intensity variations in alpha platelets are typically not useful as their fine nature makes it difficult to distinguish useful information from noise and distortion. Correct thresholding, therefore, reduces the risk of errors from these sources. It also increases efficiency as the morphological operations used can be performed more quickly on binary data. Automated thresholding procedures, such as adaptive version Otsu's method [108], have previously been used to separate the alpha and beta phases in

titanium microstructures. A full explanation of the best application of thresholding is provided in Section 5.5.1.

6.6.2 Width of alpha platelets

Applying the equation in Equation (6.7) to the orientation space gives a 2D image, $f_W(x,y)$, where the value of each pixel equals the measured with of the object that pixel lies within. The result of applying this to a microstructural image from the titanium dataset is shown in the visualisation Figure 6.11, where warmer colours represent wider platelets.

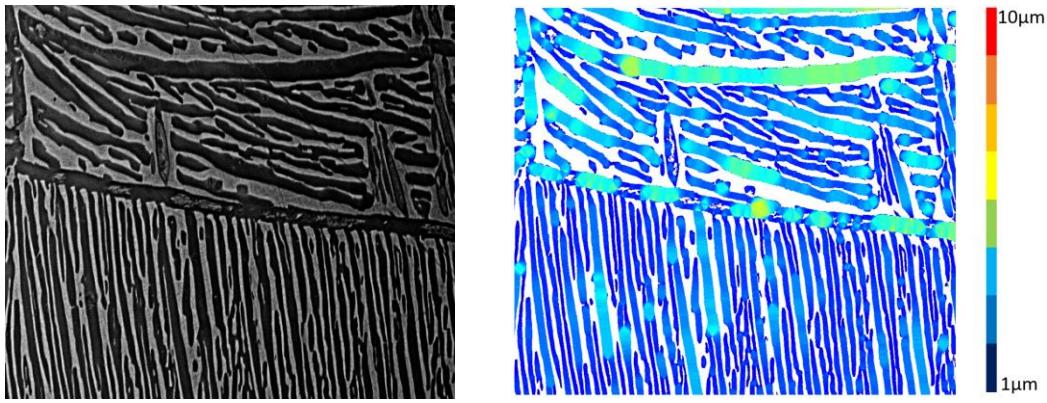

a) **b)**

Figure 6.11: Width map produces by the new technique where a) original image and b) colourmap of width

The image presented makes it easy to qualitatively asses where the widest and narrowest features are in the image. However, the purpose of this work is to determine the width of platelets in microstructures quantitatively. This is normally measured by the mean width of platelets in the image. This can be computed simply as the mean value of pixels in $f_W(x,y)$. As $f_W(x,y)$ is 0 for all pixels in the image background, only non-zero values should be considered when performing this calculation.

6.6.3 Orientation Measurements

Applying Equation (6.5) to the orientation space gives a 2D image, $f_\theta(x,y)$, where the value of each pixel equals the measured orientation of the object that pixel lies within. This can be displayed as a visualisation of platelet orientation such as the colourmap

shown in Figure 6.12, where the colour of each pixel corresponds to the orientation of its parent platelet.

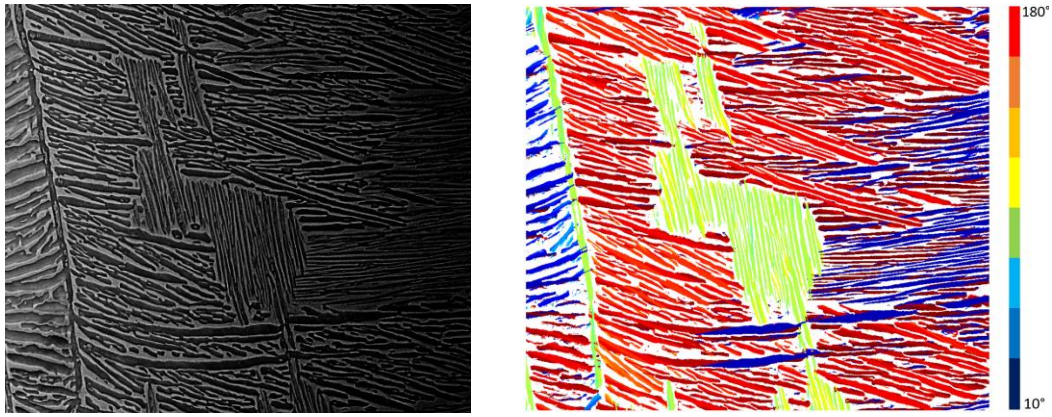

a) **b)**

Figure 6.12: Orientation map produced by the new technique where a) original image and b) colourmap of orientation

As with the width measurements, this image makes it easy to identify qualitatively the most significant orientations in the image and where deviations in orientations occur. However, it is again necessary to compute orientation information quantitatively. In this case the mean value is not informative as orientation values existing in a finite field. Therefore, a histogram representation of how frequently each orientation occurs is typically most useful. As before a value of 0 degrees is uninformative as this represents the background of the region. Hence it is important to measure orientation through the range 10-180° and not 0-170°.

6.6.4 Separation of globular alpha

Separation of globular alpha has two purposes in microstructural analysis; determining globular volume fraction and ensuring that globular and elongated objects are measured separately. Applying Equation (6.8) or Equation (6.9) to the orientation space gives a 2D image, where pixel values are informative of the shape of the object that pixel lies within. With both methods, higher pixel values are returned for more elongated grains. An example of this, using Equation (6.8) is given in Figure 6.13.

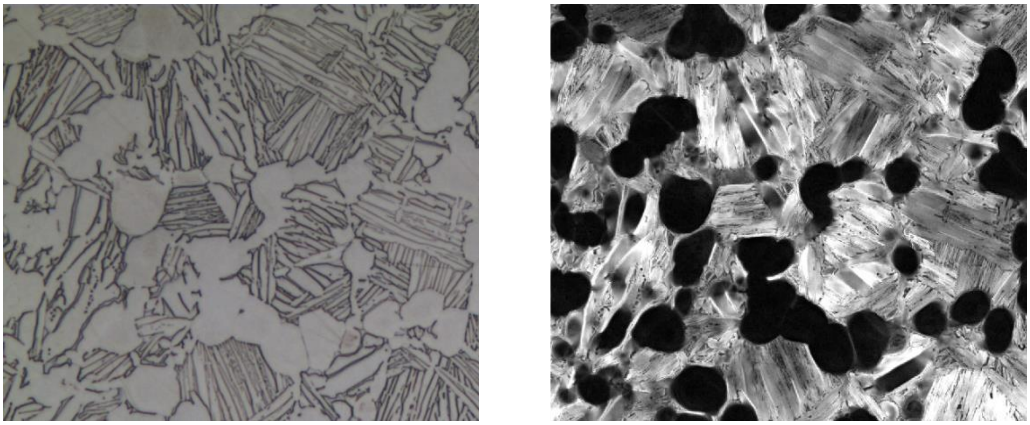

a) **b)**

Figure 6.13: Globularity map where a) original image and b) greyscale representation where higher intensity equates to more elongated structures

The image itself makes it easy to identify qualitatively where the most globular grains exist. Quantitative measurements can be achieved by thresholding this image. The exact threshold, T_s, used will depend on the application and what amount of shape variation is allowed for a grain to be considered globular. The globular volume fraction can be computed as the area below the threshold as percentage of the total alpha phase area, found by the sum of all elements in the binary image, produced by the initial thresholding of the microstructural data, described in Section 6.5.1.

$$V_g = \frac{Rd(x,y) < T_s}{\sum I_{binary}(x,y)} \quad \textbf{(6.10)}$$

As the globularity of grains is based on the variance of measurements across all angles, rather than the length to width ratio, it is difficult to intuitively link the value to a particular shape or aspect ratio. This means the threshold between globular and lamellar grains, T_s, must be chosen experimentally. Although this may initially appear to introduce subjectivity, once a threshold has been set this can be kept constant and applied consistently to all grains in every microstructure so eliminates the subjectivity between subsequent measurements, that exists in manual approaches currently deployed to measure these features. This automatic segmentation of globular alpha from platelets is particularly useful as it enables width and orientation measurements

based on globular grains to be ignored. This previously required manual corrections [11].

6.6.5 Colony measurements

The technique proposed in this section measures individual platelets but cannot be used to directly measure colonies, as it cannot inherently distinguish colony boundaries from platelet boundaries. However, as colonies consist of a cluster of adjacent, parallel platelets, the orientation information, provided by this technique, can often be used to compute regions representing colonies. The aim is to mark individual platelets of the same orientation and then join any that are adjacent to each other into a single connected region representing a colony, as in Figure 6.14 a)-c). This concept was previously presented in [6] but measurement accuracy was inconsistent, in part due to inaccuracies in the initial orientation measurements which are improved using the new technique proposed in this chapter. There were also difficulties isolating parallel platelets as this was done by searching for peaks in a histogram of all orientation values, which would not exist if platelets had an even variety of different orientations. In the proposed new approach, the orientation space makes it easier to isolate parallel platelets as they each exist on a separate orientation plane within the multidimensional space. Furthermore, false orientation measurements due to noise are spread across all planes which reduces their impact on results. These factors allow the new approach to group similarly orientated platelets together more reliably. The algorithm for identifying colonies based on the orientation response is given below, with an illustration of its operation provided in Figure 6.14.

Algorithm 2: Group platelets into colonies

Input: orientation response, w_{max}, cs

Output: colonies

1. Apply a threshold to the orientation response, R_θ, to create a binary representation where a 1 designates the 1 or more most probable orientations at each x, y location
2. For each θ in the orientation space
    a. Perform a morphological closing with a linear SE perpendicular to θ of length w
3. Find the largest 2D region in all planes of the orientation space
4. For all regions larger than cs% of the largest colony
    a. Add in adjacent regions that are only 1 orientation measurement different
5. Fill any fully enclosed holes in the region
6. Add region to output and remove any pixels in its location from the original orientation space
7. Measure regions within boundaries

Two parameters are required to allow the algorithm to decide which platelets should be grouped together and which should not. These are, the maximum width between platelets to be considered adjacent, w_{max}, and the minimum size of a cluster of platelets to consider as a colony, represented as a percentage, cs, of the largest colony in the image. An absolute value of colony size could also be set, however, a percentage of the largest colony is used for two reasons. Firstly, it allows the algorithm to select a suitable size limit automatically based on the data it is presented so this would not need to be changed manually for each image. Secondly, this parameter would reflect the order of colony to be considered. For example, if several colonies of around 100μm exist then colonies of 10μm are likely to be considered as secondary order colonies and may not be included in measurements, while if the largest colonies where 10μm

then these would be first order and should be measured with colonies around 1μm and less more likely to be ignored. The *cs* parameter makes this option available to the materials scientist to adjust depending on their analysis requirements.

The proposed algorithm applies a threshold to the orientation space to create a binary representation where for each pixel a "1" exists only on the orientation planes of the most probable platelet orientations. In the simplest case, the threshold can be set as the maximum value for each pixel. In some cases, there may be two equally likely candidate orientations even when the threshold is set to the maximum value for that pixel in orientation space. As the aim is to merge roughly parallel adjacent platelets onto a single colony, the pixel is marked as a "1" for both orientations in the binary orientation space. It is also possible to include values within a percentage of the maximum value. For example, for S_θ=10° a platelet at approximately 15° would return similar values for both 10° and 20° so it can be beneficial mark both in the binary orientation space. This would make the algorithm more lenient in how similarly orientated a platelet must be to be included in the same colony, which is particularly useful when platelets are not completely straight.

Once the orientation space has been binarised, adjacent platelets are then joined by a morphological closing each orientation plane by a SE a single pixel wide, of length w_{max} and of orientation perpendicular to the current plane, as shown in Figure 6.14 b) and c). To prevent nearby colonies from merging the largest connected component (grouping of platelets) in any single orientation plane is then identified and isolated. The remainder of the algorithm is applied only to this region to produce a marker for that corresponding colony. Any adjacent regions from neighbouring planes are added, as in Figure 6.14 d). Any holes in the resulting colony are then filled, as in Figure 6.14 e), and the pixels in this region are set to zero for all planes to prevent this colony merging to any adjacent colonies. All pixels within the area of the marker are set to zero in the orientation space and the same process is repeated with the new largest connected component until all colonies within *cs*% of the largest colony are located and can then be measured. The boundaries of the resulting colony regions are shown in Figure 6.14 f). While computing markers individually rather than simultaneously is less efficient, this approach was necessary to prevent the erroneous merging of separate colonies found when apply other techniques to our data [63].

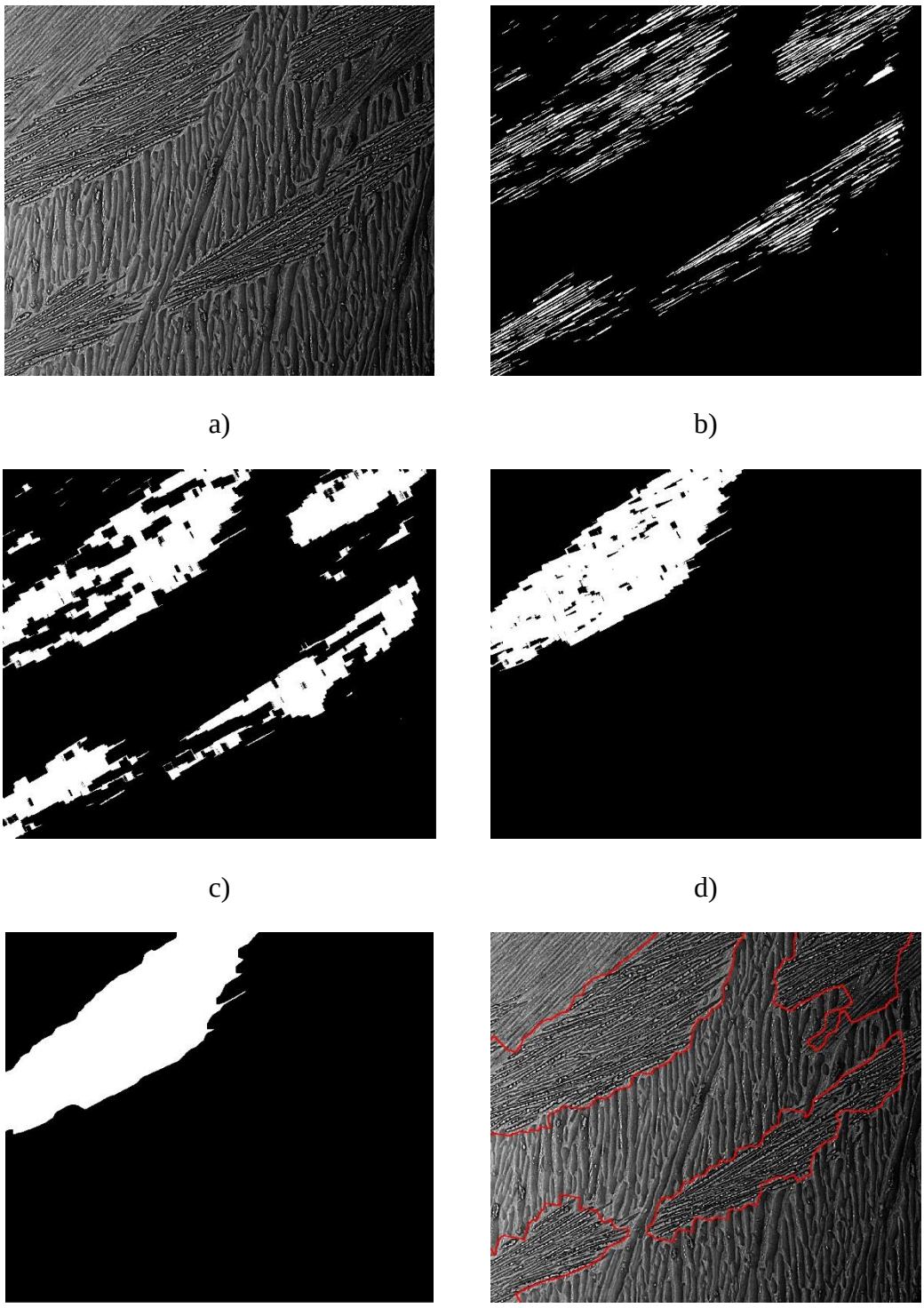

Figure 6.14: Illustration of colony identification where a) original image, b) binary orientation space where θ=30°, c) closing to join platelets, d) largest region with adjacent pixels added e) final identified region with holes filled, f) result when the processes is repeated for all regions

6.7 Summary

A new method for measuring a range of features of alpha platelets has been proposed. This is achieved by developing extensions to existing methods of measuring the orientation of thin structures in images and adding new data processing steps to also measure size and shape. To do this the image is probed by a set of SEs of varying lengths and orientations, with the morphological opening used to determine how well each SE fits each object. This improves the results that could be achieved by an existing approach where only a single length of SE is used, which was shown to limit the potential of a similar existing technique [47] which has been extended in this work. This data is then projected onto a 3-dimensional orientation space where each element represents the maximum length of SE that can fit at that location and orientation. It is shown that this new multidimensional space can be interrogated to extract measurements of object orientation, size and shape on a pixel by pixel basis without the need to segment the image. The application of the new techniques to measures features of martensitic microstructures is also described in this section. The effectiveness of the proposed method is illustrated visually in figures showing heatmaps of Ti6Al4V microstructures transformed by these methods. A novel algorithm for locating, segmenting and measuring colonies of alpha platelets comprised of martensitic microstructures is also proposed. Empirical trials to validate the accuracy and reliability of all of the above, are provided in Chapter 8. The weakness of this new approach is computational efficiency, as using a range of SEs of varying lengths applied at different orientations increases the range of morphological operations that need to be performed. In practical microstructural analysis, the run time will still typically be far less than any manual measurement with the added benefits of improved robustness and repeatability. For titanium microstructures the accuracy improvement over the fixed length method is significant, however, in other applications it should be considered whether this additional computation is necessary.

7 A SOFTWARE TOOL FOR MICROSTRUCTURAL ANALYSIS

The purpose of the novel image processing techniques proposed in this thesis is to improve the analysis of Ti-6Al-4V microstructures. However, the existence of these techniques alone does not guarantee any improvement in analysis in real world scenarios. Like many techniques of this type, proper use of the new algorithms requires the appropriate setting of parameters and awareness of which methods are suitable to each dataset. It is, therefore, critical that the techniques proposed here are made accessible to a material science audience who may not be familiar with image processing or implementing software algorithms in general.

To facilitate this, a software package is developed that embeds implementations of the methods presented in both Chapters 5 and 6 such that they can be used by non-image processing experts. The software will ask the user to specify the microstructure type under study from which a significant number of the parameters can be set automatically based only on this information. The user will then be given the option to adjust or set some optional parameters, to tweak the results dependant on the microstructure type. The parameter names and controls are kept as intuitive as possible. The software will also provide visualisation to help the user understand the effects of parameter changes. The exact parameter tweaks are recorded so that any measurements performed are repeatable.

The software tool described in this chapter is used to apply the novel algorithms presented in Chapters 5 and 6 during the validation of the new algorithms presented in Chapter 8. This helps to ensure that the results presented are relevant to real world microscopy applications, as parameters are set in the same way as would be the case if these techniques were employed either in industry or academia.

The contribution of this chapter is a novel interface and control mechanism to intuitively set parameters and apply image processing techniques to microstructural analysis.

7.1 Software requirements

The main function of the software package is to make the techniques proposed in the previous chapters accessible to those with little or no knowledge of image processing, but a good understanding of material science. It is, therefore, important that the software interface is written in plain English with as little image processing terminology used as possible. A key aim of automated methods is to reduce both measurement time and the amount of effort required, from a material scientist. To achieve this aim, the ability to batch process large datasets is important. It is also an aim of the new analysis techniques to be both robust and repeatable. These goals are often contradictory as dealing with varied datasets will regularly require parameter changes, but such changes introduce the possibility to achieve different measurements from the same datasets. To balance these objectives, the software tool designed would store any parameter changes alongside the output data so that if measurements were to be repeated, or other measurements from the same dataset were required, the same parameters could be re-used. This allows for repeatability within a single dataset, while still allowing the software to be adapted to other datasets with different properties.

7.2 Design and use of the software tool

The proposed software tool has a user interface designed to walk the user through the steps involved in performing analysis. The layout of this interface is shown in Figure 7.1. It can be observed that on the initial run of the software only the “Load Image” button is available to the user. Other options are visible, so users can familiarise themselves with the available features, but remain disabled until such time as their use is appropriate. This same theory is applied throughout, as only options that are useful at each stage are made active. The remainder of this section demonstrates the use of this tool and describes the benefits of the proposed methods of implementation. The segmentation of images of globular microstructures produced by a SEM were chosen as an example to illustrate the use of the software. If any step differs for other

microstructure types, then this difference also is described. This avoids the need to display an excessive number of figures while still providing all pertinent information about the operation of the software.

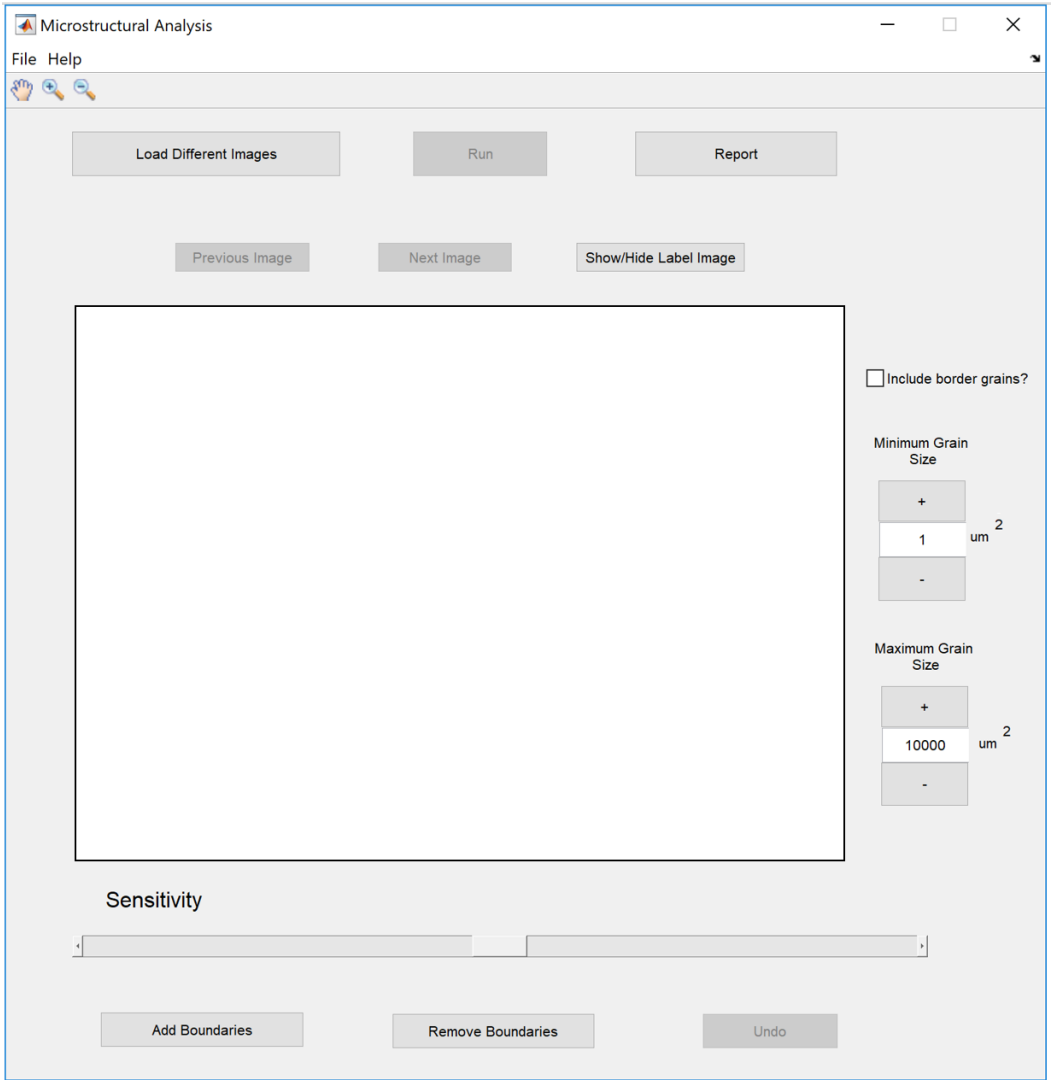

Figure 7.1: Illustration of layout of software tool

7.2.1 Image input

The first step is to load in the images to be measured and prepare them for processing. To do this the user is initially presented with a “File Selector” window, shown in Figure 7.2, upon pressing the “Load Images” button. From here it is possible to navigate to the requisite folder and select either a single, or group of images to be measured, using standard file explorer procedures. It will be shown later that the

software will provide the option to view measurements of individual images or a collation of the results from all images. Therefore, when measuring multiple datasets, where collated data about each set is required, each dataset should be loaded and analysed separately.

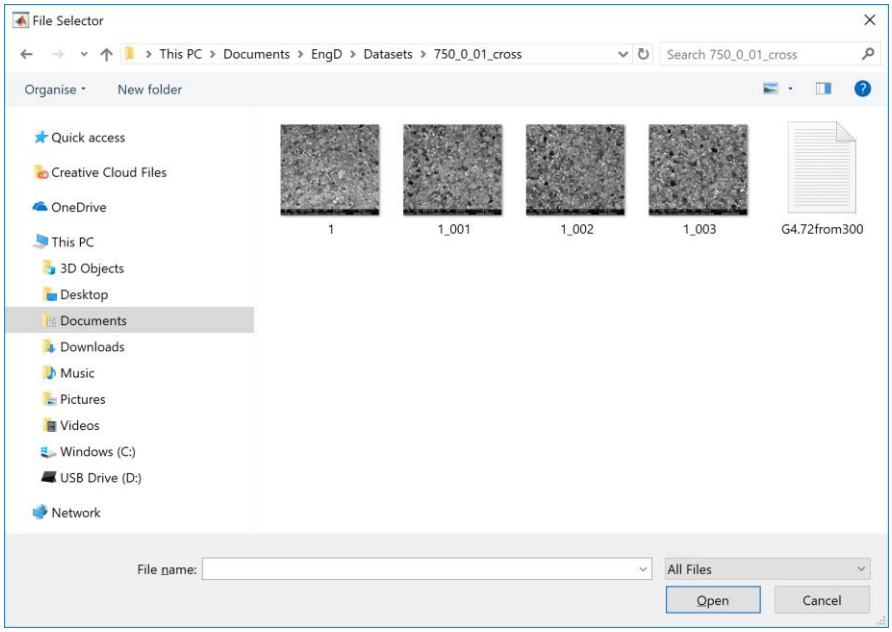

Figure 7.2: File selector for choosing digital image of microstructure to assess

The material scientist is then prompted to select the imaging technology (SEM or OM) and features of interest using checkboxes. This will inform the software which techniques from Chapter 5 and 6 are necessary to apply. Once the image is loaded the user will then be prompted to locate the scalebar by drawing a line over the bar, by the pop-up window in Figure 7.3. This makes this message impossible to miss and also provides instructions to make this process as intuitive as possible. Once the "OK" button is pressed this window will disappear to provide the user unobscured access to draw in the scalebar.

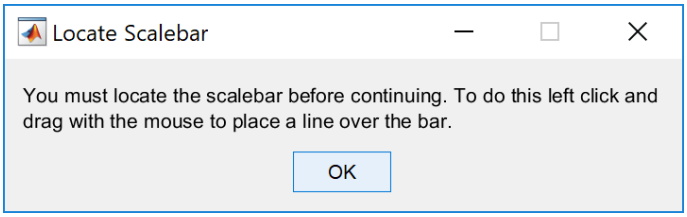

Figure 7.3: Pop-up window requesting user indicate the location of the scalebar

At this point the pan and zoom options, located in the upper left corner of the software window, will become available to aid this task. As it is assumed that all images in each batch are from the same dataset this process only needs to be completed once, each time the software is run. An example of the scalebar manually drawn on the first image loaded is shown in Figure 7.4.

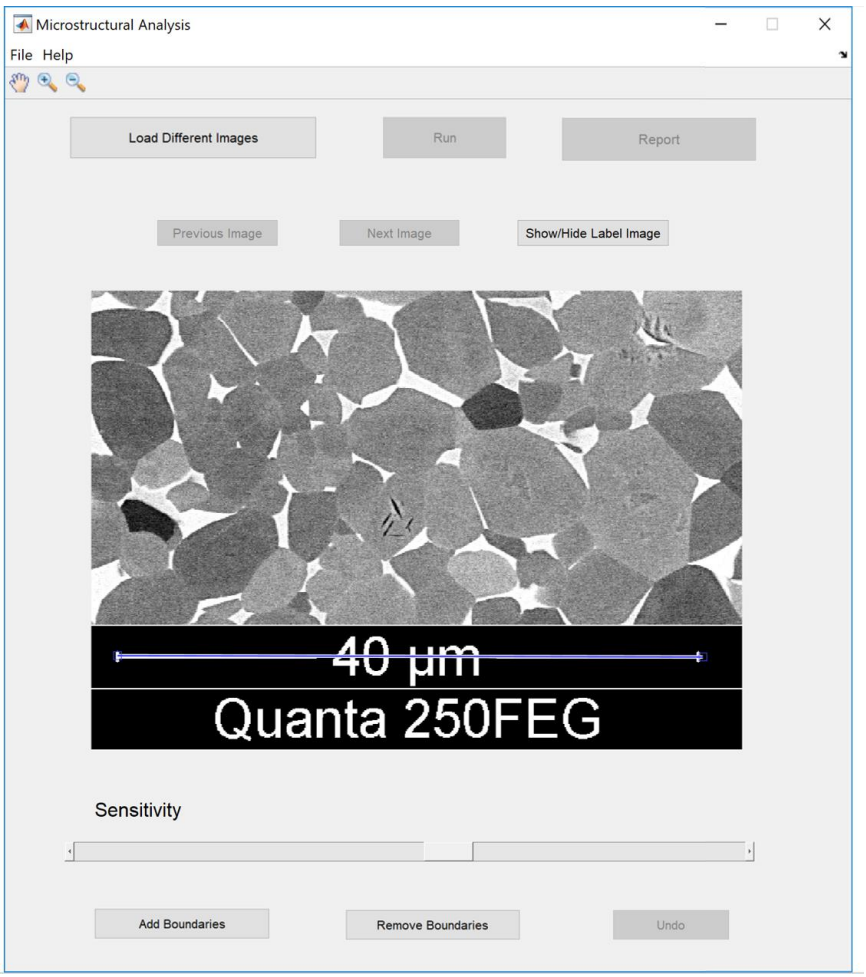

Figure 7.4: Software interface with scalebar drawn after pan and zoom

The user is then prompted to enter the scale written on the scalebar, alongside the units used, in the pop-up window shown in Figure 7.5. This information will allow the software to present measurements to the material scientist in SI units of different scales. This also makes it possible for the software to convert units as required, as is described later in this chapter.

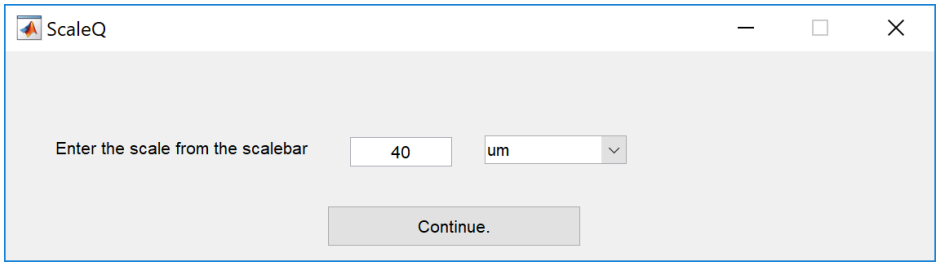

Figure 7.5: Pop-up window requesting the scale and units

As well as recording the scale through the length of scalebar drawn the software will also crop or edit the image so as to remove the scalebar based on the location information provided. For example, in the SEM images shown it is known that the scalebar exist along the bottom of the image therefore by cropping the image to a height finishing 50 pixels above the scalebar can remove this bar from automated measurements, as shown in Figure 7.6. In OM images the scale bar is normally shown as an overlay in the bottom right hand corner, so the image is cropped from the top left corner to a point 25 pixels left and upwards from where the user has drawn the scalebar.

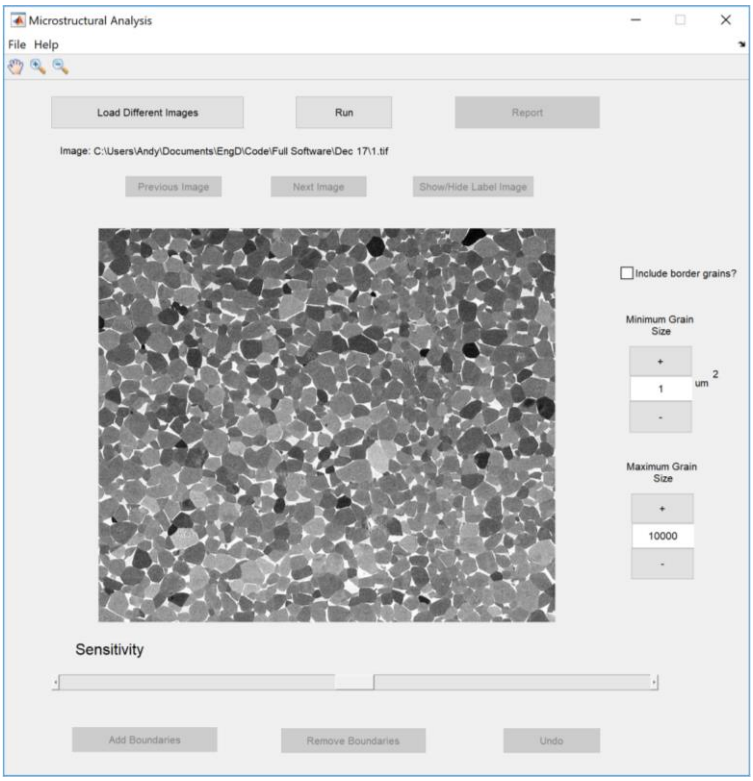

Figure 7.6: Main window with scalebar removed

7.2.2 Algorithm use and parameter selection

Once the images have been loaded into the software the "Run" button will become available. For the segmentation example shown in this chapter there is also an option to set the minimum grain size expected, as seen in Figure 7.6. By default, this is set to 1μm as this was found empirically to give good results in most microstructures in this study. This value is used to parameterise the merging algorithm proposed in Section 5.5.2. After merging it is expected that grains below this size would no longer exist, however, if any still do then these would be discounted from measurement. It is advisable to always set this at least a little above 0, as there is no microstructural image where a grain of only a few pixels could be reliably measured, but even a few such detected regions could significantly affect the average results. If platelet analysis is required, then there will be an option to set the step size between the orientation and length of SE. As such terminology would only be understood by those who were familiar with the operation of the technique in Chapter 6, these are termed "Orientation Accuracy" and "Length Accuracy". By default, these parameters are set at the level recommended in Chapter 6 with Orientation Accuracy at 10° and Length Accuracy at 2 pixels, displayed in terms of the chosen unit of length. The length of the longest SE to use must also be set, which will determine run time. This is controlled by a parameter called "Max length". An option also becomes available, so the user can adjust images that appear as particularly dark or bright. A slider is provided to make this as intuitive as possible. A full description of the effect of each parameter is provided by hovering the mouse of the title of the respective option. It should be noted that all of these are optional and good results will normally be achieved using the default values. For example, in the validation in Chapter 8 it is shown that it is not necessary to adjust any of these parameters from the default values to obtain excellent results. The software highlights this with an "Advanced" heading above the options mentioned.

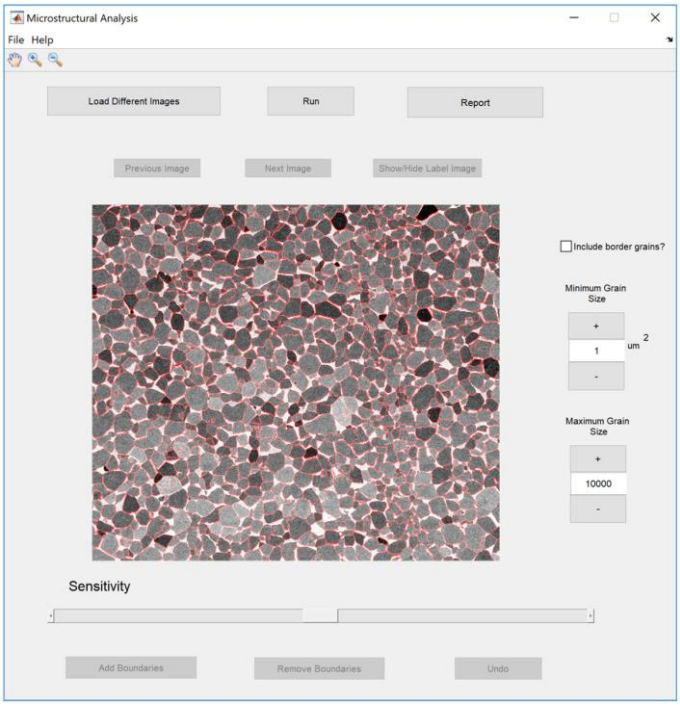

a)

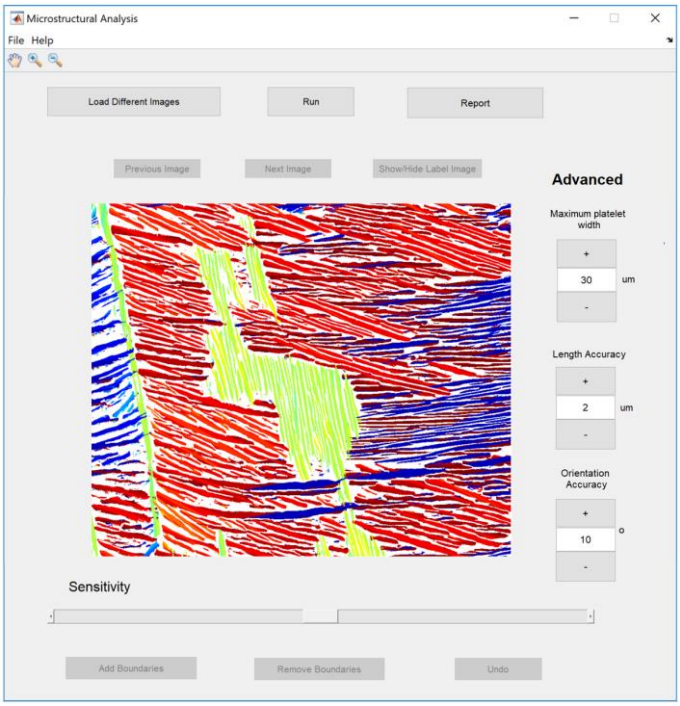

b)

Figure 7.7: Main window showing a) segmentation result b) platelet orientation

Once the “Run” button is pressed the software tool will automatically apply the most appropriate technique to measure the image based on the microstructure and image type previously selected. A visualisation of the result will then be shown in the main window. For globular grain analysis the software shows an overlay of the segmentation of the grains on top of the original, as demonstrated in Figure 7.7 a). For platelet analysis the software will show a colourmap of the orientation of each platelet, as demonstrated in Figure 7.7 b). For bi-modal microstructures where the both types of analysis are requested, the segmentation result overlay is shown by default with the colourmap of orientation visible when pressing the “Next Image” button in the software.

At this stage, for globular grain analysis, the contrast slider disappears and is replaced by a slider called “Sensitivity”. This parameter controls the level of segmentation by controlling the t_s parameters from the CGSA algorithm which specified the threshold used by the initial edge detection algorithm when computing markers. This is referred to as “Sensitivity” in the software as this is more intuitive to understand and referring to this as a threshold would only be sensible to those who knew the inner workings of the algorithm. This is a key parameter as it enables the user to determine the size of intensity change that indicates a grain boundary. It has been determined empirically that, unlike most other parameters used to control the techniques presented in this thesis, the optimal value of sensitivity differs slightly for each dataset. No similar parameter exists for platelet analysis as the most accurate result is always achieved provided that the step sizes and width factor is left at the default value. Fortunately, the speed of the segmentation algorithm allows for intuitive adjustments to be made to the segmentation by using the sensitivity parameter and observing the output segmentation result. Upon release of the sensitivity slider the segmentation results will update showing the material scientist the new segmentation result as a function of varying the “Sensitivity parameter”. A loading screen will inform the user of progress as this may take several seconds. By panning and zooming the image using the controls provided, the effect of sensitivity adjustments on segmentation can be easily observed allowing the best setting for this parameter to be determined by a material scientist. This is demonstrated in Figure 7.8 which shows the difference his parameter makes, a few changes in grain boundary detection manually annotated with yellow arrows.

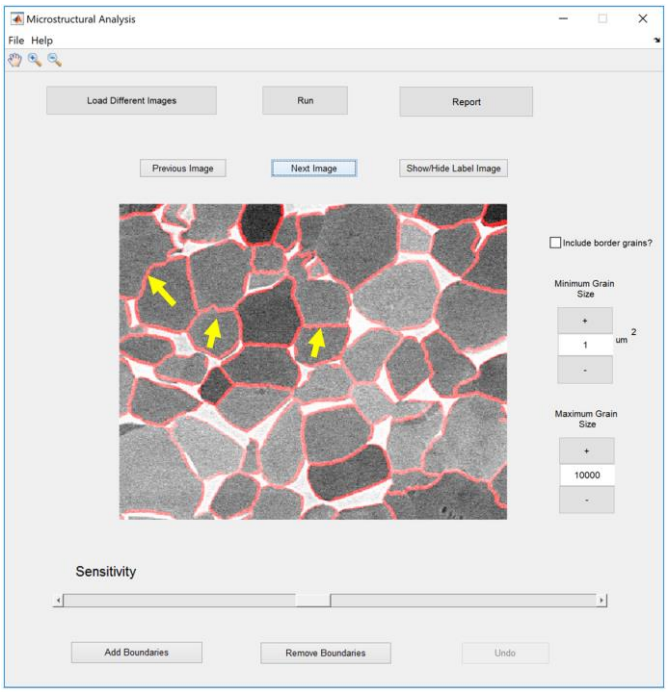

a)

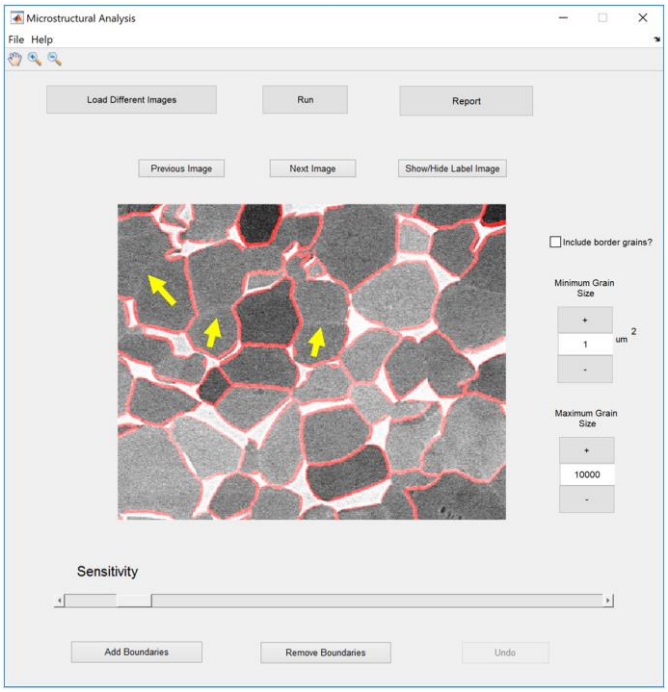

b)

Figure 7.8: Illustration of segmentation adjustment where a) is the default position b) is a lower sensitivity and yellow arrow indicate locations of segmentation change

The minimum grain size parameter can also be altered post segmentation. The "show/hide label" button can also now be used to generate a display indicating where each alpha grain is in a different colour, making it easier to distinguish which grains are considered in the final measurement, as shown in Figure 7.9 . Controls are also provided to add or remove boundaries manually. This would allow segmentation errors to be manually corrected by an expert user in cases where extreme accuracy is required. Increasing the sensitivity can produce over-segmented results and which take more time to process, particularly at the region merging stage. However, the time taken to perform an accurate segmentation of the image typically does not depend on the aforementioned parameters and typical takes around 5-20 seconds, as will be discussed in Chapter 8.

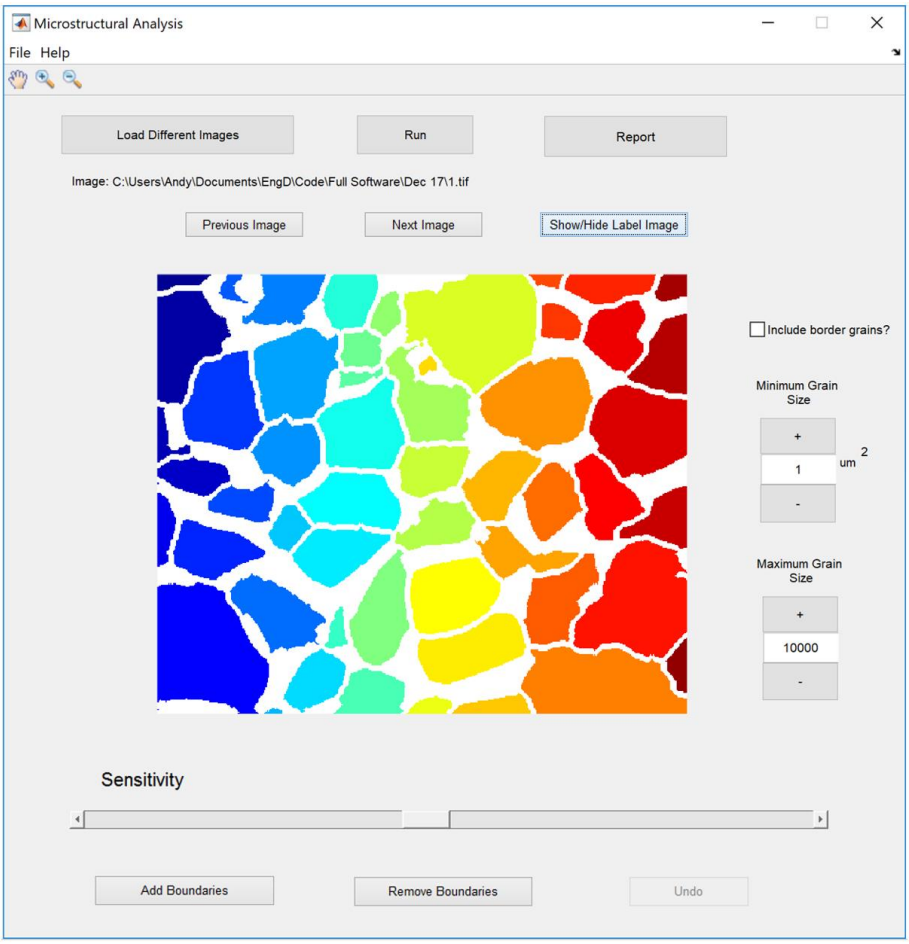

Figure 7.9: Illustration of labelled image

The technique for analysing platelets does not require an optimum parameter be found to achieve accurate results. Instead it is only necessary to set w_s, controlled by the "Maximum Platelet Width" setting, to be at least equal to the widest platelet being analysed, with any value above this threshold achieving accurate results. However, this setting will affect measurement time with an optimum value, in terms of software efficiency, existing where the maximum platelet width is set correctly. There is value in setting this correctly as measurement of platelet widths where found to take considerably longer than grain segmentation, at around 4 minutes, as discussed in Chapter 8. One option available to optimise the software run-time is to process some data with this parameter set high, so as to be slow but accurate, and use the width measurements reported to choose a more efficient parameter for further analysis on that dataset. Alternatively, a materials scientist can use either a manual measurement or best guess at platelet width and then relay on the colourmap display to catch errors. This is illustrated in Figure 7.10 which shows how errors can be spotted from this visualisation. The parameter changes available for platelet analysis require the full algorithm to be run again to refresh results. If the user alters these settings and attempts to report results a pop-up window will warn that all results reported will be based on the previous settings.

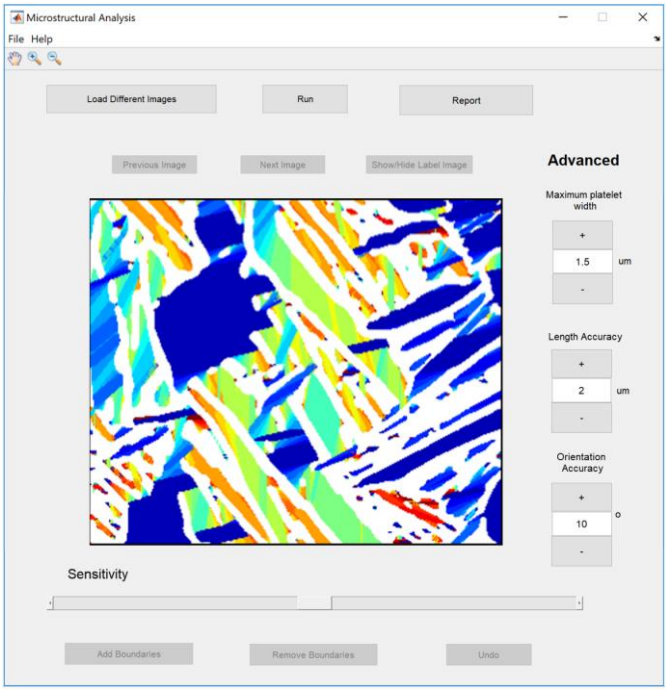

a)

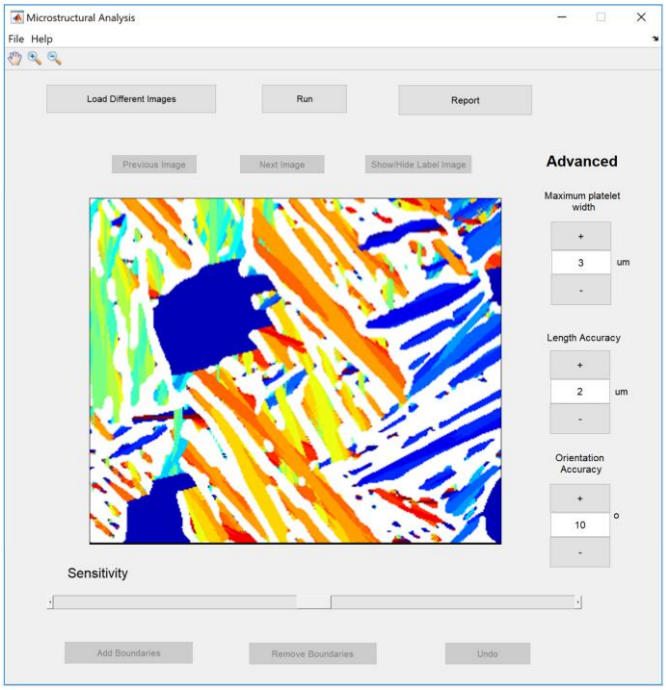

b)

Figure 7.10: Illustration of platelet orientation where a) shows inconsistency within platelets due to setting the maximum platelet width too small and b) is the corrected result

7.2.3 Reporting of results

Once any parameter adjustments have been made, the "Report" button can be pressed to display measurements. A feature of the techniques described in this thesis is that the analysis procedures provide detailed information from which a range of properties can be measured. That is, the computational time required depends almost entirely in the initial technique so there is almost no additional computational effort between reporting a single property and reporting all properties measurable using that technique. Therefore, the report screen includes all of this data, based on the features on the features to measure initially selected by the user. In the case of globular alpha grains this means grain size and the number of grains. For platelet analysis, this means the mean platelet width and the primary (dominant) orientation of these platelets. In both cases the volume fraction of alpha phase and globular volume fraction are also computed. An example results window, for a bi-modal microstructure where both globular grains and platelets are measured, is shown in Figure 7.11.

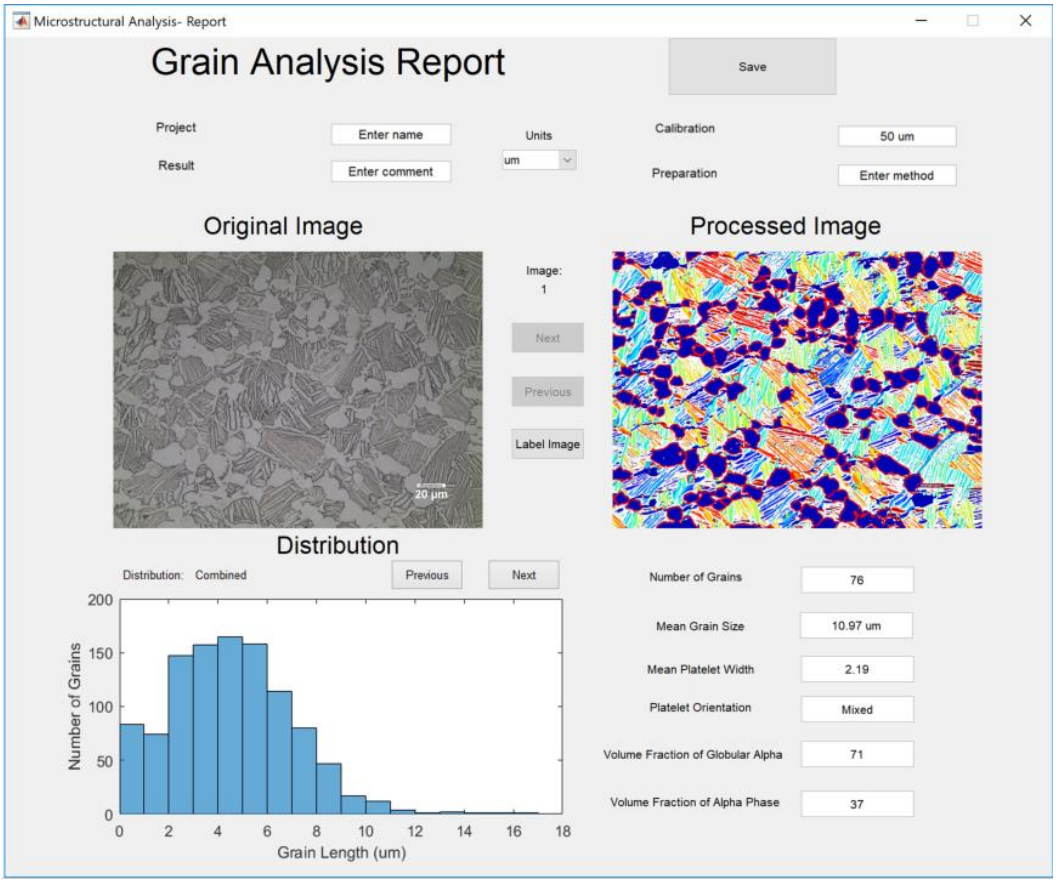

Figure 7.11: Results window

The on-screen controls allow the user to step through the data and distributions for different microstructures in the dataset, or to view the combined statistics. The segmentation, colourmap and labelled visualisations can also be viewed in this screen for reference so that the materials scientist can understand and have confidence in the source of the measurements. The “Save” button will then enable the exportations of all of this data for future reference. The option of 3 types of output are provided in a pop-up window (report only, detailed data and raw data) and the user can select any combination of data to export. The report will show only statistical data, such as grain size or platelet width, for the entire microstructure. The detailed data will save the statistics for each image individually. The raw data option will include the individual measurements of each feature in the image, for example the size of each grain, and includes the segmentation and colourmap previously shown in the interface. The report alone would match the amount of detail provided by existing manual methods so should be sufficient in most cases. However, the measurement techniques proposed in this thesis enables a far greater amount of information to be obtained which the detailed and raw data option will allow a materials scientist to exploit.

7.2.4 Conclusions

The software tool presented in this chapter provides a user-friendly way to make the image processing tools, proposed in previous chapters, available to material scientists for use in microstructural analysis. To achieve this, intuitive methods for selecting the parameters required by these techniques are proposed. The impact that the edge detection sensitivity parameter has on the algorithm provided initially appears like a weakness in the segmentation technique proposed in Chapter 5, as it was required to be adjusted between datasets to achieve the optimal results. However, the ease of manually setting this by qualitative evaluation using this software reduces the impact of this problem and, in fact, enables the software to be easily adjusted for a wider range of datasets than it would likely otherwise be capable of measuring. Although a degree of subjectivity is introduced by this, the parameters used are saved alongside any output data to ensure measurements are repeatable. It would also be possible to tune this parameter given some representative training data which could be used to optimise the edge detection threshold for a particular application. As most of the total

computational time is required by analysis techniques to gather data, rather than measuring features extracted from that data, the software is capable of outputting a wide range of information that would otherwise take multiple operations and analysis procedures to obtain by conventional methods. In Chapter 8 the use of this tool is explored further as part of a robust validation of the methods proposed in this thesis.

8 EXPERIMENTAL RESULTS AND VALIDATION

This chapter validates the techniques proposed in this thesis through experimental trials on a dataset of Ti-6Al-4V microstructural images. Novel image processing techniques have been presented in this thesis that are designed to measure these microstructures. Chapter 5 describes new methods for measuring globular grains and Chapter 6 describes novel techniques for measuring platelets. As each technique aims to measure different features, the following chapter is split into two parts, one to assess each. The proposed new techniques have both been implemented in the novel software tool that was proposed in Chapter 7, which allows both techniques to be applied to microstructural analysis problems in an intuitive, user friendly way that can easily be adopted by materials scientists. Using the proposed novel software tool allows it to be tested in the process of testing and evaluating the novel techniques it contains and demonstrates the effectiveness of the software tool itself.

The purpose of the techniques proposed in this thesis is to improve microstructural analysis, by providing an automated, repeatable and potentially faster alternative to the predominantly manual methods currently used. Validation of this is performed by measuring the properties of the microstructural data using the software tool and comparing the results with those produced by expert material scientists. If automated measurements match the measurements expert achieve with manual methods, the new techniques can be considered accurate. It can then be stated that the new methods are less labour intensive, repeatable and free from human error as these are inherent properties of an automated approach. The approximate time required to run these procedures is also assessed to determine the speed benefits of the new methods. For the measurement of features where an existing automated solution has already been identified, the proposed technique is also compared with this.

The algorithms designed in this thesis required innovations in the domain of image processing in order to achieve accurate measurements in titanium microstructural data. Segmentation of globular grains required a new algorithm with pre- and post-processing procedures aimed at reducing over-segmentation. Most notably a novel marker computation technique is proposed that performs very well when grains are clustered. Orientation and width measurements required an extension to existing methods, and new data processing techniques, to improve robustness when dealing with elongated structures of different sizes and aspect ratios. Therefore, in order to demonstrate these contributions, each section also includes a comparison with existing image processing procedures which were designed to measure similar features in image data. These procedures have not previously been applied to similar microstructural data, so the comparison only demonstrates the contribution in image processing terms and not in microstructural analysis. For the segmentation method in Chapter 5, a comparison is given between the accuracy of the segmentation itself and those produce by other techniques using known evaluation metrics. This requires a manually created ground truth segmentation, the creation of which is also described. The technique described in Chapter 6 takes measurements from an orientation space for which existing metrics to assess are not found in literature. Therefore, the results of this method are compared through raw measurements of each property. Conclusions are drawn about the relative accuracy of each of the techniques proposed in this thesis by comparing these to each other and to manually produced measurements.

8.1 Dataset and software implementation

The techniques proposed in this thesis are tested on a set of microstructural images of Ti-6Al-4V. The titanium samples were subjected to a variety of thermal and mechanical processes prior to capturing images of their microstructure. This produced microstructural variations typical of the kinds of variation expected in real world microscopy. All morphologies of microstructure described in Chapter 2 are considered, with images captured from both Scanning Electron Microscopes (SEM) and Optical Microscopes (OM). In total, titanium samples produced by 30 different experimental setups were used in the trials with 6 producing only globular microstructures, 18 producing bimodal microstructures and 6 producing only lamellar

microstructures. Bimodal microstructures are the most common microstructure type in the test dataset and are also the most useful for the following trials, as they show the widest range of measurable properties. For each sample up to 5 different images of the microstructure are captured, with 120 images used in the test dataset. An example of the different types of microstructure used are shown in Figure 8.1. As each technique is designed to measure particular microstructural features, and different microstructural images have different visible features, no single technique can be meaningfully tested on every image. Therefore, for each trial, only a subset of the available microstructural images, showing the relevant features, are used. A description of the type of image included in the subset used for each trail will included in the "Experimental Methodology" section of each trial.

The automated image processing algorithms and software interface were implemented using the MATLAB programming language. The software was run in the Windows 10 operating system on a laptop class computer with a i7-6650U 2.2Ghz processing and 8GB of ram. The measurement times discuss in this chapter correspond to this machine and it is possible that faster or slower times may be achieved on different hardware.

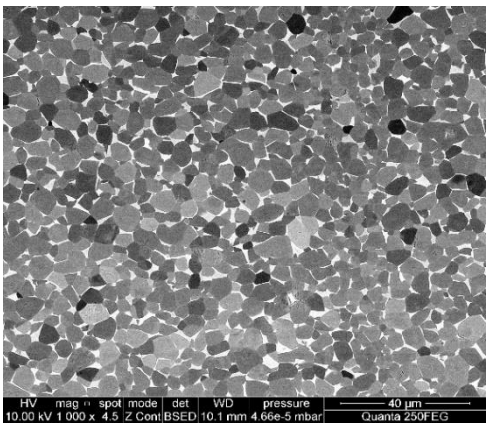

a)

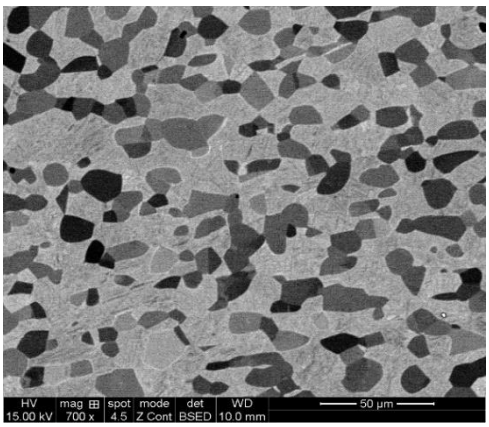

b)

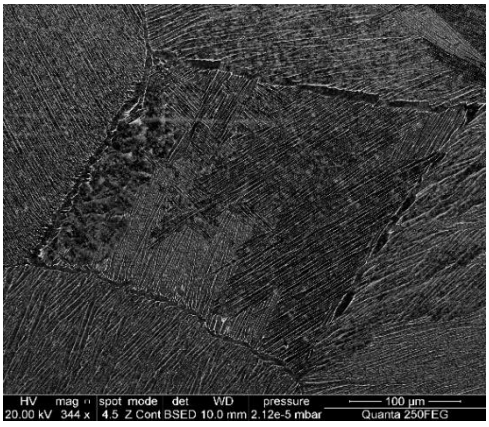

c)

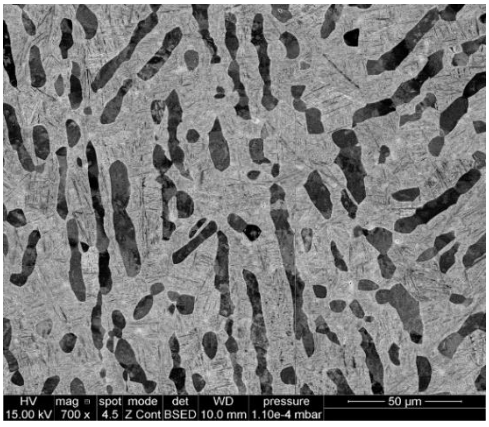

d)

e)

f)

Figure 8.1: Examples of Ti6Al4V microstructures where a) globular by SEM, b) bi-modal by SEM, c) lamellar by SEM, d) bi-modal by SEM where alpha grains are more elongated, e) bi-modal by optical where α/β laths are visible and f) bi-modal by optical where equiaxed alpha grains are more elongated

8.2 Segmentation and measurement of globular grains

This section evaluates the effectiveness of the titanium grain segmentation algorithm proposed in Chapter 5. First, and most importantly, the accuracy of measurements is validated by comparison against those produced by expert material scientists using standardised manual methods. This will illustrate whether the aim of providing a reliable automated globular alpha grain measurement technique has been achieved for globular grains. This has not previously been achieved in the literature for this type of microstructure. Additional trials are then provided to examine the benefits offered by the proposed novel algorithm when compared to alternative techniques from image processing literature [5], [77] that could have been deployed instead. To do this, the accuracy of the segmentation is examined, rather than measurement accuracy, to maintain consistency with image processing literature. Finally, the optional functions within the segmentation algorithm are then evaluated to determine where and when they are best used.

8.2.1 Experimental Methodology

A dataset of fully globular and bi-modal microstructures is used in this experiment including both OM and SEM images. The images are divided according to the material samples they belong two. The new software tool is used to apply the CGSA, proposed in Chapter 5, to each image in this dataset. Measurements of the average grain size and globular volume fraction are reported per sample. The software allows an image to be produced, showing where it has detected grain boundaries. As described in Chapter 7, this provides feedback indicating how likely the result is to be accurate and allows the user to decide if any parameters need to be adjusted. For alpha grain analysis, the first image from each sample was used to set parameter, E_s, by adjusting this parameter to find a suitable looking segmentation. Numerical results were not known at this stage and the parameter remained unchanged for all other images in that sample. The merging parameters B_c=0.4, T_i=10 and T_G=1 were chosen by manual visual inspection of a few microstructures. These values reduced the effects of scratches and artefacts but, for generality purposes this was not refined to suit any particular microstructure type in this study.

The new automated measurement approach is evaluated in two different ways.

First, the measurements of globular grains are assessed through comparison with measurements from expert material scientists using the E112 standardised measurement techniques, as described in Chapter 4. Measurements were performed on a sample by sample basis with metallurgists permitted to select the images from each sample they felt were most suitable to measure. These manual measurements included grains on the boundary of the image. Theoretically, these are only partial grains, so it may be in fact be beneficial to discount these from feature measurements. However, as these were included in the manual measurements, due to the needs of other projects, the software was also allowed to include these grains for consistency. Globular volume fraction calculations assumed any grain of aspect ratio less than 2 was globular, for both software and manual measurements. To keep the comparison consistent, the software was set to only measure the same images selected by the metallurgist, rather than all images in the sample. When comparing the results, it is important to remember that manual measurements cannot be considered as the absolute truth, due to subjectivity, bias and human error. As such errors are difficult to quantify, the expected inter-operator variation defined in industrially recognized standards [29], [31] is used as an indicator of an acceptable range of measurement. For volume fraction, inter-user repeatability of +/- 10% is expected [31] while grain size standards expect a variation of +/- 0.5G between measurement by different operators [29], which equates to +/- 16% in micrometres. As previously described, subjectivity is greater when elongated grains exist, so less variation would be expected in more globular microstructures. The difference between measurements is recorded in Table 8.1, Table 8.2 and Table 8.3. These results are colour coded with green indicating a close match, red indicating disagreement beyond what would reasonably be expected and amber indicating a difference in measurement that is on the limit of expected inter-operator variations. This experiment demonstrates that the new technique achieves the primary aim of this research and is capable of matching the results of an expert materials scientist in a shorter time and in a repeatable way.

Second, the accuracy of segmentation is then evaluated by comparing the segmentation produced by the CGSA with a manually created ground truth using the F-score metric [117]. The aim of this later experiment is to validate the contribution made by the pre- and post- processing techniques applied to the Watershed Transform to image

segmentation, rather than to microstructural analysis. The use of F-scores facilitates a more precise study of segmentation accuracy than comparison of grain size measurements, as errors do not balance out. This is also more consistent with image processing literature. To provide context, results from the CGSA are compared against alternative Watershed Segmentation techniques with markers based on the h-minima transform applied to the distance transform and the Ultimate Opening (UO), as the literature suggests these techniques are the most suitable methods among exiting segmentation algorithms. Segmentation with markers based on h-minima has been used by Cheng [118], Jung [119] and Yang [99], among others, to segment similar images, such as those of clustered nuclei. Watershed Transforms with markers computed using the UO, has been applied to recent segmentation problems by Marcotegui [77], [78]. This technique is applied to segment large varieties of different dataset. Although it has so far been less widely used on similar datasets as h-minima based methods, the UO has been applied to similar images containing cells and the key benefit of using both intensity and shape information. This was identified in the literature review identifies as a key feature for segmenting complex images, missing from several existing techniques, so is beneficial to include in this trial. F-scores are measured on a scale of 0-1 so improvements in accuracy and reliability can be easily observed.

8.2.2 Ground Truth Segmentation

To validate the accuracy of the proposed segmentation algorithms, the segmented image is compared to a manually created ground truth. The ground truth image in this case is a binary image where only alpha grains are “1” and all beta phase or grain boundaries are “0”. These were produced by an expert material scientist manually drawing in these boundaries on the perimeter of every grain in the image. This was done using image editing software with layer capabilities so that the boundaries were drawn only on a clean layer. This allowed the binary ground truth image to be created easily and ensure it was not corrupted by noise. A fill tool was then used to fill the area within hand drawn boundaries. This was done only for alpha phase grains, so that all beta phase regions are considered as background. An example of a ground truth image for a bi-modal microstructure is given in Figure 8.2.

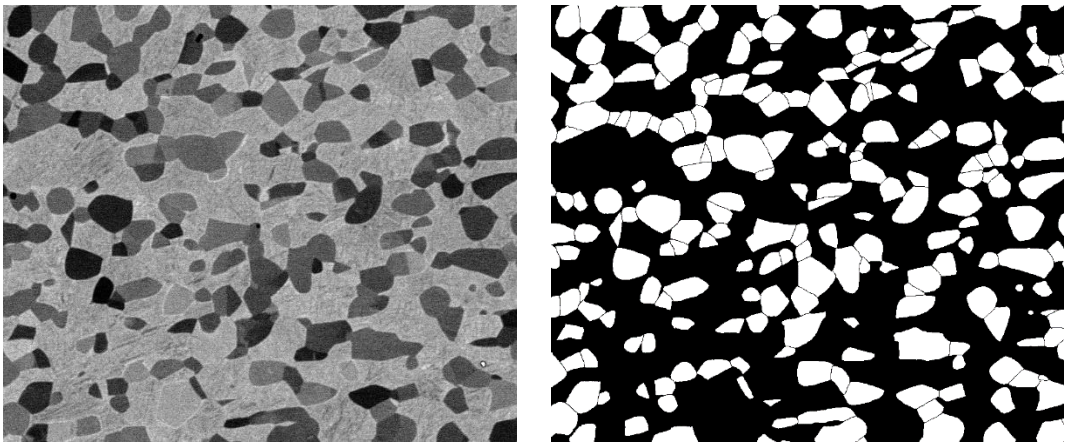

a) b)

Figure 8.2: Ground truth image where a) original image and b) manually created ground truth

Several methods exist in the literature for comparing the automatically computed segmentation to the ground truth [117], [120]. This section uses the F-score, defined in Equation (8.3), as a metric of segmentation accuracy. The F-score is the weighted average of two other metrics called precision, defined in Equation (8.1), and re-call, defined Equation (8.2), meaning the score reflects both over- and under- segmentation errors. The popularity of this metric also means these results will be more widely understood and easier to compare with similar methods in published literature. The definitions of precision recall and F-score are given in terms of the binary classification descriptors true positives (tp), false positives (fp) and false negatives (fn).

$$precision = \frac{tp}{tp + fp} \tag{8.1}$$

$$recall = \frac{tp}{tp + fn} \tag{8.2}$$

$$F - score = \frac{(\beta^2 + 1) * precision * recall}{\beta^2 * precision + recall} \tag{8.3}$$

Generally, when detecting objects, a correct identification is a tp, an identification of an object that does not exist is a fp and an object that is not detected is a fn. In image

segmentation, the detection of an object is not sufficient, as it is crucial to know whether or not the segmented area matches the ground truth area. Therefore, in order to use these metrics, it is necessary to classify each pixel as either a tp, fp or fn. A true positive would only exist if the pixel was not only detected but detected as alpha phase, but also detected as part of the correct grain. As the image is segmented into a large number of regions, this first requires both the ground truth and automatically computed segmentation to be labelled to uniquely identify each region. Each region in the ground truth is then matched to a region in the automated segmentation. This is done by finding, for each ground truth region, the segmented region with which it shares the largest area. Each region must be matched to only one other region. If any ground truth or segmented region is matched to multiple regions only the regions sharing the greatest number of shared pixels is kept as a match. The other regions are then matched to the remain regions with which they share the most pixels. This is described in Algorithm 3.

An output image where each pixel, *x*, is labelled according to its binary classification is then calculated as follows;

- Any location *x* where the label in the ground truth and automatic segmentation match are marked as a tp
- Any location *x* where the ground truth image has a label, but the segmentation has no label is marked as a fn
- Any location *x* where the segmentation has a label, but the ground truth has either no label or a different label is marked as a fp
- Any location *x* where no label exists in either segmentation is marker as a tn

An example of the result of this binary classification of a bi-modal microstructural segmentation when compared with the ground truth is shown in Figure 8.3.

Algorithm 3: Ground truth region matching

Input: S_{GT}: ground truth segmentation, S_A: automatically computed segmentation (both with each region uniquely labelled)

Output: GT_P: ground truth pairs – each row is a region in S_{GT} with the value in column 1 the best matching region in S_A and column 2 the intersecting area

Initial Pairing of Regions

1. **For** i=1:max(S_{GT})
2. GT_P(i,2) = 0
3. **For** j=1:max(S_A)
4. **If** S_{GT}(S_{GT}==i)∩ S_A(S_A==j) > GT_P(i,2)
5. GT_P(i,1) = j
6. GT_P(i,2) = S_{GT}(S_{GT}=i)∩ S_A(S_A=j)

Prevent regions pairing to multiple other regions

7. **For** i=1:max(S_{GT})
8. **For** j=1:max(S_{GT})
9. **If** GT_P(i,1) == GT_P(j,1)
10. **If** GT_P(i,2) > GT_P(j,2)
11. GT_P(j,1) = 0
12. GT_P(j,2) = *0*
13. **Else**
14. GT_P(i,1) = 0
15. GT_P(i,2) = *0*

Re-assign regions that are no longer paired

16. Delete successfully paired regions from S_{GT} and S_A.
17. Repeat steps 1-16 until all regions are paired or not additional pairs are found.

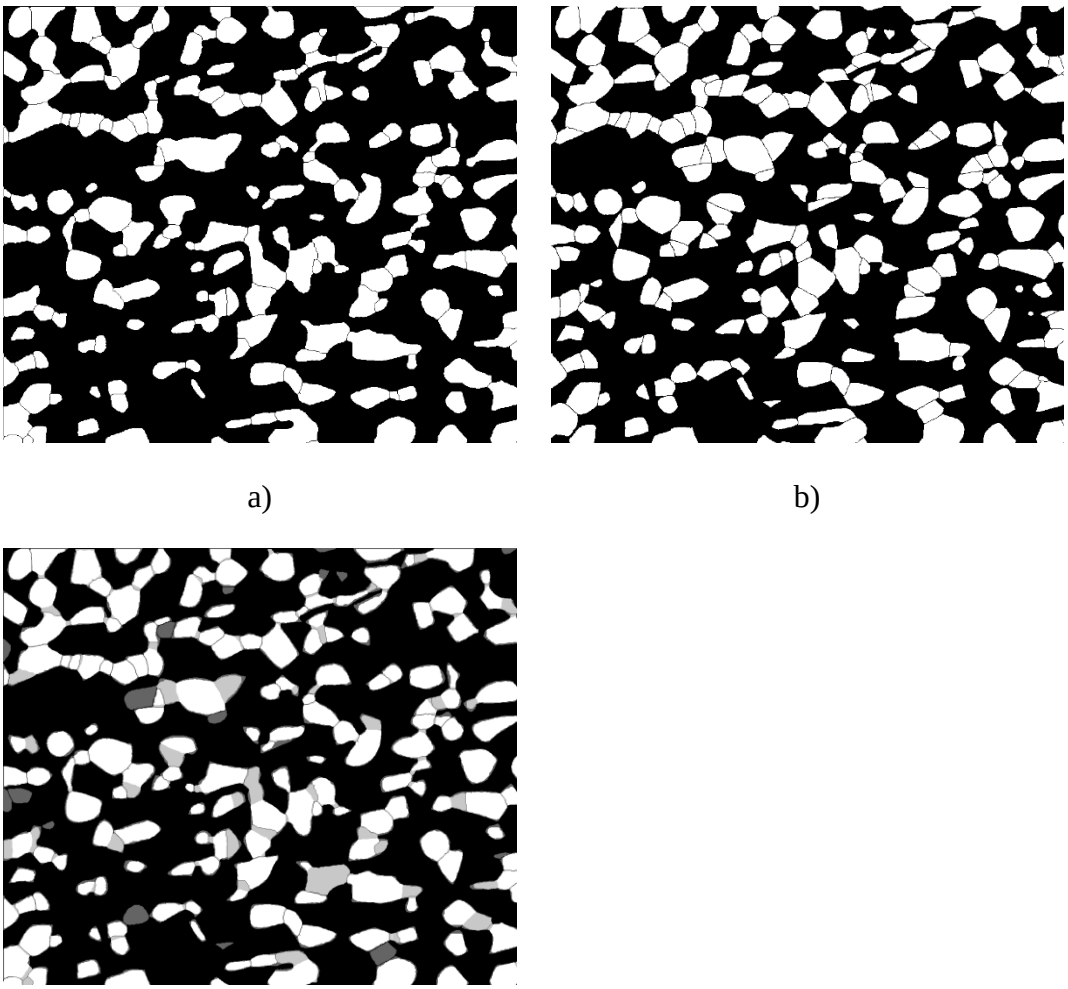

a) b)

c)

Figure 8.3: Binary classification of microstructure segmentation where a) automated segmentation, b) ground truth and c) binary classification where white pixels are tp, light grey are fp, dark grey are fn and black are tn

It is observed from this result that for bi-modal microstructures a large percentage of the image consists of tn. This is because the beta phase is easy to detect so in most cases is correctly not included in the segmentation. As the purpose of the segmentation algorithm is to find measurements of individual globular grains, this is not informative of segmentation accuracy, and its inclusion in accuracy metrics would result in a misleadingly high value in this case. This supports the decision to assess segmentation using the F-score as it does not account for tn values. The F-score can therefore be computed using the Equations (8.1), (8.2) and (8.3), where the tp, fn and fp values are a summation of how often each category appears in the binary classification image.

A key problem for the analysing segmentation accuracy is that ground truth is the opinion of a single material scientist of where grain boundaries lie. Many locations exist throughout microstructures where grain boundaries may or may not exist. There is often no clear agreement between material scientists as to the true nature of these hypothetical boundaries. It is, therefore, possible to record an error in such a case were the proposed algorithm may in fact be correct according to a different scientist's assessment. An example is shown in Figure 8.4 of two different ground truths that could be created from the same image, each by different materials scientists. A result matching one ground truth completely would give errors in the other with no result satisfying both ground truths simultaneously.

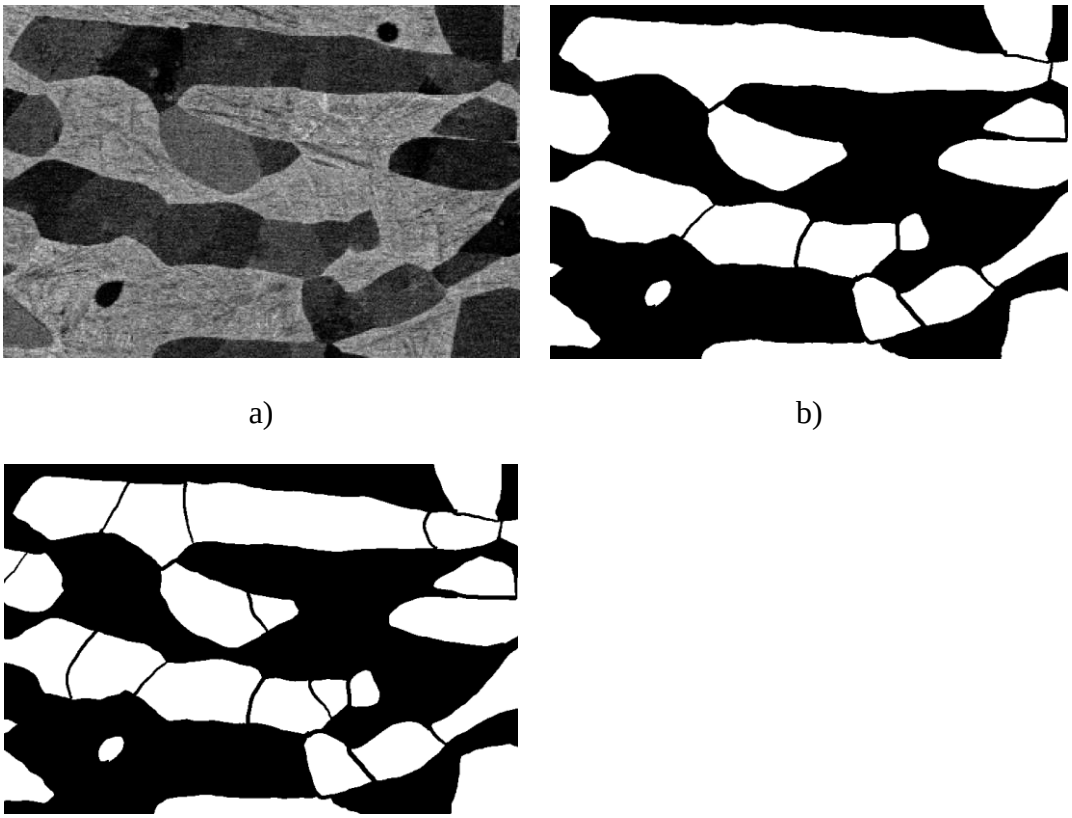

a) b)

c)

Figure 8.4: Example of a microstructure with two different ground truths generated by different materials scientists

As a result, a segmentation that is as good as can possibly be achieved may not achieve the theoretically perfect F-score of 1. Another factor to consider here is that the F-score metric punishes the algorithm for missing grains from the segmentation, i.e.

considering an alpha grain as part of the background. While this is of interest when evaluating segmentation accuracy, for microstructural measurements this would equate merely to the sub-sampling of grains and not necessarily cause any errors. It is also noteworthy that, provided that the segmentation algorithm is well balanced, in that the number of over- and under- segmentation errors are balanced, a small percentage of these may end up having minimal effects on measured results as many microstructural analysis procedures aim to measure the mean size of grains. Evaluation metrics normally do not account for this, which can lead to relatively low F-scores in segmentations that actually produce good measurements. For these reasons, the evaluation shown in this section provides a relevant comparison between segmentation algorithms but does not necessarily record accuracy scores that are informative of the accuracy of grain measurements. Conclusions about the accuracy of microstructural measurements using these techniques should, therefore, generally be made using the results experiment in Section 8.2.3, and not the analysis of segmentation accuracy in Section 8.2.4.

8.2.3 Measurement accuracy

In this section the accuracy of the microstructural measurements performed using the proposed segmentation technique are evaluated. The aim is to reveal how well the technique proposed can match the accuracy of expert material scientists. Accurate result in this section will validate the first reliable automated method for globular alpha grains in this type of microstructure and allow significant benefits to the microstructural analysis process.

8.2.3.1 Grain size

Overall, there is a good correlation in grain size measurements between existing manual procedures and the new automated analysis approach. For fully globular microstructures, grain size measurements were typically within 0.3µm for 4-5µm grains, as shown in Table 8.1.

Table 8.1: Grain Size Measurements of Fully Globular Microstructure

Sample	Grain Size (µm)			Time (seconds)
	Manual	Auto	Difference	
1	4.72± 0.76	4.51	-0.21	19.45
2	5.01±0.80	5.04	+0.03	17.46
3	4.86±0.78	4.62	-0.24	19.54
4	5.42±0.87	5.14	-0.28	18.99
5	4.18±0.67	4.59	+0.41	20.19
6	4.82±0.77	4.62	-0.2	16.89

The greatest difference between measurements was 0.41µm, which is still comfortably within the expected inter-operator variation. This is a very positive result, particularly given that grains are tightly packed in these microstructures, which often makes automatic segmentation more difficult. For bi-modal microstructures most measurements also closely matched the manual results, with grain sizes of around 10µm and disagreement between results under 0.5µm in most microstructures, shown in Table 8.2. However, there are several cases where results did not match as closely as they did for the globular microstructures. One possible reason for this is that many of the bi-modal microstructures in this study contained more elongated primary alpha than was seen in the fully globular microstructures. The boundaries of these grains are less clear, so subjectivity is expected to cause wider variations in these cases. Microstructures in samples 8 and 9 appear to have large numbers of elongated grains and also exhibit the largest difference between results. Despite this, no measurement lies significantly outside the expected inter-operator variation. Examples of the segmentation of different types of globular microstructure, from which these measurements are calculated, as shown in Figure 8.5. These images show a good quality of segmentation, reinforcing the high accuracy suggested by the similar grain size measurements. The segmentation images, particularly the OM image in Figure 8.5 f) , also shows that beta phase regions and platelets are correctly discounted from the measured segmentation.

Table 8.2: Size and Volume Fraction Measurements of Bi-Modal Microstructures

Sample	Grain Size (µm)			Time (seconds)
	Manual	Auto	Difference	
1	9.33 ±1.49	9.05	-0.28	3.79
2	11.3 ±1.81	11.2	-0.1	3.45
3	9.52 ±1.52	9.62	+0.1	2.5
4	8.81 ±1.41	7.55	-1.26	4.5
5	11.4 ±1.82	10.64	-0.76	4.21
6	10.74 ±1.72	10.5	-0.24	4.79
7	10.06 ±1.61	9.84	-0.22	4.78
8	11.57 ±1.85	9.58	-1.99	2.67
9	12.04 ±1.93	9.93	-2.07	2.98
10	8.45 ±1.35	8.04	-0.41	3.15
11	9.45 ±1.51	9.35	-0.1	3.36
12	9 ±1.44	9.26	+0.26	3.70
13	11.2 ±1.79	10.1	-1.1	3.89
14	10.25 ±1.64	9.99	-0.26	3.33
15	10.97 ±1.76	10.89	-0.08	3.19
16	12.97 ±2.08	12.94	-0.03	3.96

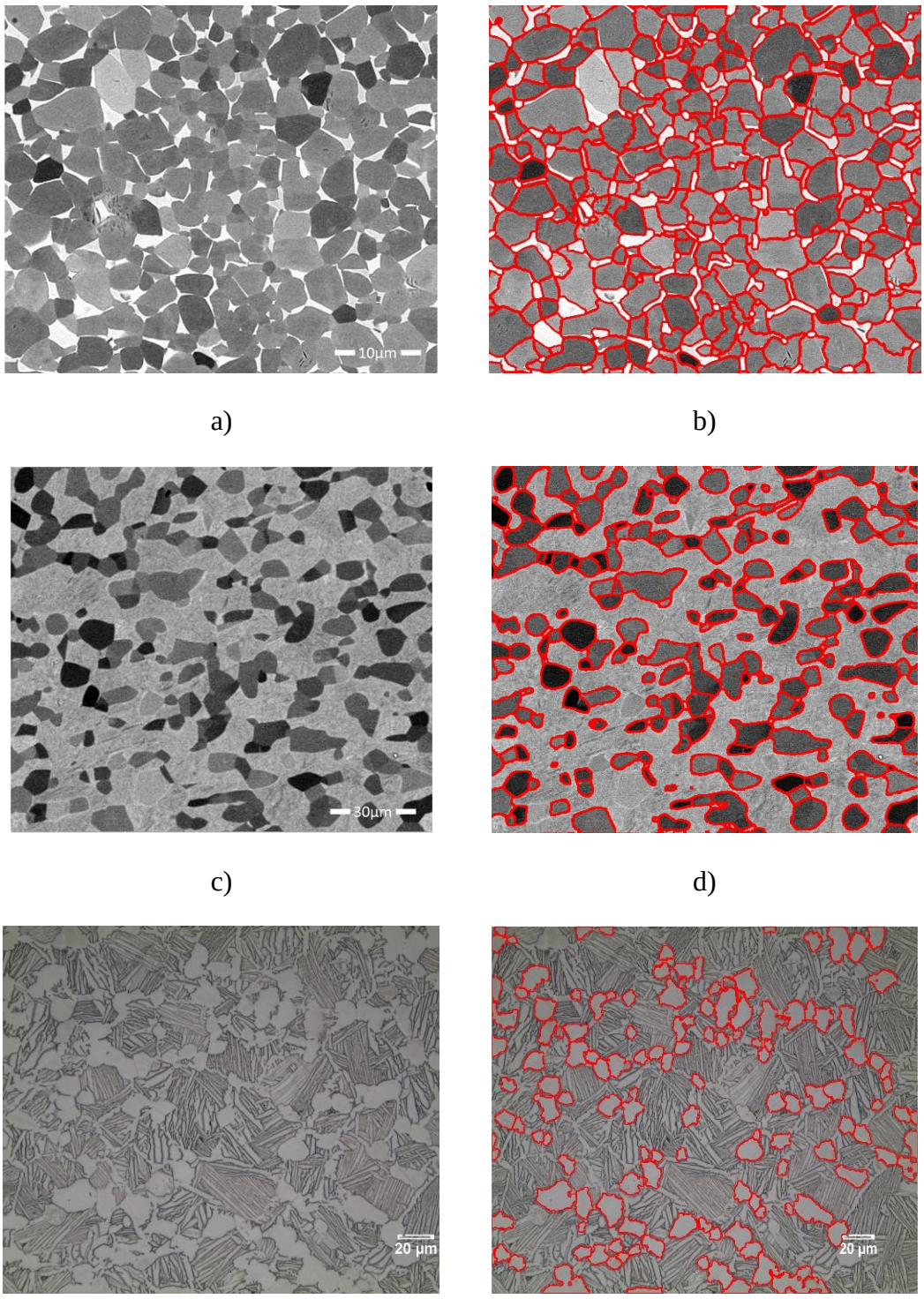

Figure 8.5: Segmentation of microstructures where a) original fully globular microstructure from SEM b) its segmentation, c) original bi-modal microstructure from SEM, d) its segmentation, e) original bi-modal microstructure from OM showing visible platelets and f) its segmentation

The time required to produce these results is drastically reduced compared to manual methods. A typical bi-modal image containing approximately 150 grains, as shown in Figure 8.5 c), was measured by the software in 3.79 seconds while the materials scientists reported it took approximately 15 minutes to accurately measure the same image. Most manual measurements were produced as part of other research projects and precise measurements times for each are not available, hence this information is not included in the tables. The globular microstructures used in this study were exceptionally large, as shown in Figure 8.5 a), and a far larger number of grains are visible. In this case the measurement time in the software increased to up to 20.19 seconds, as the software requires all 4000 grains in that image to be measured. Manual measurement times would remain at around 15 minutes, as the materials scientist could select to still only measure the required 300 grains.

8.2.3.2 Volume fraction of globular alpha

Globular volume fraction is calculated based on the same segmentation used to measure grain size, so can typically be computed in less than a second once grain sizes are already known. The automated measurements of the volume fraction of globular alpha initially appeared to be inaccurate, with almost all measurements falling outside the +/- 10% variation expected, as shown in Table 8.3. However, on closer inspection the discrepancy between manual and automated measurement was found to be very consistent, with the automated techniques always measuring globular volume fraction higher than the manual methods and this difference usually being approximately 10%. It is also observed that, subsequently, variations in volume fraction between each sample are approximately the same regardless of the measurement techniques being used, as shown in Figure 8.6. This suggests both manual and automated measurements give meaningful information about the microstructure but that some form of bias is causing measurements to disagree. A likely cause of this is the difference in how the length and width of grains are selected for measuring aspect ratio. The software fits an ellipse to the grain giving a length and width that are perpendicular to each other, with the width representing the widest part of the grain. In manual approaches placing the length and width is done subjectively, therefore, length and width may not be perfectly perpendicular, and the width measurement may be performed at a narrower section of the grain. This would result in higher aspect ratios for manual measurements and a

lower percentage of grains being classed as globular, as seen in the results in this section.

Further experiments would be required to investigate this and determine which method of measurement gives the true globular volume fraction. However, for developing an automated tool for analysing microstructures the ability to measure the same differences in volume fraction between microstructures as an expert material scientist would measure is sufficient to show the new technique provides useful information. Furthermore, due to the predictable effect of bias, the software can be calibrated, by reducing all automated measurements performed by 10%, to give results that are consistent between each measurement approach. This allows measurements from manual and automated methods to be compared without the effect of bias. The software is calibrated, rather than the manual measurements, so that all measurements are consistent with what would be achieved by an expert material scientist. However, the subjective nature of manual techniques means it is not known if this is the absolute truth. Further investigation is also required when applying such calibrations in practice, as the appropriate calibration level may differ for other datasets. With this calibration applied all results are within the expected inter-operator variation, showing the software is capable of matching the measurement of expert material scientists.

Table 8.3: Volume Fraction Measurements of Bi-Modal Microstructures

Sample	Volume Fraction of Globular Alpha (%)					Time
	Manual	Auto	Difference	Auto -10% Calibration	Difference	
1	44±4.4	56	+12	46	+2	3.79
2	70±7	80	+10	70	0	3.45
3	62±6.2	74	+12	64	+2	2.5
4	52±5.2	68	+16	58	+6	4.5
5	51±5.1	64	+13	54	+3	4.21
6	62±6.2	75	+13	65	+3	4.79
7	64±6.4	75	+11	65	+1	4.78
8	46±4.6	56	+10	46	0	2.67
9	48±4.8	59	+11	49	+1	2.98
10	47±4.7	56	+9	46	-1	3.15
11	54±5.4	65	+10	55	+1	3.36
12	57±5.7	69	+12	59	+2	3.70
13	71±7.1	82	+11	72	+1	3.89
14	67±6.7	73	+6	63	-4	3.33
15	64±6.4	71	+7	61	-3	3.19
16	48±4.8	60	+12	50	+2	3.96

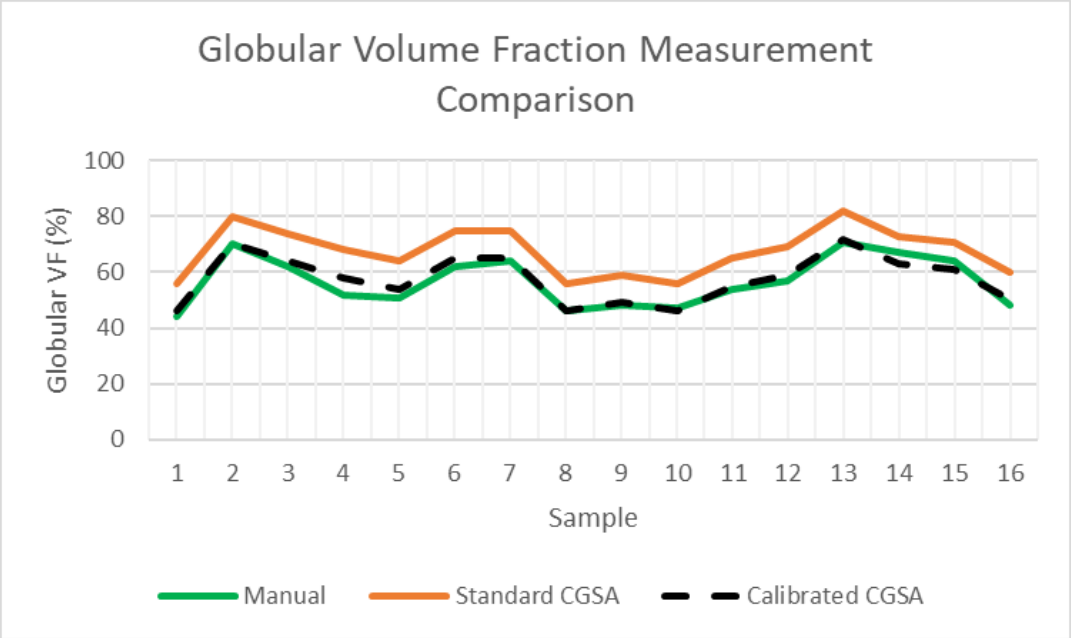

Figure 8.6: Graph showing variations in manual and automatic measurements of globular volume fraction

8.2.3.3 Comparison with existing commercial software

To further demonstrate the benefits of the new approach, a comparison is performed between the proposed technique and an existing algorithm, freely available online for use within the MIPAR software developed by Sosa *et al.* [36], more details on which can be found in Section 4.1.2.3. The "Grain Segmentation 1" algorithm within this software was selected for comparison as, it was believed to offer the best available solution for automating the analysis of globular grains at the time of writing. This belief is based on the algorithm being advertised for general metal segmentation and the strong results it achieved on initially similar looking data and it should be noted the MIPAR team have never directly made this claim. It should also be noted that part of the MIPAR service is to create new "recipes" using their software which can be provided to MIPAR users to process their own specific images for a variety of applications. The comparison presented in this thesis is not with the service the MIPAR team could provide but with the algorithms that already exist and are available through their recipe store. Therefore, this comparison does not attempt to review this software or its ultimate capability.

Both the MIPAR recipe and the segmentation technique proposed in this thesis were tested on images from the dataset used in thesis and images from the dataset provided with the MIPAR software. For both techniques, the available parameters were set to give what the operator perceived to be the best result. It is found that the MIPAR recipe works best on Sosa's microstructures and the new methods proposed in this thesis work best on the dataset used here. This is unsurprising since each algorithm was design specifically for those datasets. However, the error rate each technique achieves on the other dataset is significantly different, with the method proposed in this thesis appearing to be significantly more robust. Investigation of the algorithms and microstructural datasets show clear reasons for this. Some of the microstructures in this study are particularly complex and boundaries are less clearly visible than those in the microstructures the MIPAR recipe has been designed to work with. Segmentation results and subsequent grain measurements for such a microstructure are shown in Figure 8.7 and Table 8.4 respectively. Grain measurements of the MIPAR microstructure are given in pixels as no scale bar was present in the image. The grain segmentation algorithm implemented in MIPAR searches for dark pixels in the image which in their data indicates boundaries. However, in the dataset used in this thesis, dark pixels do not indicate boundaries, therefore, the software will predominantly detect noise, causing over-segmentation. The novel algorithm presented in Chapter 5 searches not for dark lines but instead for regions of high intensity variations, with the shape of these regions then used to estimate grain locations. These features are present in microstructures from both datasets and results in the new approach therefore achieve a better result on Sosa's microstructures than the MIPAR recipe achieves on ours. This suggests the segmentation procedure proposed in Chapter 5 is more generic and better suited to measuring different types of microstructure, particularly when boundaries are unclear. It should be noted that the MIPAR software package itself is designed to allow different algorithms to be created and added over time, including, potentially, the one proposed in Chapter 5. In fact, since the publication of the work in Chapter 5 [6], another research team has made use of the functions described by implementing them within MIPAR's user interface [113].

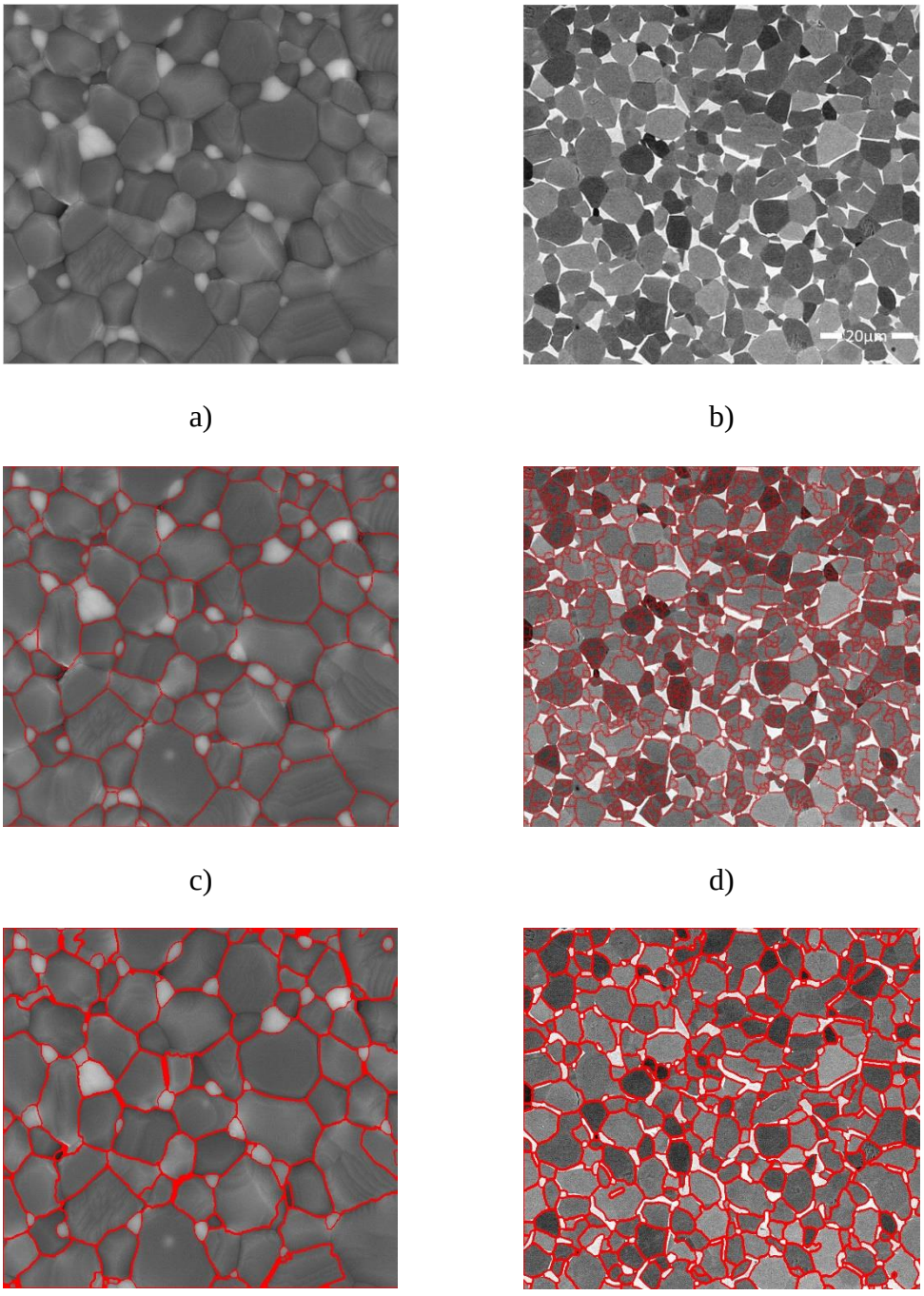

Figure 8.7: Segmentation comparison between the new methods and a recipe from MIPAR software where a) and b) are an original image from each dataset, c) and d) is the segmentation by the existing MIPAR recipe and e) and f) is the segmentation by the new method

Table 8.4: Comparison of measurement accuracy of the new segmentation technique with an algorithm from existing material analysis software

	Manual Measurement	MIPAR Measurement	Measurement for the new technique
Microstructure from this thesis	4.72µm	2.86µm	5.18µm
Microstructures from MIPAR dataset	85 pixels	88 pixels	78 pixels

8.2.4 Analysis of segmentation accuracy

In order to measure properties of globular alpha grains, an accurate segmentation technique, proposed in chapter 5, was designed to segment touching grains in noisy microstructural images. In this section, the benefits of the proposed method are demonstrated through comparison with existing image segmentation algorithms from other fields.

8.2.4.1 Comparison of F-scores

The F-scores achieved for segmentation performed by the new CGSA method, the UO and h-minima methods are given in Table 8.5. These results indicate that the CGSA achieves a higher level of accuracy overall than other methods in this test. This benefit is not evenly distributed, with certain microstructures seeing a greater accuracy benefit from the new approach than others. Most notably, the results indicate that the new algorithm is particularly useful for segmenting the larger clusters of grains most common in fully globular microstructures.

Table 8.5: Comparison of F-scores between the new method and existing techniques

Image	F-score		
	New method	Ultimate opening	H-minima
Bi-Modal 1	0.92	0.87	0.84
Bi-Modal 2	0.89	0.89	0.85
Bi-Modal 3	0.93	0.86	0.83
Bi-Modal 4	0.91	0.89	0.88
Bi-Modal 5	0.93	0.91	0.92
Bi-Modal 6	0.92	0.90	0.91
Fully Globular 1	0.85	0.65	0.64
Fully Globular 2	0.77	0.71	0.66
Fully Globular 3	0.86	0.67	0.66
Fully Globular 4	0.84	0.70	0.66

Bi-modal microstructures generally see reasonably accurate results from all methods with all achieving an F-score greater than 0.8. The new techniques are no worse than existing techniques in all bi-modal microstructures and better in most cases. In some microstructures, such as Bi-Modal 6 the existing methods are able to approximately match the results achieved by the new method. Meanwhile in Bi-Modal 3 the ultimate opening is 7% less accurate. The reasons for these differences can be explained by examining visualisations of the different segmentation results. Figure 8.8 shows the segmentation of the Bi-Modal 6 microstructure. The results show the segmentation to be broadly similar between the different methods with the exception of a small area of significant over-segmentation, marked by the yellow arrow, that exists in all but the new CGSA segmentation.

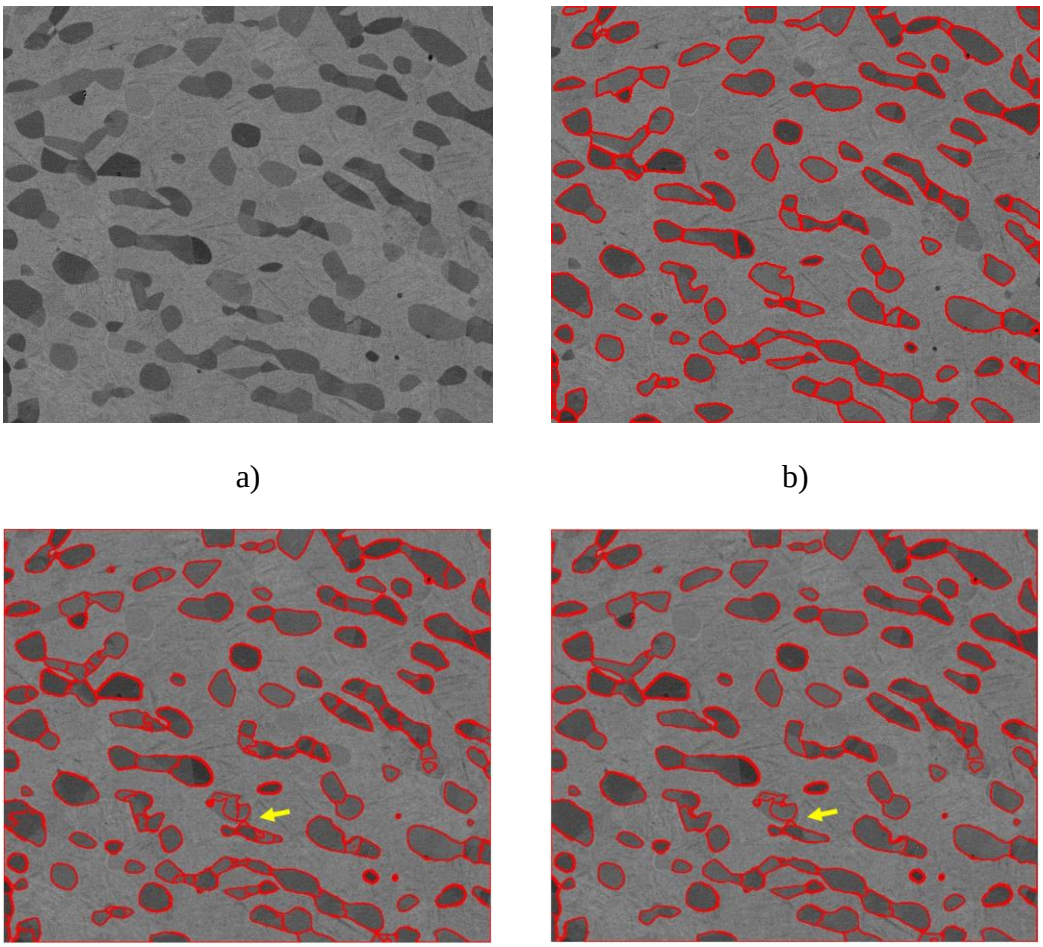

a) b)

c) d)

Figure 8.8: Segmentation of bi-modal microstructures using different techniques where a) is a Bi-Modal 6 image, b) segmentation using CGSA, c) segmentation using h-minima markers and d) segmentation using the UO markers

Figure 8.9 shows an image of the Bi-Modal 3 microstructure which is more complex than Bi-Modal 6 in a few ways. The first is that intensity variations in Bi-Modal 3 appear to be slightly greater, with more noise corrupting the data within the grains. The second difference is that the grains are slightly more clustered. While the overall segmentation appears OK, more errors are visible in the segmentation of Bi-modal 3 by existing methods than in Bi-Modal 6. As the distance transform does not include sensitivity information it struggles the most to separate the tighter clusters of grains in "Bi-Modal 3", as demonstrated by the lower F-score and visible under-segmentation

in Figure 8.9 d). As the ultimate opening can use intensity information it does not show much under-segmentation. However, it appears to be more susceptible to noise as demonstrated by Figure 8.9 c). The segmentation using the techniques proposed in this thesis, shows both fewer errors and a more balanced segmentation where no type of error appears clearly more common. This suggests that the novel algorithms presented are robust to differences between datasets.

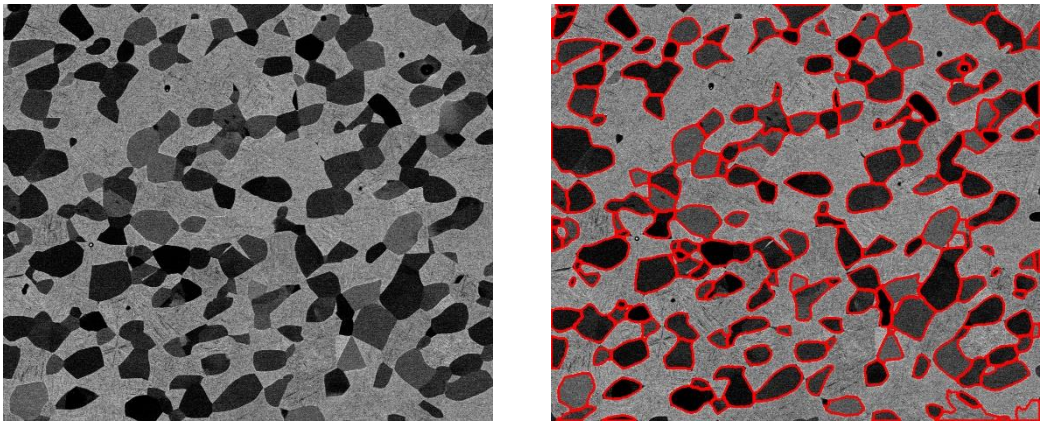

a) b)

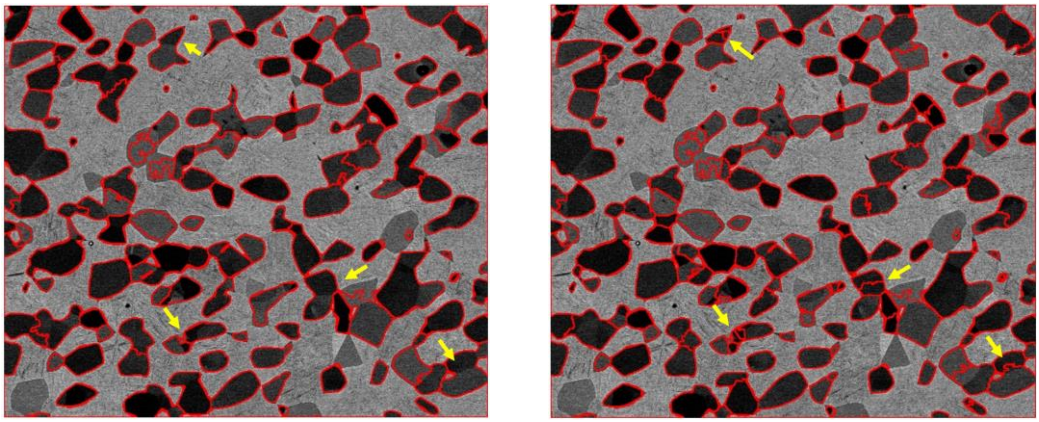

c) d)

Figure 8.9: Segmentation of bi-modal microstructures using different techniques where a) is a Bi-Modal 3 image, b) segmentation using CGSA, c) segmentation using h-minima markers and d) segmentation using the UO markers

The robustness of the new algorithm is further demonstrated by the larger difference in F-scores observed when segmenting images of fully-globular microstructures. It is clear that segmentation of these microstructures is more challenging with all methods seeing a drop-in accuracy compared to bi-modal microstructures. However, the reduction in accuracy shown by the new CSGA is far less than the reduction in accuracy when using existing techniques. The reasons for this can be observed in Figure 8.10 which gives examples of one of these microstructures and their segmentation by each method.

The fully globular microstructures have a far greater amount of clustering between grains, as shown in Figure 8.10 a), with the ground truth segmentation shown in Figure 8.10 b). This makes segmentation more challenging than in bi-modal microstructures. From Figure 8.10 c), d) and e) it can be observed that the new segmentation looks more accurate than existing methods, in line with what was shown by the F-scores. As with bi-modal microstructures the method using the h-minima of the distance transform suffers most from the clustering of grains, due to the lack of shape information provided by alpha/beta grain boundaries. As a result, under-segmentation errors can be clearly seen though-out the image. The UO again has a higher rate of over-segmentation errors, which is particularly visible towards the centre and lower right-hand corner of the image. However, for these complex microstructures there also appears to be more visible under-segmentation that was encountered in bi-modal microstructures.

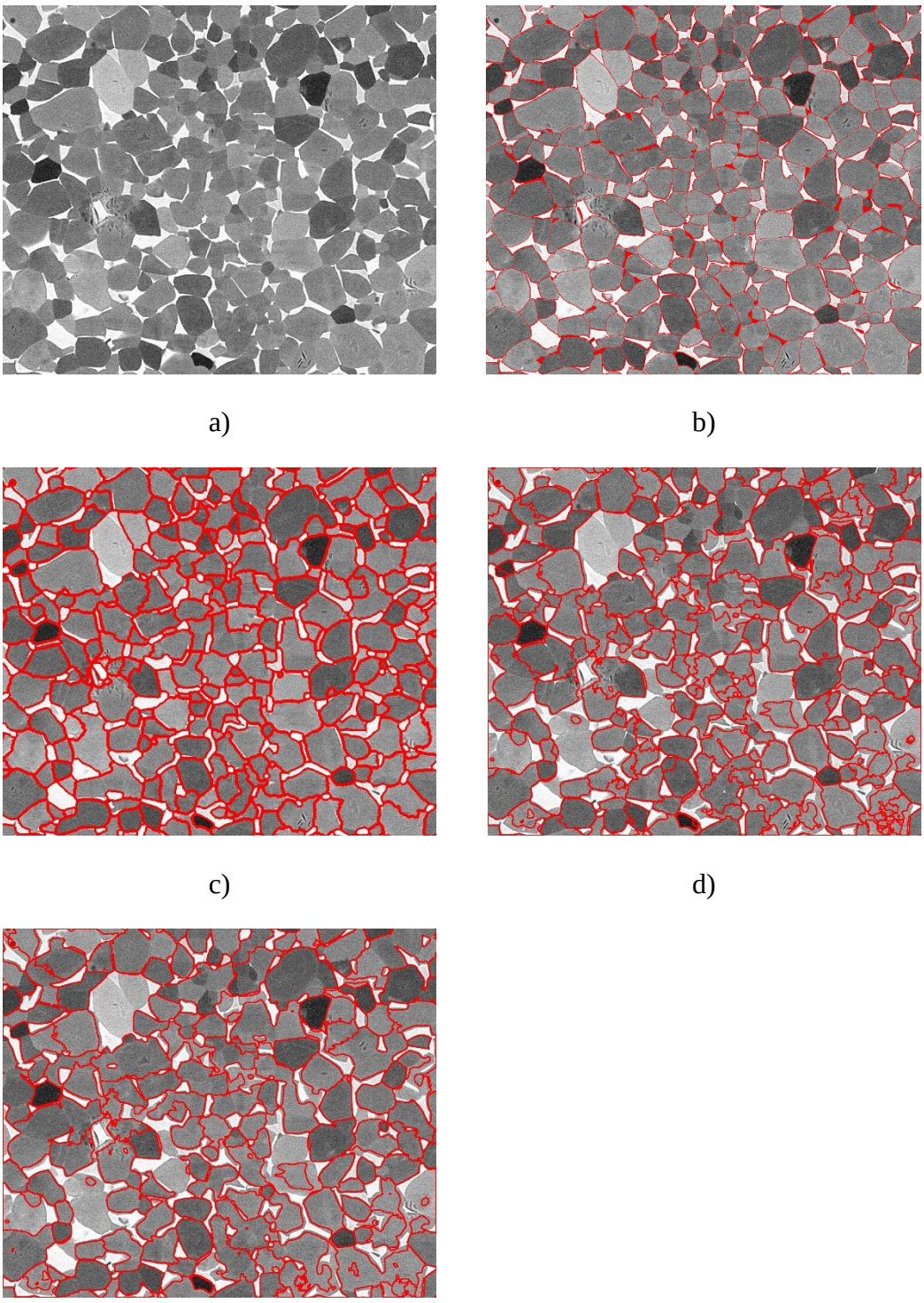

a) b)

c) d)

e)

Figure 8.10: Segmentation of bi-modal microstructures using different techniques where a) original image, b) ground truth segmentation, c) segmentation by the new method, d) segmentation by ultimate opening and e) segmentation by h-minima

The cause of errors in existing methods can clearly be seen by studying the markers produced by each approach, shown in Figure 8.11. Markers from the h-minima of the distance transform method, shown in Figure 8.11 d), clearly marks fewer regions than the proposed new technique, shown in Figure 8.11 b). This explains the higher rate of under-segmentation in the h-minima based Watershed Transform when compared to the proposed approach. The ultimate opening, whose markers are shown in Figure 8.11 c), has a few more markers than necessary for some grains, such as in the lower right-hand corner, and hence more visible over-segmentation. However, in other areas it also still produces fewer markers than requires, and fewer than achieved the new technique. This issue most commonly occurs when grains are clustered such that the complete cluster forms a globular shape, such as in the lower middle section of the image. When clusters occur in this way, the granulometric functions on which ultimate openings are based will find a single disk-shaped SE removing the entire cluster and hence generate a single marker. The CGSA proposed in this thesis uses markers is based on intensity changes and takes an edge detection function as its initial input from which to build a marker. Markers are, therefore, determined by the magnitude of intensity change chosen to detect and shape of those detected edges only. It does not study the shape of the area outside of that partially enclosed set of edges. In other words, the arrangement of grains and shape of that cluster has no effect on the segmentation result provided the boundaries between them are at least partially detectable. This makes the proposed technique more robust, which is important in highly clustered microstructure such as those of the fully globular type. This robustness is illustrated by the graph in Figure 8.12 which shows how the F-score of segmentation varies through different datasets for each technique. While other methods see a significant drop for some datasets, the performance of the proposed approach is far more consistent and has a smaller drop in accuracy in these scenarios.

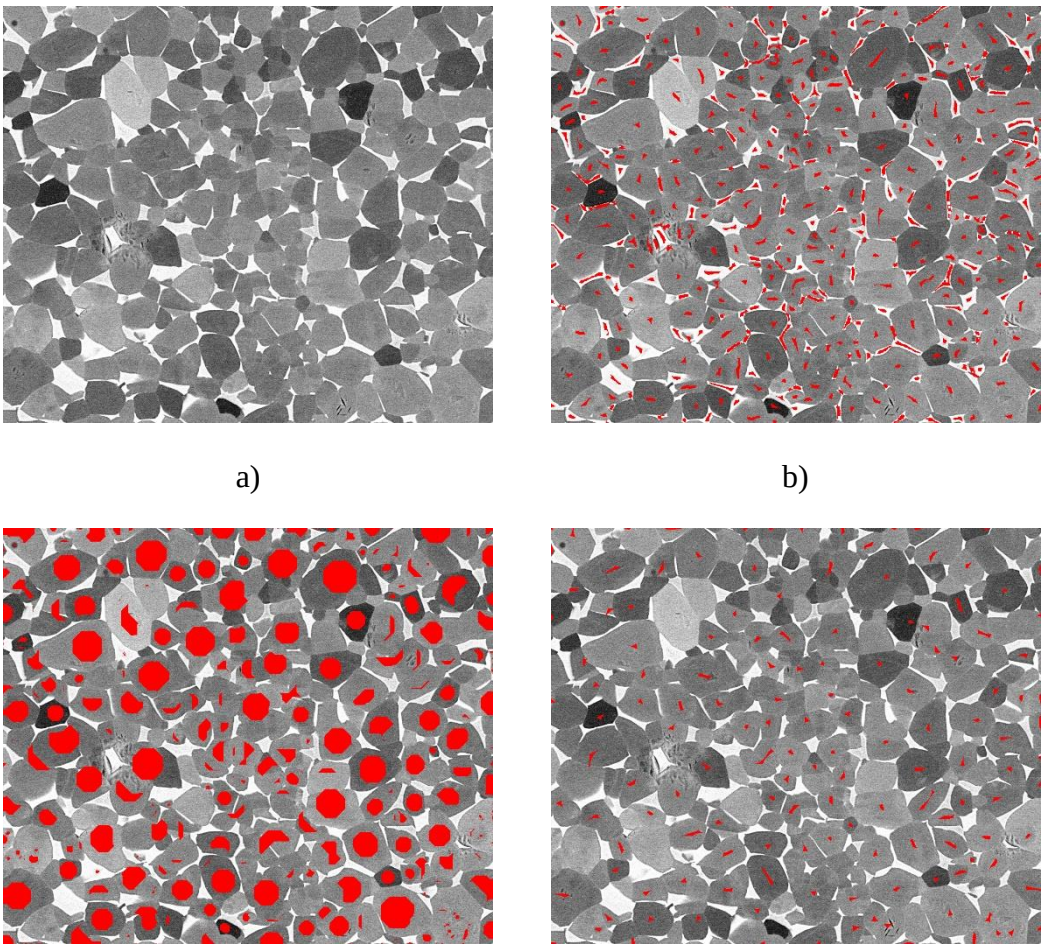

a) b)

c) d)

Figure 8.11: Markers used for segmentation in Figure 8.10 where a) original image, b) markers computed using CGM , c) markers computed by ultimate opening and d) markers computed by h-minima

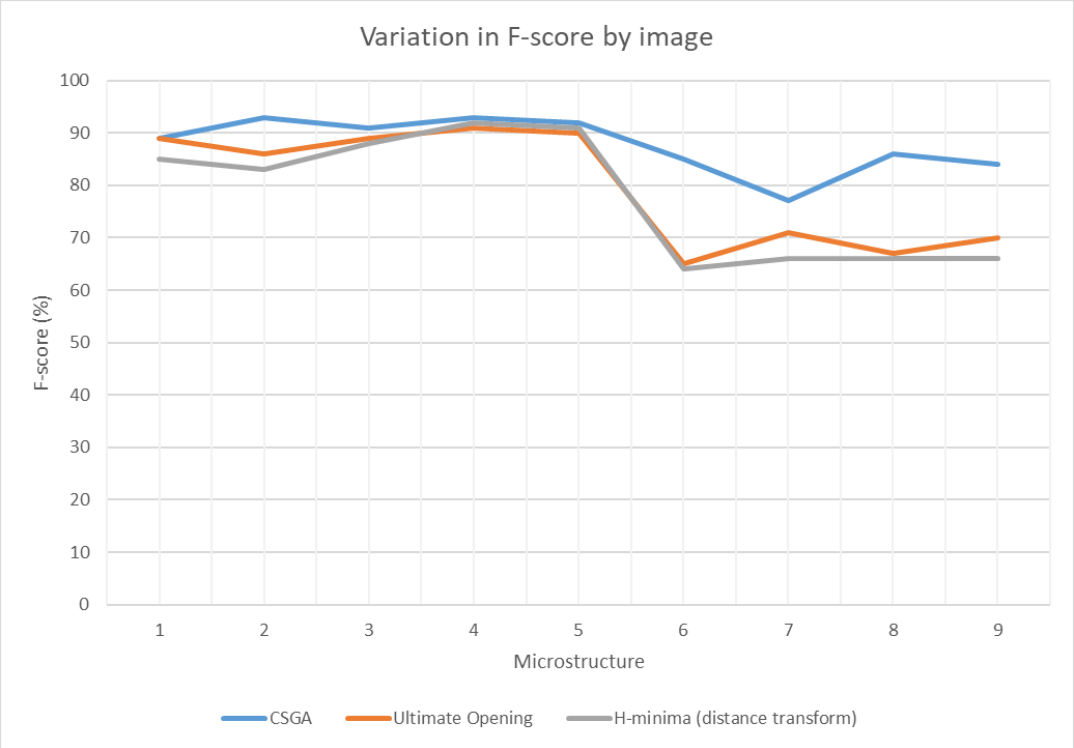

Figure 8.12: Graph of variation in F-score by image

8.2.5 Evaluation of optional functions

In the technique described in Chapter 5 there are two post-processing steps in the algorithm that are considered as optional, the artefact detection method and the additional splitting function. The reason these are consider optional is that both methods were judged to not improve results universally across the full titanium dataset. This occurs as artefacts are rare, existing in only a few of the microstructures studied, meaning the effect of artefact detection cannot be fully evaluated. As the Watershed Transforms normally over-segments more than it under-segments, increasing segmentation through the additional splitting would normally not lead to better overall measurements. An issue common to both optional functions is that false positives are possible when using them and the number of potential errors to actually solve, are relatively low. This means even a few false positive from these methods could potentially decrease the overall accuracy of results. This section aims to explore this and evaluate the extent of the benefit, or detriment, of these methods and to which microstructures they are best applied.

8.2.5.1 Additional Splitting

The additional splitting function is evaluated by comparing the F-score for each segmentation result before and after this technique is applied. The results are shown in Table 8.6. The F-score is a useful metric for this comparison as it will inform about segmentation accuracy directly, rather than the overall effect on measurements. This means that provided more errors are fixed than created by this technique the F-score will be higher. If the result is already over-segmented, then microstructural measurements would not necessarily show this.

Table 8.6: Comparison of F-score with and without additional splitting function

	Without splitting	With splitting	Difference
Microstructure 1	72	76	+4%
Microstructure 2	76	81	+5%
Microstructure 3	76	78	+2%
Microstructure 4	91	88	-3%
Microstructure 5	89	87	-2%
Microstructure 6	92	92	0%
Microstructure 7	89	87	-2%
Microstructure 8	92	91	-1%
Microstructure 9	90	91	+1%

The proposed splitting function shows clear benefit in some cases; however, results are not consistent and it appears to cause errors for some microstructures. The reason for this is that this function uses boundary shape alone to add new boundaries but such concavities are not always indicative of true grain boundaries, meaning both true and false positive boundaries are possible. It is noteworthy that the benefits came in images that were less accurately segmented, with F-scores below 80%, while cases showing an F-score greater than 90% had more errors introduced by this function than resolved. Additionally, Section 8.2.3.1 shows that for practical implementation, grain size measurements tend to be slightly smaller than expected due as under-segmentation

errors are slightly more common. This means that additional splitting may actually lead to less accurate aggregated measurements, even when the change in F-score is positive. All of this means it is not expected that this post-processing tool will be beneficial in all scenarios. Instead it is advisable to only use this function in difficult cases where there is little intensity change to indicate boundaries and clustering is high. This most often occurs in OM images and can be applied by a user via functionality in the new software tool presented in this work. A good example of the application of post-segmentation splitting is shown in Figure 8.13, which shows “Microstructure 2”.

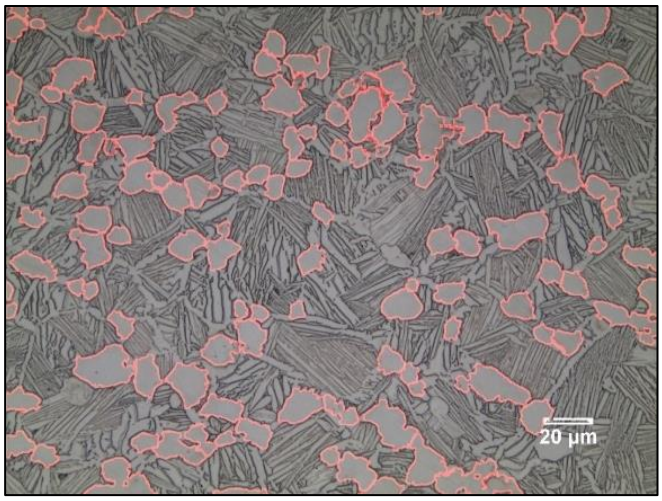

a)

b)

Figure 8.13: Example where additional splitting is beneficial where a) is original image and b) is new segmentation

8.2.5.2 Artefact detection evaluation

The artefact detection function proposed in Chapter 5 is only applicable to a few images in this study, as such artefacts are quite rare. It is, therefore, difficult to conduct a robust validation of the effectiveness of this method. For this reason, this function is not included by default and instead left as an optional function in the final software tool. It was not possible to obtain a larger dataset of images containing these artefacts, as the exact conditions causing them to occur is not known. Qualitative verification can be performed by studying the visualisation of detected artefacts shown in Figure 8.14.

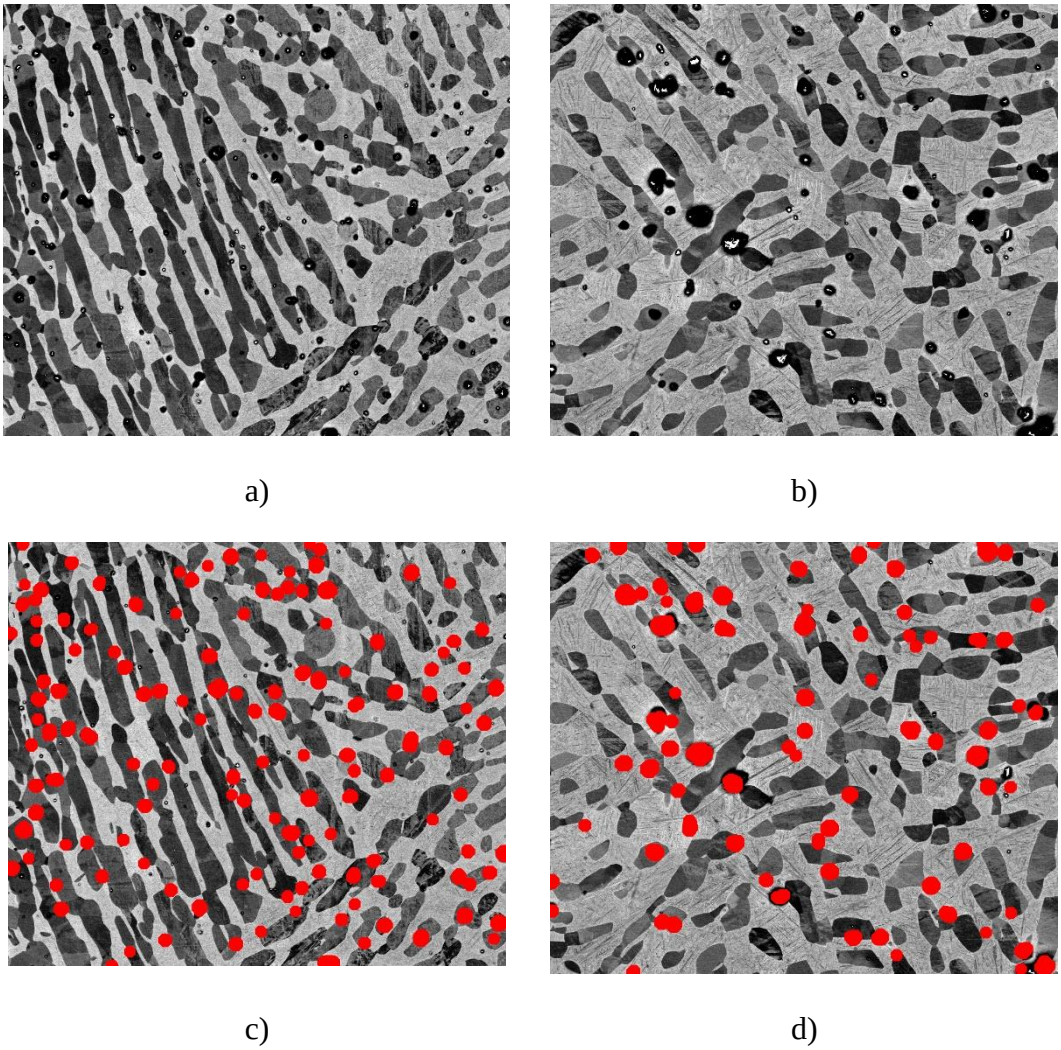

a) b)

c) d)

Figure 8.14: Detection of artefacts in microstructural images where a) and b) are original images and c) and d) show an overlay of the artefacts marked in red

It can be observed from this results that the detected method locates artefacts in the microstructures well. This alone is useful as such results could be used to alert the users to microstructural images in a batch that are potentially corrupted by these artefacts. However, as described in Chapter 5, preventing these from influencing the segmentation result is more challenging.

Table 8.7: Improvement in segmentation accuracy using artefact detection techniques

Image	F-score (%)		Grain Size Error (%)	
	With artefact removal	Without artefact removal	With artefact removal	Without artefact removal
Microstructure 1	82	81	0%	6.1%
Microstructure 2	87	87	2.7%	8.6%

The results shown in Table 8.7 give a mixed impression of the effectiveness of the proposed method of dealing with artefacts in images. When the segmentation accuracy is assessed using the F-score metric the artefact detection appears to have almost no affect. However, the difference in measured grain size between automated methods and the ground truth decreases slightly when artefact detection is used. The reason for this appears to be that artefact removal methods remove gradient information at artefact locations. As a result, there is a reduction in over-segmentation errors when artefacts are at the centre of grains, however, an increase in under-segmentation errors when artefacts are close to the boundaries, as genuine information may be removed. The consistent F-score suggests that the total area of the image being correctly measured has not changed but that the over-segmentation had a more significant effect on results. Ultimately, it will depend on the image content whether the artefact removal methods proposed here are suitable.

8.2.6 Summary of globular grain analysis

The results presented in this section confirm that the proposed image processing techniques can automate the measurement of microstructural images to a similar level of accuracy as can be achieved using existing manual procedures. In most cases the difference between measurements performed using existing manual techniques and the new automated procedures was less than 0.5um, a particularly strong result given the varied dataset. Measurement of globular volume fraction is also possible, using the new techniques. Some calibration was required to give matching results, however, the same difference in globular volume fraction between microstructures was found with or without this. The measurement time for either feature is significantly reduced, from around 15 min per image to between 3 and 20 seconds depending on the image. Not only will this reduce the resources required for microstructural analysis, allowing skilled material scientists to focus on other work, but the time saving is large enough that it would allow larger microstructural datasets to be analysed than would have previously been practical to measure. The automated nature of this approach also means repeatability is achievable, so long as no parameters within the software are changed. Furthermore, the software does not sub-sample grains in the image which typically results in far more grains being measured than using manual approaches. This increases the statistical reliability of results and prevents any potential bias effecting which grains are included in the sample. These benefits are critical in industry where material manufacturers require fast results from analysis and for results to be independent from the operator performing the analysis.

Ensuring automated techniques are accurate and robust to variations in microstructure is challenging. The new methods for globular grain analysis have been tested on microstructural images produced by different imaging technologies and of multiple microstructure types, subjected to a variety of thermal and mechanical processes. The results were positive, confirming that the proposed automated techniques are capable of measuring a wide variety of microstructures. Comparisons between the new techniques and a recent automated analysis procedure further demonstrated the superior generalisation of the proposed method. Although tested on microstructures of Ti6Al4V, this generality should allow the new method to be applied to a range of different microstructures by changing only a few parameters.

The segmentation accuracy was also measured using F-score. While several reasons were discussed as to why this is not informative of the accuracy of grain measurements it provides a good demonstration of the benefits of the proposed segmentation algorithm when compared to other image segmentation techniques. Specifically, it is shown that the new method performed better when more complex microstructures were studied and produced more consistent segmentation results overall. The analysis provided reveals that the novel marker computation method is a key reason for this. It is likely that this method to compute markers would be of benefit in other image segmentation applications featuring touching objects.

Finally, the optional post-processing functions described in Chapter 5 were assessed. Result were not as positive in these trials, confirming the decision not to use them by default in the proposed novel software tool. However, several scenarios were discussed and demonstrated where the proposed functions would be of benefit. Therefore, their inclusion in this thesis and within the proposed software module provides an additional tool that can be deployed when necessary as determined by an expert user.

8.3 Measurement and analysis of platelets

This section evaluates the effectiveness of the titanium alpha platelet measurement techniques proposed in Chapter 6. First, and most importantly, the accuracy of measurements is validated by comparison against those produced by expert material scientists. This will illustrate whether the aim of providing a reliable automated microstructural analysis technique has been achieved for alpha platelets. Additional trials are then provided to compare the accuracy of these measurements against those achieved by other automated image processing methods to demonstrate the improved robustness achieved by the new image processing techniques.

8.3.1 Experimental methodology

The validation of measurement of lamellar microstructures are performed on both lamellar and bi-modal microstructures, where alpha platelets are visible in the microstructure.

As in Chapter 6, S_θ was set to 10°, S_L was set to 2 pixels and L_{max} was set to 91 pixels for most images as this was found empirically to give the best results. In a few

exceptional cases it was instead set to 191 pixels when the unusually large objects exist, as explained in Section 8.3.2.2. This value was always set higher than any of the lath widths in the dataset so ensured accurate results as each image location was probed with a sufficiently long SE to only fit at a single orientation. The technique was used to extract 4 different microstructural properties, namely: platelet orientation; platelet width; colony size; and volume fraction of globular alpha. However, not every property was measured in each microstructure as some microstructures did not contain colonies or globular grains. Instead a subset of suitable microstructures was selected to test the measurement accuracy of each of the 4 microstructural properties.

Measurements are compared with existing microstructural analysis method in Section 8.3.2 and with existing image processing techniques in Section 8.3.3, in order to evaluate the potential contributions in each field.

For microstructural analysis, the measurements performed using the proposed automated techniques were validated through comparison with measurements of the same features performed by expert material scientists. Platelet width and colony size were measured using the ASTM E112 standard with manually chosen line segments [29], with the mean size used as a metric for comparison. Globular volume fraction was measured by an expert material scientist marking every pixel within all grains in the microstructure as either equiaxed or elongated grain and calculating the percentage of marked pixels that were globular. This is similar to the point counting method described in the E562 standard, except it is more complete so gives a more accurate representation to compare the automated measurement with. Precise measurements of the length and width are not needed for computing globular volume fraction in this instance as all non-platelets are considered globular. For platelet orientation measurements, a material scientist used a protractor to manually measure what they believed was the primary orientation in the microstructure. If there was a significant secondary orientation, then this was also measured in the same way. This metric was chosen for comparison as the mean value, used as a metric for size-based measurements, is not necessarily meaningful for properties measured over a finite field, such as orientation. However, knowledge of which orientations of platelets are most common is known to be useful as this is studied in existing research [121].

As producing accurate manual measurements of microstructural features is a non-trivial task, and can contain elements of subjectivity and human error, it is important to allow for some differences between automated and manual measurements. In this validation, automated measurements are considered to be correct if they are within the margin of error expected in accepted standards. For size-based measurements, the E112 standard expects variations of +/- 0.5G, which equates to about 16% in um. For volume fraction, the E563 standard expects variations within 10%. No expected variation for the manual orientation measurements is known.

In the field of image processing, all of the existing procedures of interest, identified in the literature review, for studying elongated objects, are used in applications where the data consists exclusively of such objects. In Ti-6Al-4V, a bimodal type of microstructure is common which contains both globular and elongated objects. The ability to filter out globular objects, gives the new algorithm a significant advantage over existing techniques in these cases. Therefore, in order to provide a fair comparison, and indicate only benefits that to the measurement of elongated structures such as platelets, bi-modal microstructures in the dataset are omitted here. The comparison with existing image processing techniques, described in Section 8.3.3, therefore, does not measure all the microstructural properties validated in Section 8.3.2 but instead only investigates properties computed directly from platelets, i.e. width and orientation. Different techniques from the literature are chosen for the comparison of width measurements than orientation measurements, as the most suitable and recent methods did not measure both features. The platelets in the chosen dataset are often not perfectly straight and vary in size and aspect ratio within each image. This makes this application challenging and a good test of the robustness of image analysis methods. In addition to the titanium images a set of artificial images are also included in these trials. These images contain no noise and consist of perfectly straight laths. As the precise properties of the artificial datasets are known, their inclusion allows the relationship between measurement accuracy and particular image features to be studied.

The improvement in orientation measurements is shown through comparison with existing methods described by Borocco *et al.* [63], which measures orientation using rotational SEs. These techniques have been shown very recently, in 2017, to be

accurate for measuring elongated structures in microstructural images of graphene. The objects measured in the existing work are extremely thin, are difficult to distinguish due to a low image resolution, in terms of pixels per object, and are not always perfectly straight. For these reasons it is believed this represents the state of the art for orientation measurement in microstructural data. However, preliminary trials suggested that this approach may not robust when the width of these structures cannot be predicted. The experiment establishes how acceptable or otherwise this weakness is for titanium microstructures and the extent of the benefit offered by the new technique. As the platelet analysis techniques proposed in this thesis are based on Borocco's work, a comparison with this is important to demonstrate the contribution of the method presented.

No very recent automated measurement for widths in microstructures were identified with the method from Collins *et al.* [11] published in 2009 being the most recent available. This method was, in-fact, first proposed by Tiley *et al.* [12] a few years earlier and also performs measurement using rotating elements, however, has documented problems measuring shorter platelets [11]. Despite this it is important to include this as it is tested on Ti-6Al-4V microstructures in the original work. These authors also cite a textbook by Russ *et al.* [55] for general image analysis that describes measurements of width in microscopic images using the distance transform, that is also relevant to include. Due to the age of these methods two, much more recent, methods used for width measurements in different applications are also included. A recent method, published in 2016, by Statella *et al.* [59] is selected as it has success in measuring the width of elongated features using granulometric techniques. Although the application, dust devils on images of the Martian surface, is very different, the data itself is relatively similar. A different width measurement approach proposed by Adhikari *et al.*[56] is also used in the comparison. This method was used to measure the width of cracks in images of concrete, where images again shared similar properties.

All of the aforementioned methods are described in the literature review in Chapter 4 and were implemented for this study based on the cited journal articles. The relative accuracy of each method is determined by comparing the difference between the measurement achieved and the ground truth measurement. For the artificial images,

this is the width and orientation at which features were drawn and for the titanium images these are provided by manual measurements performed by expert material scientists using existing standards, as previously described. As the precise properties of objects in artificial images are known this allows the relationship between measurement accuracy and the aspect ratio to be studied to confirm the hypothesis that existing methods suffer when the aspect ratio is high. Where possible parameters are kept consistent between the methods tested. This means that the same threshold is applied to create the binary image used by each technique, and that orientation step size, S_θ, was set to 10° for both the new technique and Borocco's method.

8.3.2 Comparison with existing manual standards

In this section the performance of the new technique for platelet analysis is evaluated. This is achieved by comparing the automatically produced measurements with those from existing manual procedures. Mean alpha platelet width, globular volume fraction, the main orientations of platelets and the size of platelet colonies are all considered using bi-modal and fully lamellar microstructures.

8.3.2.1 Alpha platelet width

The proposed method measures, for each pixel in the image, the width of the object that pixel resides within, as described in Section 6.6.2. The raw output of this measurement is a 2D image where pixel values correspond to the width, a colourmap of this is shown in Figure 8.15. Qualitatively this result appears accurate as fewer pixels of a deep blue colours appear where laths are wider and bands of consistent colour form across the shortest dimension of the lath. This output is useful for highlighting regions of the image where platelet width differed.

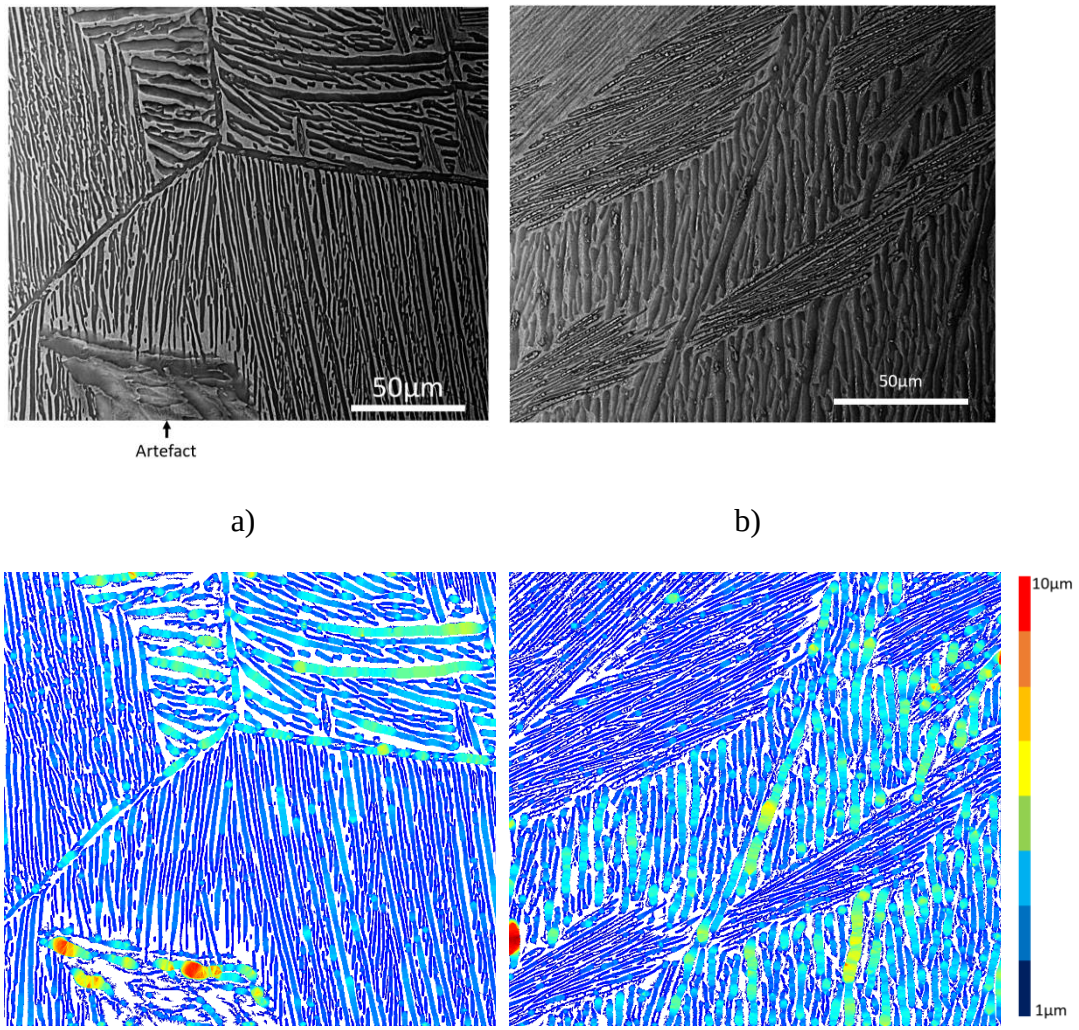

Figure 8.15: Results of width measurements of alpha platelets where a) is a microstructure with an artefact occupying an area, b) is a completely transformed microstructure and c) and d) show the a colourmap of the corresponding platelet width measurements

Table 8.8: Comparison of platelet width measurements between the new techniques and existing manual methods

	Alpha Platelet Width (um)			Measurement Time
	Manual Method	Proposed Method	Difference	
1	2.19	2.58	+0.39 (18%)	3 minutes 20 seconds
2	2.15	2.17	+0.02 (1%)	2 minutes 58 seconds
3	2.86	2.65	-0.21 (7%)	2 minutes 59 seconds
4	2.22	2.09	-0.13 (6%)	2 minutes 49 seconds
5	1.93	1.73	-0.2 (10%)	3 minutes 8 seconds
6	2.41	2.72	+0.31 (13%)	2 minutes 56 seconds
7	2.25	2.40	+0.15 (7%)	2 minutes 58 seconds
8	2.38	2.46	+0.08 (3%)	3 minutes 11 seconds

Quantitative results confirm that measurements of alpha platelet width are broadly similar between the existing manual techniques and the proposed method, as shown in Table 8.8. The majority of results were within this expected range and the microstructure that failed was only 2% outside this limit. These errors can be explained by regions in the microstructure containing an artefact, potentially caused by polishing errors, which is observable in the bottom of Figure 8.15. A material scientist will usually recognise these regions and ignore them when performing measurements. However, some areas within this may be elongated which the proposed techniques will identify as a platelet and subsequently measure. This often leads to slightly larger measurements in these cases, as in microstructure 1 and 6, shown in Figure 8.15 a) and b) respectively. Several of the microstructures used in this study contain at least some extremely fine platelets of only a few pixels wide. It is expected that this will lead to larger differences in measurement than in more magnified images although no significant correlation between platelet width and measurement accuracy was observed in this study.

8.3.2.2 Globular Volume Fraction

The proposed method measures, for each pixel in the image, the elongation of the object that pixel resides within, as described in Section 6.5.3. The raw output of this measurement is a 2D image where pixel values correspond to the elongation, a greyscale map of this, where high values equal high elongation, is shown in Figure 8.16. Qualitatively this result appears accurate as globular grains appear significantly darker than laths. This output would be useful for visualising the spatial distribution of different grain morphologies.

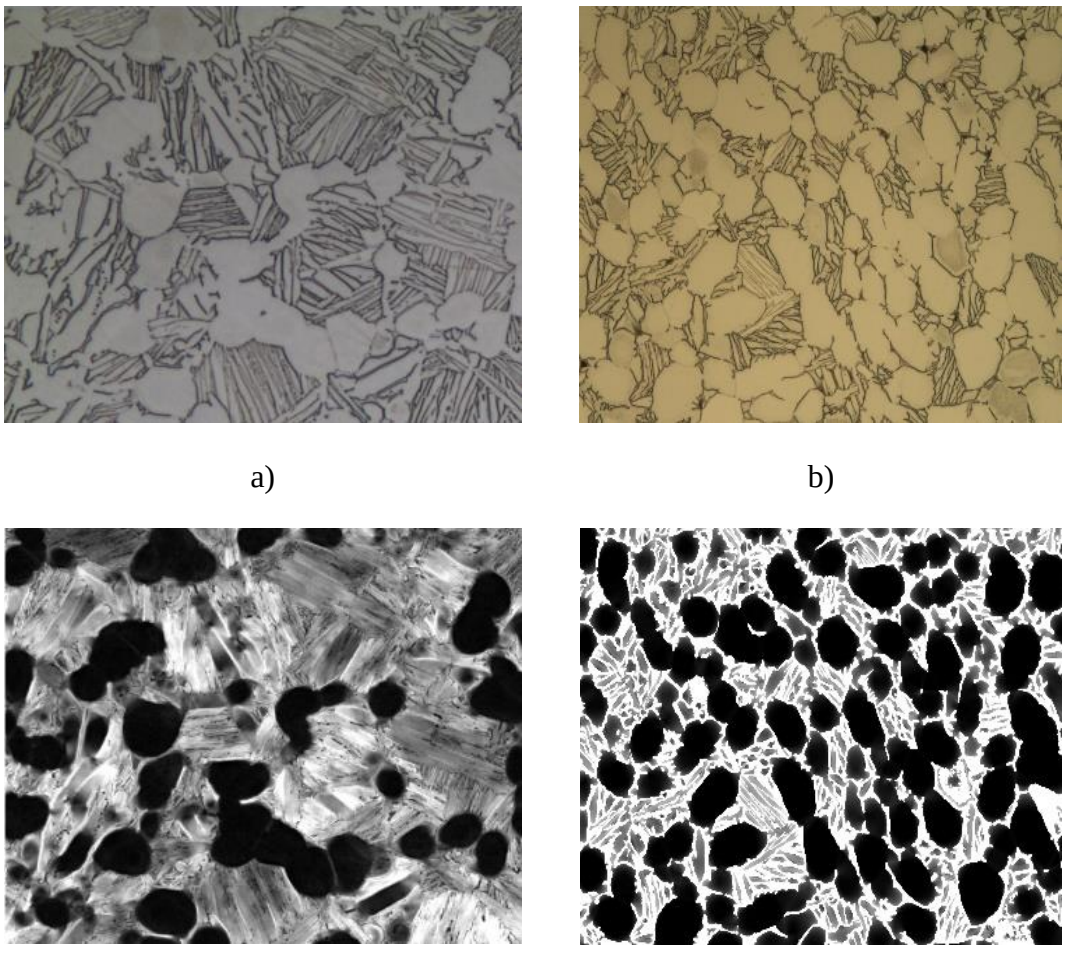

a) b)

c) d)

Figure 8.16: Greyscale representation of elongation of grains where higher intensity equates to more elongated structures and a) and b) are original images and c) and d) elongation maps

Measurements of globular volume fraction are dependent upon a threshold aspect ratio at which grains are considered globular. For manual measurements, an aspect ratio of 2:1 was considered the threshold between globular and elongated grains by the material scientist. The same material scientist selected a T_s value of 60 experimentally for the automated procedure. As this threshold is applied to an elongation measurement that considers the radius of the grain at multiple angles there is not always as a direct correlation between this value and the 2:1 aspect ratio as the experimentally selected value also accounts for protrusions and general inconsistency in grain shape, as described in Chapter 6. The same threshold was used for all microstructures under study. The measurements generally showed good agreement between manual methods and the proposed approach, as shown in Figure 8.16. In almost all microstructures, the globular volume fraction was within 5% of the expected value. This is supported by the results shown in Figure 8.16 c) and d) where a clear intensity difference, indicating whether grains are globular and elongated, can be observed. The exception was microstructure 8, which is a complex microstructure imaged using an SEM. This microstructure contains many recrystallized grains that exist in tightly packed clusters. As these clusters have no beta phase between them the linear SEs used in the new technique can exceed the boundaries between grains causing globular grains to be misidentified as platelets. This issue is illustrated in Figure 8.17 where the intensity change between grain morphologies are more difficult to observe and erroneous linear artefacts appear, indicative of the fact the SE has exceeded the grain boundary. These types of small recrystallized grains also appear in microstructure 4, also shown in Figure 8.17, and 5 but do not cause as significant errors. However, while extremely complex the results in Figure 8.17 still support the broadly accurate measurement achieved as Figure 8.17 e) and f) show elongated platelets that are mostly separated from the surrounding globular grains.

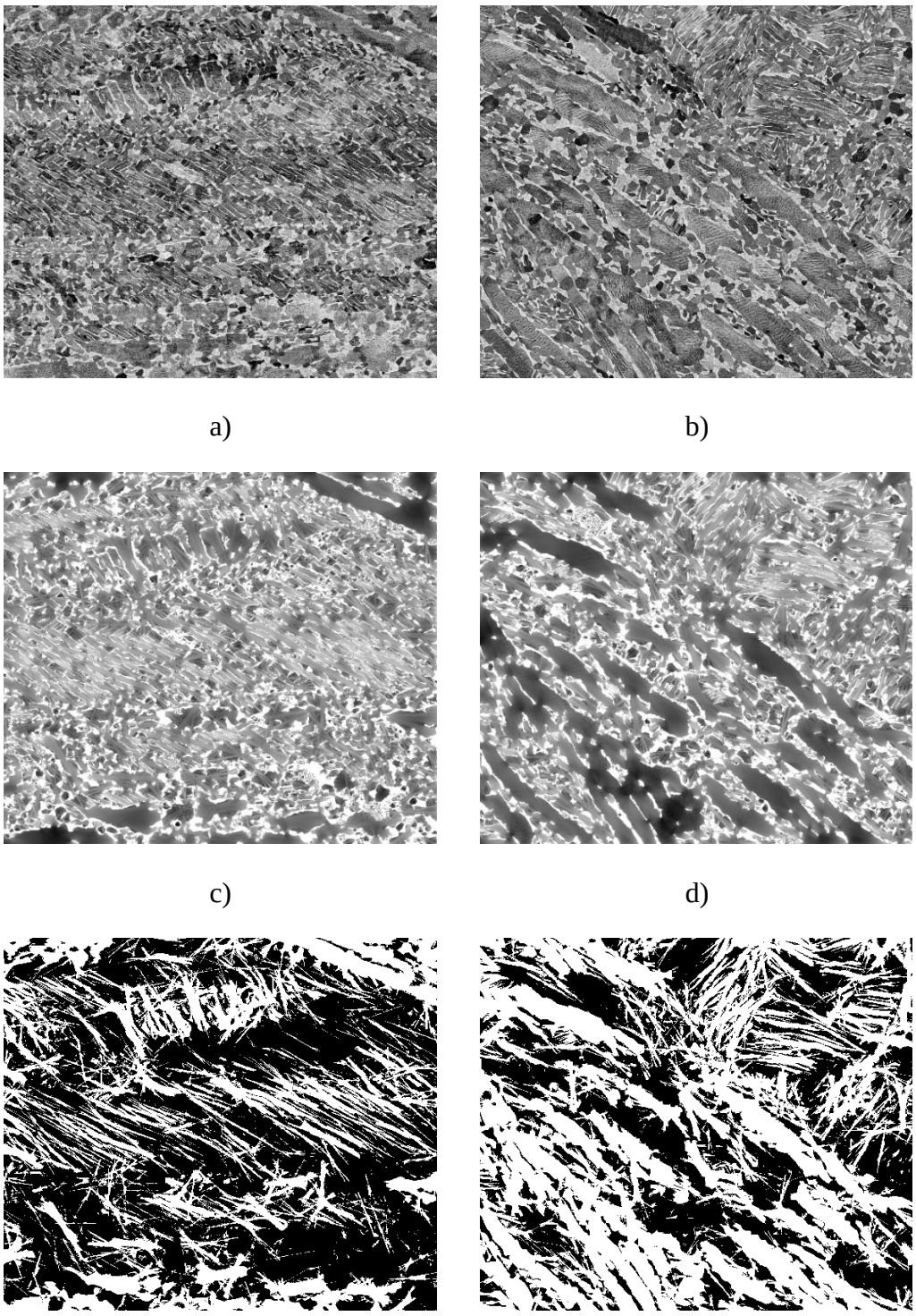

Figure 8.17: Results of globular volume fraction separation on challenging microstructures where a) original image of Microstructure 4, b) original image of Microstructure 8, c) and d) are the corresponding elongation map where pixel intensity indicates elongation and e) and f) is the resulting split into globular grains and elongated platelets

Table 8.9: Comparison of globular volume fraction measurements between the new techniques and existing manual methods

	Globular Volume Fraction (%)			Time
	Manual Method	Proposed Method	Difference	
1	71	75	+4	3 minutes 1 seconds
2	74	77	+3	2 minutes 58 seconds
3	36	34	-2	3 minutes 5 seconds
4	24	29	+5	3 minutes 4 seconds
5	25	28	+3	7 minutes 48 seconds
6	34	38	+4	8 minutes 3 seconds
7	20	19	-1	7 minutes 57 seconds
8	36	52	+16	7 minutes 51 seconds

8.3.2.3 Orientation of platelets

The proposed method measures, for each pixel in the image, the orientation of the object that pixel resides within, as described in Section 6.6.3. The raw output of this measurement is a 2D image where pixel values correspond to the orientation, a colourmap of which is shown in Figure 8.18. Qualitatively this result appears accurate as the colours within each lath are consistent and match up with the apparent orientation of the lath. This output makes it easier to observe the texture of the microstructure.

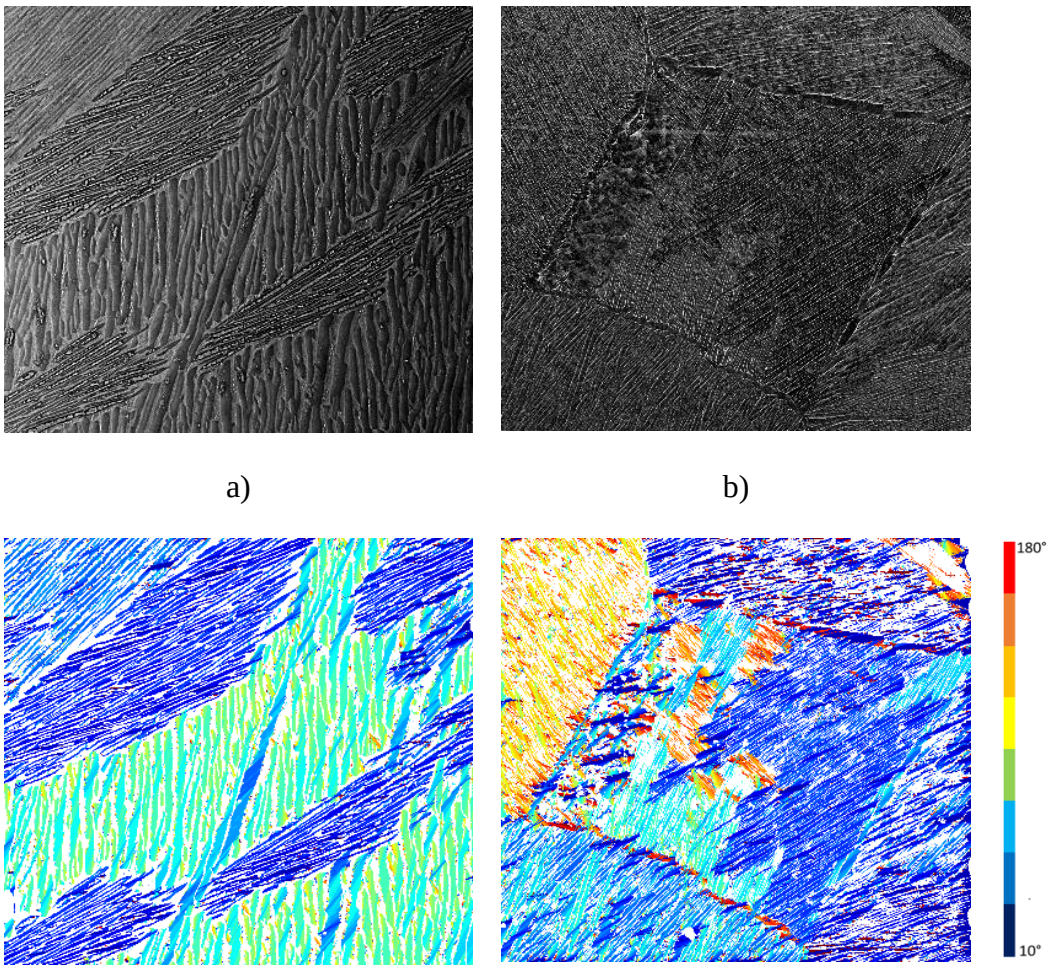

a) b)

c) d)

Figure 8.18: Colourmap of a microstructure with orientation marked by colour where a) and b) are original microstructures and c) and d) are colourmaps

Confirmation that the measurement of the orientation of alpha platelets is highly accurate using the proposed techniques, is provided by the quantitative results in Table 8.10.

Table 8.10: Comparison of platelet orientation measurements between the new techniques and existing manual methods

	Orientation of platelets						Time
	Manual Method		Proposed Method		Difference		
	Primary	Secondary	Primary	Secondary	Primary	Secondary	
1	100	175	100	180	0	5	2 minutes 57 seconds
2	90	175	90	180	0	5	3 minutes 4 seconds
3	90	None	90	None	0	0	3 minutes 3 seconds
4	90	30	80	30	10	0	3 minutes 1 seconds
5	45	90	40	60	5	30	3 minutes 5 seconds
6	30	140	30	130	0	10	3 minutes 1 seconds
7	None	None	None	None	0	0	2 minutes 57 seconds
8	None	None	None	None	0	0	2 minutes 58 seconds
9	180	None	170	None	10	10	2 minutes 59 seconds

All measurements of the most common orientation of laths in the images, referred to as the primary orientation, were within the expected variation and more than half were an exact match. There were a few cases of disagreement in the second most common platelet orientation, referred to as the secondary orientation measurement. In microstructures 1 and 2 this error was small and is likely the result of either the region of the secondary orientation being smaller and any noise being more significant. This is compounded by the artefact areas in these images as shown in Figure 8.19 a). For microstructure 5 a significant number of platelets existed at both 90 and 60 degrees and there was disagreement between manual and automated methods over which was the most significant, resulting in a larger than expected error, as shown in Figure 8.19 b).

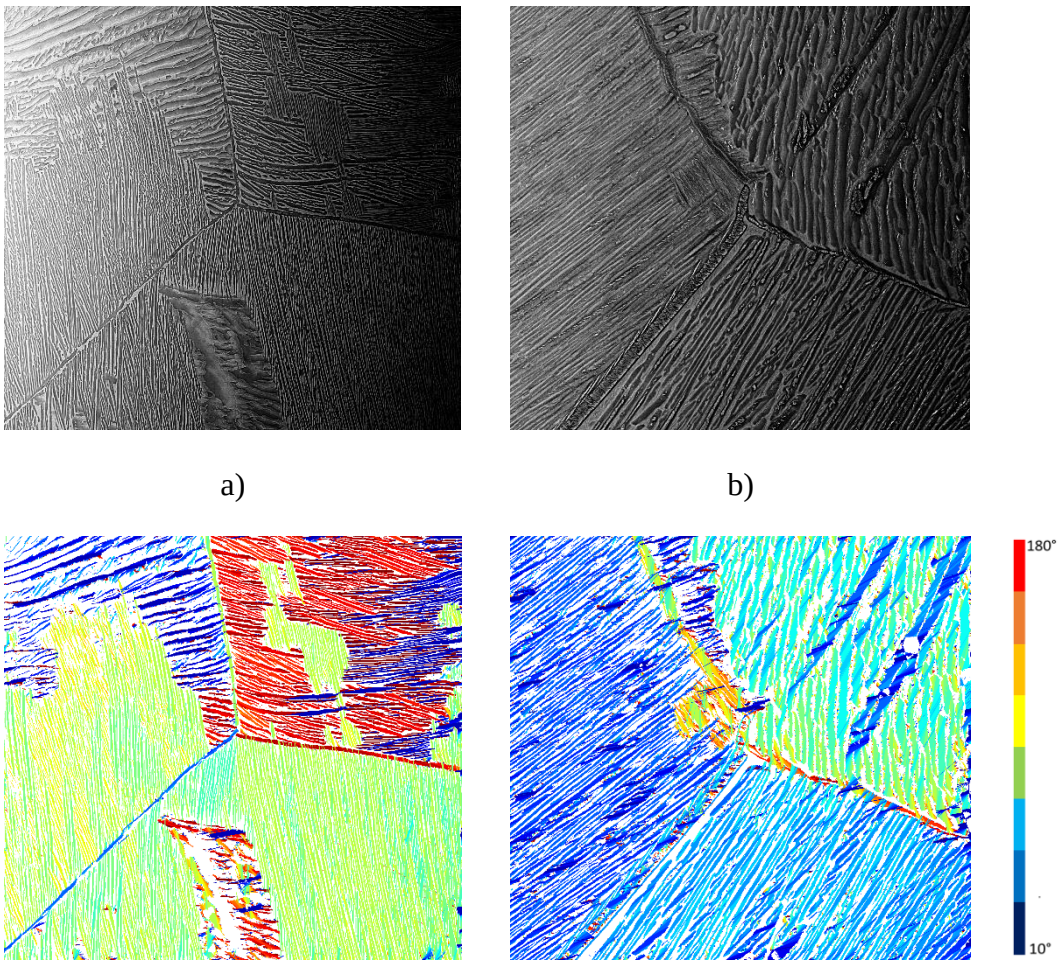

Figure 8.19: Results of orientation measurements of alpha platelets where a) is a microstructure with small disagreement in secondary orientation, b) is a microstructure with a large disagreement in secondary orientation and c) and d) are the orientation colourmaps

8.3.2.4 Colony size

Measurements of colony size are dependent upon pre-determined parameters w_{max} and *cs*, defined in Chapter 6 as the width between parallel platelets to be considered part of a colony and the percentage size of the maximum colony each other colony must exceed to be considered a primary colony. Secondary colonies are not considered in this test. Setting *cs*=10% means the software will ignore smaller lower order colonies, however, unlike other techniques evaluated in this section, a single value of w_{max} could not be used for all microstructures. A method to automatically select a suitable *w* value

for each microstructure is desirable but was not determine in this study. It was expected that this would relate to the width of platelets, however, no clear relationship between measured platelet width and the most suitable w_{max} value, determined experimentally, was observed. Further work would be required to determine what other factors affect the best w_{max} value and if this parameter can be determined automatically. For the purpose of validating the colony measurement algorithm, a material scientist, with no knowledge of the manual measurement the colonies, selected a w_{max} value for each microstructure experimentally based on a display of colony boundaries, as shown in Figure 8.20.

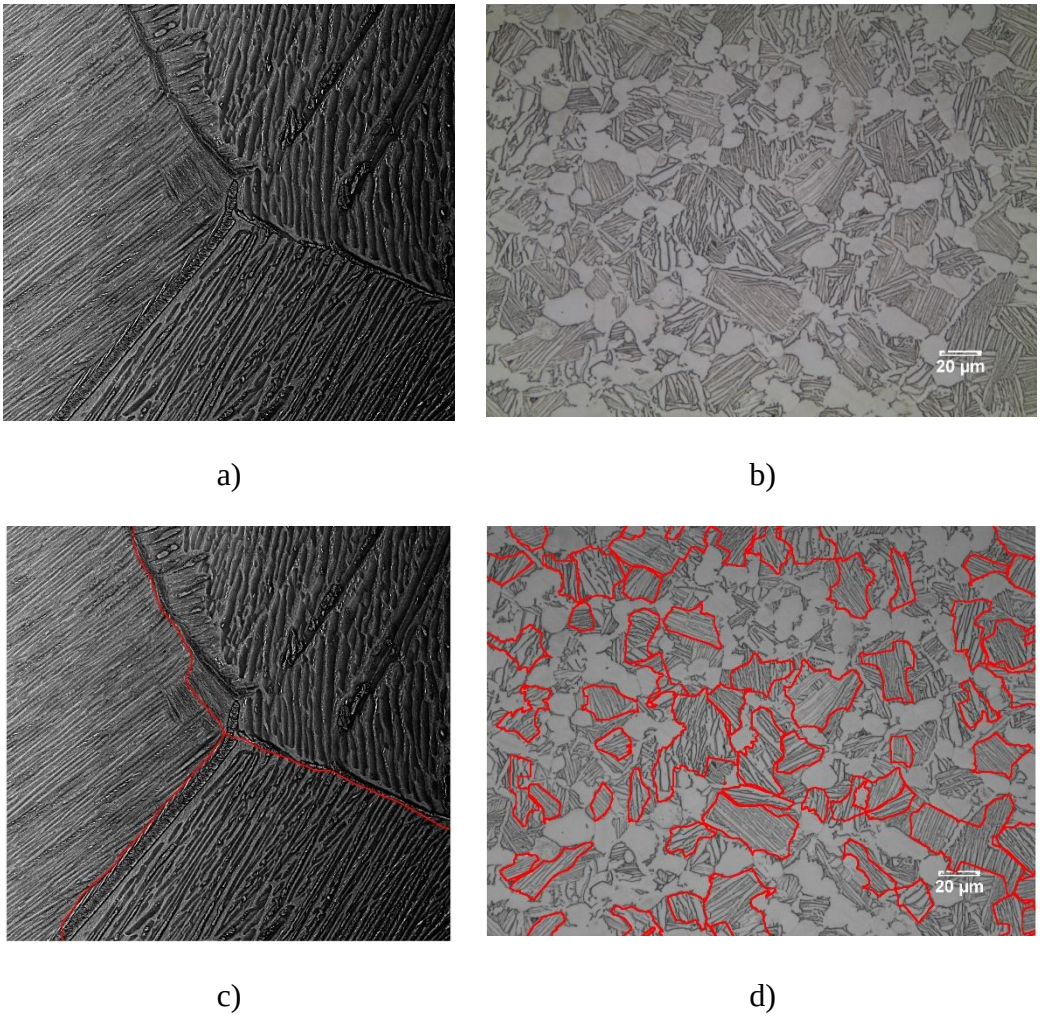

a) b)

c) d)

Figure 8.20: Results of colony identification where a) original image of a fully lamellar microstructure with triple point, b) is an bi-model microstructure and c) and d) are the colonies identified in each

Data containing visible colonies was limited in these trials and in some cases only partial boundaries could be seen in the images. The manual measurements used as a ground truth are of the visible portion of the colonies, i.e. treating all sets of parallel platelets as colonies even if the apparent colony terminated on the boundary of the image and may have in fact continued outside the field of view of the image. By allowing the software to also include colonies on the boundary, like for like measurements were produced for this comparison. It is believed that this makes the data in this section a fair comparison between manual and automated measurements, even if neither had enough initial data to measure colonies in as much detail as would be desirable for inferring microstructural properties.

Table 8.11: Comparison of colony size measurements between the new techniques and existing manual methods

	Mean Colony Size (um)		
	Manual Method	Proposed Method	Difference
1	135	129	6 (4%)
2	89	92	3 (3%)
3	198	199	1 (0.5%)
4	99	101	2 (2%)
5	82	93	11(13%)
6	19.48	20.61	1.13 (6%)
7	13.20	15.41	2.21(17%)
8	11.41	10.5	0.91(8%)

This creates an element of subjective variation between measurements of each microstructure but provided the selected value of *w* is stored results are easily repeatable. The results in Table 8.11 show the proposed algorithm does a good job of grouping adjacent platelets into colonies. However, it should be noted that this is not the sole identifier of colonies. The boundaries of primary colonies are often indicated

by triple points, where three boundaries of colonies meet, as in Figure 8.20, which are not detected by the proposed technique. If these boundaries are relatively wide or colonies are misoriented then platelets will not be merged across the triple point boundaries and results will still be accurate provided *w* is set correctly. However, in cases where these boundaries are thin it is possible for similarly orientated adjacent colonies to merge across this boundary. This contributes to the discrepancy observed in microstructure 5.

8.3.3 Comparison with other image processing techniques

In order to produce accurate measurements of alpha platelets, new image processing techniques were proposed. In this section the benefit of the proposed approach is demonstrated by comparing the results achieved with those from existing published techniques. A key benefit of the new technique is its ability to measure multiple different image features. As algorithms with the same functionality were not found in the literature the comparison instead compares measurements of features separately.

8.3.3.1 Orientation Measurements

The artificial images used in this study AR1-AR3 each contain laths of equal length and aspect ratio, although the length and aspect ratio does vary between each image. Conversely, AR4 and AR5 contain a variety of lath lengths and aspect ratios within each image. AR1 and AR 4 are shown in Figure 8.21. This set of images was created to explore the effect of both different and inconsistent aspect ratios, as it is hypothesised earlier in this thesis that other recent techniques for measuring elongated structures in microstructures would give errors for inconsistent aspect ratios.

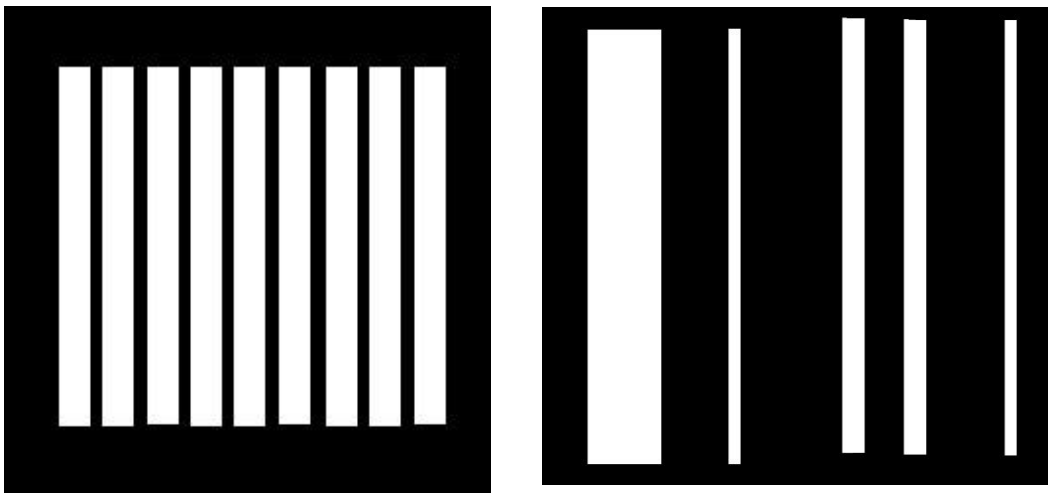

a) b)

Figure 8.21: Examples of artificial images (500x500) where a) is AR1 and b) is AR4

The technique proposed by Borocco *et al.* [63] requires a single parameter to be set, the length of SE used to probe the image. Selecting the length that provides the best results is not trivial and the best method for doing so was not addressed in the original work. Longer SEs are more likely to fit only at the true orientation, so each measurement has a higher probability of being accurate. However, longer SEs are more likely to not fit smaller object at all and return no measurement. For this experiment the SE length is selected based on the percentage of the image where the SE would fit at any orientation. This is the percentage of pixels in the alpha phase that return a valid measurement, as an SE to long the platelet at any orientation would not return any measurement. In Table 8.12 the measurements achieved by SE length that measures a maximum of 90% of the image and a minimum of 75% of the image are shown.

Table 8.12: Comparison of platelet orientation measurements between the new techniques and existing manual methods

Image	Aspect Ratio	Orientation of platelets (°)			
		Manual Method	Fixed Length SE method [63] (min 90% of image measured)	Fixed Length SE method [63] (min 75% of image measured)	Proposed Method
AR1	8	90	90	90	90
AR2	13	90	90	90	90
AR3	28	90	90	90	90
AR4	Mixed	90	80	80	90
AR5	Mixed	90	10	40	90
Ti-1	-	100	100	100	100
Ti-2	-	90	90	100	90
Ti-3	-	90	80	90	90
Ti-4	-	90	20	80	80
Ti-5	-	40	10	40	40
Ti-6	-	30	10	10	30

The measurements shown in Table 8.12 show that the technique proposed in this thesis is robust as it provides accurate measurements for all artificial images, regardless of object aspect ratio, and for the titanium microstructures as previously shown in Section 8.3.2.2. Almost all measurements of the primary orientation in both artificial and titanium images exactly matched the results obtained by an expert material scientist. The only disagreement in measurements occurs in a titanium image and is a 10° error, the smallest error possible using the chosen parameters. Meanwhile, the existing method using fixed length SEs [63] only provides accurate results in certain cases. For the images AR1-3 with no noise and consistent lath sizes measurements are a perfect match. Where the aspect ratio of laths varies, errors occur with a minimal error in AR4, where the variation in aspect ratio is low and a greater error in AR5 where the variation in aspect ratio is high. The results for the titanium images were more varied with some

measurements being acceptable and others being highly inaccurate. This is likely because some microstructures contain more consistent lath sizes than others. It is also interesting to note that more accurate measurements of lath orientation were achieved for larger SEs that measured a lower percentage of the image. This suggests that measuring fewer objects accurately is preferable to measuring everything less accurately using this method. However, the fact that 25% of laths are not included in these measured and several microstructures are still inaccurately measured means such an approach cannot be relied upon for complex images. The proposed approach not only provides the more accurate results but eliminates the need for this parameter selection and always includes every platelet in the image in the final measurements.

Colourmap images, shown in Figure 8.22, where each colour corresponds to a unique orientation value, provide a useful illustration of the improvement offered by the proposed approach. It is shown that for long and thin laths the orientation measurements are similar between methods as even a SE shorter than the lath will still normally only fit that lath at a single orientation. For example, the predominantly thin laths in Figure 8.22. g) and k) show little change in measurement between techniques. However, the thickest laths often have incorrect values using fixed length SEs as the element can fit at multiple angles. This incorrect angle can be seen as bands of colour within a lath such as in Figure 8.22 f) and h). Meanwhile in Figure 8.22. j) and l) these same laths are corrected to the expected measurement. There is still evidence of pixels within one lath having different orientation measurements due to curvature in lath boundaries, however, these are typically only 1 orientation value from other pixels while previous methods gave a wider range of measurements for a single lath.

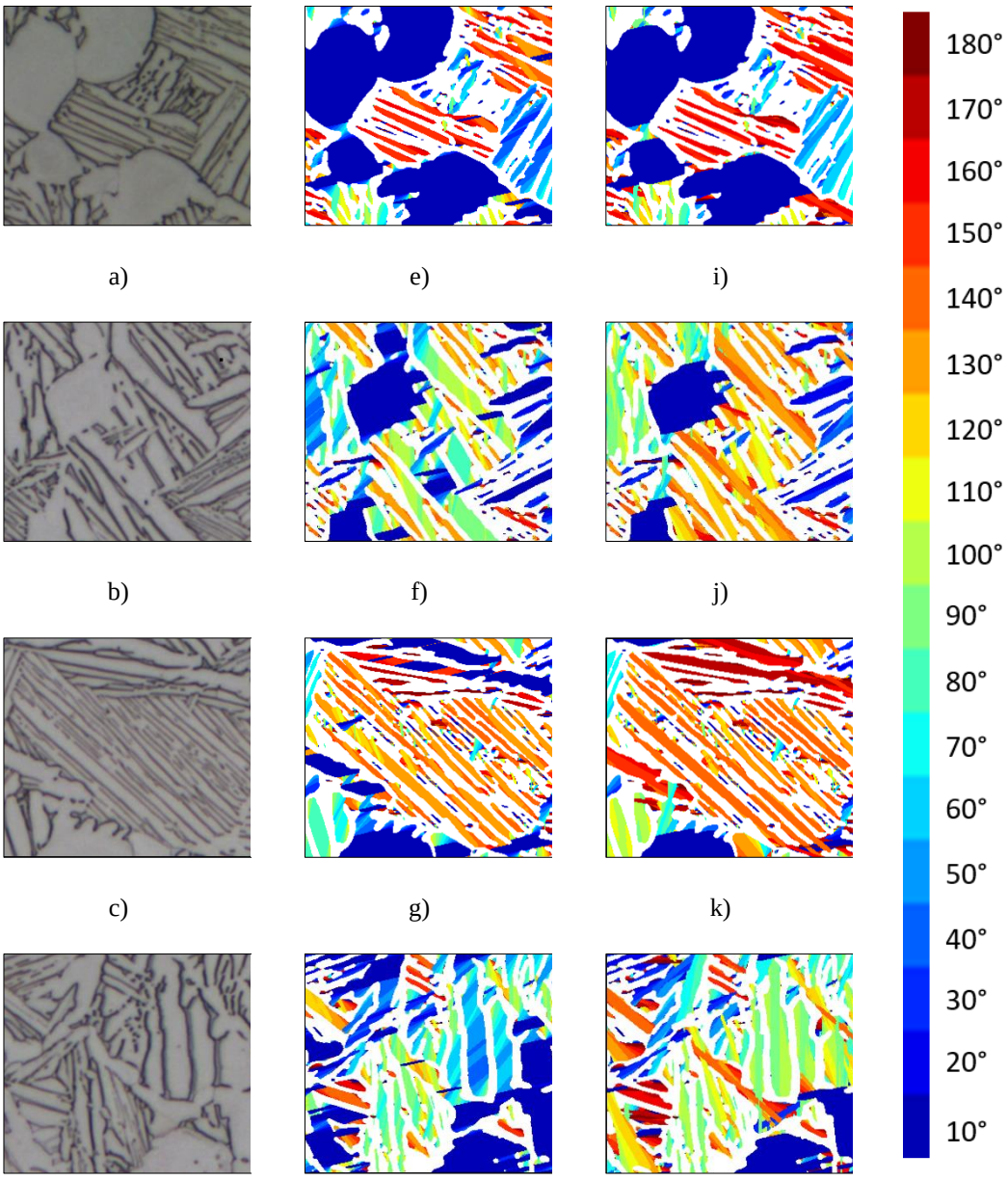

Figure 8.22: Colourmap of orientation measurements using different techniques

Overall, these images show a very good correlation between the perceived and angle of the platelet measured using the proposed technique and demonstrate a significant benefit versus the use of fixed length SEs.

8.3.3.2 Width Measurements

The artificial images used to test width measurement accuracy differ from the those used previously for evaluating orientation measurements. The reason for this is that, unlike orientation techniques [63], the alternatives for width measurements have known weakness for platelets below a specific, absolute aspect ratio, not variations in the aspect ratio. AR1-AR3 show images with elongated objects of high aspect ratio (above 20:1), which are expected to be measured well by existing methods. AR4 and AR5 show images with shorter objects, that existing authors hypothesise will not be accurately measured by existing techniques [11]. Examples of AR1 and AR 4 are shown in Figure 8.23.

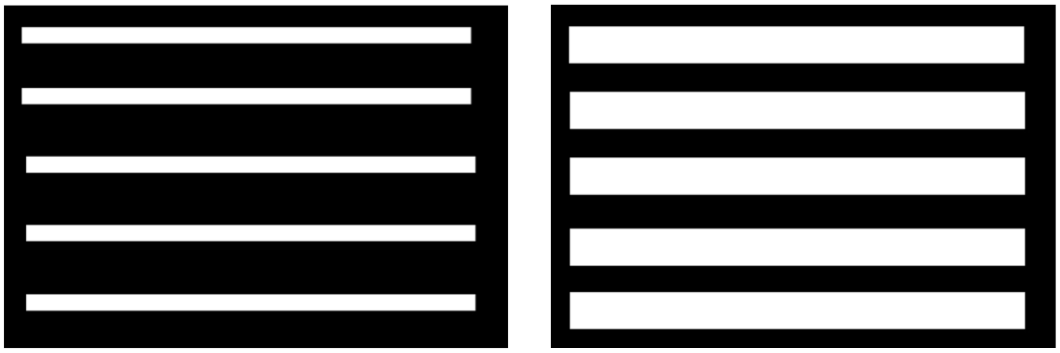

a) b)

Figure 8.23: Examples of artificial images where a) is AR1 (150x100) and b) is AR4 (1400x1200)

Unlike the comparison conducted to validate microstructural measurements, in Section 8.3.2.2, the results in Table 8.13 shows measurements in pixels rather than μm.

Table 8.13: Comparison of platelet width measurements between the new techniques and existing manual methods

	True Width	Measurement from FLOS	Mean inverse intercept [11]	Distance transform method [55]	Granulometry based method	Skeleton based method
AR1	3	3	3.35	3.93	4.09	3.9
AR2	8	7	8.28	7.83	9.89	10.38
AR3	86	85	85	86.93	89.83	90
AR4	192	191	147	189	195	209
AR5	303	303	183	289	302	345
Ti-1	10.67	9.06	7.51	23.34	11.67	6.51
Ti-2	20.87	20.67	13.39	18.71	30.61	12.41
Ti-3	25.45	27.47	15.07	27.2	19.89	5.82
Ti-4	20.11	21.36	10.43	14.96	21.02	8.12
Ti-5	16.61	18.53	9.66	21.09	15.97	6.42
Ti-6	12.85	11.35	7.4	14.69	11.12	3.99

This shows the measurements using the new FLOS approach are normally within 1 or 2 pixels of the ground truth measurement. This means that improving the accuracy of platelet width measurements would be difficult at this resolution of image and provides further assurance that this method is reliable. Mixed results were obtained by the other measurement techniques tested. Figure 8.24 shows a graph of the measurement errors from each technique as a percentage of the ground truth.

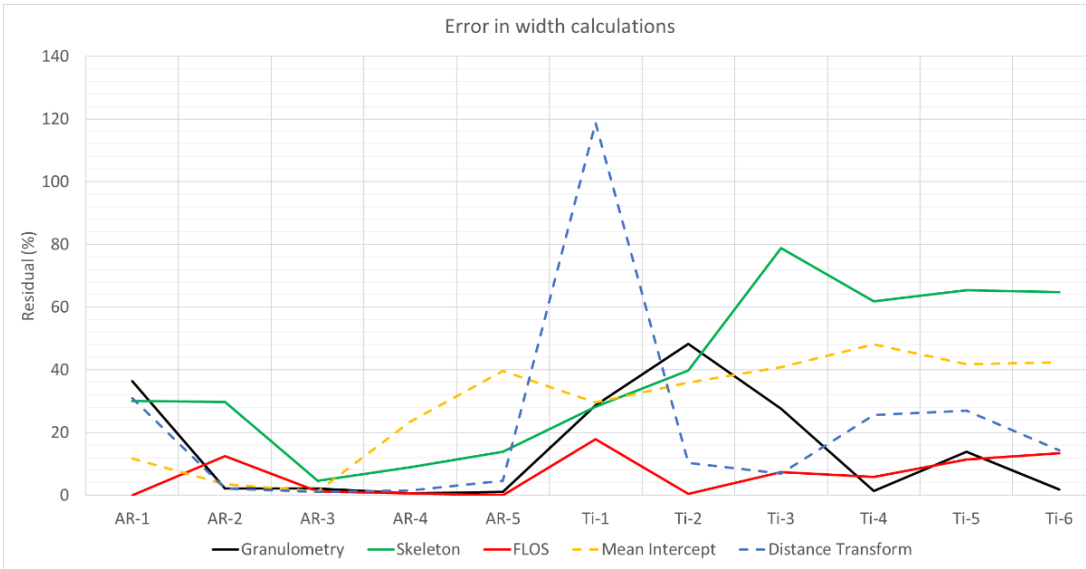

Figure 8.24: Comparison of measurement error from each method

The proposed new technique is shown to be the most robust as it has the lowest maximum error and least variation in errors. The next best method is the granulometric methods proposed by Statella *et al.* [59], which is achieves similar results to our proposed method in most cases. This similarity is perhaps not surprising as both techniques produce measurement by finding the largest SE to fit at each location in the image. However, while the method of this thesis rotates a linear SE of different lengths to achieve this, Statella uses a disk shape SE which, therefore, does not need to be rotated. This means that Statella's method is much faster than using the new FLOS, running in around 43 seconds as opposed to 3 minutes and 20 seconds for a bi-modal microstructural image. However, Statella's technique is usually slightly less accurate than the FLOS based method and gives significant errors in two microstructures, each containing some form of artefact area that an expert materials scientist would elect not to measure. While neither method has a bespoke technique designed to identify and discard these artefacts, regions of this appear globular, as does noise and artefacts on the image. The new methods in this thesis will automatically discount some of this from measurement, as the FLOS contains shape information and will only include objects with aspect ratio above 2:1 in these measurements. Statella's disk shaped granulometries do not have shape information so include measurements of every pixel in these regions, leading to significant errors. This suggest that Statella's approach is

faster in simple cases, but less robust as it is more likely to fail when other features or artefacts appear in the data.

The technique described by Collins *et al.* [11] provides good results for artificial images containing high aspect ratio objects. However, a dramatic increase in the error rate occurs when objects have a low aspect ratio. The mean inverse intercept methods [11] produce significant errors in these cases as the random line segments that are not orientated across the width of the platelet become significant, as shown in Figure 8.25 a). For platelets of a high aspect ratio the diagonal lines seen in this figure are closer to the width than in the low aspect ratio object shown, where line segments are longer. As the inverse mean is used in the width calculation, this issue makes the recorded value significantly lower than the true width, rather than higher as would be expected. This trial therefore confirms that measurements based on the mean inverse intercept are only accurate for aspect ratios below 20:1 in line with the previous finding of Collins [11]. When applied to the microstructural data the error rate was also high. This suggests that the aspect ratio of platelets in the microstructure is not high enough for this method to accurately measure mean width. Measurement of the minimum width may still be accurate but that is not a feature investigated in this thesis.

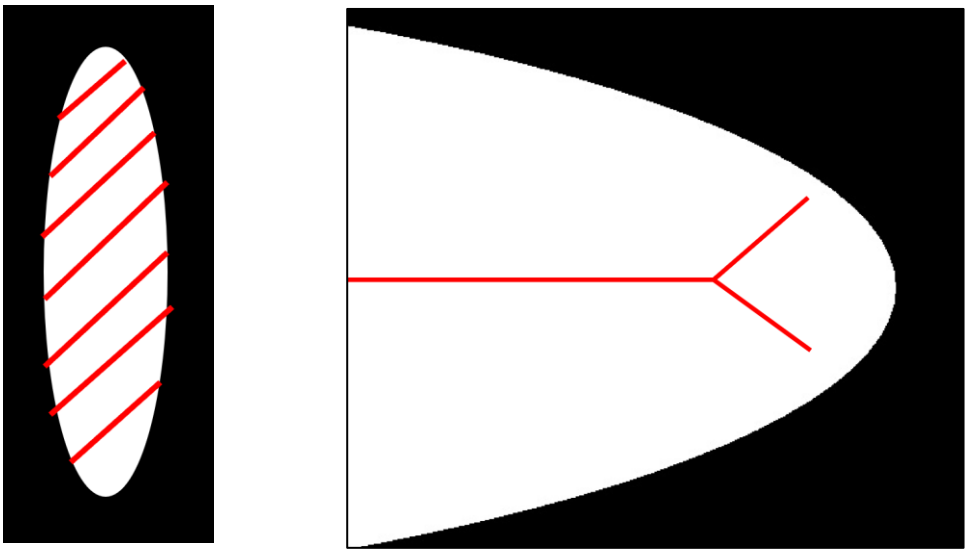

a) b)

Figure 8.25: Illustration of errors produced by each method where a) is the end of an elongated object with the skeleton overlay in red and b) is a complete object with the intercept overlay in red

Methods proposed by Russ and Adhikari *et al.* also show an increase in measurement error at higher aspect ratios, although to a lesser extent. The reason for this is they both make use of a morphological skeleton, which is assumed to exist in the geometric centre of objects. While this is true for thin, straight objects it is not true for the end of objects as shown in Figure 8.25 b). Errors in measurement can occur due to branches of the skeleton reaching into the corner of platelets, which are closer to the object boundary than the centre, resulting in smaller measurements. This effect is largest when the aspect ratio is low as a greater percentage of the skeleton is part of this protrusion than for long objects. Protrusions, or an uneven shape of platelet would lead to this effect also occur in additional locations in the image, increasing the magnitude of the problem. These results could be improved by pruning the skeleton to remove these protrusions, a relatively simple task in the artificial images. However, deformations in grain boundaries make the skeleton in alpha platelet more complex. The best method for pruning such a skeleton is likely to be application specific and other research have require bespoke algorithms for this [63]. This was not attempted in this trial as such a method was not included in the cited papers. In the trials on titanium microstructures the older method described by Russ [55] performed significantly better than the new method from Aldinhikari [56] in terms of accuracy, while both took only a few seconds to run on each microstructure. The reason for this is that the former is better suited to a titanium microstructural dataset. The uneven nature of platelets means that often the skeleton extends away from the centre of the object and into these protrusions. Although each pixel in these erroneous regions does cause and error in Russ's method the error from each pixel is usually small as they are still close to the centre. In Aldinhikari's method, however, measurement is based on the overall length of the skeleton, not its placement, so even if the protrusions are short in length they can sum to a far more significant error. Despite being better suited, Russ's methods are still only acceptably accurate for around half of the microstructures tested.

8.3.4 Computational Complexity

The new method comes at the cost of increased computational complexity as a larger number of morphological operations are performed, a wide variety of SE's used in the procedure. While a fixed length SE, proposed by other authors [63], requires only a single opening per orientation the new method requires this be multiplied by the number of lengths tested. The measurement time of platelets depends on the range of lengths and orientations of SE used. Measuring the platelets of microstructures in this experiment required L_{max} to be set between 91 and 191 pixels for accurate measurements, depending on the microstructure being measured. An L_{max} value of 191 results in 95 different lengths of SE, based on the methodology in Chapter 6, which must each must be tested at 18 different orientations, so 1710 morphological openings need to be performed on the entire image. This process took 8 minutes in the MATLAB implementation used for this thesis, run on a i7-6650U 2.2Ghz dual core processor. For images with finer platelets successful measurement where achieved with L_{max}=91 which typically required just over 3 minutes of processing time. These measurement times are significantly slower than other image processing techniques such as the segmentation approach described in Chapter 5 which could measure grain size in as little as 8 seconds, or the width measurements from the distance transform [56] that can take less than a second. However, the extensive range of SE's used are beneficial to robustness and ultimately enable features to be measured that these faster procedures are not capable of at this time. It is critical to note that the measurements are still faster than would be expected using manual methods for measuring platelets, with the expected manual measurement time being approximately 15 minutes. Additionally, platelet width, orientation and volume fraction are all measured within the same time while manual methods would require additional time to measure each feature. If the materials scientist has knowledge of the material and features to be measured, this time could be potentially dramatically reduced by tailoring $B_{\theta L}$ to a specific set of requirements. For example, if you need only measure width, L_{max} could be set far lower without affecting results as it need only exceed the width of platelets for accurate results. As laths are typically around 20 pixels wide then this time could likely be reduced to under a minute in this case. If only measuring orientation increasing S_L would decrease the resolution of width measurements but would normally not affect

the orientation measurements, so the number of computations could be reduced this way.

8.3.5 Summary

Platelets are analysed by apply linear SEs of different lengths and orientation and mapping the results to a FLOS, as described in Chapter 6. The results shown in this section prove that the proposed method is effective and robust on the varied microstructural dataset used in this thesis. Measurements taken by the new software tools and algorithms show a close match with those taken by expert materials scientists in almost all cases. As the new, automated methods can match this standard of measurement, materials scientists can benefit from the less labour intensive and repeatable nature of software algorithms to achieve consist measurements. In addition to this, the results shown demonstrate that the automated measurements are significantly faster than manual measurements in every microstructure type and feature measured. The time benefit is compounded when multiple features are measured as this often does not require any additional processing time. Further confidence in the accuracy of the new techniques are provided by qualitative review of the colourmaps provided in this chapter.

A quantitative comparison was performed with several published techniques [11], [55], [56], [59], [63]. These were based on other rotational elements, granulometries, the distance transform and morphological techniques, although none of these collect as large amount of data the new technique uses and as a result no one technique can measure every featured that the new technique is capable of. The results demonstrate that existing techniques are capable of producing accurate results for elongated objects of consistently high aspect ratios. However, the width measurements suffer when the aspect ratio of objects exceed 20:1, as discussed by other researchers and orientation measures suffer when aspect ratio varies, as correct parameters are not set. Crucially, it is shown that the microstructures in this study fall into the latter category and cannot be reliably measured using these existing techniques target at microstructural analysis. It is shown that by considering more data when calculating the properties of objects in the image the new data processing techniques can avoid these issues and produce consistently accurate results. The new technique based on variable length SEs and the

orientation space is, therefore, more robust than the first length or distance transform based approaches proposed by other researchers. This robustness comes at the cost of greater computational complexity, leading to measurements that takes minutes, while some competing methods take seconds. However, these faster methods measure only a single property and are not accurate for platelets of lower aspect ratio making them not applicable to the task and dataset presented in this thesis. It must also be considered that in order to provide fair comparison with existing techniques aimed at measuring orientation and width microstructures featuring exclusively elongated platelets were used. The ability to measure platelets in bi-modal microstructures is critical in real world microscopy and only the new methods could be directly applied to these without additional pre-processing of the image.

However, there are a few challenges that must be considered when using these techniques and areas for improvement still exist. The proposed technique does not recognise partially transformed microstructural regions, so width measurements are sometimes taken from regions that are not platelets. There are also issues with microstructures containing large numbers of recrystallized alpha grains as the SE used to take measurements can exceed the boundary between adjacent grains and distort measurements of globularisation. Methods to measure colonies do not consider triple points and use only platelet width and orientation to identify each colony. However, all of the aforementioned problems are relatively uncommon and for most microstructures investigated the results are positive with the majority of measurements produced by the new techniques closely agreeing with manual measurements produced by expert material scientists.

9 SUMMARY AND FUTURE WORK

The primary goal of this research was to improve the microstructural analysis of Ti-6Al-4V through the development of a new set of image processing techniques. It is clear that the work presented in this thesis has achieved this aim in a significant way.

Two separate image processing techniques have been presented which, when combined, can measure a wide range of microstructural features, including all of the features identified in the literature review as important for this type of microstructure. Many of these procedures could currently only be assessed through labour intensive manual procedures. The measurements produced by the new methods are proven to be consistent with what would be expected when the same measurements are performed by expert material scientists using existing procedures. However, the methods proposed in this thesis are significantly faster, are repeatable and do not require continuous manual interaction. The techniques in this thesis are also designed and tested for robustness. This means that the benefits brought by the proposed methods will be experienced on a large number of different microstructural datasets. This is demonstrated in the thesis by performing the validation of the proposed methods on a varied dataset containing different microstructure types. A software tool is also described that allows material scientists, without knowledge of image processing techniques or terminology, to apply these methods. This tool includes methods to adjust parameters in an intuitive way that can extend the range of datasets these methods can reliably be used to measure. All of this means that the potential benefits of the proposed techniques should be achievable in other industrial and academic research projects, rather than offering only a theoretical improvement.

In order for the new microstructural analysis techniques to reach the level of accuracy and robustness required, novel contributions in image processing in the form of new and extended techniques have been made. The significance of contributions in this area

are demonstrated by performing separate tests where these methods are compared to relevant techniques from image processing literature.

This chapter summarises and draws conclusions about each method proposed and the software tool, before concluding by giving a number of suggestions for possible future work in this area.

9.1 Segmentation and measurement of alpha grains

In Chapter 5, a new segmentation technique, called the CGSA, is proposed based on the Watershed Transform. The ultimate aim was to measure the mean grain size and globular volume fraction by first segmenting the image into the constituent alpha grains. Existing attempts to automate the analysis of these microstructural properties had been unsuccessful despite being identified by key authors [11] as an important research area. Manual methods of measuring these properties are instead relied upon in practice. These take approximately 15 minutes to measure a single microstructural sample and repeatability between different users could see errors of up to 16%, according to accepted standards. Techniques from other fields were identified which at first appear promising but fail to provide accurate segmentation results as they are not robust enough to cope with the varied datasets that occur during microstructural analysis.

A new technique was proposed that incorporates a range of pre- and post- processing steps into a new segmentation algorithm that is well suited to microstructural datasets. It is demonstrated that measurements of mean grain size are accurate for a range of both globular and bi-modal microstructures. Additionally, it is shown that the segmentation produced was more accurate than existing techniques from the field of image segmentation could achieve. Measurements of globular volume fraction are also accurate but required calibration that was not necessary for grain size measurements. The segmentation procedure is capable of performing 300 grain measurements in under 5 seconds and microstructures containing up to 4000 grains took around 20 seconds. This is a dramatic improvement in measurement time versus the manual methods previously required which typically took 15 minutes to perform 300 grain measurements. By using a segmentation approach, sub-sampling is almost eliminated, depending on segmentation accuracy, and all grains in the microstructure are instead

studied. In existing manual approaches, it is sometimes necessary to manually draw lines across the length and width of a grain to perform measurements. This introduces a level of subjectivity as the grains to be measured and dimension to be considered as the length and width are decided by the material scientist. By sampling every grain and empirically selecting regions to measure this source of subjectivity can be ignored. It is also thought that the change in measurement time could make it possible to test a greater number of samples when performing experiments as the cost of performing analysis is reduced, although the time to produce microscopic images is still a factor.

9.2 Analysis and measurement of elongated alpha platelets

In Chapter 6 a technique to analyse alpha platelets is presented. The ultimate aim was to measure the properties of these platelets including their width, orientation, shape (globularity) and the size of any colonies formed by these platelets. Methods exist for automating the width of these platelets, however, these methods are known to be inaccurate for platelets that are not extremely long and thin. Methods have not previously been proposed for measuring the other properties in titanium microstructures. Techniques for measuring orientation of objects in the microstructure of other materials exist, however, these are shown to not be sufficiently robust to measure the varied platelets in titanium microstructures. Image processing techniques in other areas can measure width and orientation but were also found not to be robust for the dataset in this thesis. As a result, manual methods are often relied on for width and colony size measurements. These use the same standards as grain size measurement so take 15 minutes per 150 platelets and have repeatability errors of up to 16%.

An extension to an existing technique [63], and an accompanying new data processing technique, are proposed to measure the width of a platelet in different orientations. This is achieved using a set of SEs that varied in both length and orientation. The result is mapped onto a 3D orientation space, called the FLOS, that allows all the aforementioned properties of specific platelets to be measured. An additional novel algorithm was proposed that allowed colonies to be identified in the image by grouping adjacent parallel platelets. It was shown that this method produces accurate results for all the features mentioned. Additionally, it is also demonstrated that measurements of

width and orientation are more robust than alternative image processing techniques. The proposed technique is not as fast as the segmentation technique provided in Chapter 5 and typically takes just over 3 minutes to produce results on the tested hardware. While improved hardware or more efficient implementation may be able to reduce this time, it should be noted that this time is still less than is expected by many of the manual analysis procedures. It would take 15 minutes to measure only platelet width, while all 4 properties are measured less time by the new method. Results are also repeatable, and subjectivity is eliminated as provided the parameters are set at their default setting the technique will always produce the best result it is capable of.

The technique is, however, slower than the existing image processing techniques it is compared to. It is, therefore, only beneficial to use the method proposed in Chapter 6 on complex datasets when the improved reliability it offers is required and existing methods are not suitable. This is the case for microstructures in this study.

9.3 Software tool for microstructural analysis

In Chapter 7 a new software tool is presented that incorporates the novel image processing procedures in the previous chapters. This is important as, in order to have impact in the material science domain, the techniques must be accessible and intuitive to users who are not image processing experts. While the results in Chapter 8 focus on the techniques themselves, most of the tests included were performed using this software tool. That fact that suitable results were obtained, therefore, confirms that the new software tool, in addition to the novel methods this contains, is fit for purpose. A particular benefit of the tool is that it allows for intuitive parameter selection, which is particularly vital for the proper use of the segmentation techniques from Chapter 5. Image segmentation is a complex task and it is often necessary for parameters to be changed between datasets. The proposed techniques reduce this to one significant parameter which can be easily and intuitively controlled in the tool using a slider with immediate feedback to the user on how the parameter affects the results. This slider adjusts a visual representation of the segmentation which indicates on an image in the dataset where grain boundaries are detected with the current settings. This means no knowledge of image processing is needed to tune the algorithm to new datasets. In a similar way, the size of SE with which to probe the image to measure laths can be set

in the software. After processing a visualisation will again allow the materials scientist to view the effect of the parameter change before exporting measurements. By allowing intuitive parameters changes, this software tool extends the potential applications of the proposed techniques.

9.4 Further work

The most promising avenues for further work is perhaps in expansions to the scope of the project. There are good reasons to believe that this algorithm could work very effectively on a range of other cases and not just Ti-6Al-4V, as well as sporadic evidence throughout this thesis to support that idea. More extensive trials and further refinement on datasets including a range of different microstructures may yield a tool with more wide range of uses. This also need not be limited to other microstructures as the literature review made clear that image data from other fields often share similar properties. Larger scale trials would also present the opportunity to re-visit deep learning methods that have had significant success in other fields in recent years. While the absence of good training data, and preference for a non-black box method, meant such methods were not included in this research there remain benefits to this approach that may be highly valuable in this field. For example, in recognising microstructure properties that are difficult to define in discrete rules or separate problems such as learning to predict material properties without prior image segmentation. Additionally, the techniques developed in this thesis could actively enhance deep learning approaches. For example, by using the FLOS as an input to a convolutional neural network this will provide feature space information regarding the object properties. This may avoid the issue, discussed in the literature review, where convolutional networks have limited receptive fields so miss out key feature information. By combining these approaches this may enhance the ability to detect complex feature in microstructures or classify and predict their properties.

While this chapter largely concludes that the objectives of this research have been met, there also remain a number of key areas in which improvements can still be made within the scope of the current project.

The most significant improvement that could be made is to the speed of the method proposed in Chapter 6. The technique proposed is quite exhaustive, in that it performs

an opening on the image with a very large range of SEs. Reductions in this time would be of benefit. The idea of adaptively choosing which openings were necessary was considered but experimental results did not yield any success.

Another possible improvement would be to develop an automated method for computing the sensitivity parameter used in the software tool to control the segmentation level. While the software tool provides a useful manual control, it does inject some subjectivity back into results, which the use of automated methods sought to remove. Histograms of pixel values are often used to determine a suitable threshold for binarization, so it may be possible with enough data the same could be done for sensitivity based on image gradient, as sensitivity in-fact controls an edge detection, which is a thresholding of the gradient image. Additionally, given the speed of image segmentation, it is also feasible that multiple segmentations could be produced with an algorithm designed to analyse grain size and shape to determine which segmentation is more likely. However, this would require a detailed and reliable understanding of the distribution of true grain sizes and shapes so would likely lead to over-training to a particular microstructure type or dataset. That type of approach would, therefore, not offer the robust, generalised method presented in this thesis but could allow refinement of the techniques in where high accuracy is required for a particular microstructure type.

A comparison with different data, produced by other imaging techniques would also be interesting. For example, the orientation measurements obtained by this technique have no existing 2D analysis standard. Instead the texture of microstructures is normally assessed through Electron Back-scatter Diffraction (EBSD) which studies the 3D orientation of grains. It also can use this orientation to separate adjacent grains and obtain a maps of grain sizes, similar to the segmentation generated by the CGSA. This technology is expensive, the procedure takes hours to run and material preparation must be performed to an extremely high standard. This means it is not currently feasible to use it in many situations. By contrast, an optical microscope running the new software tool could be deployed cheaply and provide results faster and easier. Given the novel work in this thesis can produce similar measurements, it would be very interesting to see what difference existed in terms of measurement accuracy. The additional information from these other technologies would further the

understanding of the true grain size and make it more realistic to evaluate the accuracy of the new automated procedures versus manual techniques. This subject was not addressed in this thesis as a use generated ground truth does not allow this to be explored and the aim was instead to provide fast, automated methods to match existing results.

REFERENCES

[1] G. Lutjering and J. C. Williams, *Titanium*, Second. Springer, 2007.

[2] C. R. Gonzalez and R. Woods, "Digital image processing," *Pearson Educ.*, 2002.

[3] I. Polmear, *Light alloys; from traditional alloys to nanocrystals*. Butterworth-Heinemann, 2005.

[4] L. Gillibert and D. Jeulin, "3D Reconstruction and analysis of the fragmented grains in a composite material," *Image Anal. Stereol.*, vol. 32, no. 2, p. 107, Jun. 2013.

[5] S. Beucher and F. Meyer, "The morphological approach to segmentation: the watershed transformation," *Opt. Eng. York-Marcel*, 1992.

[6] A. Campbell, P. Murray, E. Yakushina, S. Marshall, and W. Ion, "New methods for automatic quantification of microstructural features using digital image processing," *Mater. Des.*, vol. 141, pp. 395–406, Mar. 2018.

[7] Kumar and Ranjit, *Research Methodology*. 2011.

[8] A. Rosochowski and L. Olejnik, "Severe plastic deformation for grain refinement and enhancement of properties," *Microstruct. Evol. Met. Form. Process.*, p. 144, 2012.

[9] W. Callister and D. Rethwisch, *Materials science and engineering*. 2011.

[10] S. Semiatin and T. Bieler, "The effect of alpha platelet thickness on plastic flow during hot working of Ti–6Al–4V with a transformed microstructure," *Acta Mater.*, vol. 49, no. 17, pp. 3565–3573, 2001.

[11] P. Collins, B. Welk, T. Searles, J. Tiley, and J. Russ, "Development of methods for the quantification of microstructural features in α+ β-processed α/β titanium alloys," *Mater. Sci.*, vol. 508, no. 1–2, pp. 174–182, 2009.

[12] J. Tiley, T. Searles, E. Lee, S. Kar, and R. Banerjee, "Quantification of microstructural features in α/β titanium alloys," *Mater. Sci.*, vol. 372, no. 1–2, pp. 191–198, 2004.

[13] A. Chokshi, A. Rosen, J. Karch, and H. Gleiter, “On the validity of the hall-petch relationship in nanocrystalline materials,” *Scr. Metall.*, vol. 23, no. 10, pp. 1679–1683, 1989.

[14] H. Liu, H. Sun, B. Liu, D. Li, F. Sun, and X. Jin, “An ultrahigh strength steel with ultrafine-grained microstructure produced through intercritical deformation and partitioning process,” *Mater. Des.*, vol. 83, pp. 760–767, Oct. 2015.

[15] L. . Liu *et al.*, “Ultrafine grained Ti-based composites with ultrahigh strength and ductility achieved by equiaxing microstructure,” *Mater. Des.*, vol. 79, pp. 1–5, Aug. 2015.

[16] J. Sieniawski, W. Ziaja, K. Kubiak, and M. Motyka, “Microstructure and Mechanical Properties of High Strength Two-Phase Titanium Alloys,” in *Titanium alloys-advances in properties control*, 2013.

[17] X.-H. Shi, W.-D. Zeng, C.-L. Shi, H.-J. Wang, and Z.-Q. Jia, “The effects of colony microstructure on the fatigue crack growth behavior for Ti–6A1–2Zr–2Sn–3Mo–1Cr–2Nb titanium alloy,” *Mater. Sci. Eng. A*, vol. 621, pp. 252–258, Jan. 2015.

[18] G. Lutjering, J. Albrecht, and O. Ivasishin, “Influence of cooling rate and B grain size on the tensile properties of (a+B) Ti alloys,” in *Proceedings of the 8th World Titanium Conference*, 1995.

[19] S. . Semiatin, V. Seetharaman, and I. Weiss, “Flow behavior and globularization kinetics during hot working of Ti–6Al–4V with a colony alpha microstructure,” *Mater. Sci. Eng. A*, vol. 263, no. 2, pp. 257–271, May 1999.

[20] Wenshuo Gao, Xiaoguang Zhang, Lei Yang, and Huizhong Liu, “An improved Sobel edge detection,” in *3rd International Conference on Computer Science and Information Technology*, pp. 67–71, 2010.

[21] L. Yang, X. Wu, D. Zhao, H. Li, and J. Zhai, “An improved Prewitt algorithm for edge detection based on noised image,” in *2011 4th International Congress on Image and Signal Processing*, pp. 1197–1200, 2011.

[22] G. Matheron, “Random sets and integral geometry,” *Probab. Math. Stat.*, vol.

385969, no. 52, p. 6828, 1975.

[23] J. Serra, “Introduction to mathematical morphology,” *Comput. vision, Graph. image Process.*, vol. 35, no. 3, pp. 283–305, 1986.

[24] P. Soille, *Morphological image analysis: principles and applications*. Springer Science & Buisness Media, 2013.

[25] S. A. Bankole, J. Buckman, D. Stow, and H. Lever, “Grain-size analysis of mudrocks: A new semi-automated method from SEM images,” *J. Pet. Sci. Eng.*, vol. 174, pp. 244–256, Mar. 2019.

[26] P. Murray and S. Marshall, “A New Design Tool for Feature Extraction in Noisy Images Based on Grayscale Hit-or-Miss Transforms,” *IEEE Trans. Image Process.*, vol. 20, no. 7, pp. 1938–1948, Jul. 2011.

[27] S. Beucher and C. Lantuéjoul, “Use of watersheds in contour detection,” 1979.

[28] F. Meyer, “Topographic distance and watershed lines,” *Signal Processing*, 1994.

[29] ASTM, “E112 Standard test method for determining average grain size.” .

[30] ASTM, “E1382 Standard Test Methods for Determining Average Grain Size Using Semiautomatic and Automatic Image Analysis.”

[31] ASTM, “E562 Standard test method for determining volume fraction by systematic manual point cloud.” .

[32] ASTM, “E930 Standard Test Methods for Estimating the Largest Grain Observed in a Metallographic Section (ALA Grain Size).” .

[33] ASTM, “E1181 Standard Test Methods for Characterizing Duplex Grain Sizes.” .

[34] D. Yang and Z. Liu, “Quantification of Microstructural Features and Prediction of Mechanical Properties of a Dual-Phase Ti-6Al-4V Alloy,” *Materials (Basel).*, vol. 9, no. 8, pp. 1–14, 2016.

[35] J. Zhe, Y. He, H. Li, and X. Fan, “A new method for separating complex touching equiaxed and lamellar alpha phases in microstructure of titanium alloy,” *Trans. Nonferrous Met. Soc.*, vol. 23, no. 8, pp. 2265–2269, 2013.

[36] J. Sosa, D. Huber, B. Welk, and H. Fraser, “Development and application of MIPAR^{TM}: a novel software package for two-and three-dimensional microstructural characterization,” *Integr. Mater.*, vol. 3, no. 1, p. 10, 2014.

[37] Q. Zhang, C. Yu, Y. Peng, and Q. Peng, “Quantification of the thickness of Widmanstatten α-laths in Ti alloys,” in *5th International Congress on Image and Signal Processing (CISP)*, pp. 464–468, 2012.

[38] N. Otsu, “A Threshold Selection Method from Gray-Level Histograms,” *IEEE Trans. Syst. Man. Cybern.*, vol. 9, no. 1, pp. 62–66, Jan. 1979.

[39] H. J. G. Gundersen, T. B. Jensen, and R. Østerby, “Distribution of Membrane Thickness Determined By Lineal Analysis,” *J. Microsc.*, vol. 113, no. 1, pp. 27–43, May 1978.

[40] M. A. Tschopp, J. S. Tiley, and G. B. Viswanathan, “Automated identification and characterisation of secondary and tertiary γ' precipitates in nickel-based superalloys,” *Mater. Sci. Technol.*, vol. 26, no. 12, pp. 1414–1422, Dec. 2010.

[41] J. Tiley, G. Viswanathan, A. Shiveley, and M. Tschopp, “Measurement of γ′ precipitates in a nickel-based superalloy using energy-filtered transmission electron microscopy coupled with automated segmenting,” *Micron*, vol. 41, no. 6, pp. 641–647, 2010.

[42] B. L. DeCost and E. A. Holm, “A computer vision approach for automated analysis and classification of microstructural image data,” *Comput. Mater. Sci.*, vol. 110, pp. 126–133, Dec. 2015.

[43] D. Lowe, “Object recognition from local scale-invariant features,” in *The seventh IEEE international conference on Computer Vision*, p. 11501157, 1999.

[44] Y. Al-Kofahi, W. Lassoued, W. Lee, and B. Roysam, “Improved Automatic Detection and Segmentation of Cell Nuclei in Histopathology Images,” *IEEE Trans. Biomed. Eng.*, vol. 57, no. 4, pp. 841–852, Apr. 2010.

[45] H. Altendorf and D. Jeulin, “3D Direction mathematical morphology for analysis of fibre orientations,” *Image Anal. Stereol.*, vol. 28, no. 3, p. 143, May 2011.

[46] S. V. Costes, D. Daelemans, E. H. Cho, Z. Dobbin, G. Pavlakis, and S. Lockett, “Automatic and Quantitative Measurement of Protein-Protein Colocalization in Live Cells,” *Biophys. J.*, vol. 86, no. 6, pp. 3993–4003, Jun. 2004.

[47] H. Irshad, A. Veillard, L. Roux, and D. Racoceanu, “Methods for Nuclei Detection, Segmentation, and Classification in Digital Histopathology: A Review: Current Status and Future Potential,” *IEEE Rev. Biomed. Eng.*, vol. 7, pp. 97–114, 2014.

[48] P. Soille and H. Talbot, “Image structure orientation using mathematical morphology,” in *Proceedings. Fourteenth International Conference on Pattern Recognition*, vol. 2, pp. 1467–1469, 1998.

[49] L. Vincent, “Fast opening functions and morphological granulometries,” *Algebr. Morphol. Image Process.*, vol. 2300, pp. 253–268, 1994.

[50] E. P. Simoncelli and W. T. Freeman, “The Steerable Pyramid: A Flexible Architecture for Multi-Scale Derivative Computation,” in *International Conference on Image Processing*, pp. 444–447, 1995.

[51] M. Kass, A. Witkin, and D. Terzopoulos, “Snakes: Active contour models,” *Int. J. Comput. Vis.*, vol. 1, no. 4, pp. 321–331, 1988.

[52] G. Coleman and H. Andrews, “Image segmentation by clustering,” *Proc. IEEE*, 1979.

[53] M. G. Haberl *et al.*, “CDeep3M—Plug-and-Play cloud-based deep learning for image segmentation,” *Nat. Methods*, vol. 15, no. 9, pp. 677–680, Sep. 2018.

[54] P. Wang *et al.*, “Understanding Convolution for Semantic Segmentation,” in *2018 IEEE Winter Conference on Applications of Computer Vision (WACV)*, pp. 1451–1460, 2018.

[55] J. C. Russ, *The Image processing handbook*. 2016.

[56] R. S. Adhikari, O. Moselhi, and A. Bagchi, “Image-based retrieval of concrete crack properties for bridge inspection,” *Autom. Constr.*, vol. 39, pp. 180–194, Apr. 2014.

[57] L. Vincent, “Fast granulometric methods for the extraction of global image

information," in *11th Annual Symposium of the South African Pattern Recognition Association*, 2000.

[58] J. Serra, "Image analysis and mathematical morphology, v. 1," 1982.

[59] T. Statella, P. Pina, and E. A. da Silva, "Automated width measurements of Martian dust devil tracks," *Aeolian Res.*, vol. 20, pp. 1–6, Mar. 2016.

[60] J.-F. Rivest, "Morphological gradients," *Journal of Electronic Imaging*, vol. 2, no. 4. p. 326, 1993.

[61] W. T. Freeman and E. H. Adelson, "The Design and Use of Steerable Filters," *IEEE Trans. Pattern Anal. Mach. Intell.*, vol. 13, no. 9, pp. 891–906, 1991.

[62] P. Soille and M. Pesaresi, "Advances in mathematical morphology applied to geoscience and remote sensing," *IEEE Trans. Geosci. Remote Sens.*, vol. 40, no. 9, pp. 2042–2055, Sep. 2002.

[63] A. Borocco, C. Fellah, J. Braun, M.-H. Berger, and P. Dokládal, "Morphological Characterization of Graphene Plans Stacking", pp. 435–446, 2017.

[64] Y.-S. Chen and W.-H. Hsu, "An interpretive model of line continuation in human visual perception," *Pattern Recognit.*, vol. 22, no. 5, pp. 619–639, Jan. 1989.

[65] K. Robb, O. Wirjadi, and K. Schladitz, "Fiber Orientation Estimation from 3D Image Data: Practical Algorithms, Visualization, and Interpretation," in *7th International Conference on Hybrid Intelligent Systems (HIS 2007)*, pp. 320–325, 2007.

[66] J. Geusebroek, A. W. M. Smeulders, and J. van de Weijer, "Fast anisotropic gauss filtering," *IEEE Trans. Image Process.*, vol. 12, no. 8, pp. 938–943, Aug. 2003.

[67] M. Watson and M. Marshall, "A Novel Image Segmentation Approach for Microstructure Modelling," *Coatings*, vol. 7, no. 10, pp. 166–181, 2017.

[68] S. Ghorai, A. Mukherjee, M. Gangadaran, and P. K. Dutta, "Automatic Defect Detection on Hot-Rolled Flat Steel Products," *IEEE Trans. Instrum. Meas.*, vol.

62, no. 3, pp. 612–621, Mar. 2013.

[69] A. Carolina Sparavigna, “An image segmentation for the measurement of microstructures in ductile cast iron,” *Philica*, vol. 2017, no. 1159, 2017.

[70] P. Salembier and J. Serra, “Flat zones filtering, connected operators, and filters by reconstruction,” *IEEE Trans. Image Process.*, vol. 4, no. 8, pp. 1153–1160, 1995.

[71] D. M. Dimiduk, E. A. Holm, and S. R. Niezgoda, “Perspectives on the Impact of Machine Learning, Deep Learning, and Artificial Intelligence on Materials, Processes, and Structures Engineering,” *Integr. Mater. Manuf. Innov.*, vol. 7, no. 3, pp. 157–172, Sep. 2018.

[72] F. Meyer and S. Beucher, “Morphological segmentation,” *J. Vis. Commun. Image Represent.*, vol. 1, no. 1, pp. 21–46, 1990.

[73] D. Li, G. Zhang, Z. Wu, and L. Yi, “An edge embedded marker-based watershed algorithm for high spatial resolution remote sensing image segmentation,” *IEEE Trans. Image*, 2010.

[74] D. Willingham, B. E. Naes, P. G. Heasler, M. M. Zimmer, C. A. Barrett, and R. Shane Addleman, “Image segmentation for uranium isotopic analysis by SIMS: Combined adaptive thresholding and marker controlled watershed approach,” *J. Vac. Sci. Technol. B, Nanotechnol. Microelectron. Mater. Process. Meas. Phenom.*, vol. 34, no. 3, p. 03H106, May 2016.

[75] E. MARTINEZ, X. JOVE, F. DE LA TORRE, and E. SANTAMARIA, “Unsupervised morphological segmentation of objects in contact,” *16° Colloq. sur le Trait. du signal des images, 1997 ; p. 1379-1382*, 1997.

[76] S. Outal and S. Beucher, “Controlling the ultimate openings residues for a robust delineation of fragmented rocks,” p. 6 p., Jun. 2009.

[77] B. Marcotegui, A. Serna, and J. Hernández, “Ultimate Opening Combined with Area Stability Applied to Urban Scenes,” pp. 261–268, 2017.

[78] J. Hernández and B. Marcotegui, “Ultimate attribute opening segmentation with shape information,” in *International Symposium on Mathematical Morphology*

and Its Apllications to Signal and Image Processing, pp. 205–214, 2009.

[79] S. Beucher, "Numerical residues," *Image Vis. Comput.*, vol. 25, no. 4, pp. 405–415, Apr. 2007.

[80] S. Niu, Q. Chen, L. de Sisternes, Z. Ji, Z. Zhou, and D. L. Rubin, "Robust noise region-based active contour model via local similarity factor for image segmentation," *Pattern Recognit.*, vol. 61, pp. 104–119, Jan. 2017.

[81] Q. Zhang, L. Zhang, W. Shi, and Y. Liu, "Airport Extraction via Complementary Saliency Analysis and Saliency-Oriented Active Contour Model," *IEEE Geosci. Remote Sens. Lett.*, no. 99, pp. 1–5, 2018.

[82] P. Karn, B. Biswal, and S. Samantaray, "Robust retinal blood vessel segmentation using hybrid active contour model," *IET Image Process.*, 2018.

[83] I. Manousakas, P. Undrill, and G. Cameron, "Split-and-merge segmentation of magnetic resonance medical images: performance evaluation and extension to three dimensions," *Comput.*, 1998.

[84] L. Li, J. Yao, J. Tu, X. Lu, K. Li, and Y. Liu, "Edge-based split-and-merge superpixel segmentation," in *IEEE International Conference on Information and Automation*, pp. 970–975, 2015.

[85] A. KŘUPKA, K. ŘÍHA, and L. KŘÍŽOVÁ, "Segmentation of Sedimentary Grain in Electron Microscopy Image.," *Radioengineering*, vol. 22, no. 3, pp. 883–891, 2013.

[86] Y.-J. Liu, M. Yu, B.-J. Li, and Y. He, "Intrinsic Manifold SLIC: A Simple and Efficient Method for Computing Content-Sensitive Superpixels," *IEEE Trans. Pattern Anal. Mach. Intell.*, vol. 40, no. 3, pp. 653–666, Mar. 2018.

[87] V. Machairas, E. Decenciere, and T. Walter, "Waterpixels: Superpixels based on the watershed transformation," in *2014 IEEE International Conference on Image Processing (ICIP)*, pp. 4343–4347, 2014.

[88] Y. LeCun, Y. Bengio, and G. Hinton, "Deep learning," *Nature*, vol. 521, no. 7553, pp. 436–444, May 2015.

[89] V. H. C. de Albuquerque, P. C. Cortez, A. R. de Alexandria, and J. M. R. S.

Tavares, “A new solution for automatic microstructures analysis from images based on a backpropagation artificial neural network,” *Nondestruct. Test. Eval.*, vol. 23, no. 4, pp. 273–283, Dec. 2008.

[90] B. L. DeCost, T. Francis, and E. A. Holm, “High throughput quantitative metallography for complex microstructures using deep learning: A case study in ultrahigh carbon steel,” May 2018.

[91] I. Konovalenko *et al.*, “Investigation of the Rupture Surface of the Titanium Alloy Using Convolutional Neural Networks,” *Materials (Basel).*, vol. 11, no. 12, p. 2467, Dec. 2018.

[92] G. Litjens *et al.*, “A survey on deep learning in medical image analysis,” *Med. Image Anal.*, vol. 42, pp. 60–88, Dec. 2017.

[93] O. Ronneberger, P. Fischer, and T. Brox, “U-Net: Convolutional Networks for Biomedical Image Segmentation,” Springer, Cham, pp. 234–241, 2015.

[94] T. Brosch, L. Y. W. Tang, Y. Yoo, D. K. B. Li, A. Traboulsee, and R. Tam, “Deep 3D Convolutional Encoder Networks With Shortcuts for Multiscale Feature Integration Applied to Multiple Sclerosis Lesion Segmentation,” *IEEE Trans. Med. Imaging*, vol. 35, no. 5, pp. 1229–1239, May 2016.

[95] S. J. Pan and Q. Yang, “A Survey on Transfer Learning,” *IEEE Trans. Knowl. Data Eng.*, vol. 22, no. 10, pp. 1345–1359, Oct. 2010.

[96] NHS,“https://www.dchft.nhs.uk/gps/pathology-services/Pages/Histopathology-.aspx.” .

[97] Jierong Cheng and J. C. Rajapakse, “Segmentation of Clustered Nuclei With Shape Markers and Marking Function,” *IEEE Trans. Biomed. Eng.*, vol. 56, no. 3, pp. 741–748, Mar. 2009.

[98] Chanho Jung and Changick Kim, “Segmenting Clustered Nuclei Using H-minima Transform-Based Marker Extraction and Contour Parameterization,” *IEEE Trans. Biomed. Eng.*, vol. 57, no. 10, pp. 2600–2604, Oct. 2010.

[99] Li Yuan, Qingsong Yu, Chaomin Shen, Wenxin Hu, and Zhitong Yang, “New watershed segmentation algorithm based on hybrid gradient and self-adaptive

marker extraction," in *2016 2nd IEEE International Conference on Computer and Communications (ICCC)*, pp. 624–628, 2016.

[100] X. Zhang, F. Jia, S. Luo, G. Liu, and Q. Hu, "A marker-based watershed method for X-ray image segmentation," *Comput. methods programs*, 2014.

[101] C. F. Koyuncu, E. Akhan, T. Ersahin, R. Cetin-Atalay, and C. Gunduz-Demir, "Iterative h-minima-based marker-controlled watershed for cell nucleus segmentation," *Cytom. Part A*, vol. 89, no. 4, pp. 338–349, Apr. 2016.

[102] T. Lindeberg, "Feature Detection with Automatic Scale Selection," *Int . J . Comput. Vis.*, vol. 30, no. 2, 1996.

[103] E. Cosatto, M. Miller, H. P. Graf, and J. S. Meyer, "Grading nuclear pleomorphism on histological micrographs," in *2008 19th International Conference on Pattern Recognition*, pp. 1–4, 2018.

[104] R. Uppada, S. K. Rao, and K. S. Prasad, "Integrated Novel Multi-Phase Level Sets with Modified Marker Controlled Watershed for Segmentation of Breast Cancer Histopathological Images," vol. 9, no. issue 3. pp. 47–55, 2017.

[105] X. Qi, F. Xing, D. Foran, and L. Yang, "Robust segmentation of overlapping cells in histopathology specimens using parallel seed detection and repulsive level set," *IEEE Trans.*, 2012.

[106] M. Veta, P. J. Van Diest, R. Kornegoor, A. Huisman, M. A. Viergever, and J. P. W. Pluim, "Automatic Nuclei Segmentation in H&E Stained Breast Cancer Histopathology Images," *PLoS One*, vol. 8, no. 7, 2013.

[107] S. Dutta, A. Karmakar, H. Roy, and K. Barat, "Automatic estimation of mechanical properties from fractographs using optimal anisotropic diffusion and Voronoi tessellation," *Measurement*, vol. 134, pp. 574–585, 2019.

[108] Y. Hao and F. Zhu, "Fast Algorithm for Two-dimensional Otsu Adaptive Threshold Algorithm," *J. Image Graph.*, 2005.

[109] Y. Zhang and L. Wu, "Fast document image binarization based on an improved adaptive Otsu's method and destination word accumulation," *J. Comput. Inf. Syst.*, 2011.

[110] D. Ballard, “CM Brown Computer Vision,” *NY Prentice Hill*, 1982.

[111] B. Perret, J. Cousty, S. Guimaraes, and D. Maia, “Evaluation of Hierarchical Watersheds,” *IEEE Trans. Image Process.*, vol. 27, no. 4, pp. 1676–1688, 2018.

[112] E. Breen and R. Jones, “Attribute openings, thinnings, and granulometries,” *Comput. Vis. Image Underst.*, 1996.

[113] O. Oudat, V. Borra, D. Georgiev, and V. Karpov, “The statistics of tin whisker diameters versus the underlying film grains,” *Condens. Matter Mater. Sci.*, 2018.

[114] B. Patle, A. Reddy, A. Avinash, and K. Abhishek, “Automatic material indentification technique using digital image processing,” *Int. J. Eng. Sci. Invent. Res. Dev.*, vol. 6, no. 10, pp. 334–340, 2018.

[115] H. Farivar, U. Prahl, M. Hans, and W. Bleck, “Microstructural adjustment of carburized steel components towards reducing the quenching-induced distortion,” *J. Mater. Process. Technol.*, vol. 264, pp. 313–327, 2019.

[116] A. Ciobanu, M. Luca, T. Barbu, and C. Teodorescu-Soare, “Tube center detection in SEM images of Titania Nanotube Arrays,” in *2018 International Conference on Development and Application Systems (DAS)*, pp. 190–193, 2018.

[117] D. Powers, “Evaluation: from precision, recall and F-measure to ROC, informedness, markedness and correlation,” 2011.

[118] Jierong Cheng and J. C. Rajapakse, “Segmentation of Clustered Nuclei With Shape Markers and Marking Function,” *IEEE Trans. Biomed. Eng.*, vol. 56, no. 3, pp. 741–748, Mar. 2009.

[119] Chanho Jung and Changick Kim, “Segmenting Clustered Nuclei Using H-minima Transform-Based Marker Extraction and Contour Parameterization,” *IEEE Trans. Biomed. Eng.*, vol. 57, no. 10, pp. 2600–2604, Oct. 2010.

[120] M. Sokolova and N. Japkowicz, “Beyond accuracy, F-score and ROC: a family of discriminant measures for performance evaluation,” *Australas. join Conf. Artif. Intell.*, pp. 1015–1021, 2006.

[121] S. C. V. Lim *et al.*, “Tracking microstructure, texture and boundary misorientation evolution of hot deformed and post-deformation annealed Ti–6Al–4V alloy,” *Mater. Sci. Eng. A*, vol. 651, pp. 524–534, Jan. 2016.

APPENDICES

Appendix 1: Dataset

Dataset/Sample	Microscope type	Globular features visible	Elongated features visible	Colonies visible
1	SEM	Yes	No	No
2	SEM	Yes	No	No
3	SEM	Yes	No	No
4	SEM	Yes	No	No
5	SEM	Yes	No	No
6	SEM	Yes	No	No
17	Optical	Yes	Yes	Yes
18	Optical	Yes	Yes	Yes
19	Optical	Yes	Yes	Yes
20	SEM	Yes	No	No
21	SEM	Yes	No	No
22	SEM	Yes	No	No
23	SEM	Yes	No	No
24	SEM	Yes	No	No
25	Optical	No	Yes	No
26	Optical	No	Yes	Yes
27	SEM	Yes	Yes	Yes
28	SEM	Yes	Yes	Yes
29	SEM	No	Yes	Yes
30	SEM	No	Yes	Yes
31	SEM	No	Yes	No
32	SEM	No	Yes	No

Appendix 2: Expert Measurements

Expert measurements were taken using linear intercept techniques based on the ASTM 112 standard as described in Section 4.1.1.1 of the thesis. These techniques were deployed with the aid of the ImageJ software tool. This tool enabled the user to drag and drop line segments onto the image as required and automatically produce measurements. The software also allows image scale to be extracted in a similar fashion. The following describes an example of the steps taken to conduct measurement of a microstructure.

1. Open ImageJ and load a single microstructural image

2.Select the straight tool from the toolbar

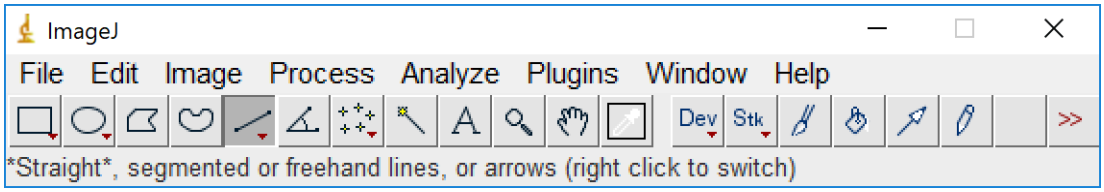

3. Draw a line across the scalebar of the image, zooming first if required

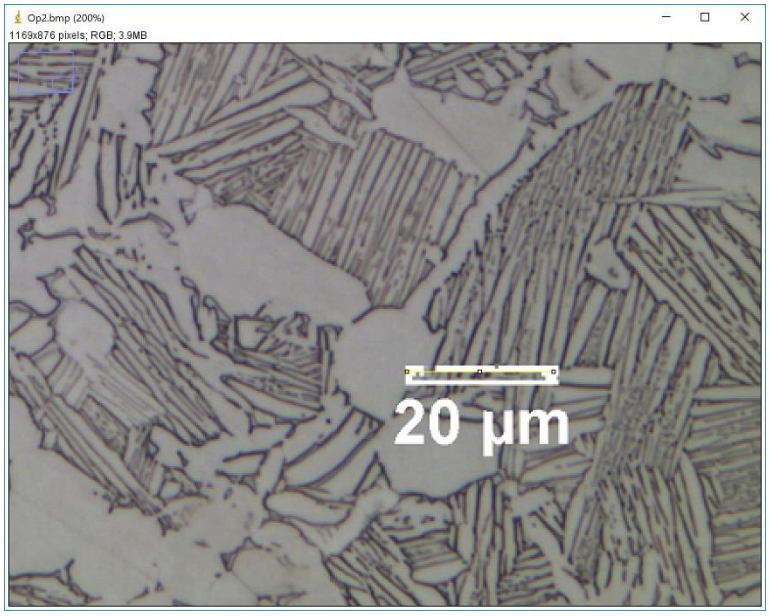

4. Select “Analyze” then “Set Scale” and enter the information from the scalebar (the length of the previously drawn line should automatically appear)

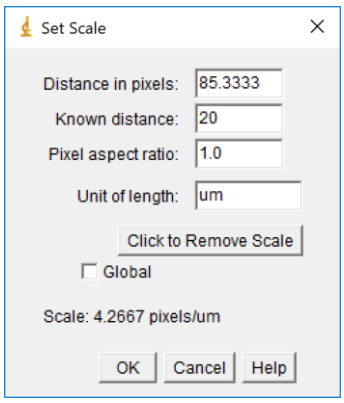

5. Make sure the “Straight” tool is selected and draw a line across the feature you wish to measure. For laths this is the width and for globular features this should be the major or minor axis.

6. Press Ctrl+t to save the line and bring up the ROI manager. Make sure “Show All” is selected so that any subsequent lines are all shown on the image and prevent repeat measurement of the same feature.

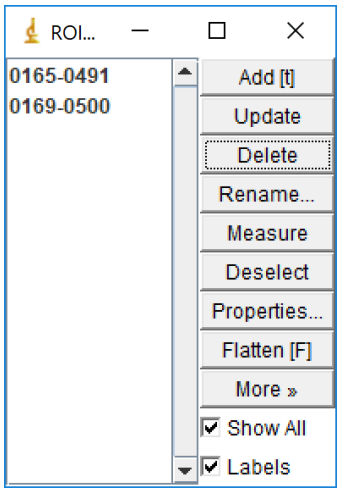

7. Drawing a line over the next feature to be measured and click “t” after each is drawn to add it to the saved axes.

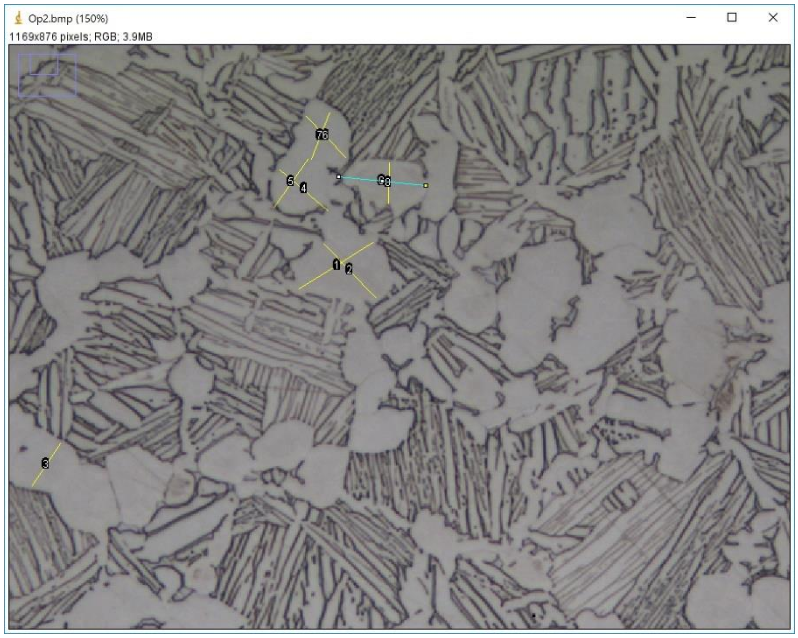

8. Continue this process until a statistically valid number of measurements can be taken from the drawn lines. Ensure that both minor and major axis are measured for each globular grain or only the width for laths. Globular and lamellar features cannot be measured simultaneously.

9. Click “Measure” in the ROI Manager window to measure all of the chosen axis of the grains. This table can then be copy and paste or exported to excel to calculate the mean measurement or other statistics.

Appendix 3: Output Report

Outputs are saved in 2 output files. A .pdf that is effectively a screenshot of the report window and an excel file that contains more detailed information, as well as summary statistics and a copy of the same information as the .pdf. An example of this file is provided below.

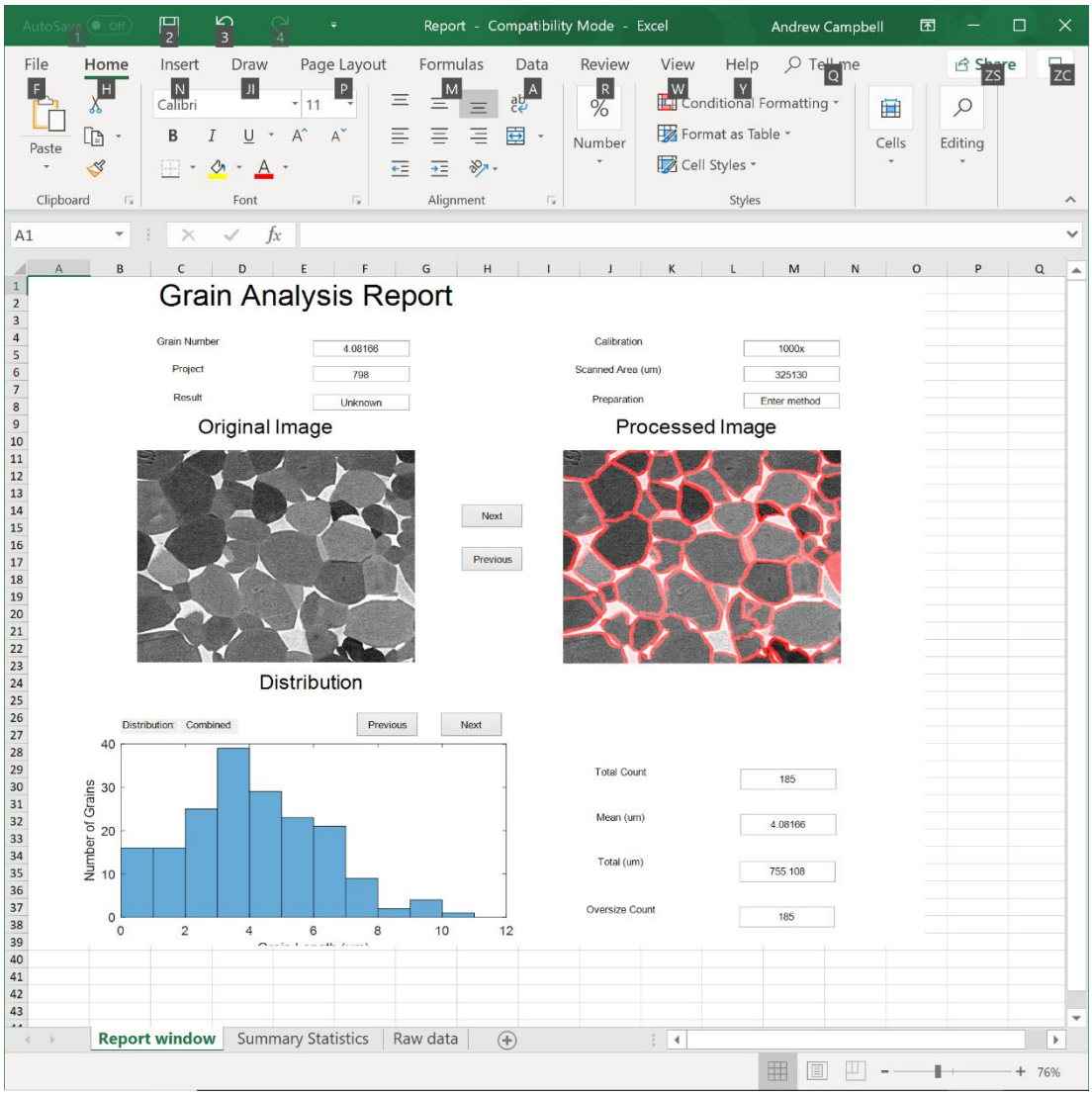

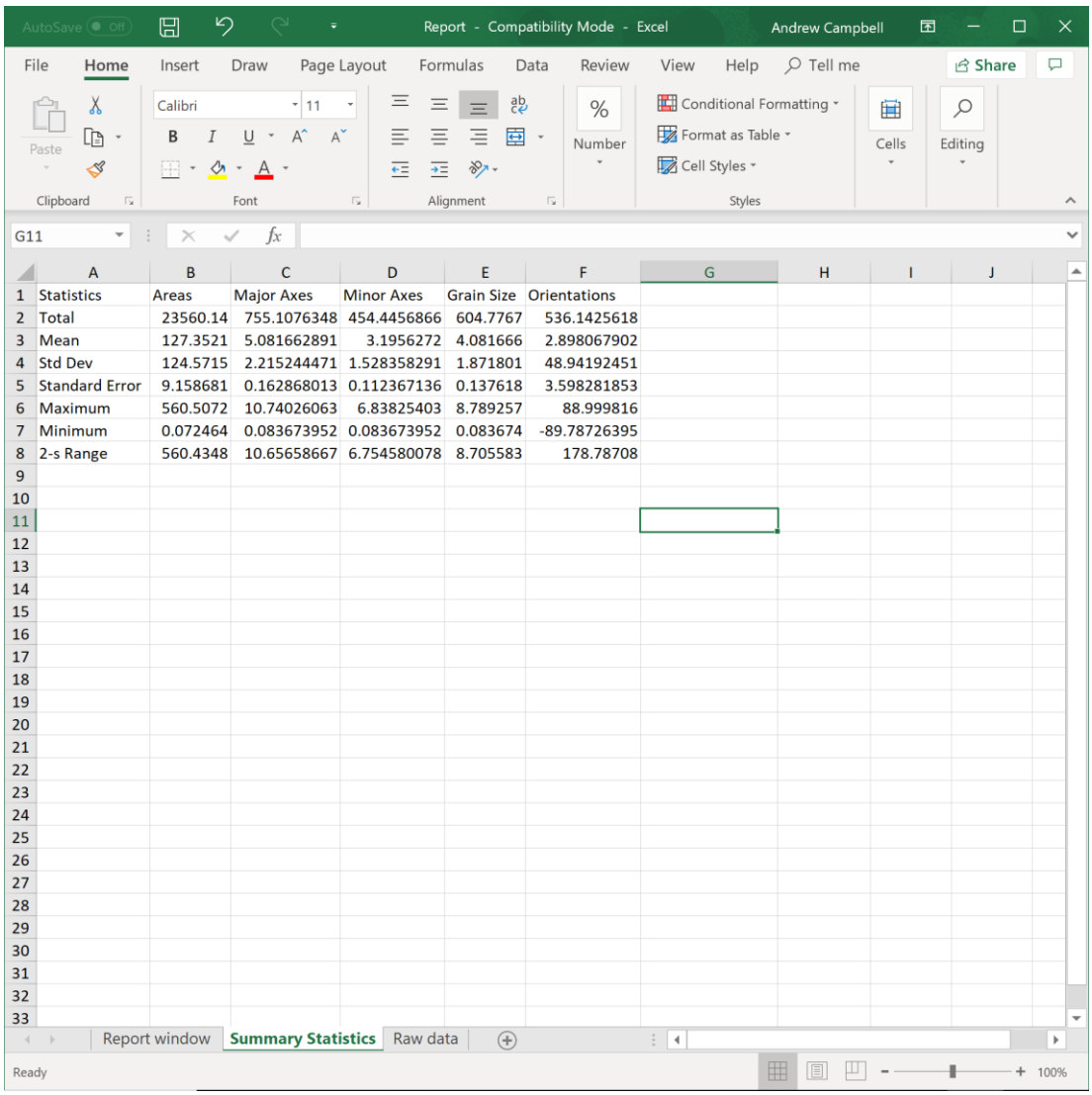

	A	B	C	D	E	F	G	H	I	J
1	Statistics	Areas	Major Axes	Minor Axes	Grain Size	Orientations				
2	Total	23560.14	755.1076348	454.4456866	604.7767	536.1425618				
3	Mean	127.3521	5.081662891	3.1956272	4.081666	2.898067902				
4	Std Dev	124.5715	2.215244471	1.528358291	1.871801	48.94192451				
5	Standard Error	9.158681	0.162868013	0.112367136	0.137618	3.598281853				
6	Maximum	560.5072	10.74026063	6.83825403	8.789257	88.999816				
7	Minimum	0.072464	0.083673952	0.083673952	0.083674	-89.78726395				
8	2-s Range	560.4348	10.65658667	6.754580078	8.705583	178.78708				
9										
10										
11										
12										
13										
14										
15										
16										
17										
18										
19										
20										
21										
22										
23										
24										
25										
26										
27										
28										
29										
30										
31										
32										
33										

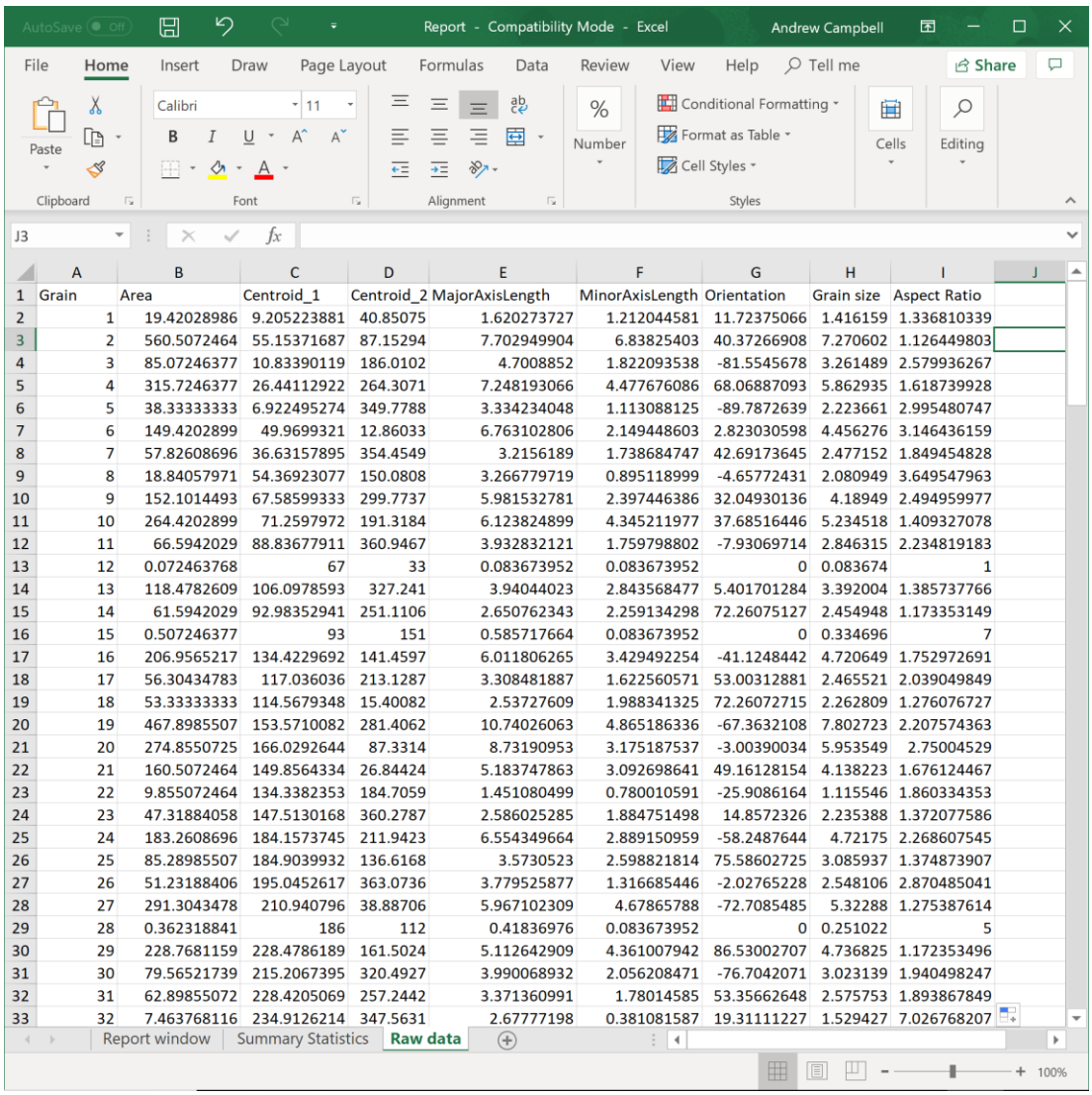

	A	B	C	D	E	F	G	H	I	J
1	Grain	Area	Centroid_1	Centroid_2	MajorAxisLength	MinorAxisLength	Orientation	Grain size	Aspect Ratio	
2	1	19.42028986	9.205223881	40.85075	1.620273727	1.212044581	11.72375066	1.416159	1.336810339	
3	2	560.5072464	55.15371687	87.15294	7.702949904	6.83825403	40.37266908	7.270602	1.126449803	
4	3	85.07246377	10.83390119	186.0102	4.7008852	1.822093538	-81.5545678	3.261489	2.579936267	
5	4	315.7246377	26.44112922	264.3071	7.248193066	4.477676086	68.06887093	5.862935	1.618739928	
6	5	38.33333333	6.922495274	349.7788	3.334234048	1.113088125	-89.7872639	2.223661	2.995480747	
7	6	149.4202899	49.9699321	12.86033	6.763102806	2.149448603	2.823030598	4.456276	3.146436159	
8	7	57.82608696	36.63157895	354.4549	3.2156189	1.738684747	42.69173645	2.477152	1.849454828	
9	8	18.84057971	54.36923077	150.0808	3.266779719	0.895118999	-4.65772431	2.080949	3.649547963	
10	9	152.1014493	67.58599333	299.7737	5.981532781	2.397446386	32.04930136	4.18949	2.494959977	
11	10	264.4202899	71.2597972	191.3184	6.123824899	4.345211977	37.68516446	5.234518	1.409327078	
12	11	66.5942029	88.83677911	360.9467	3.932832121	1.759798802	-7.93069714	2.846315	2.234819183	
13	12	0.072463768	67	33	0.083673952	0.083673952	0	0.083674	1	
14	13	118.4782609	106.0978593	327.241	3.94044023	2.843568477	5.401701284	3.392004	1.385737766	
15	14	61.5942029	92.98352941	251.1106	2.650762343	2.259134298	72.26075127	2.454948	1.173353149	
16	15	0.507246377	93	151	0.585717664	0.083673952	0	0.334696	7	
17	16	206.9565217	134.4229692	141.4597	6.011806265	3.429492254	-41.1248442	4.720649	1.752972691	
18	17	56.30434783	117.036036	213.1287	3.308481887	1.622560571	53.00312881	2.465521	2.039049849	
19	18	53.33333333	114.5679348	15.40082	2.53727609	1.988341325	72.26072715	2.262809	1.276076727	
20	19	467.8985507	153.5710082	281.4062	10.74026063	4.865186336	-67.3632108	7.802723	2.207574363	
21	20	274.8550725	166.0292644	87.3314	8.73190953	3.175187537	-3.00390034	5.953549	2.75004529	
22	21	160.5072464	149.8564334	26.84424	5.183747863	3.092698641	49.16128154	4.138223	1.676124467	
23	22	9.855072464	134.3382353	184.7059	1.451080499	0.780010591	-25.9086164	1.115546	1.860334353	
24	23	47.31884058	147.5130168	360.2787	2.586025285	1.884751498	14.8572326	2.235388	1.372077586	
25	24	183.2608696	184.1573745	211.9423	6.554349664	2.889150959	-58.2487644	4.72175	2.268607545	
26	25	85.28985507	184.9039932	136.6168	3.5730523	2.598821814	75.58602725	3.085937	1.374873907	
27	26	51.23188406	195.0452617	363.0736	3.779525877	1.316685446	-2.02765228	2.548106	2.870485041	
28	27	291.3043478	210.940796	38.88706	5.967102309	4.67865788	-72.7085485	5.32288	1.275387614	
29	28	0.362318841	186	112	0.41836976	0.083673952	0	0.251022	5	
30	29	228.7681159	228.4786189	161.5024	5.112642909	4.361007942	86.53002707	4.736825	1.172353496	
31	30	79.56521739	215.2067395	320.4927	3.990068932	2.056208471	-76.7042071	3.023139	1.940498247	
32	31	62.89855072	228.4205069	257.2442	3.371360991	1.78014585	53.35662648	2.575753	1.893867849	
33	32	7.463768116	234.9126214	347.5631	2.67777198	0.381081587	19.31111227	1.529427	7.026768207	